

## INFORMATION TO USERS

This manuscript has been reproduced from the microfilm master. UMI films the text directly from the original or copy submitted. Thus, some thesis and dissertation copies are in typewriter face, while others may be from any type of computer printer.

The quality of this reproduction is dependent upon the quality of the copy submitted. Broken or indistinct print, colored or poor quality illustrations and photographs, print bleedthrough, substandard margins, and improper alignment can adversely affect reproduction.

In the unlikely event that the author did not send UMI a complete manuscript and there are missing pages, these will be noted. Also, if unauthorized copyright material had to be removed, a note will indicate the deletion.

Oversize materials (e.g., maps, drawings, charts) are reproduced by sectioning the original, beginning at the upper left-hand corner and continuing from left to right in equal sections with small overlaps.

ProQuest Information and Learning  
300 North Zeeb Road, Ann Arbor, MI 48106-1346 USA  
800-521-0600

UMI<sup>®</sup>



University of Alberta

Development of Verification Procedures using a Flat-Panel EPID, and Application and Investigation of Radiobiological Models, for Intensity-Modulated Radiotherapy

by

Bradley John Warkentin



A thesis submitted to the Faculty of Graduate Studies and Research in partial fulfillment of the requirements for the degree of Doctor of Philosophy

in

Medical Physics

*Department of Physics*

Edmonton, Alberta

Spring 2005



Library and  
Archives Canada

Bibliothèque et  
Archives Canada

0-494-08313-1

Published Heritage  
Branch

Direction du  
Patrimoine de l'édition

395 Wellington Street  
Ottawa ON K1A 0N4  
Canada

395, rue Wellington  
Ottawa ON K1A 0N4  
Canada

*Your file* *Votre référence*

*ISBN:*

*Our file* *Notre référence*

*ISBN:*

**NOTICE:**

The author has granted a non-exclusive license allowing Library and Archives Canada to reproduce, publish, archive, preserve, conserve, communicate to the public by telecommunication or on the Internet, loan, distribute and sell theses worldwide, for commercial or non-commercial purposes, in microform, paper, electronic and/or any other formats.

The author retains copyright ownership and moral rights in this thesis. Neither the thesis nor substantial extracts from it may be printed or otherwise reproduced without the author's permission.

**AVIS:**

L'auteur a accordé une licence non exclusive permettant à la Bibliothèque et Archives Canada de reproduire, publier, archiver, sauvegarder, conserver, transmettre au public par télécommunication ou par l'Internet, prêter, distribuer et vendre des thèses partout dans le monde, à des fins commerciales ou autres, sur support microforme, papier, électronique et/ou autres formats.

L'auteur conserve la propriété du droit d'auteur et des droits moraux qui protègent cette thèse. Ni la thèse ni des extraits substantiels de celle-ci ne doivent être imprimés ou autrement reproduits sans son autorisation.

---

In compliance with the Canadian Privacy Act some supporting forms may have been removed from this thesis.

Conformément à la loi canadienne sur la protection de la vie privée, quelques formulaires secondaires ont été enlevés de cette thèse.

While these forms may be included in the document page count, their removal does not represent any loss of content from the thesis.

Bien que ces formulaires aient inclus dans la pagination, il n'y aura aucun contenu manquant.

  
**Canada**

# Abstract

Improved procedures for dosimetric verification of intensity-modulated radiotherapy (IMRT) treatments using an amorphous silicon flat-panel electronic portal imaging device (EPID) are described in this work. The two pre-treatment verification techniques compare either 2-D or 3-D dose distributions based on EPID measurements to corresponding distributions calculated by a treatment planning system (TPS). Accurate measurement of the incident fluence of an IMRT field with the EPID is the foundation of both procedures. Fluence profiles are extracted from EPID images by deconvolution with scatter kernels that characterize signal spread in the EPID. The kernels are derived using Monte Carlo simulations of dose deposition in the EPID and empirical fitting methods. In the 2-D verification, the EPID-measured fluences are convolved with a kernel describing dose deposition in a water phantom, and cross-calibrated with ion chamber measurements. The beam-by-beam 2-D verifications of three step-and-shoot IMRT treatments using the EPID are in good agreement with those performed with film, with a mean percent difference of  $0.3 \pm 1.0$  % (24 fields). For the 3-D verification technique, EPID-measured 2-D fluence modulation profiles for each field are used as input for the TPS, which then generates 3-D dose distributions. The EPID-based doses for three IMRT plans suggested that the planned TPS doses underestimated the mean dose in the critical structures of the spinal cord and the parotids by approximately 4 Gy (11 – 14 %). Radiobiological modeling calculations indicate that such underestimates may lead to clinically significant under-predictions of normal tissue complication rates.

This thesis also includes investigations regarding the application and development of radiobiological models, since their use may be particularly beneficial for IMRT. A convenient computational tool was developed that furnishes current modeling predictions of tumor control probability (TCP) and normal tissue complication probability (NTCP) for 3-D dose distributions. In a more fundamental modeling study, potential difficulties in the interpretation of fits to clinical data resulting from the inherent population heterogeneity of such data are explored. The incorporation of the dynamic processes of repair, repopulation, and resensitization in TCP models is also investigated with respect to the description of fractionation effects.

# Acknowledgements

I am truly grateful for the help and support of many people while completing this thesis. First, a huge debt is owed to those with whom I worked most closely on the various thesis-related projects. The supervision and guidance of Dr. Gino Fallone is very appreciated. His remarkable breadth of knowledge in medical physics and his ambitious efforts to investigate at the frontiers of this field so that further advancements in radiotherapy may be realized are admired. I also thank him for his tireless efforts in helping me procure scholarship support during my tenure at the University of Alberta, which is certainly not an insignificant contribution to a graduate student's success. I also greatly respect and learned much from Dr. Satyapal Rathee, and thank him for both his invaluable instruction and his subtle forms of encouragement during the EPID-related work. My friend Dr. Stephen Steciw was my full partner in the EPID work (the "Stec-like" half of "BS" Research). I thank him not only for his many ideas, but also for his great enthusiasm, which made working together so enjoyable. For the radiobiological modeling projects, I had the pleasure of working with Pavel Stavrev and Nadia Stavreva, who I consider mentors in this area of study. I always will appreciate Pavel's up-beat ("Zen"-like) and passionate approach to not only research, but also life in general. I also would like to acknowledge the efforts of my thesis and supervisory committee members, Drs. Sloboda, Hooper, and Sydora, as well as my external thesis reviewer, Dr. G.P. Raaphorst, for helpful suggestions and thoughtful consideration and review of my thesis.

The Medical Physics department at the Cross Cancer Institute has been a tremendous place to work and learn during my Ph.D. years. Everyone in the department has been very willing to help and teach whenever necessary. At the risk of forgetting many other contributions, I'd like to give a special mention to the following. Dr. Sloboda, and his graduate students (my friends) Charlie and Geetha, as well as Brad Murray, are thanked for being valuable resources of EPID knowledge. Colin Field also generously made available his expertise with the Helax-TMS treatment planning system (particularly necessary for the 3-D verification project). I am grateful for Debbi Howorko's efficient secretarial help, and for her welcome when I first arrived in Edmonton. Also crucial to my enjoyment at the Cross were the interactions with my

talented fellow graduate students, several of which I count as both colleagues and friends. In this regard, I especially want to thank Charles, Charlie, Alasdair, Isabelle, Geetha, Teo, and Deluan.

The funding support through various scholarships of the University of Alberta, the Department of Oncology, the Alberta Cancer Board, and the Alberta Heritage Foundation for Medical Research are also gratefully acknowledged. This support, which exemplifies the commitment of these organizations to research excellence in Alberta, made it possible to pursue my doctorate without being burdened by financial worries.

As important as all the professional and financial assistance received, was the personal support of those people who are most important in my life, my friends and family. Especially ... Thank you Mom and Dad for your consistent love and support, and for always being proud of me – even though it may have embarrassed me at times when I was younger, it always meant a lot to me. Also thanks to my four wonderful older sisters – Janet, Karen, Norma, and Margaret – your love and thoughtfulness has always been a great constant in my life.

To the most important person in my life, my beautiful (in so many ways) wife Heather, I can not find adequate words to say how much I appreciate you and all the things that you do for me. Finding you is the greatest “accomplishment” of my life, and your love is my greatest treasure. I will love you always.

# Table of Contents

<b>Chapter 1: Introduction .....</b>	<b>1</b>
A. Intensity-Modulated Radiotherapy (IMRT).....	1
B. Verification of IMRT Treatments .....	5
i. Characteristics of IMRT Necessitating Verification Procedures.....	5
ii. General Description of IMRT Verification Procedures.....	7
iii. Overview of the use of Film and EPIDs as IMRT Dosimeters .....	9
iv. Overview of Proposed 2-D and 3-D IMRT Verification Procedures .....	10
a. Review of EPID calibration .....	10
b. Proposed EPID-based 2-D IMRT Verification Technique.....	12
c. Proposed EPID-based 3-D IMRT Verification Technique.....	12
C. The Role of Radiobiological Modeling in IMRT.....	14
i. Inverse Optimization of IMRT treatments.....	15
ii. Adaptation of treatments.....	17
iii. Individualization of treatments.....	17
iv. Confounding Issues of Radiobiological Modeling .....	18
v. Overview of Radiobiological Investigations in this Work .....	19
D. Overview of Thesis Structure .....	20
E. References .....	21
<b>Chapter 2: EPID-based IMRT Verification – Methods.....</b>	<b>32</b>
A. Basic Experimental Details.....	32
i. EPID Measurements .....	32
ii. Fluence Measurements using a Diamond Detector .....	33
B. Physical Structure of the Varian aS500 EPID.....	34
C. Image Acquisition using the Varian aS500 EPID.....	35
i. General Description .....	35
ii. Image Acquisition using “IMRT” Mode .....	36
iii. Effect of Buffer Deadtimes and Potential Ghosting Effects on EPID Images ....	37
iv. Accuracy of IMRT Mode for Step-and-shoot IMRT.....	43
v. Flood- and Dark-field Image Corrections.....	46
vi. Correction of Fluence Profile Distortions caused by the Flood-field Correction .....	47
D. Pencil-beam Kernels Describing Blurring in the EPID .....	50
i. Monte-Carlo Dose-deposition Kernels .....	50
ii. Empirically-derived Optical Spread Kernels.....	53
iii. Original 15 MV EPID Kernels used in 2-D verifications .....	54
iv. 6 MV EPID Kernel used in 3-D Verifications.....	55
v. “New” 15 MV EPID Kernel used in 3-D Verifications.....	60
E. IMRT Verification using 2-D Beam's Eye View Dose Distributions .....	62
i. Overview of the Method.....	62
ii. Calculation of 2-D BEV Doses with the EPID.....	64
F. IMRT Verification using 3-D Dose Distributions in a Patient’s CT Anatomy .....	67

i. Calculation of 3-D Doses from EPID Measurements of Incident Fluence.....	67
ii. Normalization of Dose Distributions Calculated by the TPS.....	69
iii. TPS Dose Calculations with a “Point- Source” Model .....	70
G. Summary .....	71
H. References.....	72
<b>Chapter 3: EPID-based IMRT Verification – Results .....</b>	<b>75</b>
A. Pencil Beam Kernels used to Extract Fluence Profiles from EPID images.....	75
B. Comparisons of EPID-derived Fluence Profiles and Measured Diamond Detector Fluences .....	79
i. Open fields and IMRT Segments.....	79
ii. Sensitivity of EPID profiles to the amount of backscatter used in the EPID model .....	84
iii. Effect on EPID profiles of the short-range exponential term in $K_{back-glare}$ .....	87
iv. Sensitivity of the EPID profiles to different regions of the EPID kernel .....	89
C. EPID phantom scatter factors: measured vs. kernel-based predictions .....	92
D. Dose calibration: step-window doses.....	94
E. 2-D Verification Results.....	97
i. Comparison between ion chamber and EPID relative dose profiles .....	97
ii. Comparisons between TPS, film, and EPID doses for open-fields.....	100
iii. 2-D IMRT Verifications for three patient treatment plans .....	102
F. 3-D Verification Results.....	106
i. Comparisons of 2-D dose distributions: $D_{EPIDflu}$ , $D_{EPIDflu/pnt}$ , $D_{EPID}$ , and $D_{TPS}$ .....	106
a. Open fields and IMRT- segment field .....	107
b. Multi-segment IMRT fields.....	111
ii. Comparison of 3-D EPID doses with TLD Measurements .....	111
iii. 3-D IMRT Verification of clinical IMRT treatment plans .....	113
iv. Radiobiological significance of 3-D verification results .....	116
G. Comparison and summary of 2-D and 3-D IMRT verification procedures.....	117
H. References.....	119
<b>Chapter 4: TCP-NTCP Estimation Module.....</b>	<b>121</b>
A. Introduction.....	121
B. Methods.....	122
i. Radiobiological Models.....	122
a. Lyman (Sigmoidal Dose Response) NTCP model.....	124
b. Critical Volume (CV) NTCP model .....	125
c. TCP model based on Poisson statistics .....	126
d. TCP model incorporating radiobiological data.....	127
ii. Parameter Databases.....	128
a. Lyman databases .....	129
b. Critical Volume (“population”) databases .....	130
c. Poisson TCP databases.....	130
iii. Program Architecture .....	131

a. Input .....	131
b. Parameter Selection/Retrieval.....	131
c. Calculation of the NTCP / TCPs.....	132
d. Calculation of the probability distribution of the expected number of complications .....	133
e. Display and output .....	133
C. Results and Discussion.....	135
i. Retrospective analysis of treatments for a cohort of patients .....	135
ii. Testing of the sensitivity of model predictions to parameter values .....	138
D. Conclusion .....	139
E. References .....	139

## **Chapter 5: Investigations of Current Radiobiological Models ..... 143**

A. Theoretical Background: Cell Survival and Dose Response Relationships .....	143
i. Linear Quadratic Cell Survival Model.....	143
ii. Tumor and Normal Tissue Dose Response Models .....	148
a. Phenomenological Expressions.....	148
b. Mechanistic Models .....	150
iii. Expressions relating $D_{50}$ and $\gamma_{50}$ to Radiobiological Parameter Values .....	152
B. Evaluation of a TCP model incorporating population heterogeneity.....	158
i. Introduction.....	158
ii. Theory.....	160
iii. Methods .....	164
a. Generation of Pseudo-data .....	164
b. Fitting Techniques: Maximum-Likelihood and p-values .....	167
iv. Results.....	169
a. Evaluation of the Validity of the RH Approximation: Comparison of $TCP_{RH}$ , $TCP_{1D}$ and $TCP_{3D}$ .....	169
b. Fits to Pseudo-Data Consisting of One Fractionation Regime .....	172
c. Fits to Pseudo-Data Consisting of Three Fractionation Regimes .....	178
v. Discussion and Conclusion .....	180
C. Application of Robust TCP Models Incorporating Tumor Dynamics to Describe Fractionation Effects.....	182
i. Introduction.....	182
ii. Theory.....	183
a. Repopulation: Limitations of the Poisson or Binomial TCP models.....	183
b. Zaider-Minerbo TCP model: A Robust Method of Including Repopulation .....	185
c. Repair .....	187
d. Reoxygenation: Incorporation of time-dependent radiosensitivity.....	187
iii. Methods .....	188
a. Experimental Data.....	188
b. Fitting Technique .....	189
iv. Results.....	190
a. Repair and Repopulation.....	190
b. Resensitization .....	194

v. Conclusion .....	196
D. References .....	197
<b>Chapter 6: Conclusion.....</b>	<b>204</b>
References.....	209
<b>Bibliography .....</b>	<b>210</b>

# List of Tables

**Table 3.1.** Best-fit parameters for fits of a function that is the sum of four exponentials to the various kernels used in this work..... 78

**Table 3.2.** Dependence of the fits of EPID fluence profiles to diamond profiles for 4 x 4 and 20 x 20 cm<sup>2</sup> 6 MV open fields on the thickness of water backscatter material used in the EPID model (for EGSnrc simulations). The quality of the fits is characterized by the ratio of the  $SS_{ROI}$  and  $\Delta_{trans}$  values (described in the text) calculated for each “backscatter” kernel (without  $K_{back-glare}$ ) to the analogous values obtained using the “best”  $K_{EPID}$  kernel (no backscatter, with  $K_{back-glare}$ ). Ratio values less than one indicate a relatively better fit. .... 86

**Table 3.3.** Dependence of the fits of EPID fluence profiles to diamond profiles on the first exponential term in  $K_{back-glare}$ . The quality of the fits is characterized by the ratio of the  $SS_{ROI}$  and  $\Delta_{trans}$  values for a  $K_{back-glare}$  kernel using  $C_1 = 1037.1 \text{ cm}^{-1}$  (*i.e.* short-range delta function) to those values with a kernel with  $C_1 = 37.1 \text{ cm}^{-1}$ ..... 88

**Table 3.4.** Sensitivity of the fits of 6 MV EPID fluence profiles to diamond profiles on the different parameters ( $a_1 \dots a_7$ ) in the quadruple-exponential function (Eq. (3.1)) used to describe the shape of  $K_{EPID}$ . The quality of the fits is characterized by the ratio of the  $SS_{ROI}$  and  $\Delta_{trans}$  values for a kernel with one of the parameters modified, to the values obtained with the original (*par0*) best-fit parameters: (23.6 cm<sup>-1</sup>, 3.66 x 10<sup>-3</sup>, 3.98 cm<sup>-1</sup>, 2.37 x 10<sup>-4</sup>, 0.840 cm<sup>-1</sup>, 1.47 x 10<sup>-5</sup>, 0.128 cm<sup>-1</sup>). .... 90

**Table 3.5:** Comparison between measured and simulated values for the 15 MV EPID-phantom scatter factors for a range of square field sizes. Simulated values are calculated by convolution of an open beam primary fluence with the  $K_{EPID}$  kernel. .... 94

**Table 3.6.** Absolute doses measured with an ion chamber at 10 cm depth in water for each of the 4 x 4 cm<sup>2</sup> sub-fields comprising the “step-window” field (240 MUs total). The errors for the “water tank” doses are the deviations in the mean of two sets of measurements taken on different days..... 95

**Table 3.7.** Numerical comparison between doses measured with the TPS, film, and the EPID corresponding to the images in Fig. 3.16. Values for the mean and standard deviation of the % differences between the three methods of determining dose are provided for the 10 x 10 cm<sup>2</sup> and 2 x 2 cm<sup>2</sup> fields, both when excluding (0.5 cm inside each nominal field edge) and when including (0.5 cm outside each field edge) the penumbra region of the fields. .... 101

<b>Table 3.8.</b> Results from 2-D IMRT verifications of three clinical IMRT treatment plans based on comparison of TPS doses to measured film or EPID doses. The BEV doses are expressed as percentages of the maximum dose in the EPID distribution. The dose difference statistics (mean and standard deviation) are calculated for pixels lying within a ROI defined just outside the perimeter of each IMRT field. The given errors are the standard deviation in the mean and standard deviation for each set of values. ....	103
<b>Table 3.9.</b> Comparison of the 2-D EPID-based verification results when using the $K_{EPID}^{15MV} _{new}$ kernel instead of $K_{EPID}^{15MV} _{old}$ to describe scattering processes in the EPID...105	105
<b>Table 3.10.</b> The impact of image processing on the results of 2-D EPID-based verifications. The “unprocessed” verification assumed that $D_{EPID}$ is simply proportional to the raw EPID image, whereas the “processed” verification involved first executing image processing steps (cf. Eqs. (2.6), (2.14), (2.17)) that include deconvolution and convolution of the raw image.....	106
<b>Table 3.11.</b> Statistical comparison of different methods of calculating dose at 10 cm depth in a water phantom: $D_{EPIDflu}$ (EPID $\Psi_{mod}$ , TPS convolution), $D_{TPS}$ (TPS $\Psi_{mod}$ , TPS convolution), $D_{EPIDflu / pnt}$ (EPID $\Psi_{mod}$ , TPS convolution with a “point” source), and $D_{EPID}$ (EPID $\Psi_{mod}$ , TPS-independent convolution). Mean dose differences and standard deviations as percentages of the maximum $D_{EPID}$ dose are calculated for two ROIs (regions of interest) and a number of different fields for photon beam energies of (a) 6 MV and (b) 15 MV.....	108
<b>Table 3.12.</b> Comparisons of different methods of calculating the 2-D dose (10 cm depth, water phantom) for the multi-segment IMRT fields comprising three clinical IMRT treatment plans. Statistics are calculated for ROI2, which includes the entire field and the penumbra.....	111
<b>Table 3.13.</b> Measured TLD doses ( $\pm 3\%$ ) compared to TPS-calculated doses using fluences modeled by the TPS ( $D_{TPS}$ ) and EPID-measured fluences ( $D_{EPIDflu}$ and $D_{EPIDflu / pnt}$ ) for an IMRT treatment of an anthropomorphic head and neck phantom.....	112
<b>Table 3.14.</b> 3-D IMRT verification results: comparison of TPS ( $D_{TPS}$ ) and EPID-based ( $D_{EPIDflu}$ or $D_{EPIDflu / pnt}$ ) 3-D dose distributions for three clinical IMRT treatment plans.....	113
<b>Table 3.15.</b> Comparison of radiobiological modeling predictions of the NTCP based on TPS ( $D_{TPS}$ ) and EPID-based ( $D_{EPIDflu}$ or $D_{EPIDflu / pnt}$ ) 3-D dose distributions for three clinical IMRT treatment plans.....	117

<b>Table 4.1.</b> A list of the parameters and their description for each of the models used in the module. Abbreviations: FSU = functional sub-unit, CV=Critical Volume, LQ = linear-quadratic. ....	123
<b>Table 5.1.</b> Expressions relating the position and slope parameters, $D_{50}$ and $\gamma_{50}$ , for dose response curves calculated using the binomial TCP, Poisson TCP, Critical Element NTCP, or Critical Volume NTCP models to the radiobiological parameters for each of these models. The expressions are valid assuming that cell survival is described by the time-independent LQ model (Eq. (5.2)), and that all dose points in the dose response curves correspond to the same number of fractions, $n$ .....	156
<b>Table 5.2.</b> Radiobiological parameters used to generate the pseudo-data sets employed in the fitting exercises designed to test the RH heterogeneity model. ....	166
<b>Table 5.3.</b> The effect of different variables on the statistically acceptable range of fit values for the heterogeneity factor $\mu$ extracted from fits to pseudo-data generated for three fractionation regimes. The variables investigated are the model ( $TCP_{1D}$ or $TCP_{RH}$ ) used to fit the pseudo-data, and the characteristics of the pseudo-data: the number of patients per dose point ( $n_{pat}$ ), the number of data points ( $ndpts$ ), and the inherent strength of the $\beta$ -mechanism.....	180
<b>Table 5.4.</b> Best-fit parameter values corresponding to the fits shown in Fig. 5.17.....	191
<b>Table 5.5.</b> Best-fit parameter values corresponding to the fits shown in Fig. 5.18.....	195

# List of Figures

**Figure 1.1.** Illustration of the concept of segmental IMRT (SMLC). The images 1-6 represent individual static sub-fields (or segments). The weighted summation of the sub-fields (with respective weights of 0.250, 0.159, 0.125, 0.164, 0.130, and 0.171) produces the intensity-modulated field shown. .... 3

**Figure 1.2.** Flowchart of the inverse IMRT planning process.<sup>11</sup> ..... 4

**Figure 1.3.** Paradigm for individualization of radiotherapy based on radiobiological assays and models. .... 18

**Figure 2.1.** The acquisition time per image frame plotted as a function of the total number of frames acquired in an image for (a) 15 MV/100 MU/min, and (b) 6 MV/100 MU/min. The squares and circles represent the time/frame before and after (respectively) correcting the acquisition time for buffer delays. The vertical lines correspond to the numbers of frames at which buffer delays occur. .... 38

**Figure 2.2.** EPID pixel value (*i.e.*  $EPID_{total}$ ) per MU plotted as a function of the number of frames used to acquire an image (15 MV/100 MU/min). Eq. (2.2) is used to correct the dose response for buffer delays (closed circles). The solid line depicts the application of an additional correction for “ghosting” effects described in Ref. [10]. The data in (a) and (b) is the same: the graph in (a) shows only the data nearest the first buffer delay at 64 frames (vertical line), while (b) covers a wider range of  $n_{frame}$  values. .... 40

**Figure 2.3.** The 2-D difference images ( $EPID_{total} - EPID_{total}^{wgt-sum}$ ) expressed as a percentage of the maximum pixel value in  $EPID_{total}^{wgt-sum}$ , and the corresponding histogram for pixels within the ROI (delineated by the line in the dose difference image) are shown for linac dose rates of (a) 600 MU/min and (b) 100 MU/min. The left and right columns for each dose rate depict the effect on the differences of increasing the number of MUs used to acquire the  $EPID_{total}$  image. .... 45

**Figure 2.4.** Simplified model of the geometry of the aS500 EPID used in the EGSnrc Monte Carlo simulations used to derive  $K_{dose}$ . The cross-section of each of the five layers was 30 x 30 cm<sup>2</sup> (383 x 383 pixels). .... 52

**Figure 2.5.** Incident photon beam spectra used for EGSnrc simulations. The spectra are results of BEAMnrc simulations for Varian linac (a) 6 MV and (b) 15 MV photon beams published by Sheikh-Bagheri and Rogers.<sup>3</sup> ..... 53

<b>Figure 2.6.</b> The change in $K_{dose}^{6MV}$ derived from EGSnrc simulation when a 6.5 mm air gap layer is placed between the extrinsic build-up and copper plate layers in the EPID model depicted in Fig. 2.4.....	56
<b>Figure 2.7.</b> The change in $K_{dose}^{6MV}$ derived from EGSnrc simulation for different thicknesses (0, 1, 2, or 4 cm) of the backscatter layer in the EPID model (layer 5 in Fig. 2.4). ...	57
<b>Figure 2.8.</b> In-plane 15 MV EPID profile of a 20 x 20 cm <sup>2</sup> open field. The dashed line is used to highlight the asymmetry between the penumbras on the left and right sides of the field. It is believed that the metal R-arm below the EPID contributes additional backscatter to pixels at the top of the EPID array (corresponding to the right side of the profile). .....	60
<b>Figure 2.9.</b> Flowchart of the 2-D IMRT verification process. ....	63
<b>Figure 2.10.</b> Illustration of the steps involved in calculating the BEV dose distribution at 10 cm depth in a water phantom from an EPID image. (a) The raw EPID image of the step-window calibration field is converted to a dose image in arbitrary dose-pixel units via the shown processing steps (cf. Eqs. (2.6), (2.12), (2.14), and (2.17)). This dose image is cross-calibrated with step-window absolute doses measured with an ion chamber to generate a calibration curve that yields the linear calibration coefficient, $k_{cal}$ . (b) The same image processing steps used in (a) are utilized to convert a raw EPID image of an IMRT field to a dose image in arbitrary dose-pixel units. Using $k_{cal}$ (Eq. (2.17)), this image is then converted to an absolute dose image.....	65
<b>Figure 2.11.</b> EPID image of the step-window calibration field used to calculate the dose calibration coefficient $k_{cal}$ . There are twelve 4 x 4 cm <sup>2</sup> sub-fields corresponding to irradiations of 10 MUs (bottom left) to 120 MUs (top right) in 10 MU increments..	66
<b>Figure 2.12.</b> Flowchart of the 3-D verification process. ....	68
<b>Figure 3.1.</b> (a) 6 MV, (b) “new” 15 MV, and (c) “old” 15 MV pencil-beam kernels used to describe blurring in the EPID: the dose kernel ( $K_{dose}$ ) is generated from Monte-Carlo simulations, the back-glare kernel ( $K_{back-glare}$ ) is derived empirically, and the total EPID kernel ( $K_{EPID}$ ) is the convolution of the dose and back-glare kernels. A comparison of the three total EPID kernels is shown in (d). .....	76
<b>Figure 3.2.</b> (a) $K_{flood-phantom}$ kernel used to generate the simulated flood-field $I_{flood-sim}$ , and (b) $K_{BEVphantom}$ kernel used to convert photon fluence to BEV dose for both 6 and 15 MV. ....	77

<b>Figure 3.3.</b> Comparison of cross-plane profiles through an open 10 x 10 cm <sup>2</sup> 6 MV field derived from in-air diamond detector measurements, raw EPID images ( $EPID_{PV}$ ) before deconvolution, and EPID images after the deconvolution to extract incident fluence ( $\Psi_p$ ).....	80
<b>Figure 3.4.</b> Comparison of diamond and EPID-derived fluence profiles for (a) 2 x 2 and 4 x 4 cm <sup>2</sup> and (b) 10 x 10 and 20 x 20 cm <sup>2</sup> open 6 MV fields.....	81
<b>Figure 3.5.</b> Same as Fig. 3.4, except for 15 MV. As illustrated, the differences in the profiles between using the “new” or “old” EPID kernels in the deconvolution are negligible.....	81
<b>Figure 3.6.</b> (a) Image of the IMRT segment field corresponding to the profiles shown in Fig. 3.7(a & b). The profiles are taken along the dashed line, and the numbers identify the regions of the segment described in the text and indicated in Fig. 3.7. (b) Image of the multi-leaf collimated segment field corresponding to the profile (along the dashed line) in Fig. 3.7 (c).....	82
<b>Figure 3.7.</b> Comparison of diamond and EPID fluence profiles for multi-leaf collimated fields. (a) 6 MV and (b) 15 MV profiles along the dashed line through field shown in Fig. 3.6(a). (c) 6 MV profiles along the dashed line through field shown in Fig. 3.6(b).....	83
<b>Figure 3.8.</b> Diamond and EPID (non-optimal) profiles through a 20 x 20 cm <sup>2</sup> field. (a) The ROI (region of interest) used to calculate $SS_{ROI}$ (Eq. (3.2)) includes the four regions demarcated by the four pairs of vertical lines. (b) $\Delta_{trans}$ is the mean value of the differences between each of the four sets of horizontal lines, which are located at the tops and bases of the field edges.....	85
<b>Figure 3.9.</b> The effect of the amount of backscatter used in the EGSnrc model of the EPID on EPID 6 MV fluence profiles for 4 x 4 and 20 x 20 cm <sup>2</sup> fields. The three EPID profiles were generated with three different deconvolution kernels ( $K_{dose}$ ) corresponding to 0.5, 1.5, and 2.5 cm of water backscatter.....	87
<b>Figure 3.10.</b> Dependence of 4 x 4 and 20 x 20 cm <sup>2</sup> EPID profiles on the first exponential term ( $C_1$ ) in $K_{back-glare}$ . (a) 6 MV: use of $C_1 = 1037.1 \text{ cm}^{-1}$ (i.e. short-range delta function) instead of $C_1 = 37.1 \text{ cm}^{-1}$ primarily affects the height of the long-range tail for the 20 x 20 field. (b) 15 MV: use of $C_1 = 1037.1 \text{ cm}^{-1}$ results in a short-range over-deconvolution for both the 4 x 4 and 20 x 20 fields.....	89
<b>Figure 3.11.</b> Effect on the shape of the EPID kernel described by the quadruple-exponential fit function ( $K_{fit}$ in Eq. (3.1)) when one of the parameters ( $a_1$ , $a_3$ , $a_5$ , or $a_7$ ) is (a) decreased or (b) increased from its optimal fit value ( $a_{10}$ , $a_{30}$ , $a_{50}$ , or $a_{70}$ ).....	91

- Figure 3.12.** Effect on the 4 x 4 and 20 x 20 6 MV EPID profiles when altering the shape of the EPID kernel by changing one of the parameters ( $a_1$ ,  $a_3$ ,  $a_5$ , or  $a_7$ ) in  $K_{fit}$  from its optimal value (see Fig. 3.11 above). ..... 91
- Figure 3.13:** A comparison of the EPID dose-pixel value relationship when measured using a single irradiation of the multi-segmented “step-window” pattern, individual irradiations of an MLC-collimated 4 x 4 cm<sup>2</sup> field corresponding to different MUs, and a single 100 MU irradiation of a 10 x 10 cm<sup>2</sup> field (without MLC). The linear fits to the “step-window” (solid line) and “individual 4x4” data (dashed line) are virtually indistinguishable; the linear calibration coefficients ( $k_{cal}$ ) are as shown. ....97
- Figure 3.14.** (a) Comparison of ion chamber (IC-10) and EPID-based (after deconvolution / convolution) profiles through a 2 x 2 cm<sup>2</sup> open field at 10 cm depth in water. After blurring the EPID profile by  $K_{IC10}$  (Eq. 3.5) to compensate for the geometric blurring inherent in the IC-10 profile, there is very good agreement between the IC-10 and EPID profiles. (b) Comparison of the  $K_{IC10}$  from Eq. 3.5 to the kernel shape predicted from simple geometric considerations. .... 99
- Figure 3.15.** Comparison of ion chamber and EPID-based (both with and without the additional blurring of  $K_{IC10}$ ) profiles at 10 cm depth in water. (a) 20 x 20 cm<sup>2</sup> open field profiles. (b) profile through the multi-leaf collimated segment field depicted in Fig. 3.6(b)..... 100
- Figure 3.16.** Images of the absolute percent difference (as a percent of the maximum EPID dose) between dose measurements made with the TPS, film, and the EPID for a (a) 10 x 10 cm<sup>2</sup> and a (b) 2 x 2 cm<sup>2</sup> open field..... 101
- Figure 3.17.** Dose profiles (centre of the field, cross-plane) derived from the EPID, film, and TPS for a (a) 10x 10 cm<sup>2</sup> and a (b) 2 x 2 cm<sup>2</sup> open field..... 102
- Figure 3.18.** Dose differences (as a percent of the maximum EPID dose) between the EPID, film, and TPS for the profiles of a (a) 10 x 10 cm<sup>2</sup> and a (b) 2 x 2 cm<sup>2</sup> open field shown in Figure 3.17. .... 102
- Figure 3.19.** (a) Dose distributions for an IMRT field based on EPID and film measurements and TPS calculations. (b) Dose difference distributions for: |TPS-Film|, |Film-EPID|, and |TPS-EPID|. (c) Dose difference histogram corresponding to each dose difference image directly above it in (b). The histograms are calculated for the ROI demarcated by the dashed line around the IMRT field in (b). Doses and dose differences are expressed as a percentage of the maximum dose in the EPID image..... 104

- Figure 3.20.** (a) Dose profiles along the dashed line through the IMRT field in Fig. 3.19(a) for EPID and film measurements and TPS calculations. (b) Dose difference profiles corresponding to the profiles in (a), expressed as a percentage of the maximum EPID dose. .... 104
- Figure 3.21.** Results for a  $1 \times 10 \text{ cm}^2$  field and a 6 MV beam: (a) 2-D dose difference maps (absolute values of the differences are shown) and (b) cross-plane profile through the center of the field. The doses and dose differences are expressed as percentages of the maximum  $D_{EPID}$  dose. The  $D_{TPS}$  dose deviates significantly from the other three doses based on EPID measurements. .... 110
- Figure 3.22.** Example output from the software developed for the analysis of 3-D IMRT verifications. (a) Original TPS dose distribution,  $D_{TPS}$ . The thicker black line delineates the left parotid gland. The other lines are isodose lines, with the thinner black line representing the 70 Gy line (prescription dose = 74 Gy). (b) Dose differences between TPS and EPID-based 3-D doses,  $D_{EPIDflu} - D_{TPS}$ . The thinner white lines are the 4 Gy isodose contours for the dose difference. (c) Dose difference frequency distribution (top) and associated statistics, and the DVHs (bottom) for the selected volume of interest (left parotid) for the  $D_{TPS}$  and  $D_{EPIDflu}$  distributions. .... 114
- Figure 3.23.** Comparison of DVHs derived from TPS ( $D_{TPS}$ ) and EPID-based ( $D_{EPIDflu}$  or  $D_{EPIDflu/pnt}$ ) dose distributions generated during 3-D IMRT verifications of patient 3's treatment plan. .... 114
- Figure 4.1.** Example output from the program for a case where the user has chosen to display and analyze DDVHs for the bladder, rectum, spinal cord, and a prostate tumor. .... 134
- Figure 4.2.** Program output after analysis of lung DVHs generated from the retrospective treatment planning of a cohort of 16 breast-cancer patients using two different treatment techniques. DVH #1 (solid line) is the cumulative DVH (averaged over the 16 patients) for a "5-field" technique, while DVH #2 (dotted line) is the corresponding DVH for a "wide-tangent" technique. For each set of DVHs, radiobiological model predictions of the mean NTCP are displayed for a number of different parameter sets available in the literature. .... 136
- Figure 4.3.** Program output displaying the distribution of the number of complications predicted from the DVHs for the mandible for a group of 10 patients based on two sets of radiobiological predictions based on the Emami *et al.*<sup>17</sup> data: (a) Lyman model, Burman *et al.*<sup>18</sup> parameters (b) "population" Critical Volume model, Stavrev *et al.*<sup>8</sup> parameters. .... 137

**Figure 4.4.** Program output displaying TCP predictions for the same DDVH for four sets of user-specified parameters: (i)  $\alpha = 0.30 \text{ Gy}^{-1}$ ,  $\beta = 0.03 \text{ Gy}^{-2}$ ,  $N = 1e6$ ,  $\lambda = 0.05 \text{ days}^{-1}$ ,  $n = 25$  fractions; (ii) same as (i), but with slightly decreased cellular radiosensitivity,  $\alpha = 0.27 \text{ Gy}^{-1}$ ,  $\beta = 0.027 \text{ Gy}^{-2}$ ; (iii) same as (i), but with the rate of repopulation doubled,  $\lambda = 0.10 \text{ days}^{-1}$ ; (iv)  $\alpha = 0.17 \text{ Gy}^{-1}$ ,  $\beta = 0.017 \text{ Gy}^{-2}$ ,  $N = 1e3$ ,  $\lambda = 0.05 \text{ days}^{-1}$ ,  $n = 25$  fractions. .... 139

**Figure 5.1.** Probability curves as calculated with the Poisson, logit, and probit models defined in Eq. (5.11) and using identical parameter values of  $D_{50} = 50 \text{ Gy}$  and  $\gamma_{50} = 3 \text{ Gy}$ ..... 150

**Figure 5.2.** Dependence of  $D_{50}$  on the number of fractions ( $n$ ), as predicted by the expressions in Table 5.1 for the CV NTCP model and the Poisson TCP model. The two NTCP curves illustrate the effect of changing the  $\alpha/\beta$  ratio, while the two TCP curves show the impact of repopulation ( $\lambda = 0 \rightarrow$  no repopulation.) The other parameter values for each of the four curves are given in the text. .... 158

**Figure 5.3.** Effect of patient-to-patient variation in  $\alpha$  on the shape of TCP curves. The population model in Eq. (5.40) was used to generate curves corresponding to increasing values of  $\sigma_{\alpha}$  (*i.e.* increasing heterogeneity). The other parameter values were  $\kappa = 13.8$ ,  $\alpha = 0.30 \text{ Gy}^{-1}$ ,  $\beta = 0.03 \text{ Gy}^{-2}$ ,  $\lambda = 0.10 \text{ days}^{-1}$ , and  $T_{lag} = 0$  (and  $\sigma_{\kappa} = 0$ ,  $\sigma_{\lambda} = 0$ ). The curve labeled  $\sigma_{\alpha} = 0$  was generated using the individual TCP model (Eq. (5.38)) and the same parameter values for  $\kappa$ ,  $\alpha$ ,  $\beta$ ,  $\lambda$ , and  $T_{lag}$ ..... 161

**Figure 5.4.** Comparison of population model predictions of  $TCP_{RH}$ ,  $TCP_{1D}$ , and  $TCP_{3D}$  for a population characterized by parameter values of  $\kappa = 16$ ,  $\alpha = 0.30$ ,  $\beta = 0.03$ ,  $\lambda = 0.10$ ,  $T_{lag} = 25$ ,  $\sigma_{\alpha} = 0.075$ ,  $\sigma_{\kappa} = 2$ , and  $\sigma_{\lambda} = 0.05$  for a treatment of  $n = 30$  fractions in  $T = 39$  days..... 170

**Figure 5.5.** The maximum difference between  $TCP_{RH}$  and  $TCP_{1D}$ ,  $\Delta TCP$ , as a function of (a)  $\sigma_{\alpha}$  and (b)  $\mu$ . Curves are generated for three sets of radiobiological parameters corresponding to different values of  $\alpha$  and/or  $D_{50}$  values. The dash-dotted line demarcating the  $\Delta TCP = 5\%$  level is used for reference purposes..... 170

**Figure 5.6.** The difference between the slope ( $\theta_{50}$ ) of the  $TCP_{RH}$  and  $TCP_{1D}$  curves,  $\Delta\theta_{50}$ , as a function of (a)  $\sigma_{\alpha}$  and (b)  $\mu$ . Curves are generated for three sets of radiobiological parameters corresponding to different values of  $\alpha$  and/or  $D_{50}$  values. For reference, the  $\theta_{50}$  values for the  $TCP_{1D}$  curves range from 1.5 to 6.7 %/Gy for  $\mu$  values increasing from 1.5 to 8 for the first set; the corresponding ranges for the second and third sets are 1.9 – 6.6 and 1.5 – 6.4 %/Gy, respectively..... 172

- Figure 5.7.** Fits (lines) of the RH model to pseudo-data (circles) generated for one fractionation regime and using parameter set (a) #1 and (b) #4, the latter set assuming greater  $\beta$  strength. The numbers in the legend correspond to the assumed (pseudo-data) or fitted values of the parameters  $\mu$ ,  $\kappa'/\alpha$ , and  $\beta/\alpha$ . As shown, fits with very different values for the heterogeneity parameter  $\mu$  can fit the pseudo-data well. (The fit lines are nearly indistinguishable visually)..... 173
- Figure 5.8.** Best-fit values of  $\mu$  obtained from fits to a large number of pseudo-data sets. (a) Histogram showing the frequency of observing given values of  $\mu$ . (b) Histogram of  $\mu$  divided into three sub-groups corresponding to three different ranges of best-fit  $\beta/\alpha$  values. This illustrates the correlation between the  $\mu$  and  $\beta/\alpha$  fit parameters. .... 175
- Figure 5.9.** Histograms of the best-fit parameter values of (a)  $\mu$  and (b)  $\beta/\alpha$ , from fits to a large number of pseudo-data sets. Each histogram is divided into three sub-groups corresponding to three different ranges of best-fit  $\kappa'/\alpha$  values. This illustrates the correlation between  $\kappa'/\alpha$  and the other two fit parameters..... 175
- Figure 5.10.** Fits (lines) of the RH model to pseudo-data (circles) based on parameter values (set #2) that describe a population without heterogeneity. The numbers in the legend correspond to fit values of  $\mu$ ,  $\kappa'/\alpha$ , and  $\beta/\alpha$ . Fits suggesting considerable population heterogeneity – e.g. CV's of 20, 30, or 40 % – all describe this data set well (fit lines are nearly indistinguishable)..... 177
- Figure 5.11.** TCP curves generated for two parameter sets corresponding to different levels of heterogeneity and  $\beta$  strength, for each of two different fractionation regimes. The curves illustrate that if fitting to a clinical data set without sufficient diversity with respect to the number of fractions, the inability to distinguish between the  $\mu$  and  $\beta/\alpha$  fit parameters would lead to large uncertainties when predicting the TCP for a different fractionation regime. .... 178
- Figure 5.12.** Example of a fit using the RH model assuming a CV of  $\mu = 2.0$  to pseudo-data generated for three fractionation regimes ( $n = 15, 30, 45$ ) that inherently contains heterogeneity characterized by  $\mu = 4.0$ . The  $p$ -value of the fit is 0.19. The numbers in the legend correspond to the parameter values  $\mu$ ,  $\kappa'/\alpha$ ,  $\beta/\alpha$ ,  $\lambda/\alpha$ , and  $T_{lag}$ . .... 179
- Figure 5.13.** Fits to pseudo-data (three fractionation regimes,  $\mu = 4.0$ ) with a smaller number of dose points. Statistically acceptable ( $p$ -value  $> 0.05$ ) fits to this data can be found with  $\mu$  values as low as 0.9 and as high as 8.0. The numbers in the legend correspond to the parameters  $\mu$ ,  $\kappa'/\alpha$ ,  $\beta/\alpha$ ,  $\lambda/\alpha$ , and  $T_{lag}$ ..... 180

- Figure 5.14.** Comparison of simulated surviving clonogen distribution and corresponding predictions of binomial statistics for radiobiological parameter values of  $N = 10^4$ ,  $\alpha = 0.30$ ,  $\beta = 0.03$ , and  $\lambda = 0.17$ , and a treatment of 25 fractions of 1.7 Gy delivered in 32 days. (a) TCP immediately after treatment: simulated = 0.53, Binomial = 0.43. (b) TCP 2 weeks after treatment: simulated = 0.53, Binomial TCP = 0. .... 184
- Figure 5.15.** Comparison of Zaider-Minerbo and Binomial TCP model predictions for parameter values of  $N = 10^4$ ,  $\alpha = 0.30$ ,  $\beta = 0.03$ ,  $n = 25$ ,  $T = 32$  and (a)  $\lambda = 0$  or (b)  $\lambda = 0.35$ . .... 186
- Figure 5.16.** Magnitude of the error in the TCP based on Binomial statistics. The difference between the reference Zaider-Minerbo TCP,  $TCP_{ZM}$  and the Binomial TCP,  $TCP_{Bin}$ , is plotted as a function of  $\lambda$  for various values of  $N$ .  $TCP_{ZM}$  and  $TCP_{Bin}$  are evaluated at the predicted  $D_{50}$  dose for the  $TCP_{Bin}$  curve. .... 187
- Figure 5.17.** Fits (lines) of TCP models to six fractionation regimes ( $n$  as indicated in the legend) of the Fischer-Moulder data (symbols). (a) Binomial TCP / LQ survival: complete sub-lethal repair, no repopulation. (b) Binomial TCP / LQ-IR survival: partial sub-lethal repair, no repopulation. (c) Zaider-Minerbo (ZM) TCP / LQ-IR survival: partial sub-lethal repair, with repopulation. (d) Zaider-Minerbo TCP / single-hit (SH) survival: no repair, with repopulation. .... 192
- Figure 5.18.** Fits (lines) with the Zaider-Minerbo (ZM) TCP model to all seven fractionation regimes of the Fischer-Moulder data (symbols). (a) Without resensitization ( $\alpha$  constant) and LQ cell survival. (b) With resensitization using time-dependent expression for  $\alpha$  (Eq. (5.57)) and LQ cell survival. (c) With resensitization and single-hit cell survival ( $\beta \equiv 0$ ). (d) Radiosensitivity  $\alpha$  as a function of time corresponding to plots in (a), (b), and (c). The radiosensitivity parameters for fit (b), the only one which can describe the inverse fractionation effect manifest between the three and five fraction data, are  $\alpha_0 = 0.085 \text{ Gy}^{-1}$ ,  $\alpha_m = 0.136 \text{ Gy}^{-1}$ ,  $c_1 \equiv 0 \text{ days}^{-1}$ , and  $c_2 = 0.076 \text{ days}^{-2}$ . .... 196

# List of Abbreviations

BED	biologically effective dose
BEV	beam's eye view
CCI	Cross Cancer Institute
CE	critical element (NTCP model)
CT	computed tomography
CV	critical volume (NTCP model)
DDVH	differential dose-volume histogram
DMLC	dynamic multi-leaf collimation
DNA	deoxyribonucleic acid
DQE	detective quantum efficiency
DVH	dose-volume histogram
EBRT	external beam radiotherapy
EGSnrc	Electron Gamma Shower (a Monte Carlo Radiation Transport Code), version developed by the NRC (National Research Council of Canada)
EPID	electronic portal imaging device
FSU	functional sub-unit
GMD	generalized mean dose
IGAR	image guided adaptive radiotherapy
IMRT	intensity-modulated radiotherapy
LPL	lethal-potentially lethal (cell survival model)
LQ	linear-quadratic (cell survival model)

LQ-IR	linear-quadratic incomplete repair (cell survival model)
MLC	multi-leaf collimator
MRI	magnetic resonance imaging
MU	monitor unit
NTCP	normal tissue complication probability
PET	positron emission tomography
PLL	potentially lethal lesion
RH	Roberts and Hendry (reference to authors of a TCP model)
ROI	region of interest
RT	radiotherapy
SDD	source-to-detector distance
SH	single hit (cell survival model)
SMLC	segmental multi-leaf collimation
TCP	tumor control probability
TFT	thin-film transistor
TLD	thermoluminescent dosimeter
TPS	treatment planning system
VOI	volume of interest
ZM	Zaider and Minerbo (reference to authors of a TCP model)

# Chapter 1: Introduction<sup>†</sup>

This thesis work describes investigations related to intensity-modulated radiotherapy (IMRT), an advanced technique of external beam radiotherapy. The work can be divided into two main project areas. The first involves development of methods for verifying the dosimetric accuracy of IMRT treatments based on use of an amorphous silicon electronic portal imaging device (EPID). The methods described aim to increase both the convenience and clinical relevance of IMRT verification procedures. The second part of this thesis work studies the application and utility of current radiobiological models. Reliable radiobiological models hold the promise of not only more accurate evaluation of treatment outcomes, but also improved optimization and customization of patient treatments. The potential benefit of incorporation of radiobiological knowledge in the radiotherapy treatment planning process is particularly great for IMRT. In this thesis, radiobiological models are used to predict the biological outcomes of IMRT dose distributions, and more specifically, to assess the biological consequences of the dosimetric uncertainties quantified by IMRT verification procedures.

This introductory chapter will briefly present contextual information of relevance to the thesis work, which is discussed in detail in the following chapters.

## A. Intensity-Modulated Radiotherapy (IMRT)

External beam radiotherapy (EBRT) is one of the primary treatment modalities for localized cancers. Unfortunately, in delivering radiation dose to a tumor, surrounding normal tissues are also irradiated, which can lead to unacceptable treatment side-effects. These normal tissue complications generally restrict the dose that can be safely delivered to the tumor, which may in turn limit the likelihood of tumor control. The efficacy of radiotherapy thus relies crucially on the geometric accuracy of the dose delivery.<sup>1</sup> IMRT is a technique that facilitates a greater conformation of dose to a tumor target, while distributing normal tissue dose away from critical organs.

---

<sup>†</sup> Versions of the material throughout this thesis has been accepted for publication/published in Refs. [116-121]. See Section 1.D at the end of this chapter for further details.

IMRT represents a departure from conventional radiotherapy (RT) delivery techniques in both the mechanics of dose delivery, and in the procedures of treatment planning. With conventional EBRT techniques, the size and shape of the radiation beam from a linear accelerator (linac) treatment unit (or alternatively, but now less commonly, a Cobalt treatment unit) is determined by the settings of a pair of collimating jaws. These conventional radiation beams are thus rectangular in shape, and nearly uniform in intensity. To achieve a suitable dose distribution (*i.e.* sufficiently high tumor dose, and low normal tissue dose), the task of treatment planning for conventional RT treatments entails optimization of the number, the angles of incidence, the sizes, and the relative weights of the radiation beams, and the selection of appropriate beam-modifying devices (*e.g.* wedges). Typically, a *forward* treatment planning process is employed for the optimization of these treatment parameters: the planner uses an iterative procedure involving adjustment of parameters and re-calculation of the resulting dose distribution.

As implied by its name, in its most literal interpretation IMRT simply refers to the use of beams with a non-uniform intensity. There are a number of methods of realizing beam modulation.<sup>2,3</sup> These include the use of scanned beams,<sup>4</sup> multi-leaf collimators (MLCs) with conventional linacs, physical compensators, or tomotherapy machines.<sup>5,6</sup> Currently, the most common kind of IMRT employs a linac-based MLC, and this is the type of IMRT of interest for this thesis work. An MLC is a collimating device attached to or (more often) within a linac treatment head that consists of many independently moving, narrow collimating leaves. The resolution of the dose delivery perpendicular to the direction of leaf travel is determined by the width of the leaves. As an example, the Varian Millennium 120 MLC (Varian Medical Systems, Palo Alto, CA) model used in this work has 60 pairs of leaves, with the central 40 pairs and outer 20 pairs having widths of 0.5 cm and 1.0 cm (measured at isocenter), respectively.

The many independent leaves of an MLC provide a flexible means of generating irregularly shaped, intensity-modulated beams. In dynamic multi-leaf collimation (DMLC), the MLC leaves move while the radiation beam is on. In this “sliding window technique,” each pair of leaves defines an opening that moves across the width of the field,<sup>7</sup> with the shape and intensity-modulation of a given field being thus determined by the size of the openings (or “windows”) between all the different pairs of leaves as a

function of time.<sup>2</sup> At our institute (Cross Cancer Institute, Edmonton, AB), segmental multi-leaf collimation (SMLC) is used in clinical practice; we describe improved verification procedures for this type of IMRT in Chapters 2 and 3. In the case of SMLC, which is also referred to as “step-and-shoot” IMRT, a single intensity-modulated field is realized by delivery of a number of static, MLC-defined sub-fields (Fig 1.1) at a given beam angle. The distinguishing feature of SMLC is that the radiation beam is off while the MLC leaves are moving into the new positions defining the next sub-field.

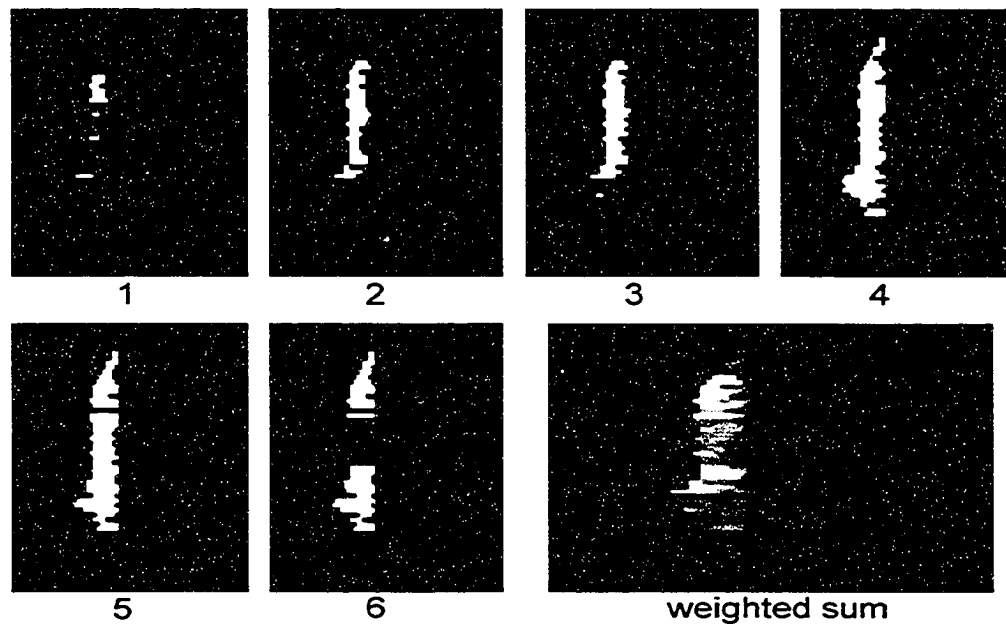


**Figure 1.1.** Illustration of the concept of segmental IMRT (SMLC). The images 1-6 represent individual static sub-fields (or segments). The weighted summation of the sub-fields (with respective weights of 0.250, 0.159, 0.125, 0.164, 0.130, and 0.171) produces the intensity-modulated field shown.

Use of intensity-modulated beams can, in theory, be combined with a *forward* treatment planning process (e.g. Refs.[8-10]), as used for conventional RT treatments. However, because of the large degree of freedom in designing the modulation profile of each beam, it is impossible to produce a truly optimal dose distribution using forward planning. Instead, the term IMRT generally implies the use of intensity-modulation in conjunction with *inverse* treatment planning. In the inverse planning process, depicted schematically in Fig. 1.2,<sup>11</sup> computers are used to optimize the fluence intensity profile of each beam. In the case of MLC-based IMRT, the optimized fluences are then converted to corresponding MLC leaf positions. To steer the optimization routine, the user

specifies quantitative treatment objectives, usually in the form of the prescribed dose to the tumor, and a limited number of dose-volume constraints for the relevant normal tissues. To reduce the computational complexity of the computer optimization, the user manually selects the number and angles of the incident beams, rather than including these parameters as part of the optimization process.

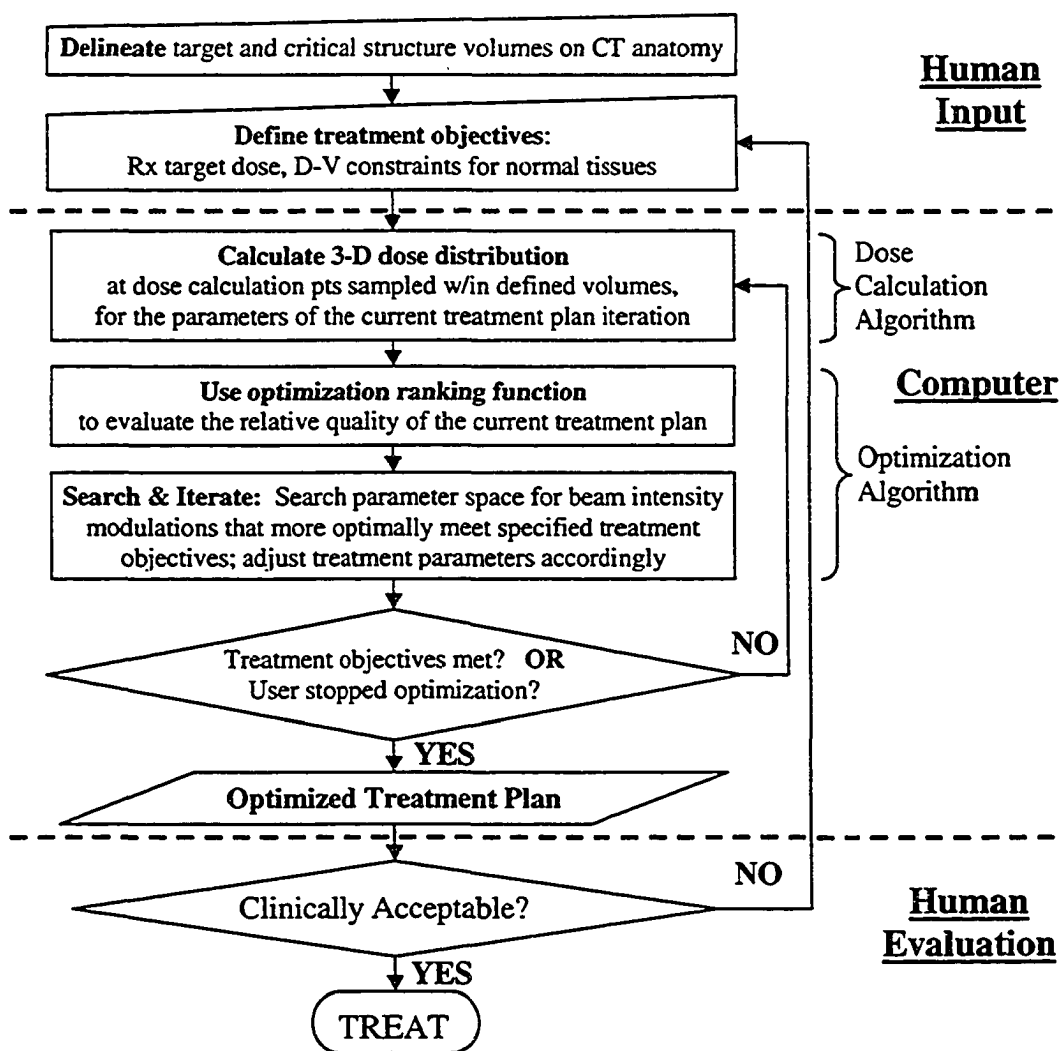


Figure 1.2. Flowchart of the inverse IMRT planning process.<sup>11</sup>

The advent of IMRT as a clinical reality is quite recent. IMRT's modern development was spurred by the availability of treatment planning systems capable of calculating dose distributions with respect to the three-dimensional (3-D) anatomical data

sets provided by CT (computed tomography), and the introduction of convenient and flexible computer-controlled methods of achieving beam modulation<sup>2</sup> (such as MLCs). Although the concept of using an MLC device for dose conformation dates back approximately 40 years,<sup>12</sup> the fundamentals of modern IMRT were mainly elucidated in works published in the late 1980's and early 1990's.<sup>13-20</sup> The clinical introduction of IMRT was somewhat later, in the late 1990's,<sup>21-24</sup> and was at first limited to a very few institutions.

IMRT enjoys the greatest advantage over conventional delivery techniques when the tumor target is irregularly shaped and/or proximal to or surrounding a critical normal tissue structure for which it is vital that the dose does not exceed a specified tolerance level. For this reason, IMRT was first used for treatment of prostate cancers, where nearby critical structures include the rectum and the bladder, and for head and neck cancers, where the spinal cord and parotid glands require sparing. IMRT has also found application in the treatment of breast and lung cancers. The Cross Cancer Institute was the first Canadian center to clinically implement inverse-planned IMRT in 2000, and has used IMRT in the treatment of head and neck and (later) lung cancers.

## **B. Verification of IMRT Treatments**

### *i. Characteristics of IMRT Necessitating Verification Procedures*

Since effective radiation therapy relies on the accuracy of dose delivery, quality assurance procedures used to detect dosimetric errors are of critical importance. The unique characteristics of IMRT place even more stringent demands on verification procedures, and make them even more essential.

The potential clinical benefits of IMRT can only be fully realized if the technological capability to precisely deliver dose is matched by an equivalent facility to ensure that the planned dose is delivered to the patient during a treatment. Fundamentally, the purpose of most verification procedures is to confirm that the 3-D dose distribution calculated by a treatment planning system (TPS) is adequately representative of the patient dose. The radiotherapy process involves the following: (1) treatment planning to generate both a dose distribution, as calculated by a TPS, and treatment parameters, including beam angles, sizes, weights, monitor units (MUs) for

each beam, MLC-controller files, *etc.*; (2) transfer of the beam parameters to the treatment unit; and, (3) delivery of the actual treatment. Thus, differences between the TPS-calculated dose and the dose actually delivered to the patient may result from inaccuracies in the dose calculation algorithm, from systematic procedural errors, or from problems with the mechanical delivery of the treatment. Errors from each of these sources are more likely in the case of IMRT treatments, than with conventional EBRT ones.

Conventional EBRT treatments are characterized by a relatively uniform dose distribution in the tumor, and low dose gradients elsewhere. The dose calculations for such distributions are generally quite reliable. Thus, if verification of a treatment of this type is considered necessary, use of a single (or few) point-dose measurement(s) is usually deemed sufficient. Since the dose changes in a predictable, well-understood manner, when there is agreement between measurement and TPS calculation at one (or a few) appropriate point(s) (*e.g.* isocenter), adequate agreement at other points in the patient volume is generally assumed.

IMRT treatments, in contrast, are distinguished by more heterogeneous dose distributions and large dose gradients, as required to achieve enhanced tumor dose conformation and critical structure dose avoidance. However, concomitant with the added benefit of these large dose gradients is an added danger. If the true position of a large dose-gradient in the delivered dose distribution is shifted with respect to the location predicted by a TPS dose calculation, an anatomical region intended to receive a high dose may actually receive a low dose, or vice versa. Clearly, single point-dose measurements are inadequate in verifying the distinctly non-uniform dose distributions of IMRT. Since agreement between planned and delivered doses at one point may indicate very little about the agreement at other points, it is necessary for measurements to more fully characterize the spatial distribution of the dose. This is especially true because dose calculations are inherently less reliable in the case of IMRT. One main reason is that it is difficult for TPS algorithms to correctly model the dose in regions of charged-particle disequilibrium, such as those where large dose gradients are present. The absence of lateral charged particle equilibrium also occurs in the small sub-fields that typically comprise step-and-shoot IMRT fields. Another common source of error in TPS

calculations is the simplified modeling of the MLC that typically fails to accurately account for inter-leaf MLC leakage effects, which include those due to the tongue-and-groove geometry present in some MLCs, and the transmission through the rounded-leaf geometry of some MLCs. Such MLC leakage and transmission effects may not always be insignificant for a given IMRT field.<sup>25,26</sup> For instance, at a junction between a set of closed leaf pairs, the TPS may under-predict the dose considerably. One function of a dosimetric IMRT verification procedure may thus be to ensure that either these overdosage regions do not lie in critical treatment areas (*e.g.* within critical normal structures), or that they are insignificant when averaged out between all fields of the IMRT treatment.

The greater complexity in both the procedure and in the delivery of IMRT treatments may also introduce additional sources of error. Systematic errors in the transfer of MLC leaf sequence files from the treatment planning computer to the record and verify system is an example of a potential procedural error. Since its mechanical design and computer control system make the MLC a complex device, occasional failures in the proper functioning of the MLC would not be unexpected<sup>27</sup> and could potentially be a source of significant dosimetric errors.

## ***ii. General Description of IMRT Verification Procedures***

Several of the procedures developed to ensure accurate and safe IMRT deliveries are described in Refs. [21,22,28]. Routine quality assurance tests specifically verifying the mechanical accuracy of the MLC leaf movements during beam delivery represent one of the most common types of IMRT verification procedure.<sup>29-37</sup> Typically with such tests, the delivery of an MLC test pattern is imaged using film or an electronic portal imaging device (EPID). The positions of the MLC leaves on the image are then compared to the expected positions, as described in the MLC controller file. Procedures involving the comparison of measured doses to TPS doses represent another type of IMRT verification test. Such *dosimetric* verifications may be used to directly assess the combined effect on IMRT dose distributions of various sources of errors (*e.g.* procedural errors, MLC delivery malfunctions, and TPS dose calculation inaccuracies).

Dosimetric comparisons can be divided into two main classes: two-dimensional (2-D) and three-dimensional (3-D) tests. A conventional 2-D technique is measurement (beam-by-beam) of the beam's-eye-view (BEV) dose distribution for each planned IMRT field at a single depth in a homogeneous (*e.g.* water) phantom.<sup>22</sup> Typical 3-D procedures involve the delivery of an entire IMRT treatment to an anthropomorphic 3-D phantom.<sup>21,38,39</sup> There are a few different ways to measure the cumulative (*i.e.* from all beams) dose distribution within the phantom. Conventional dosimeters for this task are thermo-luminescent dosimeters (TLDs),<sup>21,38</sup> placed in a variety of locations in the phantom, and radiographic film, positioned in a spiral orientation<sup>40,41</sup> to facilitate measurement of doses in more than one plane. MRI (magnetic resonance imaging) gel dosimetry<sup>42-48</sup> is an alternative (though not commonly used) technique capable of providing a complete 3-D dose distribution. Here a 3-D phantom is filled with a gel that acts as a chemical dosimeter. Absorption of dose induces chemical changes in the gel which alter the gel's relaxation parameters. After irradiation, the gel is imaged with MRI to determine relaxation rates throughout the gel, to allow a reconstruction of a 3-D dose image.

In comparison to 2-D tests, a main advantage of 3-D tests is that they provide a more complete and direct assessment of the accuracy of the TPS predictions of the complex IMRT dose distributions. They also allow the cumulative effect of dose errors from all beams to be quantified, which is not the case for beam-by-beam 2-D comparisons. Although this is generally advantageous, if significant discrepancies between measured and predicted dose distributions are suggested by a 3-D verification, it may be difficult to identify the source of the errors. To isolate the errors it may then become necessary to resort to a beam-by-beam 2-D verification. A principal disadvantage of 3-D tests is that they are very labor-intensive, and for this reason, are generally not practical if verifications are to be done for each patient's IMRT treatment plan.

At our institute (CCI, Edmonton), the treatment plan of each IMRT patient has been verified using a film-based, beam-by-beam 2-D BEV verification. In this work, we developed an analogous EPID-based 2-D technique that has since replaced the previous film-based method in clinical practice. We also developed a complementary 3-D IMRT

verification technique utilizing EPID measurements. Since a major feature of both techniques is that they are EPID-based rather than film-based, we first briefly discuss the use of film and EPIDs as dosimeters in IMRT applications in Section B.iii. We then proceed to a short overview of our 2-D and 3-D techniques in Section B.iv.

### *iii. Overview of the use of Film and EPIDs as IMRT Dosimeters*

As a result of its fine spatial resolution and two-dimensional nature, radiographic film has been the traditional choice for many IMRT verification applications.<sup>21,22,49-52</sup> Film, however, does suffer from several drawbacks. First, the energy dependence and non-linearity of the dose response of film can complicate accurate dose calibration. Film dosimetry can also be unreliable because of the sensitivity to processor conditions (*e.g.* temperature, chemical state of the developer and fixer solutions) and the variability in dose response between film batches. The use of film is also labor-intensive, requiring wet-processing and scanning of each film. The storage and archiving of film is also inconvenient.

Electronic portal imaging devices (EPIDs) were developed to be digital replacements for radiographic film in conventional portal imaging used for geometric verification of patient treatments. Another obvious potential role for EPIDs is as convenient 2-D dosimeters. Unfortunately, early generation liquid ion-chamber and camera-based fluoroscopic EPIDs<sup>53-56</sup> generally produced images of inferior contrast and spatial resolution to those obtained using film.<sup>55</sup> Despite this, significant research effort has demonstrated the potential utility of these two types of EPIDs for IMRT procedures such as quality assurance of MLC leaf positioning<sup>31,32,57-61</sup> and dosimetric verification of IMRT treatments.<sup>62-66</sup> The third and most recent class of commercial EPIDs uses flat-panel photo-diode arrays to detect the optical photons produced as a result of x-ray dose deposition in a scintillating screen. Compared to the liquid ion-chamber and fluoroscopic EPIDs, these indirect detection flat-panel imagers exhibit higher detective quantum efficiencies (DQEs). Their improved spatial resolution makes flat-panel EPIDs especially well suited for IMRT applications. A recently published work<sup>67</sup> has also described design details and a prototype of another kind of EPID – a high-DQE EPID

based on use of a thick cesium iodide (CsI(Tl)) scintillator. This type of EPID is not presently commercially available.

The Varian aS500 EPID used in this study is an example of an amorphous silicon flat-panel EPID. Because of the recent commercial introduction of this type of EPID, there had only been a few reports in the literature about their use for IMRT applications prior<sup>68</sup> to the work described in this thesis. Other more recent works in this area include those in Refs. [37,69,70].

#### *iv. Overview of Proposed 2-D and 3-D IMRT Verification Procedures*

##### *a. Review of EPID calibration*

The use of any EPID for dosimetric purposes first requires implementation of a suitable procedure establishing a relationship between pixel intensity and either fluence or dose distributions. Calibration of an EPID is more complex than for many other dosimeters. For example, simple cross-calibration of pixel response with dose measurements made with an ion chamber in a homogeneous water phantom (or in air) is generally not sufficient. The physical structure of an EPID is complex, consisting of multiple layers of different materials above and below the detector layer of the EPID. These various material layers constitute an “EPID-phantom” having dose-deposition properties that differ significantly from those of a simple water phantom. The relationship between dose and EPID response is further complicated by “optical glare,” which for an indirect flat-panel EPID is caused by the spreading of optical photons generated in the scintillating screen before reaching the photodiode array.

There are two general reported approaches for EPID calibration. One of them is an empirical method proposed by Chang *et al.*<sup>71</sup> that is based on the measurement of EPID phantom-scatter factors. In general, phantom-scatter factors are used in dose calculations to account for the increase in dose at a reference point with increasing field size that results from the greater dose originating from scatter within a phantom when more of a phantom is irradiated.<sup>72</sup> The field-size-dependent EPID phantom-scatter factors described by Chang *et al.* relate EPID pixel values to ion chamber measurements in a water phantom at the center of an open beam. Unfortunately, the use of a single phantom scatter factor for all points in a field would limit the accuracy of this type of

calibration at off-axis points. Changes in the EPID pixel/ion chamber relationship away from a beam's central axis result from changes in the relative contribution of scatter to the total signal, and also potentially from a relative over-response of the EPID to the softer off-axis beam. Thus, a calibration employing one phantom scatter factor per field is not ideally suited for verification of IMRT beams comprised of irregularly-shaped sub-fields with superposing field edges. An improved empirical approach is to calculate unique scatter factors for all points inside a field. In principle, these off-axis scatter factors can be estimated from measured central-axis scatter factor values using (for *e.g.*) Day's method.<sup>73-75</sup> However, such an approach still has limited applicability near field edges,<sup>73</sup> which for IMRT may be problematic.

A second, more flexible EPID calibration approach is based on convolution methods and scatter kernels. The convolution method is used either to convert a 2-D EPID pixel distribution to a dose distribution in a homogeneous phantom, or a known primary fluence into a portal dose distribution that is compared with the EPID image. The mathematical form of these scatter kernels can be derived either by Monte Carlo modeling of the underlying physical scattering processes, or empirically, by adjusting the kernels to obtain the best possible agreement between EPID doses obtained using the convolution method and measured ion chamber doses. Kernel-based techniques have been implemented to calibrate the dose-response of liquid-ion<sup>76,77</sup> and fluoroscopic<sup>65,78,79</sup> EPIDs. Recently, McCurdy *et al.* have applied their two-step kernel-based calibration procedure<sup>80</sup> to indirect flat-panel portal detectors.<sup>81</sup> With this approach, the scattered (in patient) energy fluence is predicted at the detector plane, and then used to calculate the dose distribution within the portal detector, through superposition with the dose deposition and optical glare kernels unique to the portal detector. In our 2-D and 3-D IMRT verification techniques we will use the EPID to measure the incident fluence of delivered IMRT fields by in essence reversing this approach. This is done by *deconvolving* a portal dose distribution with respect to dose deposition and glare kernels. The use of deconvolution techniques to extract incident fluence is conceptually straightforward, and in comparison to a strictly empirical method, should be more accurate near field edges.

### *b. Proposed EPID-based 2-D IMRT Verification Technique*

Our beam-by-beam, 2-D, EPID-based IMRT verification method is enabled by implementation of a two-staged kernel-based calibration procedure. The first step is the deconvolution step, where the raw EPID image is deconvolved directly to incident fluence using a scatter kernel composed of two elements: a dose-deposition kernel specific for the geometry of the Varian aS500 EPID generated using the EGSnrc<sup>82</sup> (National Research Council (NRC) Canada, Ottawa) Monte Carlo radiation transport code; and an empirically-derived kernel accounting for optical photon blurring, as well as any deficiencies in the Monte-Carlo based dose kernel. This deconvolution to primary fluence obviates an EPID-independent fluence estimate: we have verified the accuracy of fluences measured with the EPID by making direct comparisons of the deconvolved EPID fluence profiles with those measured using a diamond detector (PTW Freiburg, Germany). The second step of our calibration procedure is a convolution of the primary fluence with dose-deposition kernels generated using EGSnrc for the depth of 10 cm in a water phantom. To establish an absolute dose calibration relationship, the processed (*i.e.* deconvolved-convolved) EPID distribution of a calibration field is correlated to corresponding measurements of absolute dose made in a water phantom with an ion chamber. For verification purposes, an EPID-based absolute BEV dose distribution is produced for each IMRT field and then compared to the analogous 2-D dose distribution calculated by our treatment planning system. As alluded to previously, this type of 2-D dosimetric verification is intended to quantify procedural, MLC leaf movement, and TPS dose calculation errors.

### *c. Proposed EPID-based 3-D IMRT Verification Technique*

A limitation of the 2-D verification method is that it is not evident how the errors quantified in a 2-D dose at a single depth in a water phantom relate to the cumulative errors in a 3-D dose distribution in the patient from all beams in an IMRT plan. This limitation makes it difficult to assess the potential clinical significance of dosimetric errors, particularly errors that appear small in the 2-D dose distribution but might be additive in the 3-D dose distribution. This motivated the development of our “3-D”, EPID-based IMRT verification technique.

A number of researchers have investigated techniques of 3-D dose reconstruction using EPID measurements of exit fluence acquired during a treatment session with the patient in the beam.<sup>66,68,83-85</sup> Unlike these techniques, the one we describe is a more rudimentary *pre-treatment* (i.e. no patient) 3-D verification technique that exploits our method of measuring *primary* fluence with the EPID. A somewhat similar pre-treatment verification technique, but using film, has recently been described by Renner *et al.*<sup>86</sup> In their work, for each IMRT field, a 2-D dose distribution was measured using film placed below a 3 mm copper build-up plate. These 2-D distributions were then used as the primary fluence input for calculations of the 3-D dose employing an in-house pencil-beam superposition algorithm. The verification was a comparison of these doses to corresponding doses calculated by a commercial treatment planning system.

With our technique, EPID images are acquired of each IMRT field and its corresponding open field. IMRT-field and open-field 2-D fluences are then extracted using our kernel-based deconvolution technique to eliminate blurring of the fluence caused by scattering within the EPID and the water-build up placed on its surface. The ratio of IMRT-field to open-field fluences provides a 2-D relative fluence modulation profile for each IMRT field. These 2-D modulation profiles are then used as input to our commercial TPS, which then generates a 3-D dose distribution using the patient's CT data. The verification consists of comparing this 3-D dose distribution, obtained using *measured* fluence modulations, to the original inverse-planned 3-D dose distribution calculated by the same TPS, using *TPS-optimized* fluence modulations. Discrepancies between these two dose distributions are quantified and displayed along with the 3-D patient anatomy. Thus, unlike our 2-D technique, the 3-D dose differences are cumulative and arise from all the fields of an IMRT treatment.

Many of the same sources of error are probed with our 3-D technique as are with our 2-D technique. For example, since the EPID-measured fluences will contain inter-leaf leakage effects, errors in the TPS doses using TPS-optimized fluences due to the TPS's failure to account for such leakage can be identified. The 3-D verification should also identify errors resulting from inaccuracies of the TPS's modeling of very small sub-fields: in the case of the EPID-based 3-D doses, the TPS is no longer required to model the small sub-fields because the fluence modulation input is based on an EPID

measurement of the entire IMRT field. It is however noted that, since the TPS performs the dose calculation step for both the EPID-based and the original (measurement-independent) TPS-based doses, only the fluence modeling step of the TPS calculations will be verified in our 3-D method. In theory, an independent verification of the convolution/superposition step of the TPS's dose calculation would also be valuable. In practice, however, there are reasons why use of the commercial TPS to perform both dose calculations may in many circumstances be more convenient and preferable to use of an independent (*e.g.* pencil beam) algorithm to calculate dose from the EPID fluences. A clinical TPS is subject to a thorough commissioning process. Commissioning of an independent algorithm requires considerable effort, and in general it may be difficult to implement an algorithm that improves upon the accuracy of a commercial TPS. Commercial TPS dose algorithms are also routinely updated and improved by the TPS vendors. The flexibility of a commercial TPS may also be advantageous – *e.g.* it may be easier with a commercial TPS to calculate the overall dose distribution from a treatment plan combining IMRT with a conventional RT technique using other beam-modifying devices such as compensators or wedges.

The 3-D verification provides dose-volume statistics for specific clinical volumes of interest, which can be used as input for radiobiological modeling calculations of normal tissue complication probability (NTCP) and tumor control probability (TCP). Thus, a tremendous advantage of the 3-D technique is that it makes feasible a very direct evaluation of the potential clinical impact of dosimetric uncertainties in IMRT treatments.

### **C. The Role of Radiobiological Modeling in IMRT**

Ultimately, optimizing radiotherapy treatments requires not only better knowledge of the dose delivered, but also of the biological outcome of that dose. This is the purpose of radiobiological dose-response models. In the following sections, potential benefits of such models in treatment planning are discussed, and a brief overview of the radiobiological modeling work contained in this thesis is given.

### *i. Inverse Optimization of IMRT treatments*

The computer algorithms performing the inverse IMRT optimization require a mathematical ranking function to steer the search for the beam intensity modulations that best meet the clinical objectives of the treatment. Currently, commercial IMRT inverse planning algorithms almost exclusively rely on the use of so-called *physical* dose-volume metrics<sup>87</sup> to rank prospective treatment plan iterations. Commonly, a physical ranking function,  $F_{phys}(\bar{D})$ , will consist of two parts:  $F_{phys}(\bar{D}) = F_{objective}(\bar{D}) + F_{constraint}(\bar{D})$ . The “objective” piece typically formulates the treatment goal with respect to the tumor dose distribution. An example of an objective function that is frequently minimized in optimization algorithms is,

$$F_{objective}(\bar{D}) = \sum_{i \in \text{tumor}} (D_i - D_{Rx})^2, \quad (1.1)$$

where  $D_i$  is the dose calculated at point  $i$ , and  $D_{Rx}$  is the user-specified prescription dose. This objective function is based on the philosophy that, for a given integral tumor dose, a homogeneous tumor dose distribution yields the highest probability of tumor control. The “constraint” function is used to penalize dose distributions that violate the user-specified dose-volume constraints for the critical normal tissue structures.

There are limitations to the use of physical ranking functions.<sup>2,88</sup> The physical dose or dose-volume metrics are presumed surrogates for the actual biological consequence of a given dose distribution. However, these metrics may not always accurately reflect the true dose responses of tumors and normal tissues. Even though the basic philosophy of Eq. (1.1) can be supported on radiobiological considerations,<sup>89</sup> this objective function may be too simplistic in the case of the highly heterogeneous dose distributions of IMRT. As an illustration, two tumor dose distributions may give the same value for the  $F_{objective}(\bar{D})$  in Eq. (1.1), but one may represent a small, yet uniform under-dosage of the tumor, while the second may be characterized by a cold spot that is small in volume but large in dose magnitude. The biological effects of the two distributions are likely to be very different. Further, Eq. (1.1) fails to account for the fact that highly heterogeneous tumor dose distributions may be beneficial if they allow the integral tumor dose to be escalated without increasing the dose to normal tissues,<sup>90</sup> as is often the case with IMRT. Typical constraint functions also have limitations. Usually,

only a few (*e.g.* two or three) dose-volume constraints can be specified for each normal tissue of interest. However, there is a multitude of dose-volume histograms (DVHs) that may equally well satisfy these few constraints, yet may correspond to drastically different complication rates. The converse is also true, very different DVHs may in fact lead to the same complication rate. Thus, use of a very large number of dose-volume constraints is not a solution, since this may unnecessarily restrict the search for the optimal dose distribution.

Philosophically at least, the incorporation of radiobiological dose-response models in the optimization functions provides a much more direct translation between dose distributions and their biological outcome. A useful ranking function could be, for instance, one that maximizes the probability of achieving tumor control without any normal tissue complications. There has been some research into the application of biological optimization of conformal treatments.<sup>91-102</sup> When employing “pure” biological optimization based solely on dose-response calculations, often very large tumor dose heterogeneities result in the optimized dose distributions.<sup>103</sup> This is still generally deemed clinically unacceptable, since very large tumor doses may needlessly damage normal tissue embedded within the tumor.<sup>91</sup> An alternative approach is to use an optimization function that combines dose-response model predictions with physical constraints based on clinical experience. Some recent research has reported some encouraging results when adopting such a *biophysical* (or hybrid) approach:<sup>91,92,98,102</sup> dose distributions with reasonable levels of heterogeneity that are also of comparable or in some cases better clinical quality (as judged using conventional dosimetric criteria) than those obtained from pure physical optimization.

There is considerable reluctance towards implementation of biological or biophysical optimization algorithms. The first reason is that physical optimization has been well-established in clinical practice, and has been effective in producing clinically acceptable, though likely not theoretically optimal, treatment plans. The second reason is the large uncertainties that currently plague radiobiological modeling calculations (see Section C.iv). The ability of radiobiological models to properly rank competing treatment plans has been questioned in a number of works.<sup>104,105</sup> It is hoped that further

development of radiobiological models will enhance their reliability, and make their application more viable.

### *ii. Adaptation of treatments*

Radiobiological models have a great potential role in adapting treatments to treatment conditions or patient characteristics that differ from those assumed when a treatment plan is generated. This can be illustrated with a few brief examples. If one or a few fractions of a treatment are missed by a patient, radiobiological models should be employed to properly adjust subsequent treatments, *e.g.* for the effects of tumor repopulation.<sup>106</sup> A patient's radiobiological characteristics may also change during the course of treatment. In conjunction with implementation of an image-guided adaptive therapy (IGAR) protocol, it is possible that future developments will allow images acquired during treatment to track changes in, for example, tumor volume or tumor hypoxia. Again, radiobiological models in this case would be indispensable in determining how best to adjust the treatment plan. Finally, models could also be used to account for dose delivery inaccuracies, such as those detected by daily images acquired during a tomotherapy-based treatment. Corrections for such errors that do not utilize dose-response models may be error-prone. Accurate corrections in general may require detailed knowledge of dose-volume relationships of tissues. In correcting for dose errors, dose-response models may also be needed to account for differences in the treatment effect between a dose delivered on one day and the same amount of dose delivered at a later time.<sup>107</sup>

### *iii. Individualization of treatments*

One of the most natural potential applications of radiobiological modeling is in the patient-specific customization of treatment plans. The paradigm is shown in Fig. 1.3. Radiobiological assays would be used to extract parameters describing the specific characteristics (*e.g.* normal tissue and tumor radiosensitivities, proliferation rate) of an individual patient. Incorporating these parameters into appropriate radiobiological models furnishes *individual* predictions of tumor control and normal tissue probabilities. The predictions are useful, if not explicitly in the inverse IMRT optimization, at least in

helping to suggest appropriate modifications to standard treatment prescriptions or even perhaps the unsuitability of a given type of treatment for a specific patient. Recent works that investigate the potential advantages of using TCP models that exploit patient-specific data from radiobiological assays include those of Buffa *et al.*,<sup>108</sup> and Mackay and Hendry.<sup>109</sup>

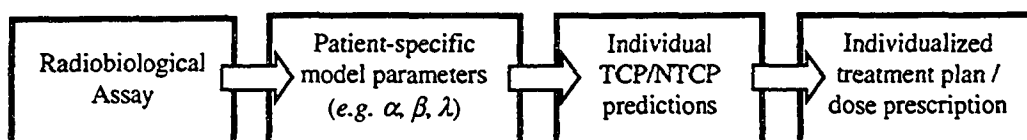


**Figure 1.3.** Paradigm for individualization of radiotherapy based on radiobiological assays and models.

#### *iv. Confounding Issues of Radiobiological Modeling*

Clearly the potential role for radiobiological modeling in radiotherapy treatment planning is significant. The advantages are even greater specifically for IMRT planning, since the effects of the very heterogeneous dose distributions of IMRT are difficult to quantify without the use of dose-response models. Presently, however, the direct use of models in such active roles as optimization, adaptation, or individualization is rare because of the deemed unreliability of current model predictions. The reasons stem from the quality of the data on which model parameter estimates are based, and ambiguities in interpretation of these estimates. Compounding the problem, even the level of uncertainty in parameter estimates is often ill-defined.<sup>110,111</sup>

Population-based (as opposed to individual) radiobiological parameter values are extracted by fitting to clinical dose-response data. Unfortunately, there has been a dearth of such clinical data, and the data that existed until recently generally had large statistical or unknown uncertainties. This situation has been recently improving because of the use of 3-D treatment planning systems and the archiving of their 3-D dose distribution calculations. Nonetheless, clinical data in general has insufficient diversity to discriminate different model parameters. For example, if, as is often the case, the patients represented in a data set have been treated with similar fractionation protocols, it would not be possible to deduce a meaningful value for a parameter descriptive of tumor repopulation effects. The similarity of dose-volume histograms (DVHs) in a data set may

also limit the biological relevance of fitted values for parameters describing tissue dose-volume characteristics. Practically, fits to clinical data are often chiefly phenomenological in nature, which limits the applicability of the fitting results to other patient populations or treatment protocols that differ from the ones represented in the original data set.

It is interesting that the converse is also true: the *diversity* of clinical data also complicates interpretation of radiobiological fitting exercises. There may be considerable variation in radiation response characteristics between individual patients in the population represented by a clinical data set. As discussed in Section 5.B, parameter estimates (*e.g.* of the radiosensitivity parameters  $\alpha$  and  $\beta$ ) can be skewed from their true values if this inherent population heterogeneity is not taken into account in the dose-response model used to fit the data.<sup>112</sup> Failure to account for population heterogeneity may also lead to unrealistically low estimates of the uncertainties in fitted parameter values. The development of population-based dose-response models is quite recent.

There are also difficulties when attempting to use patient-specific parameter values in individual (as opposed to population) dose-response models to facilitate the sort of treatment customization discussed in Section C.iii. First, as discussed by Mackay and Hendry,<sup>109</sup> uncertainties in radiobiological assay data may reduce or even reverse any prospective gains in the rates of tumor control with assay-based individualization of dose prescriptions. Also, the correlation between *in vitro* radiobiological assay results and the *in vivo* response of a patient is not well established.<sup>113,114</sup> For example, *in vitro* and *in vivo* estimates for a given radiobiological parameter often differ substantially. It is an unresolved issue to what extent this is due to intrinsic differences between *in vitro* and *in vivo* dose response characteristics, or a result of ambiguities or errors in the extraction of parameter values.

#### ***v. Overview of Radiobiological Investigations in this Work***

The radiobiological modeling work in this thesis comprises several smaller projects, rather than one large investigation. We first developed (Chapter 4) a practical computational tool that calculates radiobiological predictions of TCP and NTCP from dose-volume histogram information that characterizes treatment plan dose distributions.

The tool attempts to encapsulate and make accessible the current radiobiological modeling knowledge as it pertains to treatment planning. It is used in conjunction with the EPID project to evaluate the potential clinical consequence of dosimetric uncertainties in IMRT, as measured by our 3-D IMRT verification technique.

The projects described in Chapter 5 represent more fundamental radiobiological investigations that help further refine radiobiological models and understand their appropriate use. Though not explicitly focused on IMRT, they are certainly relevant because of the many potential applications of radiobiological modeling to IMRT. The first of these works derives explicit expressions relating phenomenological parameters describing dose-response curves to radiobiological parameters found in mechanistic models. Another larger study uses a recently proposed population TCP model to explore some of the complications inherent in attempts to extract biologically meaningful parameter estimates when fitting to clinical dose-response data. In a third project, we investigate the importance of incorporating dynamic cell processes such as repair, repopulation and resensitization in TCP models when describing or interpreting fractionation effects.

Further introduction to the radiobiological modeling projects is provided in the sections of the thesis describing each of these works.

## **D. Overview of Thesis Structure**

The structure of the remainder of this thesis is as follows. The development of the EPID-based 2-D and 3-D IMRT verification procedures is detailed in Chapters 2 and 3, with Chapter 2 describing the methods and materials, and Chapter 3 presenting the results. The development of our 2-D EPID-based IMRT verification method has also already been published (in significantly modified form) in *Medical Physics*,<sup>115</sup> while our 3-D method is the subject of an article recently accepted for publication in the same journal.<sup>116</sup> Chapter 4 describes the NTCP-TCP computational tool, and is, with a few minor modifications, identical to the article we published in the *Journal of Applied Clinical Medical Physics*.<sup>117</sup> The other radiobiological modeling investigations are, as mentioned previously, discussed in Chapter 5. They are also the foundation for a number of our manuscripts: an article in *Physics in Medicine and Biology*<sup>118</sup> presented the

derivation of expressions relating phenomenological and mechanistic model parameters; the study of dynamic cell processes in TCP models with respect to fractionated dose-response data is detailed in both an article published in 2003,<sup>119</sup> and a second recently accepted manuscript<sup>120</sup> (both in *Medical Physics*). Though no manuscript has yet been prepared, our examination of a population-based TCP model was presented at the annual conference of the AAPM (American Association of Medical Physics) in 2002.<sup>121</sup> Chapter 6 is a brief concluding chapter to the thesis.

## E. References

<sup>1</sup>A. Brahme, "Dosimetric precision requirements in radiation therapy," *Acta Radiologica Oncology* **23** (5), 379-391 (1984).

<sup>2</sup>A. L. Boyer, E. B. Butler, T. A. DiPetrillo, M. J. Engler, B. Fraass, W. Grant, C. C. Ling, D. A. Low, T. R. Mackie, R. Mohan, J. A. Purdy, M. Roach, J. G. Rosenman, L. J. Verhey, J. W. Wong, R. L. Cumberlin, H. Stone, and J. R. Palta, "Intensity-modulated radiotherapy: Current status and issues of interest," *International Journal of Radiation Oncology Biology Physics* **51** (4), 880-914 (2001).

<sup>3</sup>S. Webb, "Intensity-modulated radiation therapy: Dynamic MLC (DMLC) therapy, multisegment therapy and tomotherapy - An example of QA in DMLC therapy," *Strahlentherapie Und Onkologie* **174**, 8-12 (1998).

<sup>4</sup>A. Brahme, "Design Principles and Clinical Possibilities with a New Generation of Radiation-Therapy Equipment - a Review," *Acta Oncologica* **26** (6), 403-412 (1987).

<sup>5</sup>T. R. Mackie, T. W. Holmes, P. J. Reckwerdt, and J. Yang, "Tomotherapy - Optimized Planning and Delivery of Radiation-Therapy," *International Journal of Imaging Systems and Technology* **6** (1), 43-55 (1995).

<sup>6</sup>T. R. Mackie, T. Holmes, S. Swerdloff, P. Reckwerdt, J. O. Deasy, J. Yang, B. Paliwal, and T. Kinsella, "Tomotherapy - a New Concept for the Delivery of Dynamic Conformal Radiotherapy," *Medical Physics* **20** (6), 1709-1719 (1993).

<sup>7</sup>H.I. Amols, C. C. Ling, and S.A. Leibel, "Overview of the IMRT Process," in *A Practical Guide to Intensity-Modulated Radiation Therapy* (Medical Physics Publishing, Madison, 2003).

<sup>8</sup>N. Lee, C. Akazawa, P. Akazawa, J. M. Quivey, C. Tang, L. J. Verhey, and P. Xia, "A forward-planned treatment technique using multisegments in the treatment of head-and-

neck cancer,” *International Journal of Radiation Oncology Biology Physics* **59** (2), 584-594 (2004).

<sup>9</sup>K. Sultanem, H. K. Shu, P. Xia, C. Akazawa, J. M. Quivey, L. J. Verhey, and K. K. Fu, “Three-dimensional intensity-modulated radiotherapy in the treatment of nasopharyngeal carcinoma: The University of California-San Francisco experience,” *International Journal of Radiation Oncology Biology Physics* **48** (3), 711-722 (2000).

<sup>10</sup>D. Corletto, M. Iori, M. Paiusco, L. Brait, S. Broggi, G. Ceresoli, C. Iotti, R. Calandrino, and C. Fiorino, “Inverse and forward optimization of one- and two-dimensional intensity-modulated radiation therapy-based treatment of concave-shaped planning target volumes: the case of prostate cancer,” *Radiotherapy and Oncology* **66** (2), 185-195 (2003).

<sup>11</sup>MDS Nordion, “Helax-TMS Optimization Algorithms (Reference Manual),” (Veenendaal, The Netherlands).

<sup>12</sup>S. Takahashi, “Conformation radiotherapy: Rotation techniques as applied to radiography and radiotherapy of cancer,” *Acta Radiologica Supplement* (242), 1-42 (1965).

<sup>13</sup>A. Gustafsson, B. K. Lind, and A. Brahme, “A Generalized Pencil Beam Algorithm for Optimization of Radiation-Therapy,” *Medical Physics* **21** (3), 343-357 (1994).

<sup>14</sup>S. Soderstrom, A. Gustafsson, and A. Brahme, “The Clinical-Value of Different Treatment Objectives and Degrees of Freedom in Radiation-Therapy Optimization,” *Radiotherapy and Oncology* **29** (2), 148-163 (1993).

<sup>15</sup>D. J. Convery and M. E. Rosenbloom, “The Generation of Intensity-Modulated Fields for Conformal Radiotherapy by Dynamic Collimation,” *Physics in Medicine and Biology* **37** (6), 1359-1374 (1992).

<sup>16</sup>A. Brahme and A. K. Agren, “Optimal Dose Distribution for Eradication of Heterogeneous Tumors,” *Acta Oncologica* **26** (5), 377-385 (1987).

<sup>17</sup>A. Brahme, “Optimization of Stationary and Moving Beam Radiation-Therapy Techniques,” *Radiotherapy and Oncology* **12** (2), 129-140 (1988).

<sup>18</sup>A. M. Cormack and R. A. Cormack, “A Problem in Rotation Therapy with X-Rays - Dose Distributions with an Axis of Symmetry,” *International Journal of Radiation Oncology Biology Physics* **13** (12), 1921-1925 (1987).

<sup>19</sup>A. M. Cormack, “A Problem in Rotation Therapy with X-Rays,” *International Journal of Radiation Oncology Biology Physics* **13** (4), 623-630 (1987).

- <sup>20</sup>P. Kallman, B. Lind, A. Eklof, and A. Brahme, "Shaping of Arbitrary Dose Distributions by Dynamic Multileaf Collimation," *Physics in Medicine and Biology* **33** (11), 1291-1300 (1988).
- <sup>21</sup>J. S. Tsai, D. E. Wazer, M. N. Ling, J. K. Wu, M. Fagundes, T. DiPetrillo, B. Kramer, M. Koistinen, and M. J. Engler, "Dosimetric verification of the dynamic intensity-modulated radiation therapy of 92 patients," *International Journal of Radiation Oncology Biology Physics* **40** (5), 1213-1230 (1998).
- <sup>22</sup>C. Burman, C. S. Chui, G. Kutcher, S. Leibel, M. Zelefsky, T. LoSasso, S. Spirou, Q. W. Wu, J. Yang, J. Stein, R. Mohan, Z. Fuks, and C. C. Ling, "Planning, delivery, and quality assurance of intensity-modulated radiotherapy using dynamic multileaf collimator: A strategy for large-scale implementation for the treatment of carcinoma of the prostate," *International Journal of Radiation Oncology Biology Physics* **39** (4), 863-873 (1997).
- <sup>23</sup>K. S. C. Chao, D. A. Low, R. L. Gerber, C. A. Perez, and J. A. Purdy, "Clinical and technical considerations for head and neck cancers treated by IMRT: Initial experience," *International Journal of Radiation Oncology Biology Physics* **39** (2), 238-238 (1997).
- <sup>24</sup>D. Verellen, N. Linthout, D. VandenBerge, A. Bel, and G. Storme, "Initial experience with intensity-modulated conformal radiation therapy for treatment of the head and neck region," *International Journal of Radiation Oncology Biology Physics* **39** (1), 99-114 (1997).
- <sup>25</sup>J. D. Azcona, R. A. C. Siochi, and I. Azinovic, "Quality assurance in IMRT: Importance of the transmission through the jaws for an accurate calculation of absolute doses and relative distributions," *Medical Physics* **29** (3), 269-274 (2002).
- <sup>26</sup>American Association of Physicists in Medicine, *AAPM TG-50: Basic applications of multileaf collimators* (Medical Physics Publishing, 2001).
- <sup>27</sup>T. LoSasso, "Quality assurance of IMRT," in *A Practical Guide to Intensity-Modulated Radiation Therapy* (Medical Physics Publishing, Madison, 2003).
- <sup>28</sup>Memorial Sloan-Kettering Cancer Center, *A Practical Guide to Intensity-Modulated Radiation Therapy* (Medical Physics Publishing, Madison, 2003).
- <sup>29</sup>S. M. Zhou and L. J. Verhey, "A Robust Method of Multileaf Collimator (MLC) Leaf-Configuration Verification," *Physics in Medicine and Biology* **39** (11), 1929-1947 (1994).
- <sup>30</sup>K. Eilertsen, "Automatic detection of single MLC leaf positions with corrections for penumbral effects and portal imager dose rate characteristics," *Physics in Medicine and Biology* **42** (2), 313-334 (1997).

- <sup>31</sup>H. V. James, S. Atherton, G. J. Budgell, M. C. Kirby, and P. C. Williams, "Verification of dynamic multileaf collimation using an electronic portal imaging device," *Physics in Medicine and Biology* **45** (2), 495-509 (2000).
- <sup>32</sup>M. Partridge, P. M. Evans, M. van Herk, L. S. Ploeger, G. J. Budgell, and H. V. James, "Leaf position verification during dynamic beam delivery: A comparison of three applications using electronic portal imaging," *Medical Physics* **27** (7), 1601-1609 (2000).
- <sup>33</sup>S. S. Samant, W. Zheng, N. A. Parra, J. Chandler, A. Gopal, J. Wu, J. Jain, Y. P. Zhu, and M. Sontag, "Verification of multileaf collimator leaf positions using an electronic portal imaging device," *Medical Physics* **29** (12), 2900-2912 (2002).
- <sup>34</sup>Y. Yang and L. Xing, "Using the volumetric effect of a finite-sized detector for routine quality assurance of multileaf collimator leaf positioning," *Medical Physics* **30** (3), 433-441 (2003).
- <sup>35</sup>Y. Yang and L. Xing, "Quantitative measurement of MLC leaf displacements using an electronic portal image device," *Physics in Medicine and Biology* **49** (8), 1521-1533 (2004).
- <sup>36</sup>M. Sastre-Padro, U. A. van der Heide, and H. Welleweerd, "An accurate calibration method of the multileaf collimator valid for conformal and intensity modulated radiation treatments," *Physics in Medicine and Biology* **49** (12), 2631-2643 (2004).
- <sup>37</sup>J. Chang, C. H. Obcemea, J. Sillanpaa, J. Mechalakos, and C. Burman, "Use of EPID for leaf position accuracy QA of dynamic multi-leaf collimator (DMLC) treatment," *Medical Physics* **31** (7), 2091-2096 (2004).
- <sup>38</sup>G. Ibbott, A. Nelson, D. Followill, P. Balter, and W. Hanson, "An anthropomorphic head and neck phantom for evaluation of intensity modulated radiation therapy," <http://rpc.mdanderson.org/rpc> (2002).
- <sup>39</sup>P. Cadman, R. Bassalow, N. P. S. Sidhu, G. Ibbott, and A. Nelson, "Dosimetric considerations for validation of a sequential IMRT process with a commercial treatment planning system," *Physics in Medicine and Biology* **47** (16), 3001-3010 (2002).
- <sup>40</sup>B. Paliwal, W. Tome, S. Richardson, and T. R. Mackie, "A spiral phantom for IMRT and tomotherapy treatment delivery verification," *Medical Physics* **27** (11), 2503-2507 (2000).
- <sup>41</sup>S. L. Richardson, W. A. Tome, N. P. Orton, T. R. McNutt, and B. R. Paliwal, "IMRT delivery verification using a spiral phantom," *Medical Physics* **30** (9), 2553-2558 (2003).
- <sup>42</sup>M. J. Maryanski, R. J. Schulz, G. S. Ibbott, J. C. Gatenby, J. Xie, D. Horton, and J. C. Gore, "Magnetic-Resonance-Imaging of Radiation-Dose Distributions Using a Polymer-Gel Dosimeter," *Physics in Medicine and Biology* **39** (9), 1437-1455 (1994).

- <sup>43</sup>M. Oldham, I. Baustert, C. Lord, T. A. D. Smith, M. McJury, A. P. Warrington, M. O. Leach, and S. Webb, "An investigation into the dosimetry of a nine-field tomotherapy irradiation using BANG-gel dosimetry," *Physics in Medicine and Biology* **43** (5), 1113-1132 (1998).
- <sup>44</sup>P. Sandilos, A. Angelopoulos, P. Baras, K. Dardoufas, P. Karaiskos, P. Kipouros, M. Kozicki, J. M. Rosiak, L. Sakelliou, I. Seimenis, and L. Vlahos, "Dose verification in clinical IMRT prostate incidents," *International Journal of Radiation Oncology Biology Physics* **59** (5), 1540-1547 (2004).
- <sup>45</sup>H. Gustavsson, A. Karlsson, S. A. J. Back, L. E. Olsson, P. Haraldsson, P. Engstrom, and H. Nystrom, "MAGIC-type polymer gel for three-dimensional dosimetry: Intensity-modulated radiation therapy verification," *Medical Physics* **30** (6), 1264-1271 (2003).
- <sup>46</sup>F. Gum, J. Scherer, L. Bogner, M. Solleder, B. Rhein, and M. Bock, "Preliminary study on the use of an inhomogeneous anthropomorphic Fricke gel phantom and 3D magnetic resonance dosimetry for verification of IMRT treatment plans," *Physics in Medicine and Biology* **47** (7), N67-N77 (2002).
- <sup>47</sup>Y. De Deene, C. De Wagter, B. Van Duyse, S. Derycke, B. Mersseman, W. De Gersem, T. Voet, E. Achten, and W. De Neve, "Validation of MR-based polymer gel dosimetry as a preclinical three-dimensional verification tool in conformal radiotherapy," *Magnetic Resonance in Medicine* **43** (1), 116-125 (2000).
- <sup>48</sup>D. A. Low, J. F. Dempsey, R. Venkatesan, S. Mutic, J. Markman, E. M. Haacke, and J. A. Purdy, "Evaluation of polymer gels and MRI as a 3-D dosimeter for intensity-modulated radiation therapy," *Medical Physics* **26** (8), 1542-1551 (1999).
- <sup>49</sup>N. Dogan, L. B. Leybovich, and A. Sethi, "Comparative evaluation of Kodak EDR2 and XV2 films for verification of intensity modulated radiation therapy," *Physics in Medicine and Biology* **47** (22), 4121-30 (2002).
- <sup>50</sup>X. Wang, S. Spirou, T. LoSasso, J. Stein, C. S. Chui, and B. Mohan, "Dosimetric verification of intensity-modulated fields," *Medical Physics* **23** (3), 317-27 (1996).
- <sup>51</sup>M.A. MacKenzie, M. Lachaine, B. Murray, B. G. Fallone, D. Robinson, and G.C. Field, "Dosimetric verification of inverse planned step and shoot multileaf collimator fields from a commercial treatment planning system," *Journal of Applied Clinical Medical Physics* **3** (2), 97-109 (2002).
- <sup>52</sup>M. Bucciolini, F. B. Buonamici, and M. Casati, "Verification of IMRT fields by film dosimetry," *Medical Physics* **31** (1), 161-168 (2004).
- <sup>53</sup>P. Munro, "Portal Imaging Technology: Past, Present, and Future," *Seminars in Radiation Oncology* **5** (2), 115-133 (1995).

- <sup>54</sup>J. van Dyk, *The Modern Technology of Radiation Oncology* (Medical Physics Publishing, Madison, WI, 1999).
- <sup>55</sup>M. G. Herman, J. M. Balter, D. A. Jaffray, K. P. McGee, P. Munro, S. Shalev, M. Van Herk, and J. W. Wong, "Clinical use of electronic portal imaging: Report of AAPM radiation therapy committee Task Group 58," *Medical Physics* **28** (5), 712-737 (2001).
- <sup>56</sup>L. E. Antonuk, "Electronic portal imaging devices: a review and historical perspective of contemporary technologies and research," *Physics in Medicine and Biology* **47** (6), R31-R65 (2002).
- <sup>57</sup>A. G. Glendinning, S. G. Hunt, and D. E. Bonnett, "Recording accelerator monitor units during electronic portal imaging: application to collimator position verification during IMRT," *Physics in Medicine and Biology* **46** (6), N159-N167 (2001).
- <sup>58</sup>H. Keller, M. K. Fix, L. Liistro, and P. Ruegsegger, "Theoretical considerations to the verification of dynamic multileaf collimated fields with a SLIC-type portal image detector," *Physics in Medicine and Biology* **45** (9), 2531-2545 (2000).
- <sup>59</sup>L. S. Ploeger, M. H. P. Smitsmans, K. G. A. Gilhuijs, and M. van Herk, "A method for geometrical verification of dynamic intensity modulated radiotherapy using a scanning electronic portal imaging device," *Medical Physics* **29** (6), 1071-1079 (2002).
- <sup>60</sup>S. C. Vieira, M. L. P. Dirkx, K. L. Pasma, and B. J. M. Heijmen, "Fast and accurate leaf verification for dynamic multileaf collimation using an electronic portal imaging device," *Medical Physics* **29** (9), 2034-2040 (2002).
- <sup>61</sup>O. A. Zeidan, J. G. Li, M. Ranade, A. M. Stell, and J. F. Dempsey, "Verification of step-and-shoot IMRT delivery using a fast video-based electronic portal imaging device," *Medical Physics* **31** (3), 463-476 (2004).
- <sup>62</sup>K. L. Pasma, M. L. P. Dirkx, M. Kroonwijk, A. G. Visser, and B. J. M. Heijmen, "Dosimetric verification of intensity modulated beams produced with dynamic multileaf collimation using an electronic portal imaging device," *Medical Physics* **26** (11), 2373-2378 (1999).
- <sup>63</sup>J. W. Chang, G. S. Mageras, C. S. Chui, C. C. Ling, and W. Lutz, "Relative profile and dose verification of intensity-modulated radiation therapy," *International Journal of Radiation Oncology Biology Physics* **47** (1), 231-240 (2000).
- <sup>64</sup>A. Van Esch, B. Vanstraelen, J. Verstraete, G. Kutcher, and D. Huyskens, "Pre-treatment dosimetric verification by means of a liquid-filled electronic portal imaging device during dynamic delivery of intensity modulated treatment fields," *Radiotherapy and Oncology* **60** (2), 181-190 (2001).

- <sup>65</sup>S. C. Vieira, M. L. P. Dirkx, K. L. Pasma, and B. J. M. Heijmen, "Dosimetric verification of x-ray fields with steep dose gradients using an electronic portal imaging device," *Physics in Medicine and Biology* **48** (2), 157-166 (2003).
- <sup>66</sup>T. R. McNutt, T. R. Mackie, P. Reckwerdt, and B. R. Paliwal, "Modeling dose distributions from portal dose images using the convolution/superposition method," *Medical Physics* **23** (8), 1381-1392 (1996).
- <sup>67</sup>A. Sawant, H. Zeman, S. Samant, G. Lovhoiden, B. Weinberg, and F. DiBianca, "Theoretical analysis and experimental evaluation of a CsI(Tl) based electronic portal imaging system," *Medical Physics* **29** (6), 1042-53 (2002).
- <sup>68</sup>M. Partridge, M. Ebert, and B. M. Hesse, "IMRT verification by three-dimensional dose reconstruction from portal beam measurements," *Medical Physics* **29** (8), 1847-1858 (2002).
- <sup>69</sup>A. Van Esch, T. Depuydt, and D. P. Huyskens, "The use of an aSi-based EPID for routine absolute dosimetric pre-treatment verification of dynamic IMRT fields," *Radiotherapy and Oncology* **71** (2), 223-234 (2004).
- <sup>70</sup>J. V. Siebers, J. O. Kim, L. Ko, P. J. Keall, and R. Mohan, "Monte Carlo computation of dosimetric amorphous silicon electronic portal images," *Medical Physics* **31** (7), 2135-2146 (2004).
- <sup>71</sup>J. H. Chang, G. S. Mageras, C. C. Ling, and W. Lutz, "An iterative EPID calibration procedure for dosimetric verification that considers the EPID scattering factor," *Medical Physics* **28** (11), 2247-2257 (2001).
- <sup>72</sup>Faiz M. Khan, *The Physics of Radiation Therapy*, 3rd ed. (Lippincott Williams & Wilkins, Philadelphia, 2003).
- <sup>73</sup>F. Araki, R. Ikeda, N. Moribe, Y. Shirakawa, M. Hatemura, T. Shimonobou, Y. Hirata, T. Takada, M. Takahashi, and M. Matoba, "Dose calculation for asymmetric photon fields with independent jaws and multileaf collimators," *Medical Physics* **27** (2), 340-5 (2000).
- <sup>74</sup>M. J. Day, "A note on the calculation of dose in x-ray fields," *British Journal of Radiology* **23** (270), 368-9 (1950).
- <sup>75</sup>G. V. Menon and R. S. Sloboda, "Compensator thickness verification using an a-Si EPID," *Medical Physics* **31** (8), 2300-12 (2004).
- <sup>76</sup>M. Essers, R. Boellaard, M. vanHerck, H. Lanson, and B. Mijnheer, "Transmission dosimetry with a liquid-filled electronic portal imaging device," *International Journal of Radiation Oncology Biology Physics* **34** (4), 931-941 (1996).

- <sup>77</sup>H. Keller, M. Fix, and P. Rueggeger, "Calibration of a portal imaging device for high-precision dosimetry: A Monte Carlo study," *Medical Physics* **25** (10), 1891-1902 (1998).
- <sup>78</sup>B. J. M. Heijmen, K. L. Pasma, M. Kroonwijk, V. G. M. Althof, J. C. J. Deboer, A. G. Visser, and H. Huizenga, "Portal Dose Measurement in Radiotherapy Using an Electronic Portal Imaging Device (EPID)," *Physics in Medicine and Biology* **40** (11), 1943-1955 (1995).
- <sup>79</sup>K. L. Pasma, M. Kroonwijk, J. C. J. de Boer, A. G. Visser, and B. J. M. Heijmen, "Accurate portal dose measurement with a fluoroscopic electronic portal imaging device (EPID) for open and wedged beams and dynamic multileaf collimation," *Physics in Medicine and Biology* **43** (8), 2047-2060 (1998).
- <sup>80</sup>B. M. C. McCurdy and S. Pistorius, "A two-step algorithm for predicting portal dose images in arbitrary detectors," *Medical Physics* **27** (9), 2109-2116 (2000).
- <sup>81</sup>B. M. C. McCurdy, K. Luchka, and S. Pistorius, "Dosimetric investigation and portal dose image prediction using an amorphous silicon electronic portal imaging device," *Medical Physics* **28** (6), 911-924 (2001).
- <sup>82</sup>I. Kawrakow and D. W. Rogers, "The EGSnrc Code System: Monte Carlo Simulation of Electron and Photon Transport," NRCC Report PIRS-701, NRC Canada (2002).
- <sup>83</sup>R. J. W. Louwe, E. M. F. Damen, M. van Herk, A. W. H. Minken, O. Torzsok, and B. J. Mijnheer, "Three-dimensional dose reconstruction of breast cancer treatment using portal imaging," *Medical Physics* **30** (9), 2376-2389 (2003).
- <sup>84</sup>J. M. Kapatoes, G. H. Olivera, J. P. Balog, H. Keller, P. J. Reckwerdt, and T. R. Mackie, "On the accuracy and effectiveness of dose reconstruction for tomotherapy," *Physics in Medicine and Biology* **46** (4), 943-966 (2001).
- <sup>85</sup>J. M. Kapatoes, G. H. Olivera, K. J. Ruchala, J. B. Smilowitz, P. J. Reckwerdt, and T. R. Mackie, "A feasible method for clinical delivery verification and dose reconstruction in tomotherapy," *Medical Physics* **28** (4), 528-542 (2001).
- <sup>86</sup>W. D. Renner, M. Sarfaraz, M. A. Earl, and C. X. Yu, "A dose delivery verification method for conventional and intensity-modulated radiation therapy using measured field fluence distributions," *Medical Physics* **30** (11), 2996-3005 (2003).
- <sup>87</sup>T. Bortfeld, "Optimized planning using physical objectives and constraints," *Seminars in Radiation Oncology* **9** (1), 20-34 (1999).
- <sup>88</sup>R. Mohan, X. H. Wang, A. Jackson, T. Bortfeld, A. L. Boyer, G. J. Kutcher, S. A. Leibel, Z. Fuks, and C. C. Ling, "The Potential and Limitations of the Inverse Radiotherapy Technique," *Radiotherapy and Oncology* **32** (3), 232-248 (1994).

- <sup>89</sup>S. Webb, P. M. Evans, W. Swindell, and J. O. Deasy, "A Proof That Uniform Dose Gives the Greatest TCP for Fixed Integral Dose in the Planning Target Volume," *Physics in Medicine and Biology* **39** (11), 2091-2098 (1994).
- <sup>90</sup>W. A. Tome and J. F. Fowler, "Selective boosting of tumor subvolumes," *International Journal of Radiation Oncology Biology Physics* **48** (2), 593-599 (2000).
- <sup>91</sup>Q. W. Wu, R. Mohan, A. Niemierko, and R. Schmidt-Ullrich, "Optimization of intensity-modulated radiotherapy plans based on the equivalent uniform dose," *International Journal of Radiation Oncology Biology Physics* **52** (1), 224-235 (2002).
- <sup>92</sup>X. H. Wang, R. Mohan, A. Jackson, S. A. Leibel, Z. Fuks, and C. C. Ling, "Optimization of Intensity-Modulated 3d Conformal Treatment Plans Based on Biological Indexes," *Radiotherapy and Oncology* **37** (2), 140-152 (1995).
- <sup>93</sup>A. Niemierko, M. Urie, and M. Goitein, "Optimization of 3d Radiation-Therapy with Both Physical and Biological End-Points and Constraints," *International Journal of Radiation Oncology Biology Physics* **23** (1), 99-108 (1992).
- <sup>94</sup>R. Mohan, G. S. Mageras, B. Baldwin, L. J. Brewster, G. J. Kutcher, S. Leibel, C. M. Burman, C. C. Ling, and Z. Fuks, "Clinically Relevant Optimization of 3-D Conformal Treatments," *Medical Physics* **19** (4), 933-944 (1992).
- <sup>95</sup>P. Kallman, B. K. Lind, and A. Brahme, "An Algorithm for Maximizing the Probability of Complication-Free Tumor-Control in Radiation-Therapy," *Physics in Medicine and Biology* **37** (4), 871-890 (1992).
- <sup>96</sup>G. O. De Meerleer, Laml Vakaet, W. R. T. De Gerssem, C. De Wagter, B. De Naeyer, and W. De Neve, "Radiotherapy of prostate cancer with or without intensity modulated beams: A planning comparison," *International Journal of Radiation Oncology Biology Physics* **47** (3), 639-648 (2000).
- <sup>97</sup>W. R. T. De Gerssem, S. Derycke, C. De Wagter, and W. C. J. De Neve, "Optimization of beam weights in conformal radiotherapy planning of stage III non-small cell lung cancer: Effects on therapeutic ratio," *International Journal of Radiation Oncology Biology Physics* **47** (1), 255-260 (2000).
- <sup>98</sup>W. R. T. De Gerssem, S. Derycke, C. O. Colle, C. De Wagter, and W. J. De Neve, "Inhomogeneous target-dose distributions: A dimension more for optimization?," *International Journal of Radiation Oncology Biology Physics* **44** (2), 461-468 (1999).
- <sup>99</sup>A. Brahme, "Optimized radiation therapy based on radiobiological objectives," *Seminars in Radiation Oncology* **9** (1), 35-47 (1999).
- <sup>100</sup>A. Brahme, "Biologically based treatment planning," *Acta Oncologica* **38**, 61-68 (1999).

- <sup>101</sup>M. Alber, F. Paulsen, S. M. Eschmann, and H. J. Machulla, "On biologically conformal boost dose optimization," *Physics in Medicine and Biology* **48** (2), N31-N35 (2003).
- <sup>102</sup>P. Stavrev, D. Hristov, B. Warkentin, E. Sham, N. Stavreva, and B. G. Fallone, "Inverse treatment planning by physically constrained minimization of a biological objective function," *Medical Physics* **30** (11), 2948-2958 (2003).
- <sup>103</sup>L. Jones and P. Hoban, "A comparison of physically and radiobiologically based optimization for IMRT," *Medical Physics* **29** (7), 1447-1455 (2002).
- <sup>104</sup>V. Moiseenko, J. Battista, and J. Van Dyk, "Normal tissue complication probabilities: Dependence on choice of biological model and dose-volume histogram reduction scheme," *International Journal of Radiation Oncology Biology Physics* **46** (4), 983-993 (2000).
- <sup>105</sup>M. Langer, S. S. Morrill, and R. Lane, "A test of the claim that plan rankings are determined by relative complication and tumor-control probabilities," *International Journal of Radiation Oncology Biology Physics* **41** (2), 451-457 (1998).
- <sup>106</sup>R. G. Dale, J. H. Hendry, B. Jones, A. G. Robertson, C. Deehan, and J. A. Sinclair, "Practical methods for compensating for missed treatment days in radiotherapy, with particular reference to head and neck schedules," *Clinical Oncology* **14** (5), 382-393 (2002).
- <sup>107</sup>R. K. Sachs, W. F. Heidenreich, and D. J. Brenner, "Dose timing in tumor radiotherapy: Considerations of cell number stochasticity," *Mathematical Biosciences* **138** (2), 131-146 (1996).
- <sup>108</sup>F. M. Buffa, S. E. Davidson, R. D. Hunter, A. E. Nahum, and C. M. L. West, "Incorporating biologic measurements (SF2, CFE) into a tumor control probability model increases their prognostic significance: A study in cervical carcinoma treated with radiation therapy," *International Journal of Radiation Oncology Biology Physics* **50** (5), 1113-1122 (2001).
- <sup>109</sup>R. I. Mackay and J. H. Hendry, "The modelled benefits of individualizing radiotherapy patients' dose using cellular radiosensitivity assays with inherent variability," *Radiotherapy and Oncology* **50** (1), 67-75 (1999).
- <sup>110</sup>M. Carlone, D. Wilkins, B. Nyiri, and P. Raaphorst, "Comparison of alpha/beta estimates from homogeneous (individual) and heterogeneous (population) tumor control models for early stage prostate cancer," *Medical Physics* **30** (10), 2832-2848 (2003).

- <sup>111</sup>P. van Luijk, T. C. Delvigne, C. Schilstra, and J. M. Schippers, "Estimation of parameters of dose-volume models and their confidence limits," *Physics in Medicine and Biology* **48** (13), 1863-1884 (2003).
- <sup>112</sup>S. A. Roberts and J. H. Hendry, "A realistic closed-form radiobiological model of clinical tumor-control data incorporating intertumor heterogeneity," *International Journal of Radiation Oncology Biology Physics* **41** (3), 689-699 (1998).
- <sup>113</sup>D. Slonina, M. Klimek, K. Szpytma, and A. Gasinska, "Comparison of the radiosensitive of normal-tissue cells with normal-tissue reactions after radiotherapy," *International Journal of Radiation Biology* **76** (9), 1255-1264 (2000).
- <sup>114</sup>B. Stausbol-Gron, S. M. Bentzen, K. E. Jorgensen, O. S. Nielsen, T. Bundgaard, and J. Overgaard, "In vitro radiosensitivity of tumour cells and fibroblasts derived from head and neck carcinomas: mutual relationship and correlation with clinical data," *British Journal of Cancer* **79** (7-8), 1074-1084 (1999).
- <sup>115</sup>B. Warkentin, S. Steciw, S. Rathee, and B. G. Fallone, "Dosimetric IMRT verification with a flat-panel EPID," *Medical Physics* **30** (12), 3143-3155 (2003).
- <sup>116</sup>S. Steciw, B. Warkentin, S. Rathee, and B. Fallone, "Three-dimensional IMRT verification with a flat-panel EPID," accepted for publication in *Medical Physics* (2005).
- <sup>117</sup>B. Warkentin, P. Stavrev, N. Stavreva, C. Field, and B. Fallone, "A TCP-NTCP estimation module using DVHs and known radiobiological models and parameter sets," *Journal of Applied Clinical Medical Physics* **5** (1), 50-63 (2004).
- <sup>118</sup>N. Stavreva, P. Stavrev, B. Warkentin, and B. G. Fallone, "Derivation of the expressions for  $\gamma(50)$  and D50 for different individual TCP and NTCP models," *Physics in Medicine and Biology* **47** (20), 3591-3604 (2002).
- <sup>119</sup>N. A. Stavreva, P. V. Stavrev, B. Warkentin, and B. G. Fallone, "Investigating the effect of cell repopulation on the tumor response to fractionated external radiotherapy," *Medical Physics* **30** (5), 735-742 (2003).
- <sup>120</sup>N. Stavreva, B. Warkentin, P. Stavrev, and B. Fallone, "Investigating the effect of clonogen resensitization on the tumor response to fractionated external radiotherapy," accepted for publication in *Medical Physics* (2005).
- <sup>121</sup>P. Stavrev, B. Warkentin, N. Stavreva, and G. Fallone, "Evaluation of a closed-form tumor control probability solution," *Medical Physics* **29** (6), 1294-1294 (2002).

## Chapter 2: EPID-based IMRT Verification – Methods

This is the first of two chapters describing the development of 2-D (beam’s eye view plane) and 3-D IMRT (intensity-modulated radiotherapy) dosimetric verification procedures using an EPID (electronic portal imaging device). In this chapter, relevant operational characteristics and the signal formation process of the Varian aS500 EPID are discussed, as are details of our method of using this EPID for fluence measurements. Much of these descriptions are common to both the 2-D and 3-D IMRT verification techniques. However, since the two projects were undertaken in two distinct stages, there are also some differences. Initially the 2-D technique was developed solely for 15 MV beams, since this was the only beam energy used with the existing clinical 2-D verification method using film. For the 3-D technique, developed later, we decided to include both 6 and 15 MV photon beams. As a result, the details of the development of the kernels characterizing blurring in the EPID are slightly different for the two cases – specifically, the approximation used to describe the back-scattering and optical scattering in the EPID. This is discussed in Sections 2.D.iii-2.D.v. In the last part of this chapter, the methods of calculation of 2-D and 3-D doses based on the EPID measurements of fluence are discussed.

### A. Basic Experimental Details

#### *i. EPID Measurements*

Measurements were performed using 6 and 15 MV photon beams generated by a Varian (Varian Medical Systems, Palo Alto, CA) 21EX medical linear accelerator (linac). Unless otherwise specified, the linear accelerator was operated with a nominal dose rate of 100 monitor units (MU) per minute (with 1 MU = 1 cGy at the depth of maximum dose, at isocenter). Images of radiation fields were acquired with the aS500 EPID (Varian Medical Systems, Palo Alto, CA) and its “IMRT” acquisition mode. All images were acquired without a patient or phantom in the beam path since the purpose of this work was to develop *pre-treatment* IMRT verification procedures. The detector (*i.e.*

EPID) was placed at a nominal (specified by the pendant controller) source-to-detector-distance (SDD) of 105 cm, the smallest allowed by the R-arm that controls the EPID's movement. Since the EPID imaging plane is ~1.3 cm lower than the distance reported by the pendant, the actual SDD is ~ 106.3 cm. Use of the smallest SDD available allows the largest possible field sizes to be imaged. At this SDD, field sizes of up to approximately 37.6 x 28.2 cm<sup>2</sup> (measured at 100 cm from the source) can be imaged, since the active area of the detector is 40 x 30 cm<sup>2</sup>. At our clinic, the largest IMRT fields are about 26 cm along the narrow dimension of the EPID (y-direction).

### *ii. Fluence Measurements using a Diamond Detector*

To verify our EPID-based technique of measuring fluence profiles, EPID-based profiles were compared to profile measurements made with a diamond detector (PTW-Freiburg, Freiburg, Germany). The external shape of this detector is a cylinder approximately 20 mm in length and with a circular face of 7 mm in diameter.<sup>1</sup> Its sensitive layer is approximately 1 mm from the front face and has a thickness of ~ 0.3 mm and a circular cross-sectional area of approximately 4.4 mm<sup>2</sup>.<sup>1</sup> Diamond detectors thus have excellent intrinsic spatial resolution, making them well-suited for profile measurements. Additional characteristics of this diamond detector can be found in Refs. [1,2]. Our in-air diamond profile measurements were taken at an SDD of 106.3 cm in an empty tank used for beam-scanning measurements (Scanditronix Wellhofer North America, Bartlett, TN). The beam-scanning system allows the movement of the detector to be controlled remotely within a scanning volume of 48 x 48 x 41 (depth) cm<sup>3</sup>. A brass build-up cap for the diamond detector was used to achieve (nearly) charged-particle equilibrium for these in-air measurements. The outer diameters of the 6 and 15 MV cylindrical build-up caps are 11 mm and 16 mm, respectively (inner diameter of the opening for the diamond detector is 7 mm). Although the build-up cap reduces the spatial resolution of the detector (due to volume averaging effects), its use is necessary to minimize contributions from electron contaminants in the photon beam, and it also increases the size of the detector signal. Without adequate build-up, the signal amplitude would also be more sensitive to changes in the energy spectrum at different locations in the incident beam. Those parts of the beam with a larger percentage of low-energy

photons would produce a disproportionately larger signal, since the low-energy photons would be closer to electronic equilibrium in the detector (*i.e.* more “built-up”) than the higher energy photons.

As is conventional, it is assumed that the diamond detector profiles are representative of the incident fluence profiles, although strictly speaking, they are measurements of the dose deposited in the detector. The dose deposited will be proportional to the fluence if the energy spectrum is constant across the beam. Generally this is not the case, as the mean beam energy tends to decrease when moving further from the central beam axis.<sup>3</sup> Nevertheless, because the response of the diamond detector is reasonably energy-independent (comparable to an ion chamber in this regard), spectral effects are not expected to cause large distortions in the fluence profiles measured with the diamond detector.

All scans were acquired with the diamond detector/build-up cap in a “horizontal” orientation, with the side of the detector/build-up cap facing the incident beam and the axis of the cylindrical build-up cap in the “in-plane” (*i.e.*  $y$ ) direction. The response of the detector/cap combination is asymmetric in the in-plane direction because the active volume of the diamond detector is much closer to one end of the build-up cap along its length than the other. Thus, the edges of open fields seen in in-plane in-air profiles are (artificially) asymmetric. The response of the detector/cap is, however, symmetric when scanning in the “cross-plane” (*i.e.*  $x$ ) direction, where the beam sees a circular cross-section. Thus, the profiles of open fields shown in Section 3.B (in the next chapter) were acquired from cross-plane scans. In retrospect, symmetric scans in both the in-plane and cross-plane directions could have been obtained by using the detector/cap in a “vertical” orientation, with the beam incident on the circular face of the build-up cap.

## **B. Physical Structure of the Varian aS500 EPID**

The Varian aS500 EPID is an active matrix flat-panel imager used for megavoltage electronic portal imaging utilizing an “indirect” method of photon detection. The detector has a complex structure consisting of many different layers composed of a number of different materials. The layers can be grouped into four main regions: a build-up region lying above the phosphor, the phosphor (340  $\mu\text{m}$  thick gadolinium oxy-

sulfide,  $\text{Gd}_2\text{O}_2\text{S:Tb}$ ), a 2-D amorphous silicon flat-panel photodiode array, and all materials lying below the photodiode array. Photons incident on the detector first interact with material in the build-up region, resulting in the production of charged particles. The main build-up layer in the EPID is a 1 mm copper sheet ( $\sim 1$  cm water-equivalent<sup>4</sup>), which also filters out contaminant charged particles in the incident photon beam, and reduces the radiation scattered from the patient reaching the detector to achieve improved portal image quality. For our measurements, an additional 2 cm of solid water was placed on top of the EPID to establish full build-up for an incident 15 MV photon beam. For convenience the same amount of solid water was also used for 6 MV measurements, so that entering the linac vault was unnecessary when switching between these two beam energies. In one stage of EPID signal formation, charged particles produced in the build-up region deposit dose in the phosphor screen. This stimulates the production of optical photons (emission peak at 540 nm), the latter stage of this “indirect” detection method. A fraction of the optical photons is then detected by the photodiode array fabricated on a glass substrate. The detector signal (*i.e.* summed pixel value) is linearly proportional to the number of optical photons produced, which is in turn proportional to the energy deposited in the phosphor. The linearity of the detector response (*i.e.* pixel value vs. delivered MUs) of this and similar amorphous silicon flat-panel systems has been discussed in Refs. [4-6]. The photodiode array of the aS500 contains 512 x 384 pixels covering the active area of 40 x 30 cm<sup>2</sup> (pixel pitch = 0.0784 cm). The materials lying below the photodiode array include cables, supporting structure materials, and the metal “R-arm” used to move the EPID in and out of the beam. These materials contribute a backscatter component to the dose deposited in the phosphor layer.

## **C. Image Acquisition using the Varian aS500 EPID**

### ***i. General Description***

In addition to a reverse-biased photodiode, each pixel also contains a thin-film transistor (TFT) used for electronically transferring the charge produced in the photodiode to the pre-amplifier using a grid of “gate” (row-selection) and “data” (charge transfer) wires. These components, and the associated “read-out” and “gate-driver” electronics, are used to read the charge produced by optical photons within the

photodiode array. The “bias” wires are used to apply the reverse voltage on each photodiode. The photodiode array is read row-by-row by applying voltage to one “gate” line at a time. When a given “gate” line is activated, the TFTs for all 512 pixels in the corresponding row permit the charge stored in each photodiode to flow along the 512 “data” lines connected along the columns of the array. The charge in each pixel is amplified, read by an electrometer, and converted to a number by a 14-bit analog-to-digital converter. A single image “frame” is acquired once all 384 rows have been read in this fashion.

The timing parameters used to control the read-out of the EPID array are uniquely specified for each acquisition mode (namely “standard,” “high-quality,” and “IMRT”) and for each beam energy/nominal dose rate combination of a linac.<sup>7</sup> Read-out is triggered by “PVSync” pulses having a regular frequency that is determined from the linac pulse pattern. Even at the lowest linac dose rate of 100 MU/min, where pulse repetition times are 16.7 ms (6 MV) and 33.3 ms (15 MV) for the Varian 21EX accelerator, all 384 rows of the EPID can not be read between any two linac pulses. This means that different parts of the EPID image will register dose contributions from different linac pulses. As a representative example, if 70 rows can be read between each pair of linac pulses, and the number of pulses between consecutive reads of a given row is six, rows 1-70 will read dose from linac pulses 1-6, rows 71-140 from pulses 2-7, *etc.* Thus, in theory, pulse-to-pulse variations in the linac dose rate can lead to a band-like structure in the image, where different regions of the image have different intensities. However, in IMRT mode (discussed below), where an entire dose delivery is integrated, this is generally less problematic because dose-rate fluctuations are reduced due to averaging.

#### *ii. Image Acquisition using “IMRT” Mode*

The final image supplied by the Portal-Vision software is an average over a number of frames. Frame-averaging is performed by a “hardware adder” (capacity of 64 frames) component of the acquisition electronics. The number of frames used to create an image depends on which image acquisition mode is used. Portal-Vision’s conventional portal imaging modes (“standard” and “high-quality”) typically use either

two or four frames, the latter when better image quality is desired. In this study, a recently available “IMRT” acquisition mode designed specifically for dosimetric (as opposed to imaging) applications was used for all measurements. With this IMRT mode, frames are acquired and stored in local memory continuously for the duration of the beam delivery, rather than for a small fraction of the delivery as for the conventional imaging modes. To preserve the linearity between pixel value and the dose delivered, the frame-averaged EPID image supplied by the Portal-Vision software,  $EPID_{PV}$ , is multiplied by the number of frames used to create the image,  $n_{frame}$ , to produce an integrated dose image,  $EPID_{total}$  :

$$EPID_{total} = n_{frame} \cdot EPID_{PV} \quad (2.1)$$

Though IMRT mode is employed to measure an entire dose delivery, as discussed by Chang *et al.*,<sup>8</sup> small parts of the dose delivery are not represented in the final image. First, at the start of delivery one “reset” frame (~ 0.1 sec) is used to reset the frame buffer, so that in the first image frame, the charge read corresponds to the same number of linac pulses for all rows. Reset frames are not included in the final frame-averaged image. Also, if the last radiation pulse of a dose delivery occurs with the EPID read-out somewhere in the middle of an image frame, this partially-completed image frame is discarded. Thus a small amount of dose at the end of delivery is also generally missed. As noted by Chang *et al.*,<sup>8</sup> the amount of dose missed from the start and end of the delivery is generally small. For a typical 100 MU dose delivery where the final image is an average of more than 400 image frames, the loss of at most two frames corresponds to less than 0.5% of the total dose delivered.

### ***iii. Effect of Buffer Deadtimes and Potential Ghosting Effects on EPID Images***

Potentially more problematic for absolute dosimetric applications is the dose missed because of the limited 64-frame capacity of the hardware adder. After 64 frames have been acquired, the EPID’s frame buffer must be cleared so that additional frames can be acquired: this process takes approximately 0.16 sec.<sup>8</sup> After clearing the buffer, the EPID also uses a reset frame before resuming acquisition of the frames used to create the final image. The total buffer-related deadtime (including buffer clearing and the reset

frame) and the frame acquisition rate for each linac energy/dose-rate combination were determined from the acquisition times ( $T_{acq}$ ) and numbers of frames (statistics provided by the Portal-Vision software) from a series of images containing different numbers of image frames (*i.e.* with and without buffer delays). The acquisition time per frame ( $T_{acq}/n_{frame}$ ) is plotted as a function of  $n_{frame}$  in a given image in Fig. 2.1 for image acquisition for both 15 MV and 6 MV beams at 100 MU/min. As illustrated, the uncorrected time per frame increases every 64 frames. After a buffer deadtime,  $T_{buffer}$ , of 272 msec (15 MV/100 MU/min) or 258 msec (6 MV/100 MU/min) is subtracted from the total acquisition time for every time the buffer requires clearing, the corrected time per frame,  $T_{frame}$ , remains constant at approximately 133 msec (7.5 frames/sec) and 93 msec (10.7 frames/sec) for 15 MV/100 MU/min and 6 MV/100 MU/min, respectively. Our buffer deadtimes are consistent with the delay of  $\sim 270$  msec reported by other authors<sup>8,9</sup> for measurements at 300 MU/min. It is noted that a Portal-Vision software patch that corrects for the problem of buffer deadtime and is based on work of Manser *et al.*,<sup>9</sup> is now available from Varian.

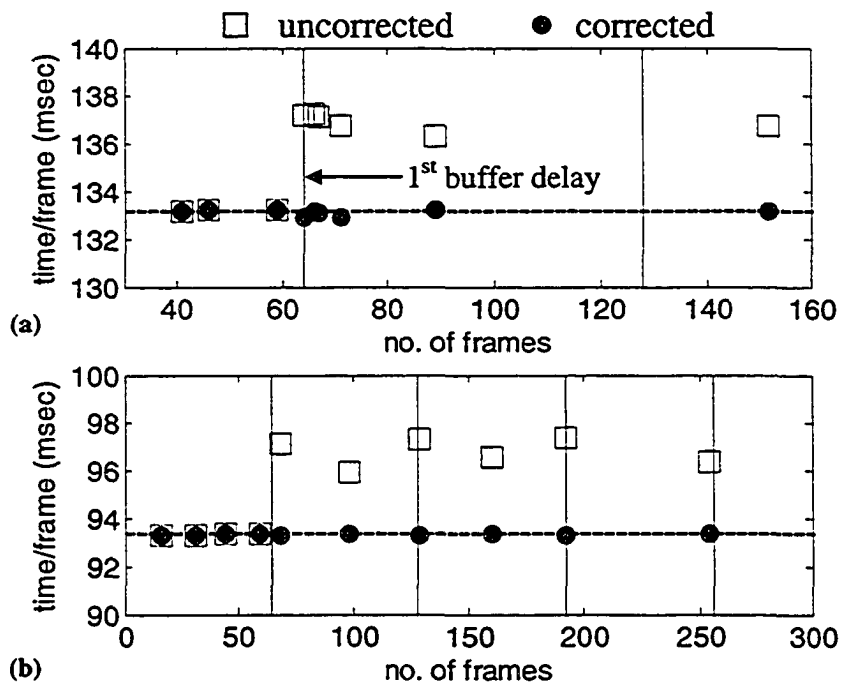


**Figure 2.1.** The acquisition time per image frame plotted as a function of the total number of frames acquired in an image for (a) 15 MV/100 MU/min, and (b) 6 MV/100 MU/min. The squares and circles represent the time/frame before and after (respectively) correcting the acquisition time for buffer delays. The vertical lines correspond to the numbers of frames at which buffer delays occur.

Any dose delivered during a buffer deadtime will not be represented in the final image. For a simple open-field irradiation, where dose is being delivered continually at a nearly fixed rate, the amount of missed dose should be approximately proportional to the total buffer deadtime as a percentage of  $T_{acq}$ . Based on this assumption, a simple correction<sup>8</sup> factor for the integrated EPID image,  $EPID_{total}$ , would be,

$$C_{buffer}(n_{frame}) = \left( \frac{T_{acq}}{T_{acq} - n_{buffer}T_{buffer}} \right) = \left( 1 + \frac{n_{buffer}T_{buffer}}{n_{frame}T_{frame}} \right), \quad (2.2)$$

where  $n_{buffer}$  is the number of buffer delays and is equal to the quotient of  $\left( \frac{n_{frame} - 1}{64} \right)$ ,

and the “buffer-corrected”  $EPID_{total}$  is given by  $EPID_{total|buffer} = EPID_{total} \cdot C_{buffer}(n_{frame})$ .

For images with a large number of frames, the correction term  $\frac{n_{buffer}T_{buffer}}{n_{frame}T_{frame}}$  will

approach a constant value of  $\frac{T_{buffer}}{64T_{frame}}$ , equal to 4.3 % and 3.2 % for 6 MV/100 MU/min

and 15 MV/100 MU/min, respectively. Figure 2.2 shows the integrated pixel value ( $EPID_{total}$ ) per MU delivered as a function of the number of frames in an image. The pixel values refer to the mean value of the central 50 x 50 pixels (3.9 x 3.9 cm<sup>2</sup>) in each image of a 10 x 10 cm<sup>2</sup> field delivered with a 15 MV/100 MU/min beam. The drop in the uncorrected detector dose-response immediately after a buffer delay is evident in Fig. 2.2(a). After applying the correction in Eq. (2.2), the pixel value per MU before and after the first buffer delay are in much better agreement. However, as illustrated in Fig. 2.2(b), after the first buffer delay, the corrected detector dose response (*i.e.* pixel value/MU) tends to increase with an increasing number of frames (*i.e.* increasing MUs), rather than remaining roughly constant as desired.

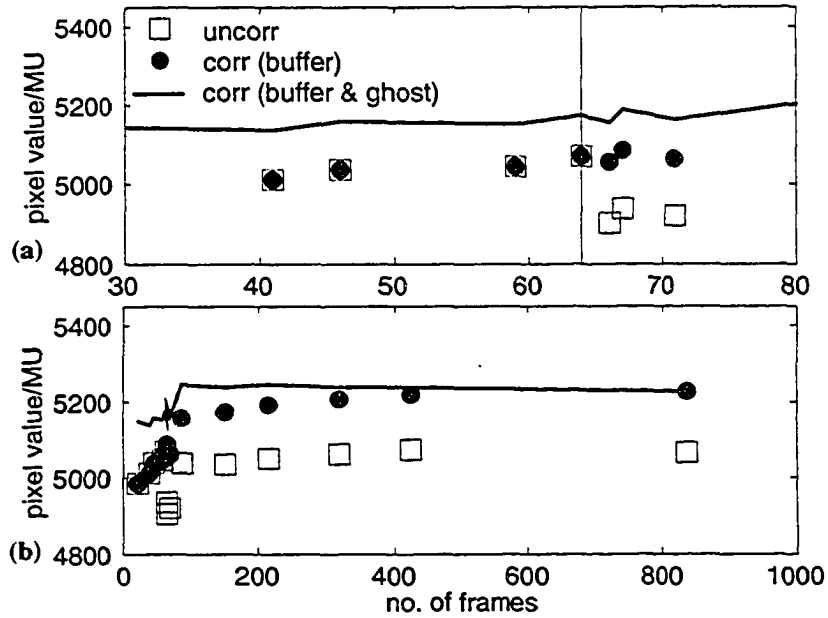


**Figure 2.2.** EPID pixel value (i.e.  $EPID_{total}$ ) per MU plotted as a function of the number of frames used to acquire an image (15 MV/100 MU/min). Eq. (2.2) is used to correct the dose response for buffer delays (closed circles). The solid line depicts the application of an additional correction for “ghosting” effects described in Ref. [10]. The data in (a) and (b) is the same: the graph in (a) shows only the data nearest the first buffer delay at 64 frames (vertical line), while (b) covers a wider range of  $n_{frame}$  values.

A potential explanation of this trend is a “ghosting” effect,<sup>10,11</sup> where residual signal from preceding frames is manifest in subsequent frames. The main source of this residual signal is believed to originate from charge capture and release processes in the amorphous silicon photodiodes.<sup>11</sup> Eventually, the corrected dose response does stabilize at a nearly constant value. The corrected dose response for the last four points shown in Fig. 2.2(b), which correspond to 50, 75, 100 and 200 MUs (or 215, 320, 424 and 838 frames), agree within  $\sim 0.6\%$ , while the last two of these points agree within 0.1%. Assuming that the “ghosting” explanation is valid, this stability suggests that an equilibrium in the capture and release processes is reached after approximately 70 MUs or 300 frames (for 15 MV/100 MU/min). This is quite consistent with the findings of McDermott *et al.*,<sup>10</sup> who found that the response of an amorphous silicon EPID stabilized to within  $\sim 0.5\%$  only after approximately 40 seconds of irradiation, which would correspond to 67 MUs at 100 MU/min in our example. McDermott *et al.* devised an empirical “ghosting” correction factor,

$$G(t) = 1 - 234.3 \exp(-7.8t) - 0.036 \exp(-0.46t) - 0.026 \exp(-0.034t), \quad (2.3)$$

where  $t$  is the time of irradiation in seconds, and the corrected EPID signal is  $EPID_{total}|_{ghost} = EPID_{total} / G(t)$ . The solid line in Fig. 2.2 depicts the measured dose response of the aS500 EPID corrected both for the buffer delay (Eq. (2.2)) and the “ghost” effect (Eq. (2.3)), *i.e.*  $EPID_{total}|_{buffer-ghost} = EPID_{total} \cdot C_{buffer}(n_{frame}) / G(t)$ . The ghost correction significantly improves the stability of the EPID response, although it appears that the  $G(t)$  in Eq. (2.3) may be too small for the shorter irradiations corresponding to less than 100 frames. It is not unexpected that the appropriate ghosting correction would be slightly different for our measurements made with a Varian aS500 EPID, since McDermott *et al.* derived their  $G(t)$  from measurements made with an Elekta iViewGT (Elekta Inc., Norcross, Georgia) EPID. A fit to our data shown in Fig. 2.2 suggested a ghosting correction for the Varian aS500 (15 MV/100 MU/min) that can be described by the equation,  $G(t) = 1 - 0.062 \exp(-0.086t)$ .

Also suggested by Fig. 2.2(b), is that the *uncorrected* (*i.e.* without use of Eq. (2.2) or Eq. (2.3)) dose response is reasonably stable for irradiations corresponding to the range from 100 to 300 frames. In this range, the uncorrected dose response actually is more constant in general than the dose response corrected for the buffer delays alone: the reduction in the pixel value/MU ratio due to the buffer deadtime is partially compensated by an increase in this ratio due to the apparent ghosting mechanism. Also, as the number of image frames increases, the change in the uncorrected dose response immediately after a buffer deadtime decreases. For example, immediately before and after the sixth such buffer delay (at 384 frames), the correction  $\frac{n_{buffer} T_{buffer}}{n_{frame} T_{frame}}$  changes from 2.7 % to 3.2 %:

this implies that the *uncorrected* dose response changes by at most  $\sim 0.5$  % due to the buffer deadtime for images composed of more than 400 frames, equivalent to an open-field delivery of  $\sim 100$  MUs at 15 MV/100 MU/min.

Errors introduced by buffer deadtimes and ghosting into the integrated dose image are more difficult to predict for step-and-shoot IMRT fields. For example, since the shape of the field changes, and the dose delivery stops between segments when the leaves are moving, the effect of buffer deadtimes will depend on where they occur in the treatment delivery. Thus, a simple correction such as that given in Eq. (2.2) is no longer

valid. This can be illustrated by considering a hypothetical 100-frame image of a two-segment IMRT field. If the buffer delay at 64 frames occurs during leaf movement, when the dose delivered should be nearly zero, the buffer delay will have no impact on  $EPID_{total}$ , and use of Eq. (2.2) would incorrectly over-predict the dose. If instead, the buffer delay occurs during segment 2, the buffer deadtime will cause the dose delivered during segment 2 to be under-represented in the final uncorrected  $EPID_{total}$  image. In theory, to restore a more accurate representation of the actual dose delivered, segment 2's contribution should be multiplied by a correction factor,  $1 + \frac{T_{buffer}}{n_{frame}(2)T_{frame}}$ , where

$n_{frame}(2)$  is the number of frames acquired while segment 2 was delivered; segment 1's contribution should be left uncorrected. More generally, a correction for step-and-shoot IMRT fields analogous to the correction in Eq. (2.2) for open-fields, would be to multiply  $EPID_{total}$  by a 2-D pixel correction map,

$$\left[ \sum_i \left( 1 + \frac{n_{buffer}(i)T_{buffer}}{n_{frame}(i)T_{frame}} \right) D_{xy}(i) \right] / \left[ \sum_i D_{xy}(i) \right],$$

where the sums are over the number of segments in the IMRT field,  $n_{buffer}(i)$  is the number of buffer delays occurring in segment  $i$ , and  $D_{xy}(i)$  is the 2-D dose contribution of segment  $i$ . In practice, however, such a correction would be difficult. First, since one does not have access to the individual frames contained in the  $EPID_{total}$  image, the doses of each segment  $D_{xy}(i)$  would need to be estimated. Also, it is not simple to predict exactly where the buffer delays will occur with respect to the beam delivery. Knowledge of the exact time needed between each segment to move the MLC leaves to the new positions would require analysis of the dynamic log files generated by the linac's control system.<sup>12</sup> Thus, rather than attempting a complicated correction of this type to account for buffer delays, we instead chose to use acquisition parameters that would minimize potential errors. It is also noted that the ghosting correction suggested by McDermott *et al.*<sup>10</sup> was published after completion of most of the work published in this thesis. Since this correction was derived for continuous irradiation, it also would require modification for proper application to step-and-shoot IMRT delivery.

#### iv. Accuracy of IMRT Mode for Step-and-shoot IMRT

The use of a large number of frames, and thus a longer irradiation time for each segment, was found to improve the accuracy of the dose images of step-and-shoot IMRT fields obtained using IMRT acquisition mode. This is as expected for the following reasons. First, the impact of “ghosting” effects on  $EPID_{total}$  will be reduced. As shown in Fig. 2.2 for the case of open fields, the dose-response does approach a constant value for sufficiently long irradiations, as the ghosting effect stabilizes due to an equilibrium between charge capture and release. Also, since the time for leaf movements between segments is independent of the amount of dose delivered, the proportion of frames acquired when the radiation is off between segments will be reduced when the number of MUs (and hence the number of frames) is increased. As a result, the EPID will see a more nearly constant dose rate, which also stabilizes ghosting effects. Finally, when a large number of frames are acquired during all segments, distortions caused by a buffer delay to the relative contribution of a single segment to the cumulative image will be reduced.

We verified the improved accuracy achieved using an increased number of frames by comparing the single  $EPID_{total}$  image for the entire delivery of a twelve-segment IMRT field to the weighted summation of IMRT-mode images taken individually of each of the twelve segments. Each weighted image,  $EPID_{total}^{wgt-sum}$ , was calculated using:

$$EPID_{total}^{wgt-sum} = \sum_i EPID_{total}^{segment}(i) \cdot wt(i) \cdot \frac{MU_0}{MU^{segment}(i)}. \quad (2.4)$$

In Eq. (2.4),  $EPID_{total}^{segment}(i)$  is the image of an individual segment  $i$  acquired using  $MU^{segment}(i)$  MUs;  $MU_0$  is the number of MUs used to acquire the  $EPID_{total}$  image, and the weight  $wt(i)$  is the fraction of the total number of MUs for each segment  $i$ , as specified in the MLC controller file used for  $EPID_{total}$  image acquisition. Assuming proper operation of the MLC controller, the  $EPID_{total}$  and  $EPID_{total}^{wgt-sum}$  images should be nearly identical except for the buffer dead-times and ghosting effects. Figure 2.3

shows ( $EPID_{total} - EPID_{total}^{wgt-sum}$ ) images and the corresponding difference histograms for those pixels lying within the delineated ROI. The differences are expressed as a percentage of the maximum pixel value in the  $EPID_{total}^{wgt-sum}$  image. In Fig. 2.3(a), the differences are calculated for two cases: when the  $EPID_{total}$  image is acquired using 100 MUs (314 frames) and when a much larger 800 MUs (1025 frames) are delivered. Individual segment images ( $EPID_{total}^{segment}(i)$ ) were each separately acquired using 50 MUs (53 or 54 frames). With this number of MUs, the dose-response is within  $\sim 1\%$  of its stable value, and the image is acquired before the occurrence of the first buffer deadtime. These measurements were made using a 15 MV beam, and a dose rate of 600 MU/min, which is the dose rate we had initially intended to use for our EPID measurements. As illustrated, the agreement between the single ( $EPID_{total}$ ) and the weighted-sum ( $EPID_{total}^{wgt-sum}$ ) images improves substantially when using the larger number of MUs: the mean and standard deviation of ( $EPID_{total} - EPID_{total}^{wgt-sum}$ ) within the ROI for the 100 MU case are  $-2.0\%$  and  $2.1\%$ , respectively, while only  $-0.8\%$  and  $0.7\%$  for the 800 MU case. A similar set of dose difference comparisons for the same IMRT field is depicted in Fig. 2.3(b) for measurements using a 15 MV beam and the lowest available dose rate of 100 MU/min. Single images of the entire IMRT field are acquired with 100 MUs (564 frames) and 200 MUs (986 frames); images of the individual segments are again acquired using 50 MUs (218 frames). For this dose rate, good agreement between the  $EPID_{total}$  and  $EPID_{total}^{wgt-sum}$  images is already obtained using 100 MUs: the mean and the standard deviation in the ROI are  $-0.8\%$  and  $0.5\%$ , respectively, roughly equivalent to the agreement observed using 800 MUs at the higher 600 MU/min dose rate.

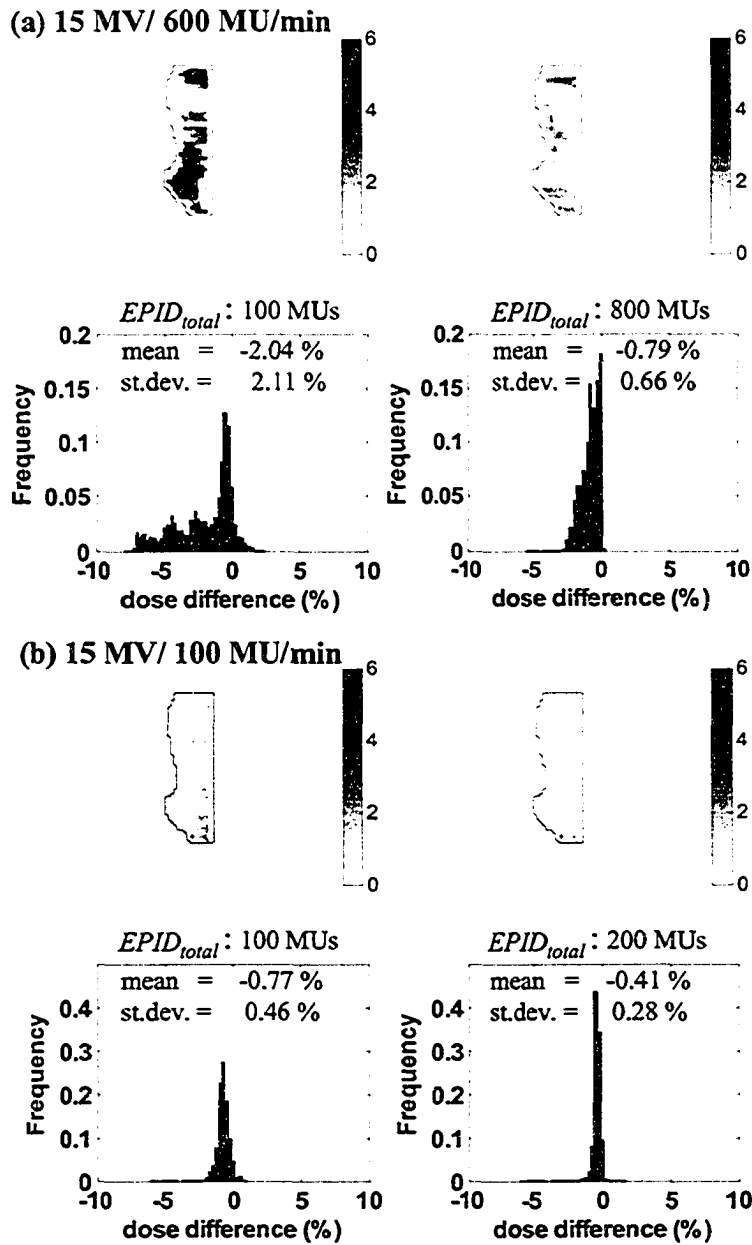


Figure 2.3. The 2-D difference images ( $EPID_{total} - EPID_{total}^{wgt-sum}$ ) expressed as a percentage of the maximum pixel value in  $EPID_{total}^{wgt-sum}$ , and the corresponding histogram for pixels within the ROI (delineated by the line in the dose difference image) are shown for linac dose rates of (a) 600 MU/min and (b) 100 MU/min. The left and right columns for each dose rate depict the effect on the differences of increasing the number of MUs used to acquire the  $EPID_{total}$  image.

Thus, the results in the previous and this section imply that, provided a sufficient number of image frames are acquired, use of the single *uncorrected*  $EPID_{total}$  image to determine the actual dose delivered with an IMRT field will at worst lead to relatively

small errors. Figure 2.3(b) also indicates that the agreement between  $EPID_{total}$  and  $EPID_{total}^{wgt-sum}$  does improve further when using 200 MUs at 100 MU/min, as the mean and standard deviation are reduced to -0.4 % and 0.3 %, respectively. However, this slight improvement in the agreement also comes at the cost of an approximate doubling of delivery time to more than 2 minutes per IMRT field. Since it is desirable to streamline the IMRT verification process as much as possible, we decided that a suitable compromise between speed and accuracy was to verify each IMRT field using 100 MUs at 100 MU/min. Though the time of delivery, the total number of frames, and the apparent accuracy are fairly similar between using 800 MU at 600 MU/min and 100 MU at 100 MU/min, we chose to use the lower 100 MU/min dose rate for all verification measurements primarily to reduce the total dose delivered to the EPID. This was to prevent any potentially unnecessary damage caused by excessive radiation exposure.

#### *v. Flood- and Dark-field Image Corrections*

A number of corrections are automatically applied by the Portal-Vision software to the EPID images. First, using a predetermined *defect map* of pixels with anomalously small signals, the software replaces the value of each of these defective pixels with an average of the values of neighboring pixels. The EPID images are also corrected using dark-field and flood-field images acquired during the routine calibration procedure of the EPID. A dark-field image,  $\overline{EPID}_{dark}$ , is acquired in the absence of radiation and is used to correct for the electrometer offset values for each pixel due to dark current. To reduce statistical noise in these offsets values, the dark-field image is an average over a large number (60) of image frames. The flood-field image,  $\overline{EPID}_{flood}$ , is acquired in an open radiation field covering the entire active area of the EPID, and is generated using 30 image frames. To correct pixel values for differences between pixels in their dose-sensitivity, the pixel values of an uncorrected raw EPID image of a given radiation field,  $\overline{EPID}_{uncorr}$ , are divided by the pixel values of the flood-field. The corrected image supplied by the Portal-Vision software,  $EPID_{pv}$ , can thus be expressed by the following equation,<sup>7</sup>

$$EPID_{PV} = \left\{ \frac{\overline{EPID_{uncorr}} - \overline{EPID_{dark}}}{\overline{EPID_{flood}} - \overline{EPID_{dark}}} \right\} \cdot k_{FFmean} \quad , \quad (2.5)$$

defect  
corrected

where  $k_{FFmean}$  is a scaling factor representing the mean pixel value of the flood-field image after it is dark-field corrected. Dark-field and flood-field images are acquired for each given beam energy/dose rate combination, since these images depend on the EPID's timing parameters.

During normal clinical use of the EPID for portal imaging, the pixel sensitivities and dark currents usually change gradually over time. Typically, such small changes do not adversely affect image quality, and routine dark- and flood-field calibrations are thus performed relatively infrequently – perhaps every month. However, for quantitative dosimetric applications, changes in pixel sensitivities and dark currents are more important. Thus, as a precaution to ensure the best possible accuracy, dark- and flood-field calibration procedures were performed before every set of our experimental measurements. For convenience, these calibration images were acquired with 2 cm of extra solid-water build-up placed on the detector and the (nominal) SDD set to 105 cm – the same set-up used for all subsequent EPID measurements.

#### ***vi. Correction of Fluence Profile Distortions caused by the Flood-field Correction***

For dosimetric applications, the flood-field image should ideally be generated using a spatially uniform energy fluence incident on the EPID. However, this is not the case for our calibration, since the flood-field image is generated using an open beam that contains the horns arising from a linac's flattening filter. As a consequence, the automatic flood-field correction – the division in Eq. (2.5) – not only corrects the image for pixel-to-pixel differences in dose-response, but unfortunately also removes the sensitivity to the true “horned” shape of the input dose profile. If this is not taken into account, the flood-field correction will thus introduce spatial distortions in any dose distributions derived from EPID images.

There are different methods of attempting to prevent such distortions, while still correcting for pixel-to-pixel variations in sensitivity. One way is to use a more perfectly uniform input dose distribution. Typically this could be done by placing additional solid water on the EPID (*e.g.* Refs. [13,14]) so that the EPID is at an effective depth of

measurement (usually about 10 cm water-equivalent) where the profile of the open beam is as flat as possible (*i.e.* the “horns” have been minimized). We chose not to use this approach for the following reasons. Firstly, for the purpose of streamlining our verification procedure, we wished to use the same amount of solid-water build-up for both the calibration and the verification images. Use of a large amount of build-up would cause excessive blurring of the EPID images of IMRT fields, and will make attempts to accurately extract the primary fluence from these images through deconvolution more error-prone. Secondly, since there is no depth at which the distribution is perfectly flat, we attempted to devise a more generic correction procedure.

Our correction procedure involves restoring the shape of the flood-field input by multiplying (pixel-by-pixel) the original EPID image,  $EPID_{PV}$ , by a “pseudo-simulated” EPID flood-field image containing no variability in pixel sensitivity,  $I_{flood-sim}$ . The corrected (and integrated) EPID image is thus described by the equation,

$$EPID_{corr}(x, y) = n_{frame} \cdot EPID_{PV}(x, y) \cdot I_{flood-sim}(x, y). \quad (2.6)$$

By doing this, the only remaining effect of the division in Eq. (2.5) will be to correct for pixel dose-response variations, as desired. The 2-D flood field  $I_{flood-sim}$  is generated by convolving ( $\otimes$ ) the flood-field fluence,  $\Psi_{flood}$ , with a pencil-beam kernel,  $K_{EPID}$ , which describes the blurring processes in the EPID:

$$I_{flood-sim}(x, y) = \Psi_{flood}(x, y) \otimes K_{EPID}(x, y). \quad (2.7)$$

The details of  $K_{EPID}$  are described in Section 2.D. The flood-field fluence distributions for both 6 and 15 MV photon beams were derived from dose calculations done using our treatment planning system (TPS) [Helax-TMS, Nucletron B.V., Veenendaal, The Netherlands]. For each energy, a beam’s eye view (BEV) dose distribution for a flood-field beam ( $D_{flood-TPS}$ ) was calculated at a depth of 3 cm in a rectangular phantom measuring 40 x 30 x 5.5 (depth) cm<sup>3</sup>. The phantom was modeled in the TPS to approximate the geometry of the EPID. Since our TPS only provides a very limited choice of phantom materials, the actual materials constituting the EPID structure could not be used, and the phantom was simply modeled as water. The depth of 3 cm is approximately the same effective water-equivalent depth of our EPID measurements. To

calculate  $\Psi_{flood}$ , the TPS flood-field dose distributions are deconvolved ( $\otimes^{-1}$ ) with a EGSnrc-generated (EGSnrc, National Research Council (NRC) Canada, Ottawa)<sup>15</sup> pencil-beam kernel,  $K_{flood-phantom}$ , used to describe the pencil beam 2-D dose distribution at 3 cm depth of this phantom:

$$\Psi_{flood}(x, y) = D_{flood-TPS}(x, y) \otimes^{-1} K_{flood-phantom}(x, y) . \quad (2.8)$$

We later verified the above method of deriving  $\Psi_{flood}$  by comparing to in-air measurements of the flood-field relative fluences ( $\Psi_{flood|meas}$ ) made with an IC10 ion chamber (15 MV) or with a diamond detector (6 MV) in a Wellhofer scanning tank. For this purpose we generated a second set of simulated flood-field images,  $I_{flood-sim|meas}$ , calculated using the measured  $\Psi_{flood|meas}$  in Eq. (2.7), rather than the  $\Psi_{flood}$  calculated using Eq. (2.8). For comparison purposes,  $I_{flood-sim}$  and  $I_{flood-sim|meas}$  were each normalized to the central pixel of their respective distributions, and the difference image,  $I_{flood-sim|meas} - I_{flood-sim}$ , was then calculated. For the 15 MV images, the differences are reasonably small. Within a ROI covering the central 28 x 28 cm<sup>2</sup>, the mean, minimum, and maximum differences are -0.5 %, -1.9 % and 1.7 % respectively, and the standard deviation is 0.6 %. In the same ROI, the corresponding differences for the 6 MV simulated flood-fields are 0.8 %, -1.6%, and 4.3 %, and the standard deviation is 1.4 %, indicating a somewhat worse agreement in the 6 MV case. However, it is probable that at least part of these larger discrepancies is in fact due to errors in the measured fluence for the 6 MV flood-field. The central in-plane profile in this measured fluence shows a relatively large asymmetry: if real, such an asymmetry would have been detected in the routine quality assurance scans of this linac, since it is larger than would be tolerated clinically.

For all the IMRT verification calculations, we used  $I_{flood-sim}$ , the simulated EPID flood-field based on the fluence extracted from TPS calculations. For the 2-D verification (see Section 2.E) of one treatment plan (15 MV, eight fields), we repeated the analysis using  $I_{flood-sim|meas}$ . When using  $I_{flood-sim|meas}$  instead of  $I_{flood-sim}$ , the mean dose difference (TPS – EPID) changed by a maximum of 0.14 % for any single field, and

was an average of  $0.01 \pm 0.08$  % different over the eight fields. Similarly, the maximum change in the standard deviation of the dose difference was only 0.10 %, and the average difference was  $0.01 \pm 0.05$  %. This suggests that the choice of method of deriving the flood field fluence (measured or TPS-based) has a negligible impact on the verifications.

## D. Pencil-beam Kernels Describing Blurring in the EPID

The foundation of both the 2-D and the 3-D IMRT pre-treatment verification procedures is the EPID's ability to accurately measure the 2-D relative incident energy fluence distributions actually delivered by a radiation beam. However, the  $EPID_{corr}$  in Eq. (2.6) does not directly reflect the fluence distribution incident on the detector, but rather includes the blurring caused by spatial spreading of scattered x-ray photons in the build-up and phosphor layers, as well as optical photons in the phosphor layer. Our method thus requires deconvolution (*i.e.* “de-blurring”) using kernels describing x-ray and optical scattering that were derived using a “semi-empirical” approach employing Monte Carlo and empirical fitting techniques.

### *i. Monte-Carlo Dose-deposition Kernels*

The main source of blurring occurs in the dose-deposition stage of the formation of the EPID output signal. Mathematically, the dose,  $D_{phosphor}(x', y')$ , deposited at a point  $(x', y')$  at a given depth in the phosphor can be expressed quite generally as a superposition of the incident polyenergetic photon fluence,  $\Psi_p(x, y, \bar{p}_\gamma, E_\gamma)$ , with a dose deposition pencil-beam kernel,  $K_{dose}(x', y', x, y, \bar{p}_\gamma, E_\gamma)$ ,

$$D_{phosphor}(x', y') = \sum_{E_\gamma} \sum_{\bar{p}_\gamma} \int \Psi_p(x, y, \bar{p}_\gamma, E_\gamma) K_{dose}(x', y', x, y, \bar{p}_\gamma, E_\gamma) dx dy. \quad (2.9)$$

In Eq. (2.9),  $E_\gamma$ ,  $\bar{p}_\gamma$ , and  $(x, y)$  describe the energy, direction, and spatial coordinates on the phosphor surface, respectively, of the photons comprising the incident energy fluence. To extract the energy fluence from the dose, an inverse operation of the superposition in Eq. (2.9) could be attempted. In practice, however, such a task is computationally challenging. It also requires *a priori* assumptions about the energy spectrum and its dependence on off-axis location, as well as a full characterization of the kernel

$K_{dose}(x', y', x, y, \bar{p}_\gamma, E_\gamma)$ . The latter would be difficult because of the many variables on which the kernel potentially depends. Thus, to simplify calculations, we assumed that the full superposition can be approximated by a convolution operation,

$$D_{phosphor}(x', y') = \int \Psi_p(x, y) K_{dose}(x - x', y - y') dx dy \equiv \Psi_p(x, y) \otimes K_{dose}(x, y). \quad (2.10)$$

In the frequency domain convolution becomes a simple multiplication,

$$FT[D_{phosphor}(x', y')] = FT[\Psi_p(x, y)] \cdot FT[K_{dose}(x, y)], \quad (2.11)$$

where  $FT$  refers to the Fourier transform operation. The main assumption in this approach is that the kernel is spatially invariant: that the dose deposition depends only on the relative locations of the given points in the detector and fluence planes, and not on their absolute locations. Implicitly this assumes that: (1) the scattering properties of the detector are the same at all points in the detector; (2) the shape of the incident energy spectrum is the same for all points in the photon beam; and (3) the beam is normally incident on the detector (*i.e.* no kernel-tilting).

The form of  $K_{dose}$  was derived using the EGSnrc (National Research Council (NRC) Canada, Ottawa) Monte Carlo software package to simulate the dose deposition in the EPID phosphor caused by an incident pencil beam. Since full specifications detailing the dimensions and material compositions of all components of the EPID were not available, the simplified model of the EPID shown in Fig. 2.4 was used for our simulations. This model contains five prominent layers of the detector: the extrinsic water build-up (2.0 cm thickness,  $\rho=1.0 \text{ g/cm}^3$ ), the copper plate (0.1 cm,  $\rho=8.93 \text{ g/cm}^3$ ), the phosphor ( $\text{Gd}_2\text{O}_2\text{S}$ , 0.034 cm,  $\rho=3.67 \text{ g/cm}^3$ ), the glass substrate for the photodiode array ( $\text{SiO}_2$ , 0.11 cm,  $\rho=2.3 \text{ g/cm}^3$ ), and a water backscatter layer, used to approximate the materials lying below the active detection layer in the EPID. The choice of backscatter thickness differed for 6 and 15 MV beams, and is discussed specifically in Sections 2.D.iii-2.D.v below. The model had a cross-section of  $30 \times 30 \text{ cm}^2$ , and the dose was scored in the phosphor layer, which was divided into  $383 \times 383$  pixels each measuring  $0.0784 \times 0.0784 \text{ cm}^2$ . The scoring and set-up of the simulation geometry were simplified by using the DOSxyz code (NRC, Ottawa). The incident photon energy spectra used for the simulations were the Varian 6 and 15 MV photon beam central-axis

spectra (Fig. 2.5) generated by Sheikh-Bagheri and Rogers,<sup>3</sup> who used the BEAMnrc (NRC, Ottawa) Monte Carlo code to model the output from the heads of a number of commercial linacs for a 10 x 10 cm<sup>2</sup> field. Changes in  $K_{dose}$  resulting from variation in the incident energy spectra with off-axis beam location and due to differences in the amount of head scatter with changing collimation were not investigated in this work. The normally-incident pseudo-pencil beam was pixel-sized, 0.0784 x 0.0784 cm<sup>2</sup>, and centered on the EPID model's cross-section. Simulations were performed with the photon and electron cutoffs set to 10 keV kinetic energy ( $ECUT = 0.521$  MeV,  $PCUT = 0.010$  MeV), and using the PRESTA-II electron-step and "exact" boundary-crossing algorithms.

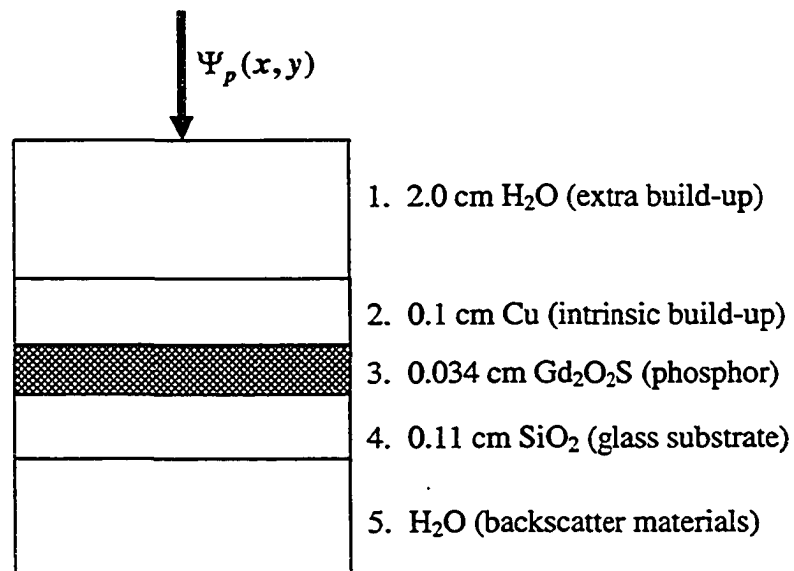


**Figure 2.4.** Simplified model of the geometry of the aS500 EPID used in the EGSnrc Monte Carlo simulations used to derive  $K_{dose}$ . The cross-section of each of the five layers was 30 x 30 cm<sup>2</sup> (383 x 383 pixels).

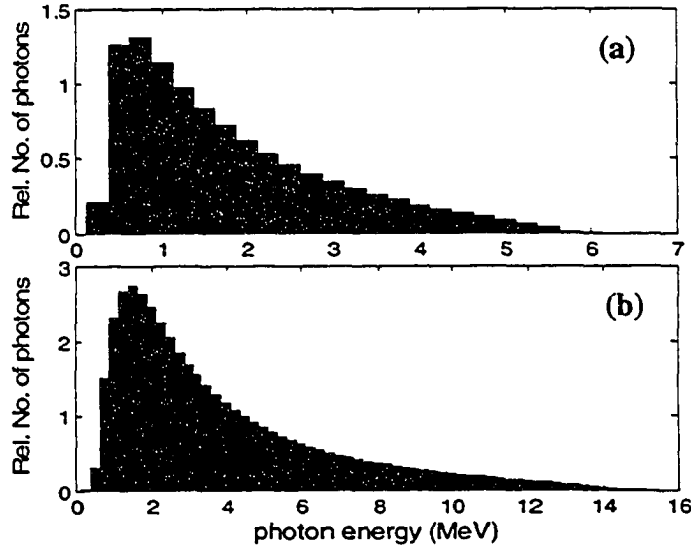


**Figure 2.5.** Incident photon beam spectra used for EGSnrc simulations. The spectra are results of BEAMnrc simulations for Varian linac (a) 6 MV and (b) 15 MV photon beams published by Sheikh-Bagheri and Rogers.<sup>3</sup>

## ii. Empirically-derived Optical Spread Kernels

Additional blurring of the EPID image is caused by optical glare, the spreading of optical photons before reaching the photodiode array. Due to the linearity of this detector system, if it is assumed that this process can also be described with a spatially-invariant kernel,  $K_{glare}$ , an overall blurring kernel,  $K_{EPID}$ , can be then expressed as a convolution of the glare and dose-deposition kernels,  $K_{EPID} = K_{dose} \otimes K_{glare}$ . We did not, however, explicitly model optical spreading to generate  $K_{glare}$ . Rather, to create the overall EPID kernel, we instead convolved  $K_{dose}$  with an empirical function designated  $K_{back-glare}$

$$K_{EPID} = K_{dose} \otimes K_{back-glare} \quad (2.12)$$

The empirical kernel is designed to not only describe any optical spreading, but also to account for any deficiencies in the modeling used to generate  $K_{dose}$ , particularly uncertainties in the modeling of the backscatter material. The corrected EPID image,  $EPID_{corr}$ , calculated with Eq. (2.6), can thus be represented by the convolution of the incident fluence with this total kernel,

$$EPID_{corr} = \Psi_p \otimes K_{EPID} . \quad (2.13)$$

The incident fluence can then be derived very simply using,

$$\Psi_p(x, y) = IFT \left[ \frac{FT[EPID_{corr}(x, y)]}{FT[K_{EPID}(x, y)]} \right], \quad (2.14)$$

with *IFT* representing the inverse Fourier transform operation. For our calculations, all Fourier transform operations were performed using pre-packaged MATLAB (The Mathworks Inc., Natick, MA) routines, and were done using Cartesian coordinates and pixel spacing equal to the pixel pitch of the EPID (0.0784 cm). The empirical  $K_{back-glare}$  is chosen as the one that results in the best agreement for open fields between EPID fluences obtained from Eqs. (2.6), (2.12), and (2.14) and corresponding beam profiles measured with a diamond detector.

As noted in the introduction to this chapter, the original 15 MV EPID kernel used for the 2-D verification analysis differs slightly in its development from the 6 and 15 MV kernels derived later for the 3-D verification project. The primary differences involve the thickness of backscatter used in the simplified EPID model, and the empirically-derived  $K_{back-glare}$  kernel. These differences are clarified in the following sections, which describe each of the kernels in more detail.

### ***iii. Original 15 MV EPID Kernels used in 2-D verifications***

In deriving the original 15 MV dose kernel for 2-D verifications, we used a 2.5 cm thick water backscatter layer in our simplified EGSnrc EPID model, based on results reported by Kim *et al.*<sup>16</sup> To generate the kernel,  $1.8 \times 10^8$  incident photon histories were used in the EGSnrc simulations, which resulted in a statistical uncertainty of approximately 5.5 % in the kernel amplitude for the pixel located 2 cm from the center of the pencil beamlet. We first investigated whether this dose kernel,  $K_{dose}^{15MV}$ , could alone describe the blurring properties of the EPID, since there is some uncertainty if optical glare contributes noticeably to image blurring for flat-panel imaging systems. For example, the works of Munro and Bouius<sup>5</sup> and Siebers *et al.*<sup>17</sup> have suggested a negligible glare contribution, while McCurdy *et al.*<sup>4</sup> found that the use of a glare kernel significantly improved the agreement between measured and simulated portal images.

Since there were appreciable discrepancies between the diamond profiles and the EPID-based fluence profiles derived from Eq. (2.14) using  $K_{EPID} = K_{dose}^{15MV}$ , our results suggested that an additional kernel ( $K_{back-glare}^{15MV}$ ) was necessary.

A double exponential form was used for  $K_{back-glare}^{15MV}$ ,

$$K_{back-glare}^{15MV}(r) = \exp(-C_1 r) + C_2 \exp(-C_3 r), \quad (2.15)$$

where  $r = \sqrt{\Delta x^2 + \Delta y^2}$  is the radial distance from the center of this pencil-beam kernel, and  $C_1$ ,  $C_2$ , and  $C_3$  are fitting parameters. Values of  $C_1 = 37.1 \text{ cm}^{-1}$ ,  $C_2 = 0.00136$ ,  $C_3 = 2.46 \text{ cm}^{-1}$  were obtained by fitting the EPID-based profile to the diamond profile in the tail region of a  $10 \times 10 \text{ cm}^2$  open field. The spatial extent of this kernel was limited to a radius of 2.5 cm (*i.e.*  $K_{back-glare}^{15MV} = 0$  for  $r > 2.5 \text{ cm}$ ), since increasing this radius did not improve the quality of the fit. These parameters also yielded good agreement for a similar comparison using a  $4 \times 4 \text{ cm}^2$  field, but a slight under-deconvolution for a  $20 \times 20 \text{ cm}^2$  field. However, the slightly poorer agreement in the tail of the larger field was not considered particularly problematic. Since most of the segments comprising step-and-shoot IMRT fields are comprised of relatively small sub-fields, it was considered more important to fit the smaller fields. This was supported by the fact that these fit parameters provided very good agreement between EPID-derived and diamond profiles through a segment of a clinical IMRT field.

#### ***iv. 6 MV EPID Kernel used in 3-D Verifications***

In our initial attempts to generate the 6 MV EPID kernels, we used 2.5 cm of backscatter in our Monte Carlo simulations, as was done for the 15 MV case. We also initially tried using the same empirical kernel, *i.e.*  $K_{back-glare}^{6MV} = K_{back-glare}^{15MV}$ . However, the resulting total EPID kernel produced poor agreement between the EPID and diamond fluence profiles. Specifically, for the smaller open fields, the EPID profiles showed evidence of over-deconvolution: near the base of the field's penumbra, the EPID profile would dip, before rebounding to a higher level in the tail region. Using no empirical kernel, *i.e.*  $K_{back-glare}^{6MV} = 1$ , much improved the agreement between the EPID and diamond

profiles; however, for the smallest open fields tested ( $4 \times 4 \text{ cm}^2$  and  $2 \times 2 \text{ cm}^2$ ), there still appeared to be slight over-deconvolution.

These results prompted a re-examination of the use of our simplified EPID model. Although the layers included in this model were expected to describe the majority of the scattering in the EPID, the missing layers – air gaps, the front and back covers, structural foam and plastic layers, glues, *etc.* – may also contribute a non-negligible scattering component. In a recent work, von Wittenau *et al.*<sup>18</sup> used Monte Carlo simulations to study the different sources of blurring in a representative model of a flat-panel imaging system. They found that while the detector components (*i.e.* scintillator and electronics) accounted for the short-range (sub-millimeter) part of the blurring kernel, components upstream and downstream of the detector layers dominated the mid-range (millimeter-to-centimeter) and long-range (up to tens of centimeters) regions of the kernel, respectively: these latter parts of the kernel contribute significantly to the overall blurring in the image.

For our model, deficiencies in the “upstream” modeling may potentially be less serious because of the use of a large amount (2 cm) of extrinsic water build-up. Small, but appreciable, errors in the kernel can still be expected, however. This is illustrated in Fig. 2.6, which shows a statistically-significant change in the 6 MV dose kernels when an air gap layer of 6.5 mm thickness is inserted between the water build-up and the copper plate (see Fig. 2.4). (For this example, no backscatter was used in either of these models.)

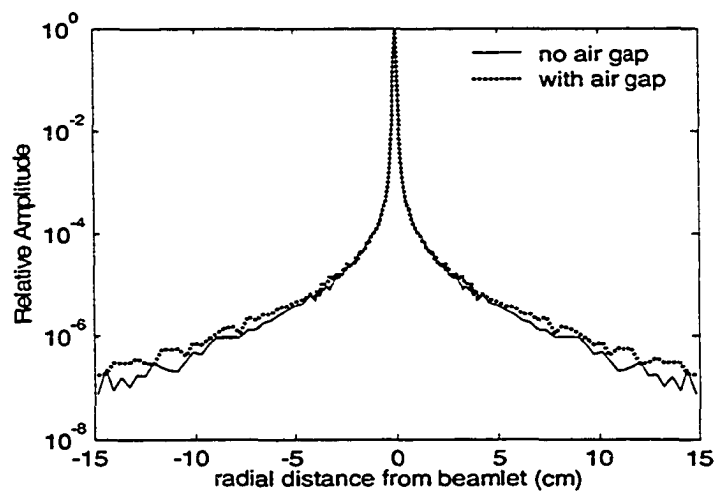


**Figure 2.6.** The change in  $K_{dose}^{6MV}$  derived from EGSnrc simulation when a 6.5 mm air gap layer is placed between the extrinsic build-up and copper plate layers in the EPID model depicted in Fig. 2.4.

Much larger errors in the dose kernel can be expected from the simplified modeling of the backscatter, since it is unclear how well the 2.5 cm thick uniform layer of water in the original model approximates the different components made of various materials (including metals) that actually comprise the downstream EPID components. Thus, our revised approach to modeling the EPID was to attempt to optimize the thickness of the water backscatter layer to obtain the best agreement between the EPID and diamond profiles. A series of EGSnrc simulations were performed to generate  $K_{dose}^{6MV}$  kernels corresponding to backscatter thicknesses ranging from 0 (no backscatter) to 5.0 cm, in 0.5 cm increments. As illustrated in Fig 2.7 and expected from the results of von Wittenau *et al.*,<sup>18</sup> changing the thickness of backscatter primarily affects the longer-range part of the kernel. Unfortunately, none of these  $K_{dose}^{6MV}$  kernels (with  $K_{back-glare}^{6MV} = 1$ , *i.e.* no empirical kernel) yielded optimal profile agreement for all open fields considered – 2 x 2, 4 x 4, 10 x 10, and 20 x 20 cm<sup>2</sup>. Of the backscatter thicknesses investigated, 1.5 cm and 2.0 cm gave the best fits on average for this range of field sizes; however, the fits for individual field sizes were still less than optimal (see Section 3.B.ii). Large field sizes were fit better using larger amounts of backscatter, while the smaller field sizes suggested the use of very little or no backscatter.

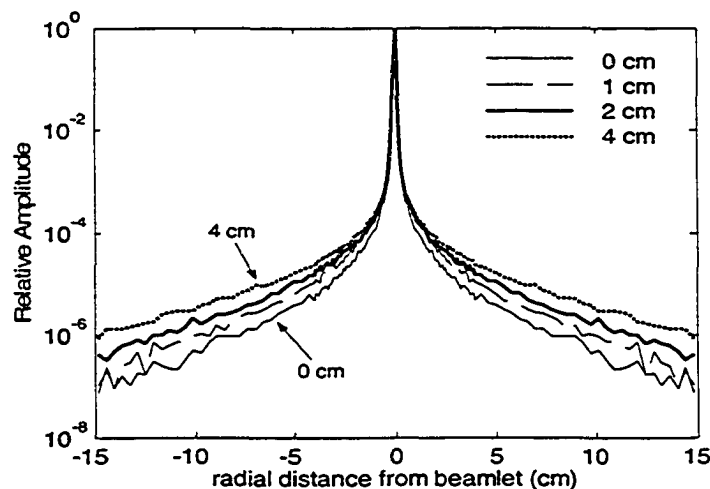


**Figure 2.7.** The change in  $K_{dose}^{6MV}$  derived from EGSnrc simulation for different thicknesses (0, 1, 2, or 4 cm) of the backscatter layer in the EPID model (layer 5 in Fig. 2.4).

The final kernel used for IMRT verifications was generated using the following method. First, simulations were performed ( $3 \times 10^8$  histories, 4.7 % statistical uncertainty at  $r = 2$  cm) with an EPID model having no backscatter layer, *i.e.* only layers 1-4 in Fig 2.4. No backscatter was used to ensure adequate fits for the smallest field sizes. We then convolved this  $K_{dose}^{6MV}$  kernel with an empirical kernel  $K_{back-glare}^{6MV}$  having a triple exponential form,

$$K_{back-glare}^{6MV}(r) = \exp(-C_1 r) + C_2 \exp(-C_3 r) + C_4 \exp(-C_5 r), \quad (2.16)$$

to create an overall kernel  $K_{EPID}^{6MV}$  that also described the blurring in large fields well. The fit parameters  $C_1$ ,  $C_2$ ,  $C_3$ ,  $C_4$ , and  $C_5$  were extracted by fitting the EPID and diamond profiles in the tail regions of the  $2 \times 2$ ,  $4 \times 4$ ,  $10 \times 10$ , and  $20 \times 20$  cm<sup>2</sup> open fields simultaneously. There is never perfect agreement between the diamond and EPID profiles. For example, the penumbras of the EPID profiles have in general a slightly sharper slope because of the slight blurring of the in-air diamond measurements due to the brass cap placed over the diamond detector for build-up and to minimize dose from contaminant electrons. There is thus some degree of subjectivity in the fitting procedure. A “semi-automated” procedure was used: MATLAB computer code was written to help steer the fits, with visual evaluation of the fits of the profiles for both the open fields and the IMRT segment field used to help determine the final set of parameter values.

The final fit parameters used for  $K_{back-glare}^{6MV}$  are  $C_1 = 37.1$  cm<sup>-1</sup>,  $C_2 = 1.57 \times 10^{-5}$ ,  $C_3 = 0.405$  cm<sup>-1</sup>,  $C_4 = 1.40 \times 10^{-6}$ , and  $C_5 = 0.0153$  cm<sup>-1</sup>. The value of  $C_1 = 37.1$  cm<sup>-1</sup> characterizing the short-range exponential term used here for  $K_{back-glare}^{6MV}$  is the same value of  $C_1$  used previously for the  $K_{back-glare}^{15MV}$  kernel. The implicit hypothesis was that the first exponential terms in Eqs. (2.15) and (2.16) describe the blurring due to optical glare: this blurring is expected to have a very short (sub-millimeter) range,<sup>18,19</sup> and is not expected to be very dependent on the energy of the incident photon beam. However, a more explicit modeling of the optical blurring would be required to make this hypothesis more than purely speculative.

Without the use of backscatter in our EPID model, it is not surprising that the parameters used to characterize  $K_{back-glare}^{6MV}$  describe a kernel with a large long-range

component. It is interesting to note that the “glare” kernel reported by McCurdy *et al.*<sup>4</sup> also had a relatively broad tail. Since it seems that these authors used a model of the EPID that also lacked backscatter, their kernel is likely also compensating primarily for deficiencies in the simplified modeling of the EPID, rather than actual optical photon processes. For comparison, our  $K_{back-glare}^{15MV}$  kernel, derived in conjunction with an EPID model with 2.5 cm of water backscatter, has a long-range component that is much smaller than either McCurdy *et al.*’s kernel or our  $K_{back-glare}^{6MV}$ .

An important observation is that the overall kernel could not be modeled adequately by simply approximating the “downstream” EPID components with a uniform water backscatter. This seems to suggest that if a more rigorous derivation of the kernel is desired, one that relies less on empirical corrections, a more thorough modeling of the EPID is necessary. Further, it is also noted that the scatter from the downstream components is not uniform across the EPID array: a disproportionate amount of scatter will reach the top of the array, due to the location of the metal R-arm below the EPID; the electronics located on the top and right sides of the EPID array may also contribute additional scatter. For example, this is manifest as an asymmetry in an in-plane EPID profile of a 20 x 20 cm<sup>2</sup> open field (Fig. 2.8). Recently, Ko *et al.*,<sup>20</sup> whose preliminary work<sup>16</sup> had used the uniform 2.5 cm water backscatter layer for EGSnrc modeling of the EPID, investigated the problems associated with these backscatter non-uniformities. Their suggested solution requires inserting a lead plate between the glass substrate of the photodiode array and the support structures in the EPID when making measurements. Since the suggestion postdates the completion of the present work and also involves modification of the EPID (which is used clinically), it was not pursued in this study.

The two “kinks” seen at the top of the in-plane profile depicted in Fig. 2.8 are row artifacts of this image acquisition mode (IMRT mode, 15 MV/100 MU/min) that occur near row 139 and row 278 of the imager. The periodicity of the artifacts suggest that they are a consequence of the timing parameters of this mode, and are likely a function of the number of imager rows that can be scanned between consecutive PVSynC pulses. A similar set of artifacts is also evident when using IMRT mode at 6 MV (100 MU/min). The 6 MV artifacts are smaller in magnitude, but affect more rows. Attempts were made to correct the EPID images for these artifacts by replacing the measured pixel values of

the affected rows with pixel values interpolated from unaffected nearby rows. The proposed correction worked well for open fields. However, for IMRT fields, where there are many large gradients, it was difficult to devise an algorithm that reliably corrected for the artifact without also smoothing out the gradient regions. Since we considered the smoothing of these gradients (and consequent loss of spatial resolution) worse than the artifacts themselves, we did not implement any corrections for these artifacts.

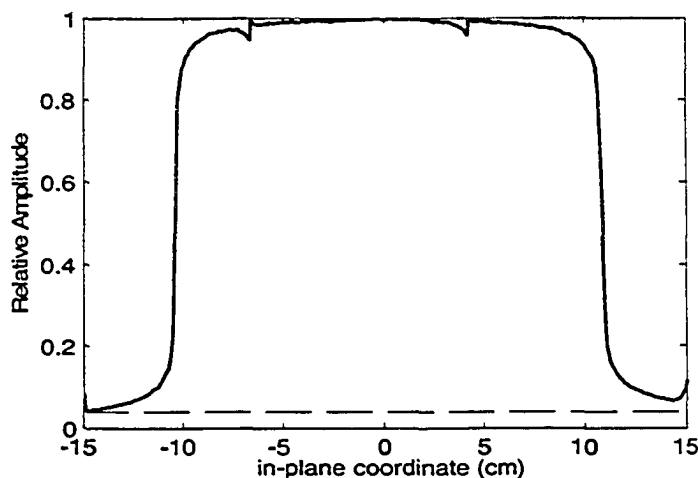


**Figure 2.8.** In-plane 15 MV EPID profile of a 20 x 20 cm<sup>2</sup> open field. The dashed line is used to highlight the asymmetry between the penumbras on the left and right sides of the field. It is believed that the metal R-arm below the EPID contributes additional backscatter to pixels at the top of the EPID array (corresponding to the right side of the profile).

#### *v. “New” 15 MV EPID Kernel used in 3-D Verifications*

The EGSnrc kernels for the 3-D verification project were generated using newer hardware (dual Intel Xeon 2.0 GHz and P4 2.4 GHz machines) and newer releases of the EGSnrc software than was available for the 2-D project (dual P3 0.6 GHz, Linux operating system). In addition to the new 6 MV kernels, the 15 MV kernels were also re-generated with the newer software/hardware platforms. Both Linux-based and (later) Window-based machines were used, where the latter ran the EGSnrcMP (where “MP” = multi-platform) version of the EGSnrc software. The kernels were found to be independent of which operating system platform was used, within statistical fluctuations. However, the newer 15 MV dose kernels were slightly different than those generated originally using the older version of the software, despite the fact that all user-defined parameters were the same in both cases. Specifically, using the same 2.5 cm of water

backscatter in the original 15 MV simulations, the long-range component of the  $K_{dose}^{15MV}$  kernel is slightly larger using the newer version of the EGSnrc software (see Section 3.A). By generating multiple versions of  $K_{dose}^{15MV}$  corresponding to different thicknesses of backscatter ranging from 0.5 to 4.0 cm in 0.5 cm increments, it was found that the old  $K_{dose}^{15MV}$  kernel was best approximated with a 1.5 cm thick backscatter layer when using the newer software. No systematic attempt was made to identify the changes (if any) in the fundamental physics modeling in the EGSnrc code that caused this discrepancy.

Despite differing from the original kernel, the overall agreement for all field sizes between the EPID and diamond profiles was approximately equivalent using the newer  $K_{dose}^{15MV}$  ( $3 \times 10^8$  histories, statistical uncertainty of  $\sim 4.0\%$  at  $r = 2$  cm) with 2.5 cm water backscatter, and the original form for  $K_{back-glare}^{15MV}$  described above in Section 2.D.iii. However, the quality of the fits to the individual field sizes was not identical for the new and old  $K_{dose}^{15MV}$  kernels. Specifically, the larger long-range component of the new kernel was better able to fit the larger  $20 \times 20$  cm<sup>2</sup> field than the original kernel, whereas the smaller field sizes were fit slightly better with the old kernel. Obviously, this implies that there is some uncertainty in the empirical derivation of the “optimal” kernel.

Unless otherwise specified, the results (reported in Chapter 3) for the 2-D verifications were all generated using the original, older version of  $K_{EPID}^{15MV}$ , while the newer 3-D verifications used the newer version of this kernel, based on the newer EGSnrc software, but still with 2.5 cm of backscatter in the EPID model. We also re-analyzed the 2-D verification results for three clinical IMRT treatment plans using the newer version  $K_{EPID}^{15MV}$  (see Chapter 3). Essentially this serves as one test of the sensitivity of the 2-D verification procedure to inaccuracies in the empirical determination of the kernel. Where distinction is necessary, the original and new 15 MV kernels will be designated  $K_{EPID}^{15MV}|_{old}$  and  $K_{EPID}^{15MV}|_{new}$ , respectively.

## E. IMRT Verification using 2-D Beam's Eye View Dose Distributions

### *i. Overview of the Method*

A schematic of the 2-D verification technique is illustrated in Fig. 2.9. In the treatment planning stage, the TPS is used to generate an inverse-planned IMRT treatment based on the patient's CT anatomy, and specified dose prescription and dose-volume constraints. For the first step of the 2-D verification, the TPS-modeled IMRT beams are exported from the treatment plan for the patient CT data, and imported into a second treatment plan for a simple water phantom measuring 50 x 50 x 25 (depth) cm<sup>3</sup>, which has been modeled in the TPS. The TPS is then used to calculate the 2-D beam's-eye-view (BEV) dose distribution at 10 cm depth for each IMRT field individually. In addition to the IMRT field, a 5x5 cm<sup>2</sup> open field normally incident on the BEV water phantom is also modeled in the TPS in the same dose plan. This 5 x 5 cm<sup>2</sup> open field is positioned near the corner of the phantom, so that there is minimal scatter contribution to the 5 x 5 field from the IMRT field (and vice versa). The 2-D dose values for the IMRT field are normalized to the dose at the center of the 5x5 field. Since the dose for a 5 x 5 cm<sup>2</sup> field at 10 cm depth in water is known from commissioning data, the IMRT dose distributions can then be converted to absolute doses (in cGy).

For linac delivery of the IMRT fields, the TPS-modeled step-and-shoot segments of each IMRT field are translated into instructions that can be read by the MLC controller, which are then transferred to the treatment unit's computer. The second step of the verification is the *measurement* of a 2-D BEV dose distribution for each IMRT field delivery, as realized via these MLC controller files. A comparison of the measured 2-D doses and the analogous doses calculated by the TPS completes the verification.

Previously at our clinic, the BEV doses had been measured using film placed at 10 cm depth in a phantom consisting of slabs of solid water.<sup>21</sup> The phantom measured approximately 25 x 25 x 25 cm<sup>3</sup> and the source-to-film distance was 100 cm. The limitations of film-based techniques have been outlined in the Introduction (Section 1.B.iii). For clinical 2-D IMRT verifications, dose measurements are now performed with the EPID using the methods described below.

The registration of film, EPID and TPS dose images was required to generate the film/EPID, TPS/film, and TPS/EPID dose difference comparisons presented in Sections

3.E.ii and 3.E.iii. For this purpose, the film and TPS images were first re-sampled to the EPID pixel spacing using a MATLAB routine for bilinear interpolation. A Fourier cross-correlation algorithm<sup>21</sup> first implemented for our clinical film-based IMRT verifications was then used to perform the main part of the registration. Final small image shift adjustments (*e.g.* one or two pixels) were made, if necessary, based on minimization of the standard deviation of each dose difference distribution within a region of interest (ROI) in the image defined just outside the field edges. It is noted that this method of image registration will remove any systematic shifts between the linac's dose delivery and the TPS coordinate system. However, this is not problematic, since such shifts should be detected and corrected during the routine quality assurance and maintenance procedures performed on each linac.

All TPS dose calculations discussed in this work (both 2-D and 3-D verifications) were performed using a well-known pencil-beam convolution dose algorithm<sup>22,23</sup> that is employed in the commercial Helax-TMS (Nucletron B.V., Veenendaal, The Netherlands) system. This is the algorithm used clinically at our institute for calculation of the dose distributions of IMRT treatments.

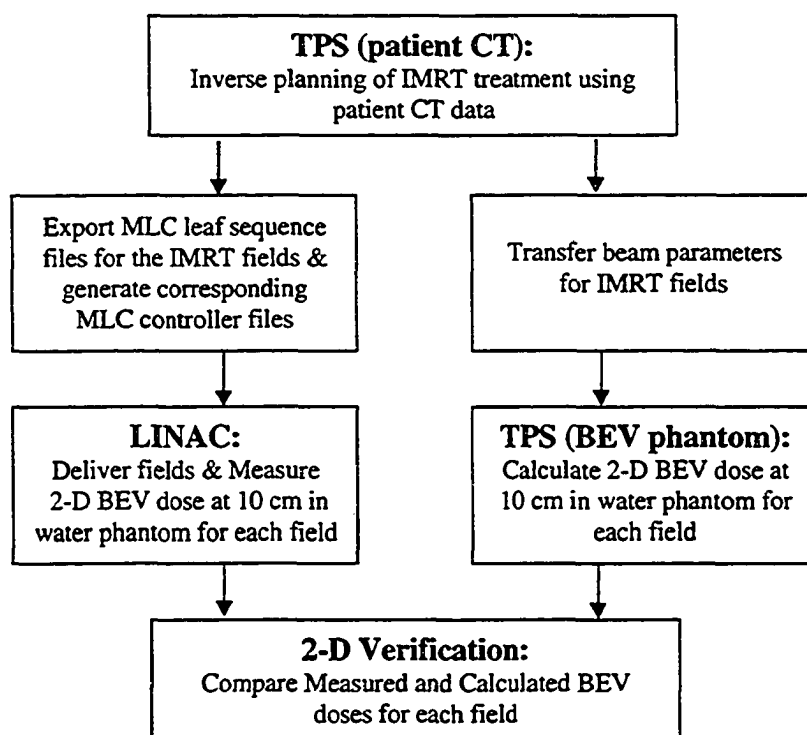


Figure 2.9. Flowchart of the 2-D IMRT verification process.

## ii. Calculation of 2-D BEV Doses with the EPID

The process of calculating EPID-based doses ( $D_{EPID}$ ) is summarized by the equation,

$$D_{EPID}(x, y) = (\Psi_p(x, y) \otimes K_{BEVphantom}(x, y)) \cdot k_{cal} \quad , \quad (2.17)$$

and depicted in Fig. 2.10. The EPID-measured incident fluence profile for each IMRT field,  $\Psi_p(x, y)$ , is first calculated using Eq. (2.14). This fluence is then convolved with a dose-deposition kernel,  $K_{BEVphantom}$ , to yield a dose image (in arbitrary dose-pixel units) at 10 cm depth in a water phantom, as required for verification. To generate  $K_{BEVphantom}$ , EGSnrc was used to simulate and score the dose deposition at 10 cm depth when a pixel-sized photon pencil beam is normally incident on a 30 x 30 x 25 cm<sup>3</sup> water phantom. The energy spectra and EGSnrc parameters for these simulations were the same as those previously described for the EPID kernels. The calibration factor,  $k_{cal}$ , is used to convert the doses in arbitrary dose-pixel units to doses in absolute units of cGy.

To calculate the EPID-calibration factor,  $k_{cal}$ , an additional EPID image of a “step-window” calibration field is also acquired during each verification, in addition to the images of each of the IMRT fields. The step-window is a twelve-segment step-and-shoot field that delivers a 4 x 3 grid of 4 x 4 cm<sup>2</sup> square sub-fields, as depicted in Fig. 2.11. It was initially devised to expedite the generation of an H&D (Hurter and Driffield) curve, by providing a well-sampled twelve point calibration curve with the irradiation of only a single piece of film. Using a total linac delivery of 240 MUs, the squares correspond to irradiations of 10 to 120 MUs in 10 MU increments. The doses for each square are not quite linearly spaced because of differing percent contributions from scatter and MLC leakage radiation. Using the same procedure as discussed for the IMRT fields, the EPID “step-window” image is converted to a dose distribution, in arbitrary dose-pixel units, at 10 cm depth in a water phantom. The mean of the dose-pixel values in a 15 x 15 pixel (1.2 x 1.2 cm<sup>2</sup>) region in the centre of each step-window square,  $DosePix_{EPID}(i)$  (where  $i = 1$  to 12), is then calculated. In separate experiments, the absolute point dose at the center of each square,  $Dose_{ion}(i)$ , was also measured using an

ion chamber placed at 10 cm depth in a water phantom. The dose-calibration factor,  $k_{cal}$ , is the coefficient providing the best linear fit,  $Dose_{ion} = k_{cal} \cdot DosePix_{EPID}$ , to the twelve  $(DosePix_{EPID}(i), Dose_{ion}(i))$  points.

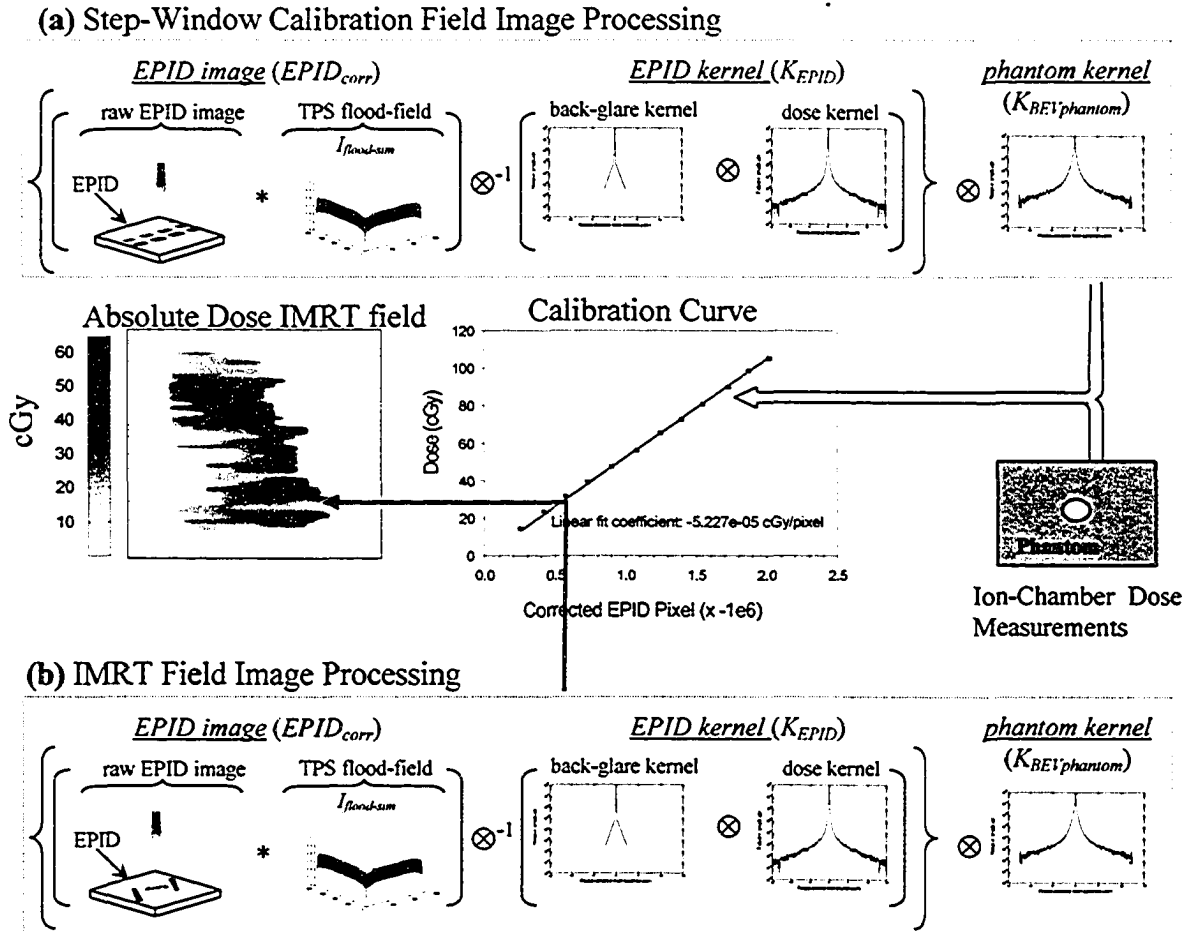


**Figure 2.10.** Illustration of the steps involved in calculating the BEV dose distribution at 10 cm depth in a water phantom from an EPID image. (a) The raw EPID image of the step-window calibration field is converted to a dose image in arbitrary dose-pixel units via the shown processing steps (cf. Eqs. (2.6), (2.12), (2.14), and (2.17)). This dose image is cross-calibrated with step-window absolute doses measured with an ion chamber to generate a calibration curve that yields the linear calibration coefficient,  $k_{cal}$ . (b) The same image processing steps used in (a) are utilized to convert a raw EPID image of an IMRT field to a dose image in arbitrary dose-pixel units. Using  $k_{cal}$  (Eq. (2.17)), this image is then converted to an absolute dose image.<sup>†</sup>

<sup>†</sup> Special thanks to my colleague Dr. Stephen Steciw for producing this figure.



**Figure 2.11.** E PID image of the step-window calibration field used to calculate the dose calibration coefficient  $k_{cal}$ . There are twelve  $4 \times 4 \text{ cm}^2$  sub-fields corresponding to irradiations of 10 MUs (bottom left) to 120 MUs (top right) in 10 MU increments.

The 15 MV step-window point-doses were first measured in a phantom consisting of slabs of solid water, as was done previously at our clinic for the clinical 2-D verifications using film. At a later time, we made step-window point-dose measurements for both 6 and 15 MV beam energies, using an IC-10 ion chamber (Scanditronix Wellhofer North America, Bartlett, TN) in a Wellhofer scanning tank filled with (liquid) water. For all such experiments, the absolute doses were calculated in the following manner. Ion chamber readings were recorded for each of the twelve step-window measurement points, and also for a  $10 \times 10 \text{ cm}^2$  open field (all at 10 cm depth). Using the absolute dose for the  $10 \times 10 \text{ cm}^2$  field from TG-51<sup>24</sup> calibration results to calculate a conversion factor, the ion-chamber readings at the step-window points could be converted to absolute dose values. So that  $k_{cal}$  could be corrected for day-to-day fluctuations in the linac output, the relative output of the linac was measured both on the day the absolute ion chamber doses were measured and on the day an IMRT verification was performed. The linac outputs were measured using a routine QA (quality assurance) procedure, where readings taken with a PR-06C (Capintec Inc., Ramsey, NJ) ion chamber

in a polystyrene cylindrical jig-phantom are cross-calibrated with previous TG-51 measurements using a “jig-factor”.

## F. IMRT Verification using 3-D Dose Distributions in a Patient’s CT Anatomy

### i. Calculation of 3-D Doses from EPID Measurements of Incident Fluence

The 3-D IMRT verification process is illustrated in Fig. 2.12. For each field in the IMRT treatment plan, two EPID images ( $EPID_{corr}$ ) are acquired: an “MLC” image of the delivered step-and-shoot sequence of the IMRT field, and an image of the corresponding “open-field” defined solely by the secondary collimators, with these collimators located at the same positions as used for the first image. The 2-D relative fluence profile for each of these images is again calculated using Eq. (2.14). The *measured* 2-D fluence modulation,  $\Psi_{mod}(x, y)$ , for each IMRT field is then determined from the “MLC”-to-“open-field” ratio of the relative incident fluences:

$$\Psi_{mod}(x, y) = \frac{\Psi_p(x, y)|_{MLC}}{\Psi_p(x, y)|_{open}} . \quad (2.18)$$

The measured  $\Psi_{mod}(x, y)$  from Eq. (2.18) for each field is re-sampled on a larger  $0.15 \times 0.15 \text{ cm}^2$  grid (defined at 100 cm from the linac source) using a simple linear interpolation algorithm written in MATLAB. It is then formatted appropriately as a “compensator” file that can be read by the TPS. Use of this “virtual” compensator has the effect of replacing the modulation modeled by the TPS for the optimized step-and-shoot MLC sequence for each field with the modulation measured using the EPID. The TPS, with the measured  $\Psi_{mod}(x, y)$ , is then used to re-calculate the cumulative (*i.e.* all beams together) 3-D dose distribution,  $D_{EPIDflu}$ , with respect to the patient’s CT anatomy. Note that the beam energy, main collimator settings, and relative beam weights are all identical to those used to calculate the original planned dose distribution,  $D_{TPS}$ , based on the *TPS-optimized* fluence modulations. A type of “3-D IMRT verification” is

then furnished by comparing the new, measurement-dependent  $D_{EPIDflu}$  dose with the planned, measurement-independent  $D_{TPS}$ .

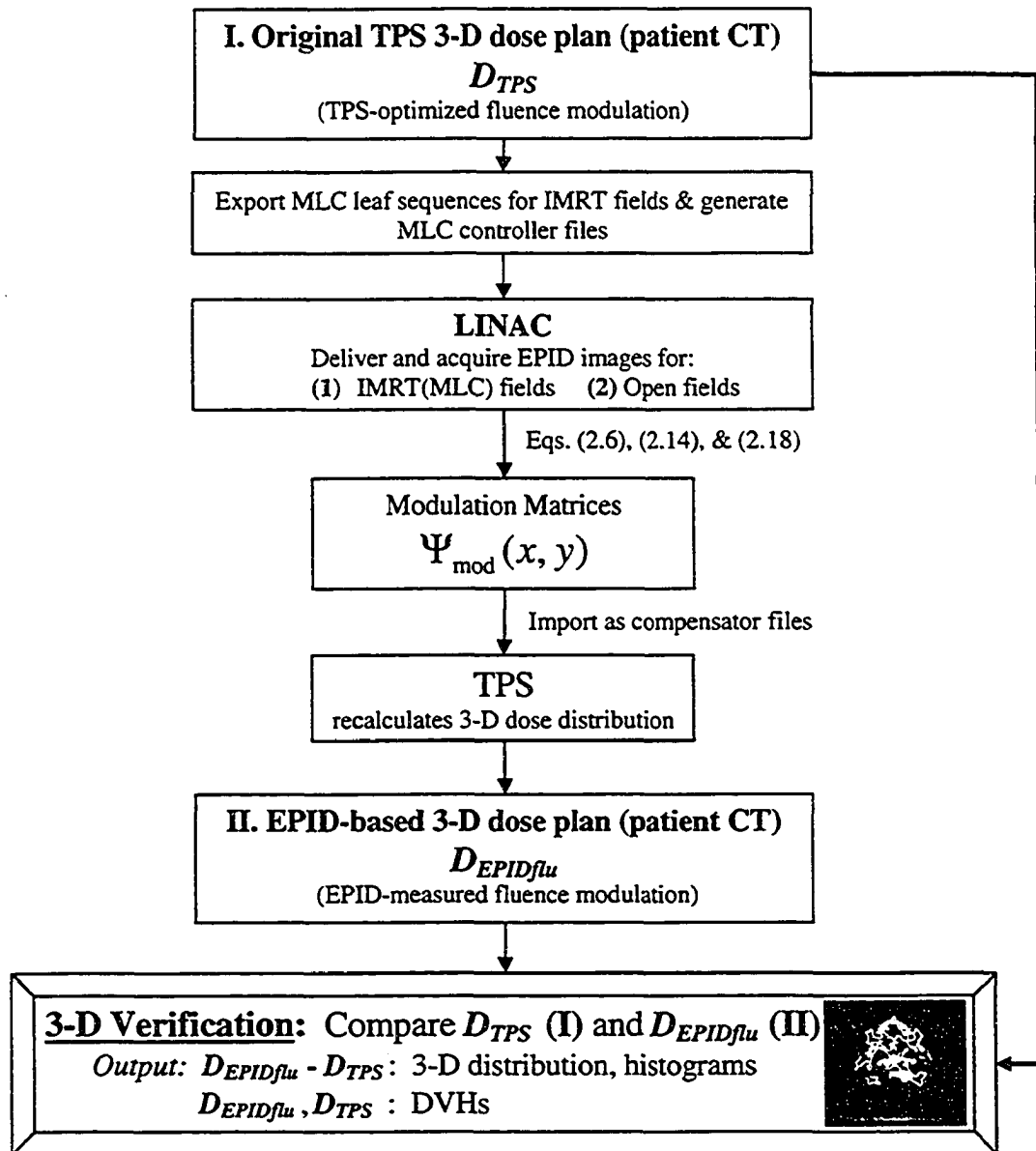


Figure 2.12. Flowchart of the 3-D verification process.

Registration of the  $D_{EPIDflu}$  and  $D_{TPS}$  doses was accomplished with the following technique. During the EPID measurements, an EPID image of an open  $10 \times 10 \text{ cm}^2$  field is also acquired. The center of the radiation field with respect to the pixel coordinates of the EPID image is determined from the locations of the four edges of this symmetric,

square field in the EPID image, as determined by standard edge detection techniques. This allows the measured  $\Psi_{\text{mod}}(x, y)$  matrix, and thus the imported compensator file, to be properly aligned with the TPS coordinate system. This method of registration is effective, provided routine quality assurance of the linac ensures that the isocenter defined by the lasers used in the set-up of patients for treatment coincides with the center of the 10 x 10 cm<sup>2</sup> radiation field.

## ii. Normalization of Dose Distributions Calculated by the TPS

Our TPS internally calculates a patient dose distribution with respect to a standard reference dose, defined as the dose at the depth of maximum dose ( $d_{\text{max}}$ ) in a water phantom at 100 cm SSD for a 10 x 10 cm<sup>2</sup> field. For output, the TPS then converts this *un-normalized* dose distribution, where all doses are relative to the fixed reference dose, to a *normalized* distribution, where all doses are expressed relative to a user-specified normalization point or volume in the patient plan, and a corresponding user-specified dose level. Consistent with the convention used at our clinic for IMRT plan normalization, the  $D_{\text{EPIDflu}}$  and  $D_{\text{TPS}}$  doses were normalized such that the median dose in the planning target volume (PTV)<sup>25</sup> matched a specified prescription dose. However, use of this normalization forces the *normalized* median doses to be identical for the EPID-based and planned TPS doses: thus, any difference in the *un-normalized* (*i.e.* with respect to the reference dose) median dose between the two cases due to discrepancies between the measured and the TPS-optimized  $\Psi_{\text{mod}}(x, y)$  will be lost. To establish a common normalization for the two dose distributions and thus restore sensitivity to differences in the *un-normalized* median doses, the  $D_{\text{EPIDflu}}$  distribution was multiplied by a normalization correction factor,  $N_{\text{corr}}$ ,

$$D_{\text{EPIDflu}} \rightarrow N_{\text{corr}} \cdot D_{\text{EPIDflu}} \quad (2.19)$$

In theory,  $N_{\text{corr}}$  is the ratio of the *un-normalized* median dose calculated for the uncorrected EPID-based distribution to that of the TPS-based distribution. In practice, there is no straightforward way to calculate this ratio, since the TPS can be used to report *un-normalized* doses (with respect to the standard dose) only for *points* of interest, and not for volumes of interest. Thus, to calculate  $N_{\text{corr}}$  the EPID-based and TPS-based dose

distributions were temporarily normalized to a single normalization point located at isocenter. The median *normalized* PTV doses using this new point normalization were then calculated, and are designated  $D_{EPIDflu,PTV}$  and  $D_{TPS,PTV}$  for the EPID-based and TPS-based doses, respectively. The *un-normalized* doses at the normalization point for the two dose distributions,  $^{unnorm}D_{EPIDflu,normpt}$  and  $^{unnorm}D_{TPS,normpt}$ , were also recorded, so that the *normalized* median doses could be corrected for differences in the *un-normalized* doses at the normalization point. The normalization correction factor,  $N_{corr}$ , was then calculated from the following equation:

$$N_{corr} = \frac{D_{EPIDflu,PTV} \cdot ^{unnorm}D_{EPIDflu,normpt}}{D_{TPS,PTV} \cdot ^{unnorm}D_{TPS,normpt}}. \quad (2.20)$$

### iii. TPS Dose Calculations with a “Point- Source” Model

In its dose calculation algorithm, the TPS models beam penumbra by including an additional penumbra dose convolution kernel dependent on “beam-size” parameters, rather than explicitly modifying the energy fluence itself. However, EPID-measured 2D-fluences intrinsically describe the beam penumbra, as supported by the good agreement between open field fluence distributions measured with the EPID and those measured with a diamond detector (see Chapter 3). Therefore, EPID-derived fluence modulations ( $\Psi_{mod}$ ) imported into the TPS already contain penumbral blurring at the treatment field edges. The TPS, however, treats the imported  $\Psi_{mod}$  as a virtual compensator and thus applies the penumbra dose kernel to calculate the EPID-based dose ( $D_{EPIDflu}$ ): this introduces an unnecessary additional blurring at the treatment field edges. Since the planned  $\Psi_{mod}$  does not contain the penumbral blurring, this problem does not exist for the  $D_{TPS}$  dose. To quantify the significance of this effect, EPID-based dose calculations were also performed with the “beam-size” parameters used in the penumbra kernel reduced from ~0.5 cm to 0.001 cm, to effect a “point-source” that avoids additional penumbral blurring. EPID-based doses calculated using this “point-source” TPS model are designated as  $D_{EPIDflu|pnt}$ .

## **G. Summary**

This chapter provided the background material necessary to understand the development of our 2-D and 3-D EPID-based IMRT verification procedures. In the first sections of this chapter, relevant properties and image acquisition characteristics of the Varian aS500 EPID were described. Specifically, we discussed the recently available “IMRT” acquisition mode, which effectively allows the EPID to be used as an integrating dosimeter. The accuracy of the IMRT mode for measuring dose distributions from step-and-shoot IMRT fields was assessed, and issues of buffer deadtime and ghosting effects relevant to use of the IMRT mode were addressed. Also described was a correction we devised to account for distortions in the raw EPID image pixel intensity distributions caused by the flood-field correction that is automatically applied by the EPID’s Portal Vision software.

Our 2-D and 3-D IMRT verification procedures rely on the ability to accurately measure fluence distributions with the EPID. For this purpose, we developed a kernel-based deconvolution technique that converts the pixel intensity distribution of a raw EPID image to a 2-D incident fluence distribution using pencil-beam kernels describing image blurring processes in the EPID. The methods used to generate the necessary kernels were described in this chapter. These methods include Monte Carlo simulations of the dose deposition in the EPID, and empirical fitting techniques to account for both optical glare, and any deficiencies in the Monte Carlo-derived dose deposition kernels due to the simplified modeling of the EPID structure.

Finally, this chapter provided an overview of the processes of the 2-D and 3-D IMRT verification techniques. For the 2-D technique, the EPID-measured fluences are convolved with a kernel characterizing dose deposition in a water phantom, and then cross-calibrated with ion-chamber absolute dose measurements, to generate an EPID-based BEV dose distribution at 10 cm depth in water. The 2-D verification compares this EPID-based BEV dose distribution with the analogous distribution calculated by the TPS. In the case of the 3-D verification, the fluence modulation distribution of each field of an IMRT treatment plan is measured with the EPID. These measured modulations are imported back into the TPS, which is then used to re-calculate a cumulative 3-D dose

distribution in a patient's CT anatomy. To complete the 3-D verification, the 3-D dose distribution based on EPID-measured fluences is compared to the original planned 3-D distribution based on TPS-optimized fluences.

In the following chapter, results of 2-D and 3-D IMRT verifications are presented.

## H. References

- <sup>1</sup>C. De Angelis, S. Onori, M. Pacilio, G. A. P. Cirrone, G. Cuttone, L. Raffaele, M. Bucciolini, and S. Mazzocchi, "An investigation of the operating characteristics of two PTW diamond detectors in photon and electron beams," *Medical Physics* **29** (2), 248-254 (2002).
- <sup>2</sup>A. Fidanzio, L. Azario, R. Miceli, A. Russo, and A. Piermattei, "PTW-diamond detector: Dose rate and particle type dependence," *Medical Physics* **27** (11), 2589-2593 (2000).
- <sup>3</sup>D. Sheikh-Bagheri and D. W. Rogers, "Monte Carlo calculation of nine megavoltage photon beam spectra using the BEAM code," *Medical Physics* **29** (3), 391-402 (2002).
- <sup>4</sup>B. M. C. McCurdy, K. Luchka, and S. Pistorius, "Dosimetric investigation and portal dose image prediction using an amorphous silicon electronic portal imaging device," *Medical Physics* **28** (6), 911-924 (2001).
- <sup>5</sup>P. Munro and D. C. Bouius, "X-ray quantum limited portal imaging using amorphous silicon flat-panel arrays," *Medical Physics* **25** (5), 689-702 (1998).
- <sup>6</sup>Y. El-Mohri, L. E. Antonuk, J. Yorkston, K. W. Jee, M. Maolinbay, K. L. Lam, and J. H. Siewerdsen, "Relative dosimetry using active matrix flat-panel imager (AMFPI) technology," *Medical Physics* **26** (8), 1530-1541 (1999).
- <sup>7</sup>Varian Medical Systems, "PortalVision aS500 Rel.6, Reference Manual," (Palo Alto, CA, 2000).
- <sup>8</sup>J. Chang and C.C. Ling, "Using the frame averaging of aS500 EPID for IMRT verification," *Journal of Applied Clinical Medical Physics* **4** (4), 287-299 (2003).
- <sup>9</sup>P. Manser, R. Treier, H. Riem, M. K. Fix, D. Vetterli, R. Mini, and P. Rueggsegger, "Dose response of an A-Si : H EPID on static and dynamic photon beams," *Medical Physics* **29** (6), 1269-1269 (2002).
- <sup>10</sup>L. N. McDermott, R. J. W. Louwe, J. J. Sonke, M. B. van Herk, and B. J. Mijnheer, "Dose-response and ghosting effects of an amorphous silicon electronic portal imaging device," *Medical Physics* **31** (2), 285-295 (2004).

- <sup>11</sup>J. H. Siewerdsen and D. A. Jaffray, "A ghost story: Spatio-temporal response characteristics of an indirect-detection flat-panel imager," *Medical Physics* **26** (8), 1624-1641 (1999).
- <sup>12</sup>D.W. Litzenberg, J.M. Moran, and B.A. Fraass, "Verification of dynamic and segmental IMRT delivery by dynamic log file analysis," *Journal of Applied Clinical Medical Physics* **3** (2), 63-72 (2002).
- <sup>13</sup>H. Parsaei, E. El-Khatib, and R. Rajapakshe, "The use of an electronic portal imaging system to measure portal dose and portal dose profiles," *Medical Physics* **25** (10), 1903-1909 (1998).
- <sup>14</sup>P. B. Greer and C. C. Popescu, "Dosimetric properties of an amorphous silicon electronic portal imaging device for verification of dynamic intensity modulated radiation therapy," *Medical Physics* **30** (7), 1618-1627 (2003).
- <sup>15</sup>I. Kawrakow and D. W. Rogers, "The EGSnrc Code System: Monte Carlo Simulation of Electron and Photon Transport," NRCC Report PIRS-701, NRC Canada (2002).
- <sup>16</sup>J.O. Kim, J.V. Seibers, P.J. Keall, and R. Mohan, "A Monte Carlo Model of an Amorphous Silicon Flat Panel Imager for Portal Dose Prediction," Proceedings of the 7th International Workshop on Electronic Portal Imaging, Vancouver, Canada, 2002.
- <sup>17</sup>Jeffrey V. Siebers, Jong Oh Kim, Lung Ko, Paul J. Keall, and Radhe Mohan, "Monte Carlo computation of dosimetric amorphous silicon electronic portal images," *Medical Physics* **31** (7), 2135-2146 (2004).
- <sup>18</sup>A. E. S. von Wittenau, C. M. Logan, M. B. Aufderheide, and D. M. Slone, "Blurring artifacts in megavoltage radiography with a flat-panel imaging system: Comparison of Monte Carlo simulations with measurements," *Medical Physics* **29** (11), 2559-2570 (2002).
- <sup>19</sup>C. Kausch, B. Schreiber, F. Kreuder, R. Schmidt, and O. Dossel, "Monte Carlo simulations of the imaging performance of metal plate/phosphor screens used in radiotherapy," *Medical Physics* **26** (10), 2113-24 (1999).
- <sup>20</sup>L. Ko, J. O. Kim, and J. V. Siebers, "Investigation of the optimal backscatter for an aSi electronic portal imaging device," *Physics in Medicine and Biology* **49** (9), 1723-1738 (2004).
- <sup>21</sup>M.A. MacKenzie, M. Lachaine, B. Murray, B. G. Fallone, D. Robinson, and G.C. Field, "Dosimetric verification of inverse planned step and shoot multileaf collimator fields from a commercial treatment planning system," *Journal of Applied Clinical Medical Physics* **3** (2), 97-109 (2002).

- <sup>22</sup>A. Ahnesjo, "Dose Calculation Methods in Photon Beam Therapy using Energy Deposition Kernels," Ph.D. Thesis, Stockholm University, 1991.
- <sup>23</sup>Helax-TMS (Nucletron), "Helax-TMS Dose Calculation Reference Manual," (Veenendaal, The Netherlands, 1998).
- <sup>24</sup>P. R. Almond, P. J. Biggs, B. M. Coursey, W. F. Hanson, M. S. Huq, R. Nath, and D. W. O. Rogers, "AAPM's TG-51 protocol for clinical reference dosimetry of high-energy photon and electron beams," *Medical Physics* **26** (9), 1847-1870 (1999).
- <sup>25</sup>Faiz M. Khan, *The Physics of Radiation Therapy*, 3rd ed. (Lippincott Williams & Wilkins, Philadelphia, 2003).

## Chapter 3: EPID-based IMRT Verification – Results

In this chapter, results for the EPID-based IMRT verification projects are presented. The various kernels used to extract fluence profiles from EPID images are presented first, followed by comparisons of these EPID-based profiles to analogous profiles measured using a diamond detector. In the main part of the chapter, separate sections report results from the 2-D and then, the 3-D IMRT verification projects.

### A. Pencil Beam Kernels used to Extract Fluence Profiles from EPID images

The Monte-Carlo generated dose kernel ( $K_{dose}$ ), the empirically-derived back-glare kernel ( $K_{back-glare}$ ), and the resulting overall EPID kernel ( $K_{EPID} = K_{dose} \otimes K_{back-glare}$ ) used to describe the blurring processes in the EPID are shown in Figure 3.1. The 3-D verification results were generated with the 6 MV and the “new” 15 MV kernels illustrated in Fig. 3.1(a) and (b), while Fig. 3.1(c) depicts the “old” 15 MV kernels used to produce the 2-D verification results. In this and other figures displaying pencil-beam kernels, the kernels are normalized to unity on the pencil beam axis. As expected from the discussion in Section 2.D.iv, Fig. 3.1 illustrates that for the 6 MV case, the empirical  $K_{back-glare}$  has a large long-range tail: at radial distances greater than  $\sim 5$  cm from the center of the kernel, the dominant contribution to the overall  $K_{EPID}$  kernel is from  $K_{back-glare}$ , and not  $K_{dose}$ . This relatively large long-range component in  $K_{back-glare}$  compensates for the diminished long-range tails in  $K_{dose}$  due to the lack of backscatter in the simplified EPID model in the EGSnrc simulations. In contrast, for the 15 MV case where the EGSnrc model contained 2.5 cm of water backscatter, the empirical back-glare kernel mainly broadened the short and medium ranges ( $r < 2.5$  cm) of the total EPID kernel. Overall, a much smaller empirical “correction” was necessary in the 15 MV case, indicating that the 2.5 cm of backscatter was more representative of

the actual scattering properties of the EPID in the 15 MV case, than the use of no backscatter was in the 6 MV case.

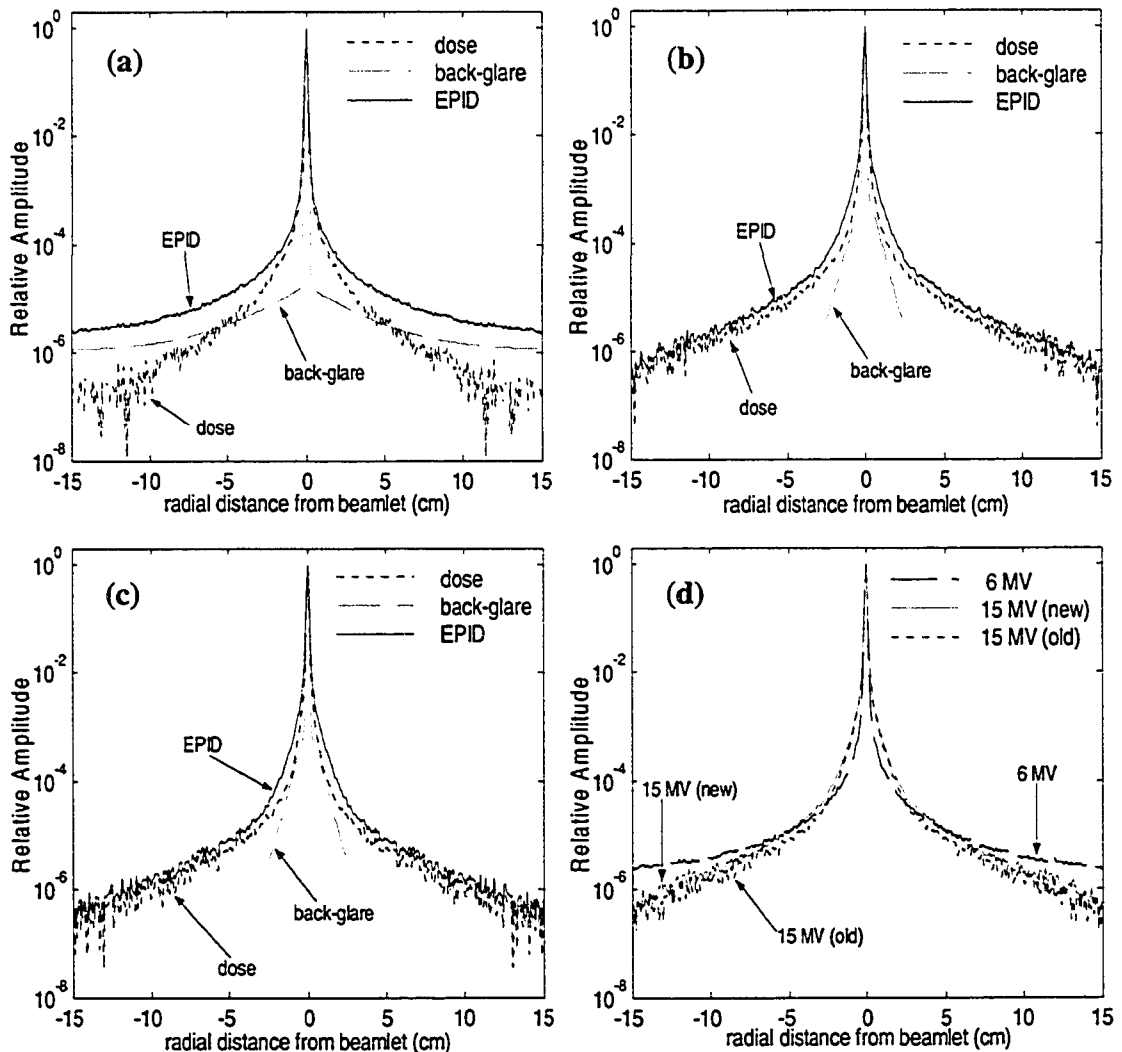


**Figure 3.1.** (a) 6 MV, (b) "new" 15 MV, and (c) "old" 15 MV pencil-beam kernels used to describe blurring in the EPID: the dose kernel ( $K_{dose}$ ) is generated from Monte-Carlo simulations, the back-glare kernel ( $K_{back-glare}$ ) is derived empirically, and the total EPID kernel ( $K_{EPID}$ ) is the convolution of the dose and back-glare kernels. A comparison of the three total EPID kernels is shown in (d).

A comparison of the 6 MV and 15 MV ("old" and "new")  $K_{EPID}$  kernels is shown in Fig 3.1(d). The 6 MV kernel is significantly narrower for radii below  $\sim 2$  cm from the kernel center, but has an appreciably larger amplitude in the long-range tail ( $r > \sim 6$  cm). This is consistent with the following explanation. Since the near-range part of the kernel results mainly from the transport of electrons released in primary interactions, the 15 MV kernel is broader in this region because of the longer range of the higher-

energy electrons produced from the 15 MV incident beam. However, photon backscatter cross-sections are larger for the lower energy 6 MV beam, explaining the larger long-range tail for the 6 MV case. The differences between the “new” and “old” 15 MV kernels are subtle, with the main difference being the slightly larger amplitude of the long-range tail of the “new” kernel.

The 6 and 15 MV  $K_{flood-phantom}$  kernels needed to generate the simulated flood-fields  $I_{flood-sim}$  (Section 2.C.vi), and the  $K_{BEVphantom}$  kernels which convert EPID-derived incident photon fluences to 2-D BEV dose distributions are shown in Fig. 3.2(a) and 3.2(b), respectively. Both kernels characterize dose deposition in a uniform water phantom:  $K_{flood-phantom}$  at 3 cm depth in a 5.5 cm thick phantom,  $K_{BEVphantom}$  at 10 cm depth in a 25 cm thick phantom. For similar reasons as described above for the EPID kernels, the shape of the 6 MV kernels is narrower in the short-range and slightly broader in the long-range than the corresponding 15 MV kernels.

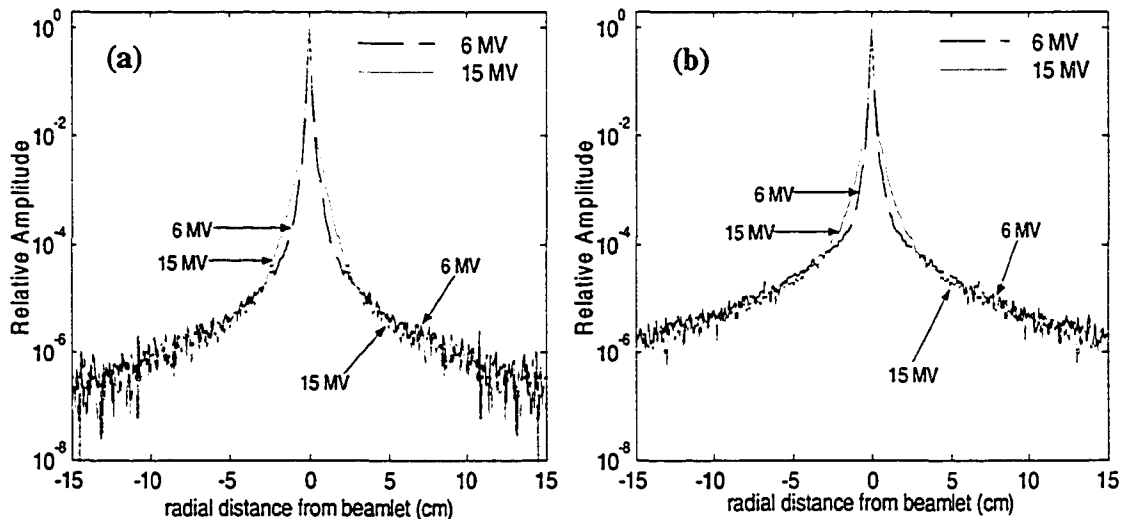


**Figure 3.2.** (a)  $K_{flood-phantom}$  kernel used to generate the simulated flood-field  $I_{flood-sim}$ , and (b)  $K_{BEVphantom}$  kernel used to convert photon fluence to BEV dose for both 6 and 15 MV.

To describe the overall shape of the  $K_{EPID}$ ,  $K_{dose}$ ,  $K_{flood-phantom}$ , and  $K_{BEVphantom}$  kernels, each was fit to the following function, which is the sum of four exponential terms:

$$K_{fit}(r) = \exp(-a_1 r) + a_2 \exp(-a_3 r) + a_4 \exp(-a_5 r) + a_6 \exp(-a_7 r). \quad (3.1)$$

The best-fit parameters ( $a_1 \dots a_7$ ) for each kernel are given in Table 3.1. To perform the fits, we implemented a computerized fitting routine based on a Monte Carlo search algorithm<sup>1</sup> and minimization of a weighted sum-of-squares difference between the logarithm of the fitted and original kernels. As discussed in Section 2.D, the empirical kernel,  $K_{back-glare}$ , was assumed to be the sum of two (15 MV) or three (6 MV) exponentials: these parameters are also reproduced in Table 3.1.

Kernel	$K_{fit}(r) = \exp(-a_1 r) + a_2 \exp(-a_3 r) + a_4 \exp(-a_5 r) + a_6 \exp(-a_7 r)$						
	$a_1$ ( $\text{cm}^{-1}$ )	$a_2$	$a_3$ ( $\text{cm}^{-1}$ )	$a_4$	$a_5$ ( $\text{cm}^{-1}$ )	$a_6$	$a_7$ ( $\text{cm}^{-1}$ )
$K_{EPID}^{6MV}$	23.6	$3.66 \times 10^{-3}$	3.98	$2.37 \times 10^{-4}$	0.840	$1.47 \times 10^{-5}$	0.128
$K_{EPID}^{15MV} _{new}$	19.4	$1.12 \times 10^{-2}$	3.62	$1.19 \times 10^{-3}$	1.46	$5.12 \times 10^{-5}$	0.311
$K_{EPID}^{15MV} _{old}$	21.1	$1.82 \times 10^{-2}$	5.13	$2.60 \times 10^{-3}$	1.90	$4.05 \times 10^{-5}$	0.321
$K_{dose}^{6MV}$	29.5	$1.19 \times 10^{-2}$	8.32	$8.46 \times 10^{-4}$	2.22	$5.84 \times 10^{-5}$	0.538
$K_{dose}^{15MV} _{new}$	22.6	$1.33 \times 10^{-2}$	5.25	$3.05 \times 10^{-4}$	1.12	$3.17 \times 10^{-5}$	0.306
$K_{dose}^{15MV} _{old}$	25.0	$2.07 \times 10^{-2}$	6.20	$3.72 \times 10^{-4}$	1.39	$2.63 \times 10^{-5}$	0.324
$K_{back-glare}^{6MV}$	37.1	$1.57 \times 10^{-5}$	0.405	$1.40 \times 10^{-6}$	0.0153	N/A	N/A
$K_{back-glare}^{15MV}$	37.1	$1.36 \times 10^{-3}$	2.46	N/A	N/A	N/A	N/A
$K_{flood-phantom}^{6MV}$	21.7	$6.80 \times 10^{-2}$	6.01	$5.78 \times 10^{-4}$	1.50	$3.06 \times 10^{-5}$	0.368
$K_{flood-phantom}^{15MV}$	17.9	$6.18 \times 10^{-2}$	4.16	$2.30 \times 10^{-3}$	1.79	$1.88 \times 10^{-5}$	0.328
$K_{BEVphantom}^{6MV}$	20.1	$5.72 \times 10^{-2}$	5.27	$4.07 \times 10^{-4}$	0.690	$3.50 \times 10^{-5}$	0.192
$K_{BEVphantom}^{15MV}$	16.6	$4.72 \times 10^{-2}$	3.39	$8.96 \times 10^{-4}$	0.947	$3.89 \times 10^{-5}$	0.218

Table 3.1. Best-fit parameters for fits of a function that is the sum of four exponentials to the various kernels used in this work.

The original, non-parametric forms of the  $K_{EPID}$ ,  $K_{dose}$ ,  $K_{flood-phantom}$ , and  $K_{BEVphantom}$  kernels were used to generate the 2-D and 3-D verification results. The parametric forms were given in Table 3.1 to supply a convenient mathematical description of these kernels that may be useful for other investigators, perhaps to compare with kernels they themselves derive. The parametric kernels are also used in the tests described in Section 3.B.iv that investigate the sensitivity of the shape of the EPID profiles to different parts of the  $K_{EPID}$  kernel.

## B. Comparisons of EPID-derived Fluence Profiles and Measured Diamond Detector Fluences

### *i. Open fields and IMRT Segments*

In Fig. 3.3, a cross-plane profile for a  $10 \times 10 \text{ cm}^2$  6 MV field fluence is shown for each of the following: an in-air measurement with a diamond detector; the raw, uncorrected EPID image ( $EPID_{PV}$ ) of the field; and the EPID-derived relative fluence that is extracted from this raw EPID image using the kernels characterized above in Section 3.A in conjunction with the deconvolution technique summarized by Eqs. (2.6), (2.12), and (2.14) in Chapter 2. In comparison to the in-air diamond measurement, the raw EPID profile has a significantly larger amplitude in the tail of the profile, and a significant downward rounding towards the field edges in the open part of the field. In contrast, after deconvolution, the corrected EPID profile restores the shape of the profile in the open part of the field, which is nearly flat with a very slightly horned shape (from the flattening filter), and also matches the tail region of the field very well. The corrected EPID profile actually reproduces the expected shape of the incident photon fluence in the penumbra somewhat better than the diamond profile: the diamond profile has a comparatively shallower slope in the penumbra due to the additional blurring caused by the build-up cap used for the in-air measurements.

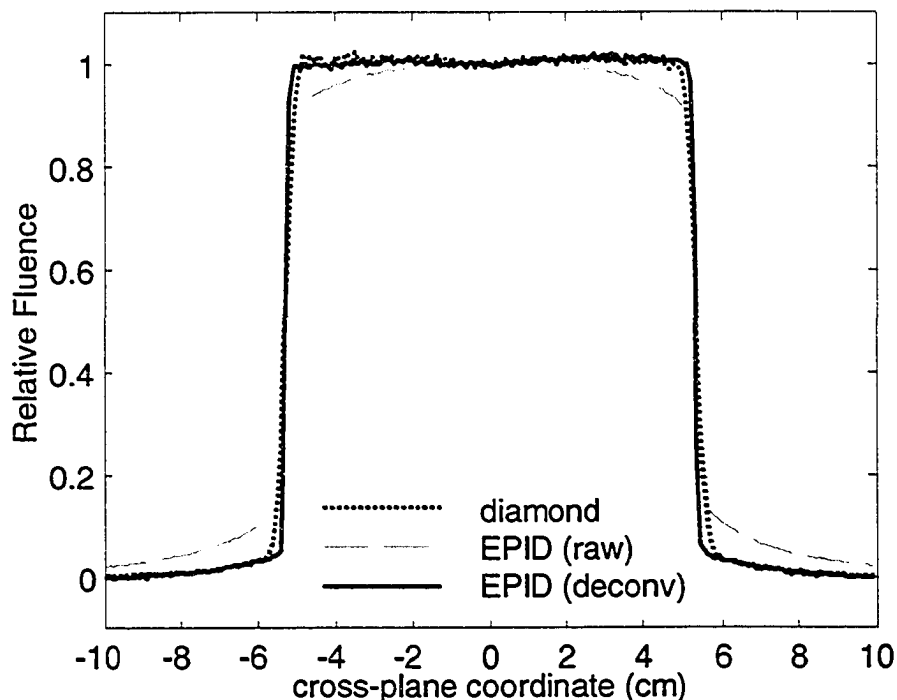


**Figure 3.3.** Comparison of cross-plane profiles through an open  $10 \times 10 \text{ cm}^2$  6 MV field derived from in-air diamond detector measurements, raw EPID images ( $EPID_{pv}$ ) before deconvolution, and EPID images after the deconvolution to extract incident fluence ( $\Psi_p$ ).

Additional comparisons of diamond and corrected EPID fluence profiles are shown for a range of open fields of sizes  $2 \times 2$ ,  $4 \times 4$ ,  $10 \times 10$ , and  $20 \times 20 \text{ cm}^2$  in Fig. 3.4 for 6 MV, and in Fig. 3.5 for 15 MV. Each profile has been normalized to its own mean value of the central eleven pixels (0.9 cm). As illustrated, the diamond and EPID profiles agree very well for all field sizes, indicating that the final versions of the EPID kernels are able to describe the blurring properties of the EPID detector adequately for purposes of deconvolution. Fig. 3.5 suggests that differences between the EPID profiles using the old EPID kernel,  $K_{EPID}^{15MV}|_{old}$ , and those using the new version,  $K_{EPID}^{15MV}|_{new}$ , are relatively insignificant.

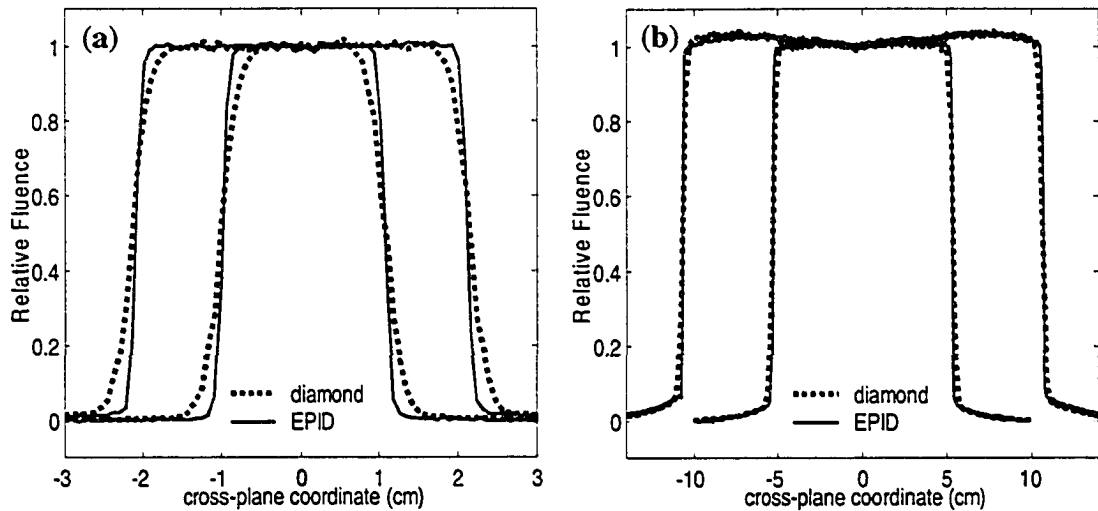


**Figure 3.4.** Comparison of diamond and EPID-derived fluence profiles for (a)  $2 \times 2$  and  $4 \times 4$   $\text{cm}^2$  and (b)  $10 \times 10$  and  $20 \times 20$   $\text{cm}^2$  open 6 MV fields.

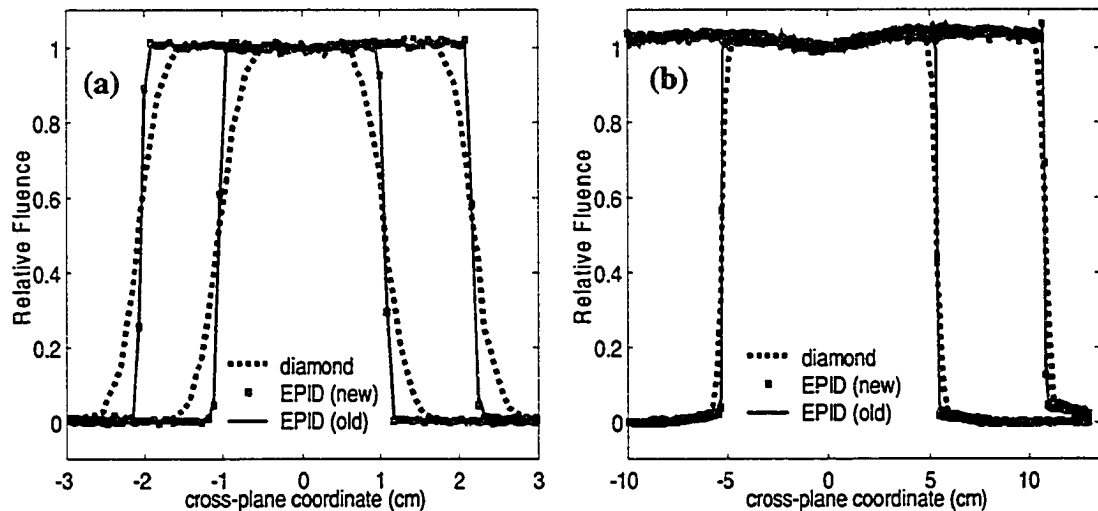


**Figure 3.5.** Same as Fig. 3.4, except for 15 MV. As illustrated, the differences in the profiles between using the “new” or “old” EPID kernels in the deconvolution are negligible.

The EPID and diamond relative fluences are also compared in Fig. 3.7(a) (6 MV) and 3.7(b) (15 MV) for in-plane profiles taken through the segment of the step-and-shoot IMRT field depicted in Fig. 3.6(a). The numbers 1-6 are used to identify different regions of this IMRT segment in both the diagram of the segment and in the corresponding profiles. The EPID profiles are again in good overall agreement with the diamond profiles. However, the EPID profiles again exhibit sharper slopes in the penumbral regions, at the edges of the different regions. For example, the troughs between regions 2 and 3, and 3 and 4, are not as deep for the diamond profiles; as before, this is a consequence of the blurring from the diamond’s build-up cap. Also because of

this blurring, the diamond fluence amplitude for the narrow region #1 is significantly less than for the other wider regions; in contrast, the EPID-based prediction of the fluence for region #1 is nearly the same as for the other regions. In general, the EPID fluence profile is slightly more uniform in the open-field sections of the field, particularly for the 15 MV case. For these reasons, it is believed that the EPID profiles represent the actual shape of the incident fluence slightly better than the diamond profiles for IMRT fields, as was also found for the open-fields. An additional comparison of 6 MV diamond and EPID profiles, which shows similar results, is depicted in Fig. 3.7(c) for the multi-leaf collimated field shown in Fig. 3.6(b).

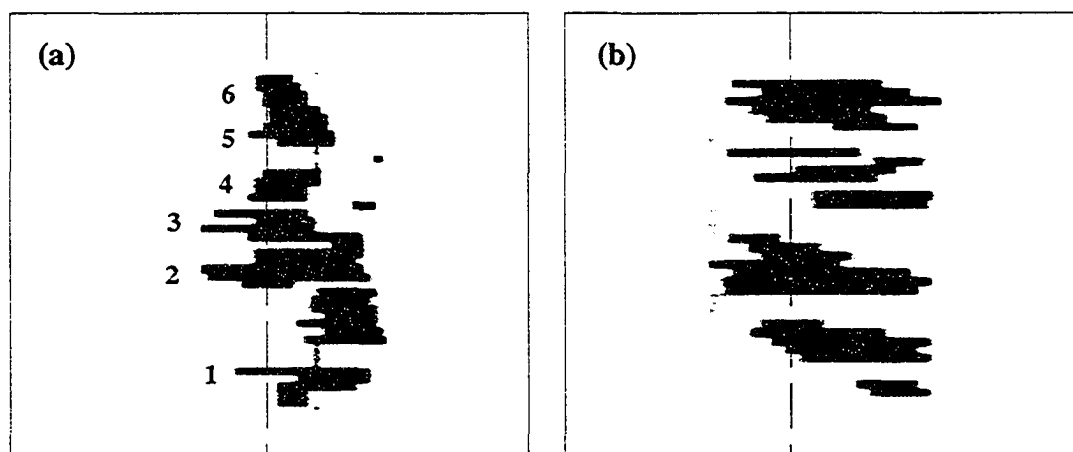


**Figure 3.6.** (a) Image of the IMRT segment field corresponding to the profiles shown in Fig. 3.7(a & b). The profiles are taken along the dashed line, and the numbers identify the regions of the segment described in the text and indicated in Fig. 3.7. (b) Image of the multi-leaf collimated segment field corresponding to the profile (along the dashed line) in Fig. 3.7 (c).

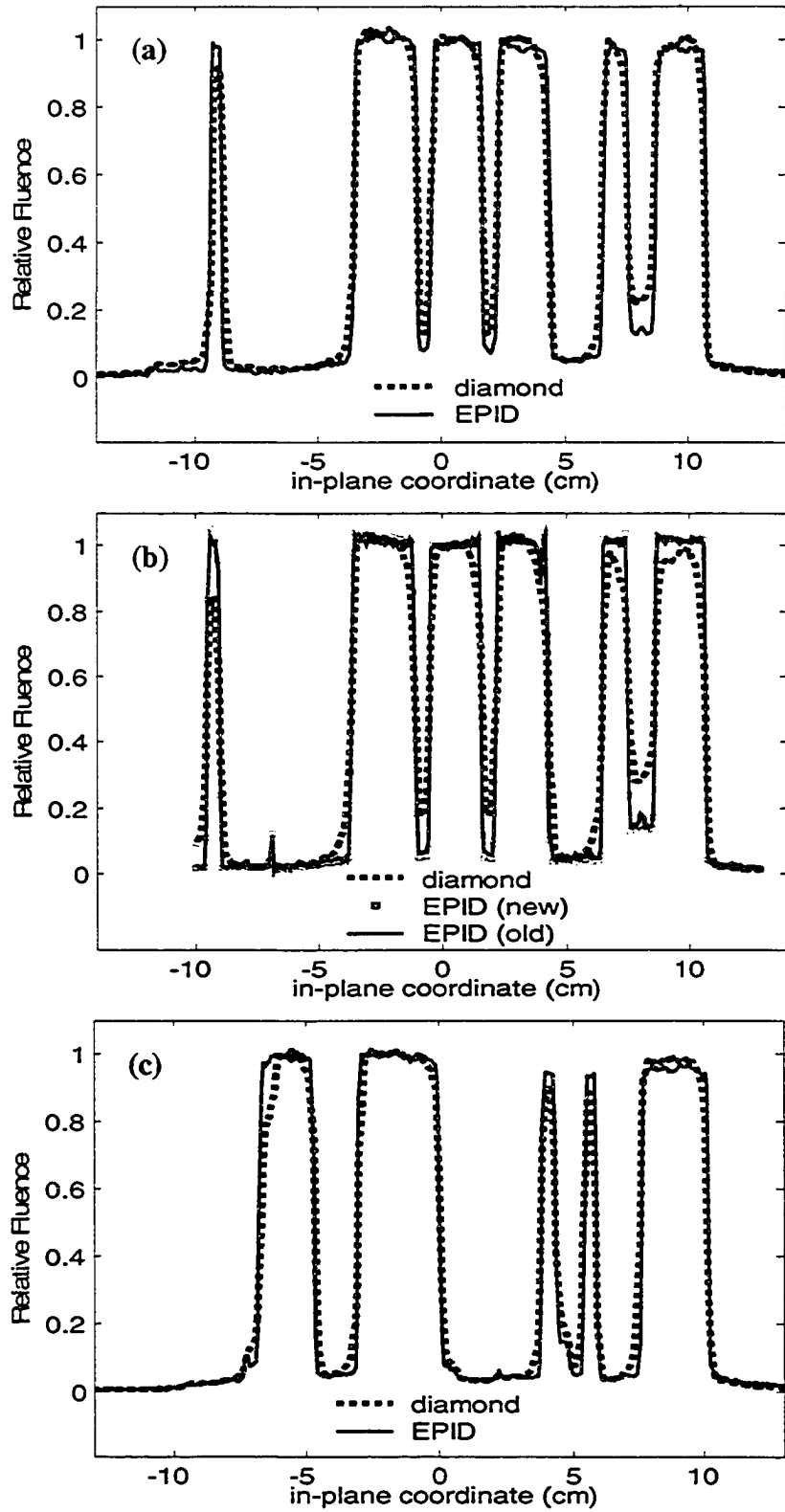


**Figure 3.7.** Comparison of diamond and EPID fluence profiles for multi-leaf collimated fields. (a) 6 MV and (b) 15 MV profiles along the dashed line through field shown in Fig. 3.6(a). (c) 6 MV profiles along the dashed line through field shown in Fig. 3.6(b).

## ii. Sensitivity of EPID profiles to the amount of backscatter used in the EPID model

For the 6 MV case, the sensitivity of the EPID-derived fluences to the amount of backscatter used in the EGSnrc EPID model was investigated. For this purpose, different dose-deposition kernels ( $K_{dose}$ ) corresponding to different thicknesses of uniform water backscatter were generated; the different “backscatter” EPID kernels were created without implementing any empirical kernel correction, *i.e.*  $K_{back-glare} = 1$ , and thus  $K_{EPID} = K_{dose}$ . EPID fluences were then extracted using each of these “backscatter” kernels for both a small 4 x 4 cm<sup>2</sup> and a large 20 x 20 cm<sup>2</sup> field, and compared to the corresponding diamond profiles. The diamond profiles were re-sampled at the points of the EPID pixels using a MATLAB cubic spline interpolation routine. For each “backscatter” kernel and field size, two figures of merit (FOM) were calculated to characterize the degree of agreement between the EPID and diamond profiles. The first FOM is the sum of the squared difference between the EPID and diamond profiles for all pixels within a region of interest (ROI):

$$SS_{ROI} = \sum_{i \in ROI} (EPID(i) - diamond(i))^2. \quad (3.2)$$

The ROI, shown in Fig. 3.8(a), included the tail region and a portion of the open-field nearest the field edges. However, this ROI excluded the high-gradient penumbra part of the profiles, since disagreement between the diamond and EPID profiles is expected (and to some extent desired) here because of the build-up cap blurring evident in the diamond profiles. In general,  $SS_{ROI}$  provides a good indication of the quality of the EPID-to-diamond fit. However, it is not always sensitive to a short-range “over-deconvolution” of a profile, which manifests as a spurious under-prediction of the fluence at the base, and an over-prediction at the top of a sharp edge. Thus, a second “transient-detecting” FOM,  $\Delta_{trans}$ , was calculated that is the mean of the absolute differences of the amplitude of the diamond and EPID profiles calculated at the base and peak of the profiles at both field edges (Fig. 3.8(b)). As a baseline, the two FOMs  $SS_{ROI}$  and  $\Delta_{trans}$  were also calculated for the comparison between the diamond profiles and the EPID fluences derived with the “best” final version of the  $K_{EPID}$  kernel (no backscatter, but using  $K_{back-glare}$ ), the version actually utilized for our IMRT verifications. Table 3.2 reports the ratios of the

values of  $SS_{ROI}$  and  $\Delta_{trans}$  for the “backscatter” kernels to the corresponding values calculated using the “best” kernel. These ratios are designated  $SS_{ROI}|_{best}^{back}$  and  $\Delta_{trans}|_{best}^{back}$ . Values of these ratios much greater than 1 suggest a significantly worse EPID-to-diamond fit using the given “backscatter” kernel, while values near one indicate that the “backscatter” and “best” kernels yield a similar fit for that particular field size. Note that since the tail region has a larger amplitude for larger field sizes, and thus discrepancies between the diamond and EPID profiles in the tail region are potentially greater,  $SS_{ROI}|_{best}^{back}$  ratios will generally be more sensitive to poor fits of the “backscatter” kernels for larger field sizes. Some measure of the breadth of each kernel was quantified by calculating  $Kernsum = \sum_{i,j} K(i,j)$ , the sum of the values of all 383 x 383 pixels (spanning 30 x 30 cm<sup>2</sup>) for each kernel ( $K(i,j)$ , where  $i,j = 1,2, \dots, 383$ ). Before calculating  $Kernsum$ , the kernels were first normalized so that the central pixel of the kernel has a value of one (*i.e.*  $K(192,192)=1$ ). The ratio of this sum for the “backscatter” and “best” kernels,  $Kernsum|_{best}^{back}$ , is also given in Table 3.2.

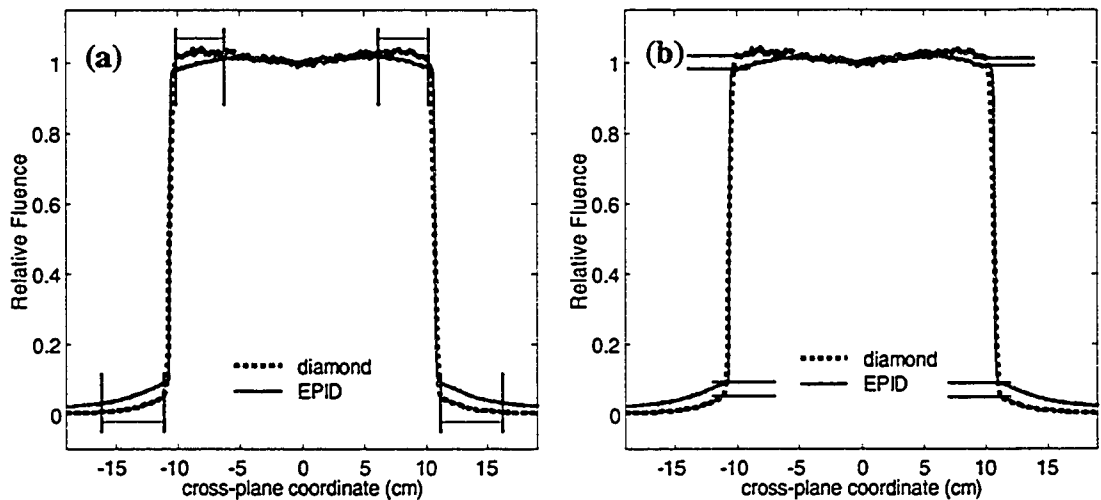


**Figure 3.8.** Diamond and EPID (non-optimal) profiles through a 20 x 20 cm<sup>2</sup> field. (a) The ROI (region of interest) used to calculate  $SS_{ROI}$  (Eq. (3.2)) includes the four regions demarcated by the four pairs of vertical lines. (b)  $\Delta_{trans}$  is the mean value of the differences between each of the four sets of horizontal lines, which are located at the tops and bases of the field edges.

backscatter thickness (cm)	$K_{\text{ernsum}} _{\text{best}}^{\text{back}}$	$SS_{\text{ROI}} _{\text{best}}^{\text{back}}$		$\Delta_{\text{trans}} _{\text{best}}^{\text{back}}$	
		4 x 4 cm <sup>2</sup>	20 x 20 cm <sup>2</sup>	4 x 4 cm <sup>2</sup>	20 x 20 cm <sup>2</sup>
0	0.67	2.0	37.9	1.4	6.5
0.5	0.71	1.3	28.5	0.7	5.0
1.0	0.74	1.5	18.8	2.1	3.5
1.5	0.77	2.4	10.8	3.1	1.9
2.0	0.80	3.6	5.4	3.9	0.9
2.5	0.83	5.1	2.4	4.5	0.9
3.0	0.85	6.6	2.0	5.0	2.2
3.5	0.88	8.1	3.9	5.4	3.5
4.0	0.90	9.5	8.0	5.7	4.7
5.0	0.94	12.1	21.4	6.2	6.8

**Table 3.2.** Dependence of the fits of EPID fluence profiles to diamond profiles for 4 x 4 and 20 x 20 cm<sup>2</sup> 6 MV open fields on the thickness of water backscatter material used in the EPID model (for EGSnrc simulations). The quality of the fits is characterized by the ratio of the  $SS_{\text{ROI}}$  and  $\Delta_{\text{trans}}$  values (described in the text) calculated for each “backscatter” kernel (without  $K_{\text{back-glare}}$ ) to the analogous values obtained using the “best”  $K_{\text{EPID}}$  kernel (no backscatter, with  $K_{\text{back-glare}}$ ). Ratio values less than one indicate a relatively better fit.

The results in Table 3.2 demonstrate the necessity of the empirical  $K_{\text{back-glare}}$  kernel to adequately describe blurring in the EPID for the 6 MV case. None of the “backscatter” kernels, irrespective of how much backscatter was used in the EPID model, could alone (*i.e.* without use of a  $K_{\text{back-glare}}$  kernel) describe sufficiently both the 4 x 4 and 20 x 20 cm<sup>2</sup> fields. The “backscatter” kernel that fit the smaller 4 x 4 field best was the one corresponding to 0.5 cm of backscatter. Use of this kernel resulted in values for  $SS_{\text{ROI}}|_{\text{best}}^{\text{back}}$  and  $\Delta_{\text{trans}}|_{\text{best}}^{\text{back}}$  of 1.3 and 0.7, respectively, for this field; on the other hand, this kernel fit the 20 x 20 field very poorly ( $SS_{\text{ROI}}|_{\text{best}}^{\text{back}}$  and  $\Delta_{\text{trans}}|_{\text{best}}^{\text{back}}$  = 28.5 and 5.0, respectively). The 2.5 cm backscatter kernel produced a reasonable, though not optimal, fit to the 20 x 20 field, yielding values of 2.4 and 0.9 for  $SS_{\text{ROI}}|_{\text{best}}^{\text{back}}$  and  $\Delta_{\text{trans}}|_{\text{best}}^{\text{back}}$ . The fit to the 4 x 4 field using this kernel was, however, now unacceptable ( $SS_{\text{ROI}}|_{\text{best}}^{\text{back}}$  and  $\Delta_{\text{trans}}|_{\text{best}}^{\text{back}}$  = 5.1 and 4.5, both  $\gg$  1). Intermediate values of backscatter thickness gave relatively poor fits for both the 4 x 4 and 20 x 20 field sizes. In Fig. 3.9, diamond detector profiles for both field sizes are compared to EPID-based profiles for the 0.5, 1.5

and 2.5 cm “backscatter” kernels. It is noted that Siebers *et al.*<sup>2</sup> found that 1.0 cm of uniform backscatter provided good agreement between simulated EPID images and measured portal images for a range of field sizes. However, they also used a much more complete model of the EPID detector than the simplified one used for our simulations (Fig. 2.4), which likely explains why they did not require explicit use of an optical glare kernel or an empirical kernel correction (*e.g.*  $K_{back-glare}$ ).

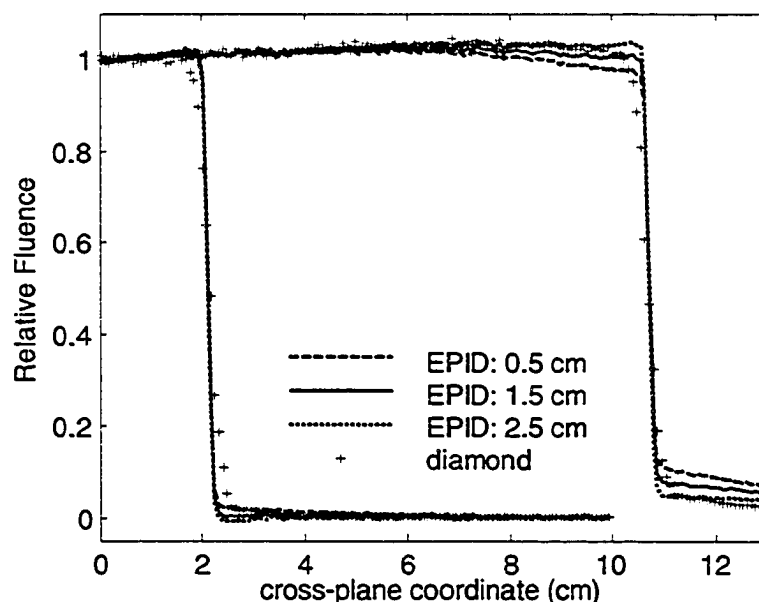


**Figure 3.9.** The effect of the amount of backscatter used in the EGSnrc model of the EPID on EPID 6 MV fluence profiles for 4 x 4 and 20 x 20 cm<sup>2</sup> fields. The three EPID profiles were generated with three different deconvolution kernels ( $K_{dose}$ ) corresponding to 0.5, 1.5, and 2.5 cm of water backscatter.

### iii. Effect on EPID profiles of the short-range exponential term in $K_{back-glare}$

We had hypothesized that the first exponential term in both the 6 and 15 MV  $K_{back-glare}$  empirical kernels may describe short-range optical blurring. For both incident photon energies, the length parameter characterizing this short-range exponential was  $C_1 = 37.1 \text{ cm}^{-1}$  in Eq. (2.16). To investigate the sensitivity of the EPID profiles to this particular exponential term, we generated a second set of  $K_{back-glare}$  kernels with  $C_1 = 1037.1 \text{ cm}^{-1}$  and the other parameters unchanged. Use of this large value of  $C_1$  effectively makes the short-range part of the kernel a delta function, which would imply that there is no short-range blurring. The ratios of the  $SS_{ROI}$  and  $\Delta_{trans}$  values calculated

for the kernel (for each energy) with  $C_I = 1037.1 \text{ cm}^{-1}$  to the values using  $C_I = 37.1 \text{ cm}^{-1}$ ,  $SS_{ROI}|_{37}^{1037}$  and  $\Delta_{trans}|_{37}^{1037}$ , are reported in Table 3.3. As indicated by these values and displayed in Fig. 3.10, the dependence of the EPID profiles on  $C_I$  for the two photon energies is different. In the 15 MV case, changing the short-range parameter (*i.e.*  $C_I = 1037.1 \text{ cm}^{-1}$ ) in  $K_{back-glare}$  produces an over-deconvolution in the short-range of the fields. This is suggested visually in Fig. 3.10 and numerically by the values of 2.0 (4 x 4) and 1.4 (20 x 20) for  $\Delta_{trans}|_{37}^{1037}$ . However, in the 6 MV case, increasing  $C_I$  to  $1037.1 \text{ cm}^{-1}$  has less effect on the short-range part of the fields; rather it has the greatest impact on the height of the tail for the 20 x 20 field ( $SS_{ROI}|_{37}^{1037} = 1.9$ ), which implies a long-range effect. Thus, short-range effects, such as optical glare, can be described by the  $C_I$  parameter alone only for the 15 MV empirical kernel, and not for our implementation of the 6 MV kernel. In retrospect, this is not surprising. There were no long-range components in  $K_{back-glare}^{15MV}$ , with the span of this kernel being restricted to radii less than 2.5 cm. In contrast, however,  $K_{back-glare}^{6MV}$  is dominated by long-range exponentials used to approximate the missing backscatter in the EPID model. As a result, the overall impact on  $K_{back-glare}^{6MV}$  of changing solely the  $C_I$  parameter is more complicated and more difficult to predict, since  $K_{back-glare}^{6MV}$  is convolved with  $K_{dose}^{6MV}$  to get the overall  $K_{EPID}^{6MV}$  kernel.

Photon Energy (MV)	$Kernsum _{37}^{1037}$	$SS_{ROI} _{37}^{1037}$		$\Delta_{trans} _{37}^{1037}$	
		4 x 4 $\text{cm}^2$	20 x 20 $\text{cm}^2$	4 x 4 $\text{cm}^2$	20 x 20 $\text{cm}^2$
6	0.83	1.3	1.9	1.4	1.0
15	0.84	1.1	1.1	2.0	1.4

**Table 3.3.** Dependence of the fits of EPID fluence profiles to diamond profiles on the first exponential term in  $K_{back-glare}$ . The quality of the fits is characterized by the ratio of the  $SS_{ROI}$  and  $\Delta_{trans}$  values for a  $K_{back-glare}$  kernel using  $C_I = 1037.1 \text{ cm}^{-1}$  (*i.e.* short-range delta function) to those values with a kernel with  $C_I = 37.1 \text{ cm}^{-1}$ .

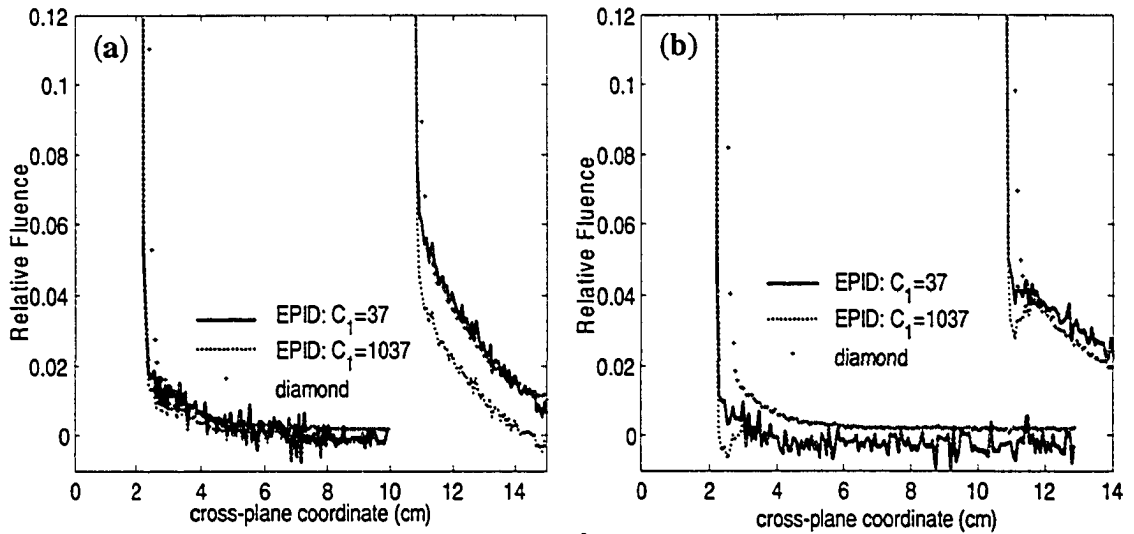


**Figure 3.10.** Dependence of  $4 \times 4$  and  $20 \times 20 \text{ cm}^2$  EPID profiles on the first exponential term ( $C_1$ ) in  $K_{back-glare}$ . (a) 6 MV: use of  $C_1 = 1037.1 \text{ cm}^{-1}$  (i.e. short-range delta function) instead of  $C_1 = 37.1 \text{ cm}^{-1}$  primarily affects the height of the long-range tail for the  $20 \times 20$  field. (b) 15 MV: use of  $C_1 = 1037.1 \text{ cm}^{-1}$  results in a short-range over-deconvolution for both the  $4 \times 4$  and  $20 \times 20$  fields.

#### iv. Sensitivity of the EPID profiles to different regions of the EPID kernel

The sensitivity of the 6 MV EPID profiles to the different regions of the EPID kernel was studied by varying, one at a time, the best-fit parameters ( $a_1 \dots a_7$  in Table 3.1) of the quadruple exponential function (Eq. (3.1)) used to characterize the shape of  $K_{EPID}$ . For example, assuming the original best-fit parameter values ( $par0$ ) are ( $a_{10}, a_{20}, a_{30}, \dots, a_{70}$ ), one new kernel was generated using the parameters,  $par = (a_1, a_{20}, a_{30}, \dots, a_{70})$ , where  $a_i = a_{i0} \cdot Const$ . For each such kernel,  $Const$  is selected so that the  $Kernsum$  is approximately 10 % larger or smaller than the  $Kernsum$  calculated for the kernel based on the original  $par0$  parameters. The ratios of the  $SS_{ROI}$  and  $\Delta_{grad}$  values calculated for each kernel using a modified set of parameters ( $par$ ) to those values for the original ( $par0$ ) kernel are designated  $SS_{ROI}|_{par0}^{par}$  and  $\Delta_{trans}|_{par0}^{par}$ . These ratios are given in Table 3.4. Also reported are the value of  $Const$  for each kernel, the corresponding  $Kernsum$  ratios,  $Kernsum|_{par0}^{par}$ , and whether the modified kernel resulted in more or less deconvolution than the unmodified kernel.

Modified Param.	deconv: more/less	Const	Kernsum <sub>par0</sub> <sup>par</sup>	SS <sub>ROI</sub> <sub>par0</sub> <sup>par</sup>		$\Delta_{trans}$ <sub>par0</sub> <sup>par</sup>	
				4 x 4 cm <sup>2</sup>	20 x 20 cm <sup>2</sup>	4 x 4 cm <sup>2</sup>	20 x 20 cm <sup>2</sup>
$a_1$	less	0.91	1.10	0.8	2.8	0.5	3.4
$a_1$	more	1.12	0.90	1.9	1.9	1.9	1.8
$a_2$	less	0.001	0.93	0.8	1.1	0.9	1.4
$a_2$	more	2.50	1.10	1.3	2.4	4.7	1.5
$a_3$	more	0.64	1.11	6.5	1.8	7.3	3.6
$a_3$	less	10.0	0.93	0.8	1.1	0.9	1.4
$a_4$	less	0.01	0.90	4.0	7.2	3.3	7.2
$a_4$	more	2.00	1.10	8.3	3.3	5.1	5.3
$a_5$	more	0.71	1.10	6.2	11.3	2.8	6.3
$a_5$	less	6.00	0.90	4.0	7.4	3.3	7.2
$a_6$	less	0.41	0.90	1.0	19.3	0.5	6.6
$a_6$	more	1.58	1.10	1.8	14.9	1.4	4.6
$a_7$	more	0.62	1.10	1.1	13.4	1.1	3.0
$a_7$	less	1.85	0.90	0.9	18.4	0.8	5.9

**Table 3.4.** Sensitivity of the fits of 6 MV EPID fluence profiles to diamond profiles on the different parameters ( $a_1 \dots a_7$ ) in the quadruple-exponential function (Eq. (3.1)) used to describe the shape of  $K_{EPID}$ . The quality of the fits is characterized by the ratio of the  $SS_{ROI}$  and  $\Delta_{trans}$  values for a kernel with one of the parameters modified, to the values obtained with the original ( $par0$ ) best-fit parameters: (23.6 cm<sup>-1</sup>, 3.66 x 10<sup>-3</sup>, 3.98 cm<sup>-1</sup>, 2.37 x 10<sup>-4</sup>, 0.840 cm<sup>-1</sup>, 1.47 x 10<sup>-5</sup>, 0.128 cm<sup>-1</sup>).

Fig. 3.11 shows the effect on the kernel shape of changing the  $a_1$ ,  $a_3$ ,  $a_5$ , or  $a_7$  parameters by the amounts tabulated in Table 3.4; the corresponding impact on the EPID profiles are illustrated in Fig. 3.12. Note that these four parameters characterize four length scales in the kernel. The original best-fit values of 23.6, 3.98, 0.840, and 0.128 cm<sup>-1</sup> represent nominal length scales of 0.0424 (“short” range), 0.251 (“short-mid”), 1.19 (“mid”), and 7.81 cm (“long”). The amplitudes of the latter three length scales are characterized by the parameters  $a_2$ ,  $a_4$ , and  $a_6$ , respectively. As expected, there is a significant correlation between the amplitude and length parameter of each exponential term: for example, increasing the amplitude  $a_2$  has a similar (though not identical) effect on the EPID profiles as decreasing the value of  $a_3$  (*i.e.* increasing the range of this term). For this reason, the  $a_2$ ,  $a_4$ , and  $a_6$  parameters are not explicitly discussed below.

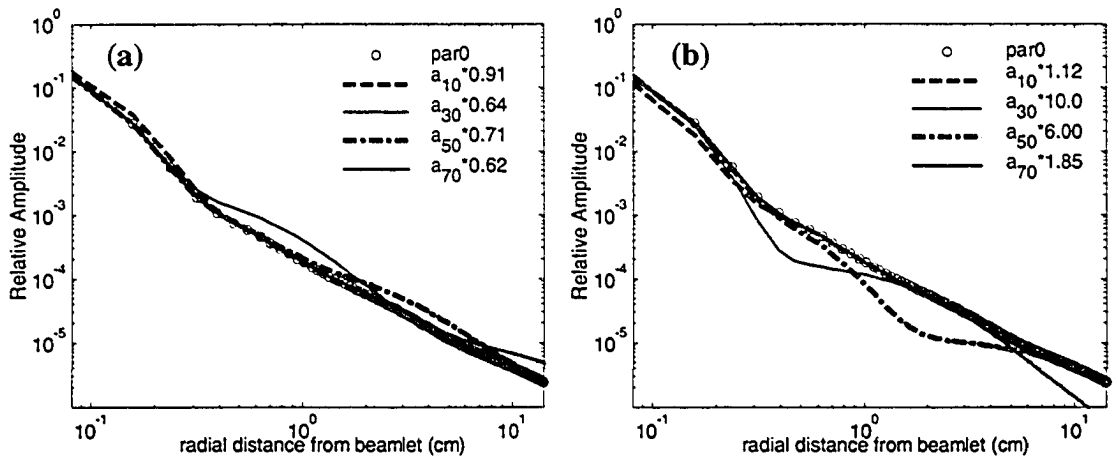


**Figure 3.11.** Effect on the shape of the EPID kernel described by the quadruple-exponential fit function ( $K_{fit}$  in Eq. (3.1)) when one of the parameters ( $a_1$ ,  $a_3$ ,  $a_5$ , or  $a_7$ ) is (a) decreased or (b) increased from its optimal fit value ( $a_{10}$ ,  $a_{30}$ ,  $a_{50}$ , or  $a_{70}$ ).

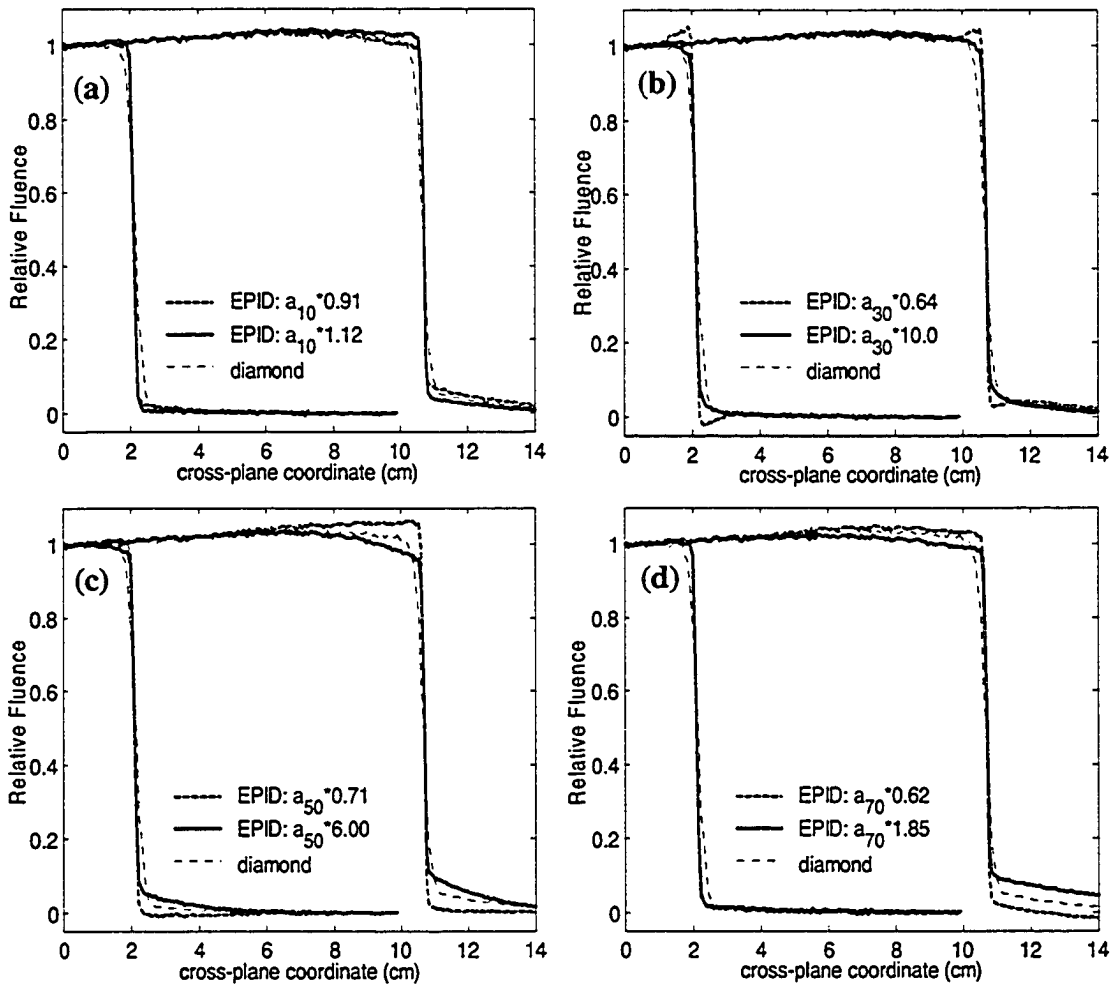


**Figure 3.12.** Effect on the 4 x 4 and 20 x 20 6 MV EPID profiles when altering the shape of the EPID kernel by changing one of the parameters ( $a_1$ ,  $a_3$ ,  $a_5$ , or  $a_7$ ) in  $K_{fit}$  from its optimal value (see Fig. 3.11 above).

Decreasing  $a_3$  results in a significant short-range over-deconvolution. This is evident in the dip at the base and spike at the top of the field edge in the profiles in Fig. 3.12(b), and also in the  $\Delta_{trans}|_{par0}^{par}$  values of 7.3 and 3.6 for the 4 x 4 and 20 x 20 field, respectively. The shape of the EPID profiles is much more stable, however, with respect to an increase in  $a_3$ . Increasing the best-fit  $a_3$  value,  $a_{30}$ , by a factor of ten makes the kernel much narrower for radii between  $\sim 0.5$  and 1.5 cm (Fig. 3.11(b)), but decreases the quality of the fit of the EPID profiles to the diamond profiles by only a small amount (e.g.  $SS_{ROI}|_{par0}^{par}$  and  $\Delta_{trans}|_{par0}^{par}$  values near one). It was also found that this kernel (with  $a_3 = 10a_{30}$ ) can be fit well with a function that is the sum of three exponentials. This suggests that a triple-exponential function may sufficiently describe the blurring in the EPID practically, *i.e.* for the purposes of deconvolution to relative fluence.

Since the  $a_5$  parameter value characterizes the “mid” range of the kernel, changing its value does not produce as severe an over- or under-deconvolution near the base or top of the profile as does changing the  $a_3$  parameter. Instead, the  $a_5$  parameter most obviously affects the *slope* of the top and tail of the profile. The effects of changing  $a_5$  are manifest for both the 4 x 4 and 20 x 20 fields. In contrast, but as expected, modifying the “long” range  $a_7$  parameter affects primarily the larger 20 x 20 field, and tends to change the *height* of the tail of the profile. As observed for the short-range exponential in  $K_{back-glare}^{6MV}$  (Sect. 3.B.iii), the shortest range  $a_1$  parameter in the fit to the  $K_{EPID}$  kernel does not display a clearly short-range behavior. Rather, its effect is probably closest to that of the long-range  $a_7$  parameter.

### C. EPID phantom scatter factors: measured vs. kernel-based predictions

To verify the ability of the derived EPID kernels to describe scattering in the EPID, we compared measured EPID-phantom scatter factors ( $S_{PE}$ ) to values predicted using our  $K_{EPID}$  kernel, for the 15 MV case. The concept of field-size dependent  $S_{PE}$  factors was introduced by Chang *et al.*<sup>3</sup> to facilitate EPID calibration. The factors are used to relate EPID pixel values to doses measured with an ion chamber in a phantom on

the central axis of an open beam. To measure  $S_{PE}$ , EPID images were acquired for several square field sizes. The value of  $S_{PE}$  for a field size  $fs$ , defined at 100 cm from the source (isocenter), was calculated as follows,<sup>3</sup>

$$S_{PE}(fs) = \frac{MREP(fs)/S_c(fs)}{MREP(fs_{ref})/S_c(fs_{ref})}. \quad (3.3)$$

In Eq. (3.3),  $MREP$  is the mean of the raw EPID pixel values in a small central region (11 x 11 pixels, or 0.9 x 0.9 cm<sup>2</sup>) of the field,  $fs_{ref}$  is 10x10 cm<sup>2</sup> at isocenter, and  $S_c$  is the collimator scatter factor.<sup>4</sup> The values of  $S_c$  were measured using an IC-10 ion chamber with a 1.6 cm diameter brass build-up cap, and were the average of measurements made on two separate occasions. To generate the predicted EPID phantom scatter values, a simulated EPID image for each field size was produced by convolving an input fluence image with  $K_{EPID}$ . For comparison, simulated EPID images were created employing both the “new” and the old versions of the 15 MV kernel ( $K_{EPID}^{15MV}|_{new}$  and  $K_{EPID}^{15MV}|_{old}$ ). The fluence map for each field size was obtained from the flood-field fluence distribution by truncating it to the field dimensions. Predicted  $S_{PE}$  factors were calculated as the ratio of mean pixel values in the small central region of the simulated EPID images for each field size and the 10x10 cm<sup>2</sup> field. A comparison of measured and predicted EPID-phantom scatter factors is summarized for several field sizes in Table 3.5. As indicated, there is reasonable agreement between measured and predicted values: the values agree within ~ 1 % for fields up to 16 x 16 cm<sup>2</sup> in size for the “old”, and up to 20 x 20 cm<sup>2</sup> for the “new” 15 MV kernel. Generally, the agreement for the “old” kernel is slightly better for the smaller field sizes (< 10 x 10), while the “new” kernel better predicts the  $S_{PE}$  for the larger field sizes (> 10 x 10). This is a consequence of the slightly higher amplitude of the long-range tail component of the “new” kernel (see Section 2.D.v). The approximate 1 % discrepancy between measured and simulated values of  $S_{PE}$  is perhaps not insignificant given that the  $S_{PE}$  values deviate from one by only  $\pm 5\%$  for field sizes from 4 x 4 cm<sup>2</sup> to 20 x 20 cm<sup>2</sup>; nevertheless, this level of consistency suggests that the ability of the convolution kernels to describe the scattering properties of the aS500 EPID is adequate for our dosimetric applications.

Field Size (cm <sup>2</sup> )	Measured	Simulated		Field Size (cm <sup>2</sup> )	Measured	Simulated	
	$S_{PE}$ ( $\pm 0.010$ )	$S_{PE}$	$S_{PE}$		$S_{PE}$ ( $\pm 0.010$ )	$S_{PE}$	$S_{PE}$
		$K_{EPID}^{15MV} _{old}$	$K_{EPID}^{15MV} _{new}$			$K_{EPID}^{15MV} _{old}$	$K_{EPID}^{15MV} _{new}$
3 x 3	0.920	0.927	0.911	12 x 12	1.013	1.009	1.011
4 x 4	0.947	0.950	0.937	14 x 14	1.023	1.013	1.016
5 x 5	0.963	0.964	0.954	16 x 16	1.032	1.022	1.028
6 x 6	0.974	0.974	0.966	18 x 18	1.041	1.027	1.034
8 x 8	0.991	0.988	0.985	20 x 20	1.049	1.030	1.039
10 x 10	1.000	1.000	1.000				

**Table 3.5:** Comparison between measured and simulated values for the 15 MV EPID-phantom scatter factors for a range of square field sizes. Simulated values are calculated by convolution of an open beam primary fluence with the  $K_{EPID}$  kernel.

#### D. Dose calibration: step-window doses

The absolute doses measured with an ion chamber at 10 cm depth in a water phantom at the center of each of the twelve 4 x 4 “step-window” sub-fields (see Section 2.E.ii) are provided in Table 3.6. These doses are used to calculate  $k_{cal}$ , which converts arbitrary EPID dose pixel units to cGy, facilitating calculation of 2-D BEV dose distributions.  $k_{cal}$  is the slope of the linear regression between ion chamber doses and the doses predicted by the EPID at 10 cm depth in a water phantom using the EPID's deconvolved fluence and a water dose deposition kernel (see Fig 2.11 in Chapter 2). Table 3.6 reports two sets of 15 MV and one set of 6 MV measurements. The first set of 15 MV doses, measured in a *solid* water phantom, was used to generate the 2-D verification results. The second 15 MV and the sole 6 MV sets of doses were measured in a water tank and used for tests verifying the 3-D technique (see Section 3.F.i below). The “water-tank” doses are average values for two sets of experiments performed on different days.

There is good agreement between the “solid water” and the “water tank” 15 MV doses. The individual doses differ by at most 1.0 cGy, and the mean of the absolute deviation for the twelve doses is 0.5 cGy. The values of  $k_{cal}$  obtained with the “water tank” and “solid water” doses differ by a negligible 0.1 %. The errors given for the “water tank” are the deviations in the means for the values measured on the two different days. The maximum and mean absolute differences between the two measurements are 0.9 and 0.5 cGy for the 6 MV case, and 2.8 and 0.7 cGy for 15 MV. The uncertainties in

the value of  $k_{cal}$  arising from the deviations in the two sets of measurements are  $\pm 0.2\%$  (6 MV) and  $\pm 0.5\%$  (15 MV).

Step-window sub-field (MUs)	solid water phantom doses (cGy) 15 MV	water tank doses (cGy)	
		15 MV	6 MV
10	14.2	13.2 $\pm$ 0.1	11.3 $\pm$ 0.2
20	23.0	22.1 $\pm$ 0.2	19.1 $\pm$ 0.3
30	31.1	30.5 $\pm$ 0.1	26.2 $\pm$ 0.2
40	38.7	38.3 $\pm$ 0.0	32.4 $\pm$ 0.3
50	46.9	46.3 $\pm$ 0.6	39.8 $\pm$ 0.1
60	55.5	55.8 $\pm$ 0.0	47.8 $\pm$ 0.2
70	64.7	64.7 $\pm$ 0.2	54.7 $\pm$ 0.0
80	71.8	72.3 $\pm$ 0.1	61.3 $\pm$ 0.1
90	79.7	78.8 $\pm$ 1.4	67.3 $\pm$ 0.5
100	88.6	88.8 $\pm$ 0.5	75.9 $\pm$ 0.4
110	97.3	97.5 $\pm$ 0.3	83.0 $\pm$ 0.3
120	104.0	104.5 $\pm$ 0.6	88.2 $\pm$ 0.4

**Table 3.6.** Absolute doses measured with an ion chamber at 10 cm depth in water for each of the 4 x 4 cm<sup>2</sup> sub-fields comprising the “step-window” field (240 MUs total). The errors for the “water tank” doses are the deviations in the mean of two sets of measurements taken on different days.

Changes in the dose sensitivity of the EPID, during the course of an IMRT verification, may introduce uncertainties in the dose calibration factor,  $k_{cal}$ . In our IMRT verification procedure, *one* step-window calibration image is acquired for every set of patient IMRT fields (typically eight fields). However, to quantify the uncertainty in  $k_{cal}$  arising from changes in the EPID’s sensitivity, we performed “test” verifications where three step-window calibration images were acquired – one before, one mid-way, and one after the irradiation of the patient IMRT fields. This experiment was performed on two different occasions. Averaging over these two occasions, the value of  $k_{cal}$  before the patient fields was 1.5 % lower, and the value after the patient fields was 0.4 % higher, than the mid-way value. A reasonable estimate of this uncertainty in the dose calibration was thus considered to be 1.5 %. Ghosting effects are the probable cause of this change in dose sensitivity.<sup>5</sup> The dose sensitivity does appear to stabilize somewhat eventually, as

the last value of  $k_{cal}$  is much closer to the mid-way value than the first value. It is thus likely that the magnitude of this error could be reduced by pre-irradiating the EPID before acquiring the verification images.

Factors such as field size and MLC leakage are also potentially important in the calibration of the aS500 EPID because of the expected energy-dependence of the pixel response that may result from the high atomic numbers of the copper plate and gadolinium screen. The step-window is more representative of the actual IMRT fields being verified than simple open fields. Like IMRT fields, the step-window field is a multi-segment, MLC field. Also, the  $4 \times 4 \text{ cm}^2$  sub-fields that comprise the step-window are more similar in size to the sub-fields of an IMRT field than, for example, the  $10 \times 10 \text{ cm}^2$  field that is commonly used for calibration.

To investigate any possible errors in the “step-window” calibration, a second calibration curve was generated using a series of EPID images of a MLC-collimated  $4 \times 4 \text{ cm}^2$  beam centered on the central axis. For this field, the main collimator jaws were set considerably outside the MLC collimators ( $20.4 \times 10.2 \text{ cm}^2$ ) to mimic a typical sub-field in a step-and-shoot IMRT field. Each EPID image was obtained with a different dose ranging from 20 – 200 MUs. As illustrated in Fig. 3.13, the  $k_{cal}$  obtained from a linear fit to the individual  $4 \times 4 \text{ cm}^2$  corrected-EPID images is nearly identical (within 0.5 %) to that obtained using the step-window technique. This provides confidence in the reliability of the step-window calibration. Fig. 3.13 also shows an additional data point corresponding to an open  $10 \times 10 \text{ cm}^2$  field defined only by the secondary jaws. This point agrees within ~1% with the straight-line fits of the step-window and “individual  $4 \times 4$ ” calibration measurements. This result tends to suggest that the calibration is not particularly sensitive to the type of field used to calibrate the detector response, and that any spectral differences between  $10 \times 10 \text{ cm}^2$  and  $4 \times 4 \text{ cm}^2$  fields do not lead to large uncertainties in the dose calibration.

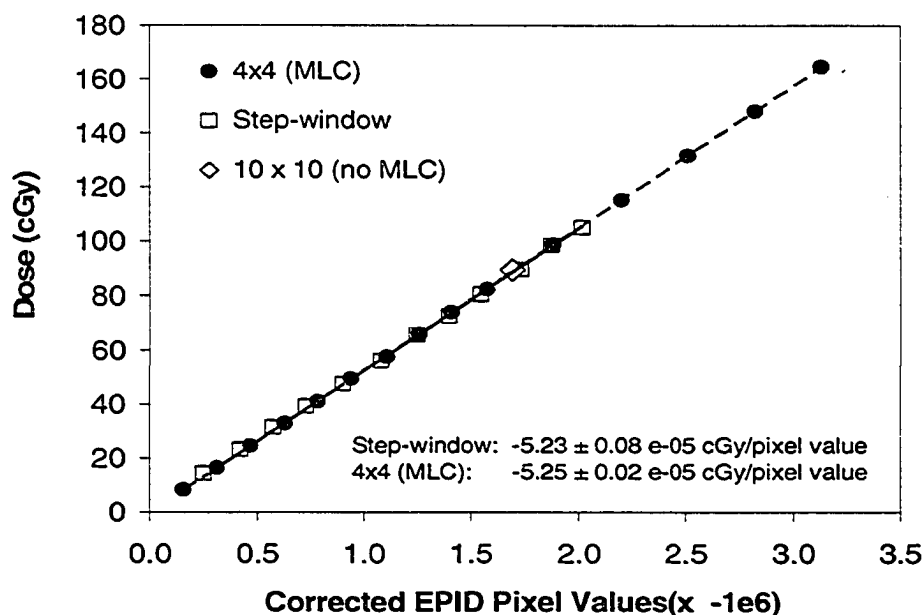


**Figure 3.13:** A comparison of the EPID dose-pixel value relationship when measured using a single irradiation of the multi-segmented “step-window” pattern, individual irradiations of an MLC-collimated 4 x 4 cm<sup>2</sup> field corresponding to different MUs, and a single 100 MU irradiation of a 10 x 10 cm<sup>2</sup> field (without MLC). The linear fits to the “step-window” (solid line) and “individual 4x4” data (dashed line) are virtually indistinguishable; the linear calibration coefficients ( $k_{cal}$ ) are as shown.

To summarize, uncertainty in  $k_{cal}$  results from the uncertainties of approximately 0.5 %, 1.5 %, and 1.0 % in the ion-chamber absolute doses, the changes in the EPID’s dose sensitivity during IMRT verification, and in potential field-size and beam energy dependencies of the dose response, respectively

## E. 2-D Verification Results

### *i. Comparison between ion chamber and EPID relative dose profiles*

Relative 15 MV profiles of the BEV dose at 10 cm depth in a water phantom were calculated for our EPID-based technique and compared to doses measured with an IC-10 ion chamber in a scanning water tank. This serves as a check of the accuracy of the deconvolution/convolution processes that form the basis of the EPID-based dose calculation. The use of a convolution method rather than a superposition technique (*c.f.* Eqs. (2.9) and (2.10)) assumes that the kernels describing blurring in the EPID and dose-deposition in the BEV phantom are spatially invariant. As discussed by Sharpe and Battista,<sup>6</sup> the difference between superposition, which accounts for kernel tilting, and

convolution, which does not, is generally small for smaller field sizes and larger SSDs (*e.g.*  $\geq 100$  cm). However, for large field sizes there may be appreciable discrepancies between the two methods, particularly in the shape of the penumbral regions (*e.g.* 10 % near the beam edge of a 6 MeV  $30 \times 30$  cm<sup>2</sup> photon field with a 100 cm SSD<sup>6</sup>).

The EPID-to-ion chamber comparison for a small  $2 \times 2$  cm<sup>2</sup> open field is shown in Fig. 3.14(a). For this and the other open field comparisons, the profiles were normalized to the mean value of a small central part of each profile. As illustrated, there is good agreement between the EPID and ion-chamber profiles. The IC-10 profile is, however, slightly more rounded, because of the blurring caused by the finite dimensions of the IC-10 chamber ( $\sim 3$  mm radius, 6.3 mm length). Thus, to facilitate a more meaningful comparison, in addition to the ion-chamber and EPID profiles ( $Prof_{IC10}(x)$  and  $Prof_{EPID}(x)$ , respectively), we generated a third profile that is the 1-D convolution of the EPID profile with an IC-10 “blurring” kernel,  $K_{IC10}(x)$ :

$$Prof_{EPIDblur}(x) = Prof_{EPID}(x) \otimes K_{IC10}(x). \quad (3.4)$$

For a small  $2 \times 2$  cm<sup>2</sup> field size it can reasonably be assumed that the difference between convolution and superposition is negligible. Hence, we attempted to find a  $K_{IC10}(x)$  that produced an excellent match in the shapes of the  $Prof_{IC10}(x)$  and  $Prof_{EPIDblur}(x)$  profiles for the  $2 \times 2$  field; we then used the same  $K_{IC10}(x)$  for other, larger field sizes. An appropriate form for  $K_{IC10}(x)$  was found to be,

$$K_{IC10}(x) = \exp(-x^2 / 2\pi\sigma^2), \quad (3.5)$$

a Gaussian with  $2\pi\sigma^2 = 3.3^2$  mm<sup>2</sup>. The shape of this  $K_{IC10}(x)$  is compared to the shape of the IC-10 blurring kernel that would be predicted from the nominal geometric dimensions of the detector (*i.e.* a circular cylinder with radius of 3 mm) in Fig. 3.14(b). In comparison to the “geometric” kernel, the tail of the  $K_{IC10}(x)$  based on Eq. (3.5) is longer, but its width is otherwise very comparable.

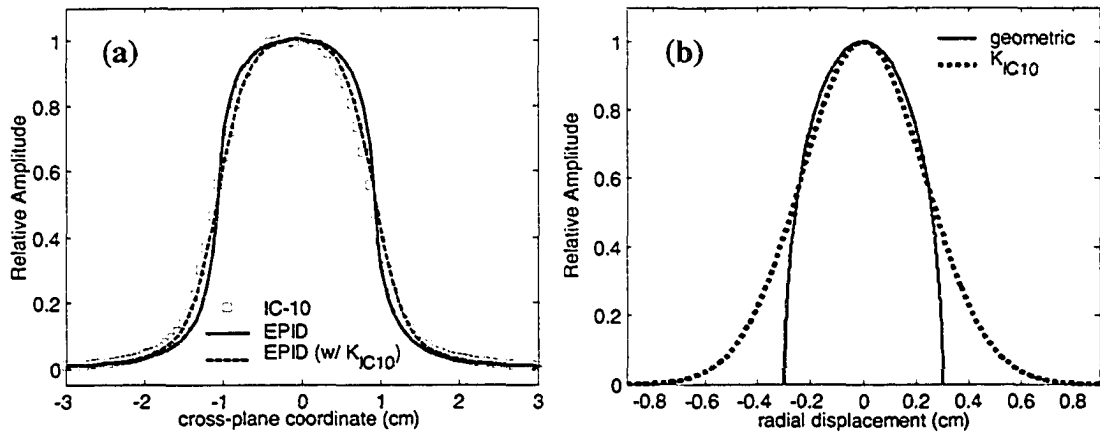


**Figure 3.14.** (a) Comparison of ion chamber (IC-10) and EPID-based (after deconvolution / convolution) profiles through a  $2 \times 2 \text{ cm}^2$  open field at 10 cm depth in water. After blurring the EPID profile by  $K_{IC10}$  (Eq. 3.5) to compensate for the geometric blurring inherent in the IC-10 profile, there is very good agreement between the IC-10 and EPID profiles. (b) Comparison of the  $K_{IC10}$  from Eq. 3.5 to the kernel shape predicted from simple geometric considerations.

Fig. 3.15(a) shows profile comparisons for a large  $20 \times 20 \text{ cm}^2$  open field. As depicted, there is exceptionally good agreement between the EPID and the ion-chamber profiles, even for large fields. This suggests that potential errors introduced via our use of simpler convolution techniques, rather than more complicated superposition ones, are small and should have a negligible impact on our 2-D verifications results. One probable explanation for this is that any errors occurring in the deconvolution stage (EPID image  $\rightarrow$  EPID fluence) may be largely offset by similar errors, but in the opposite direction, in the second convolution step (fluence  $\rightarrow$  dose) of the calculation.

The accuracy of the EPID-based dose calculation is further confirmed in Fig. 3.15(b), which compares profiles through the IMRT segment field previously depicted in Fig. 3.6(b). Again  $Prof_{IC10}(x)$  and  $Prof_{EPIDblur}(x)$  agree very well. It is interesting to note that the original, un-blurred EPID profile,  $Prof_{EPID}(x)$ , has slightly deeper troughs between the sub-fields in this field, and a significantly larger amplitude for the narrow sub-fields (the third and fourth peaks from the left in Fig. 3.15(b)). This suggests again that, as a result of the superior spatial resolution of the EPID detector, the EPID profiles are more representative of the delivered dose profile than the profiles measured with an ion chamber.

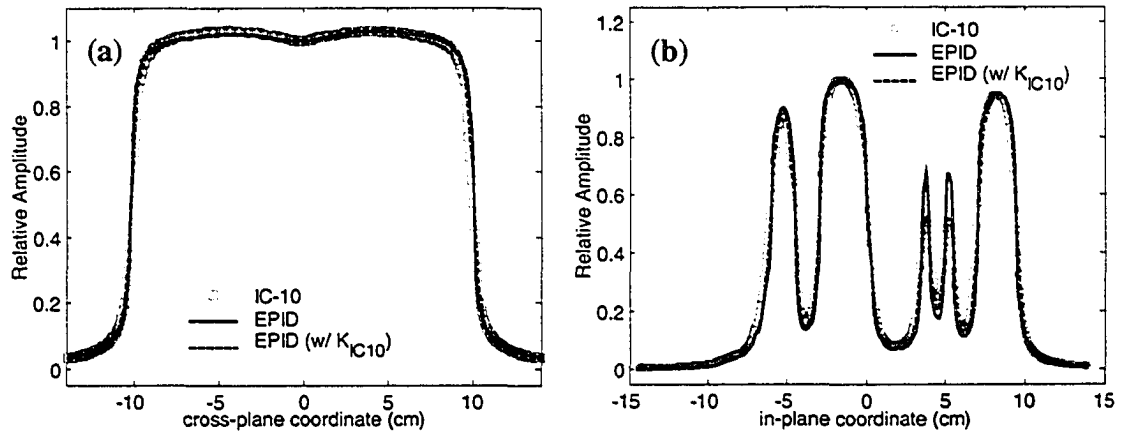


**Figure 3.15.** Comparison of ion chamber and EPID-based (both with and without the additional blurring of  $K_{IC10}$ ) profiles at 10 cm depth in water. (a) 20 x 20 cm<sup>2</sup> open field profiles. (b) profile through the multi-leaf collimated segment field depicted in Fig. 3.6(b).

### ii. Comparisons between TPS, film, and EPID doses for open-fields

To demonstrate the feasibility of our EPID-based IMRT verification method, 2-D dose distributions measured with the EPID are also compared with analogous distributions from film (Kodak XV) measurements and TPS calculations. H&D curves for film calibration were generated using the step-window technique described earlier. Absolute dose distributions for each method of determining dose (TPS, film, or EPID) were first measured/calculated independently, and then for comparison purposes, all doses were converted to percent values by dividing by the maximum dose in the EPID image (assigned a value of 100%). To clearly illustrate potential disagreements between the three methods of determining dose, these comparisons are first presented for open fields (Figs. 3.16 – 3.18). Images of the absolute percent difference (relative to the maximum dose in the EPID image) between i) the TPS and film, ii) film and the EPID, and iii) the TPS and the EPID are shown for MLC-shaped 10 x 10 cm<sup>2</sup> and 2 x 2 cm<sup>2</sup> fields. The mean and standard deviation of the percent differences for each of these three difference images are summarized in Table 3.7. These statistics are generated for two regions of interest: one defined 0.5 cm inside each nominal field edge to exclude the penumbra, and a second defined 0.5 cm outside each field edge to include the penumbra. Central cross-plane absolute dose profiles and the corresponding dose difference profiles for TPS, film and EPID measurements are also shown in Figs. 3.17 and 3.18 for the 10 x 10 and 2 x 2 cm<sup>2</sup> open fields. In the penumbra region, the agreement is best between film

and the EPID; large discrepancies are evident between the TPS and the two measurement-based methods. The TPS/film and TPS/EPID penumbral agreements are particularly poor for the 2x2 cm<sup>2</sup> field. These results emphasize the limitations of the treatment planning system in modeling penumbra and in its small-field dosimetry. This highlights the need for an independent verification of treatment planning dose calculations done for IMRT treatments. Figs. 3.16 – 3.18 and Table 3.7 also indicate that the TPS and EPID mean doses agree quite well within the central region of the fields, while the TPS and film mean doses are in slightly worse agreement.

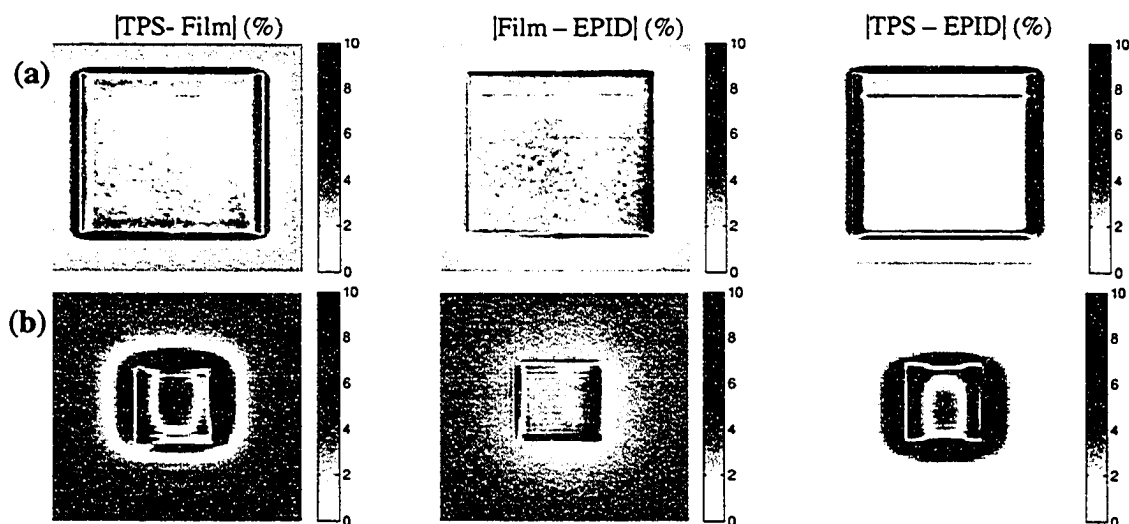


**Figure 3.16.** Images of the absolute percent difference (as a percent of the maximum EPID dose) between dose measurements made with the TPS, film, and the EPID for a (a) 10 x 10 cm<sup>2</sup> and a (b) 2 x 2 cm<sup>2</sup> open field.

Field Size (cm <sup>2</sup> )	TPS – Film (%)		Film – EPID (%)		TPS – EPID (%)	
	mean	std. dev.	mean	std. dev.	mean	std. dev.
10 x 10 (excl. penumb.)	1.3	1.1	-1.6	0.9	-0.3	1.2
10 x 10 (incl. penumb.)	1.7	3.2	-1.6	2.4	0.1	4.0
2 x 2 (excl. penumb.)	4.1	1.6	-2.1	0.3	2.0	1.8
2 x 2 (incl. penumb.)	3.0	5.4	0.0	3.0	3.0	6.5

**Table 3.7.** Numerical comparison between doses measured with the TPS, film, and the EPID corresponding to the images in Fig. 3.16. Values for the mean and standard deviation of the % differences between the three methods of determining dose are provided for the 10 x 10 cm<sup>2</sup> and 2 x 2 cm<sup>2</sup> fields, both when excluding (0.5 cm inside each nominal field edge) and when including (0.5 cm outside each field edge) the penumbra region of the fields.

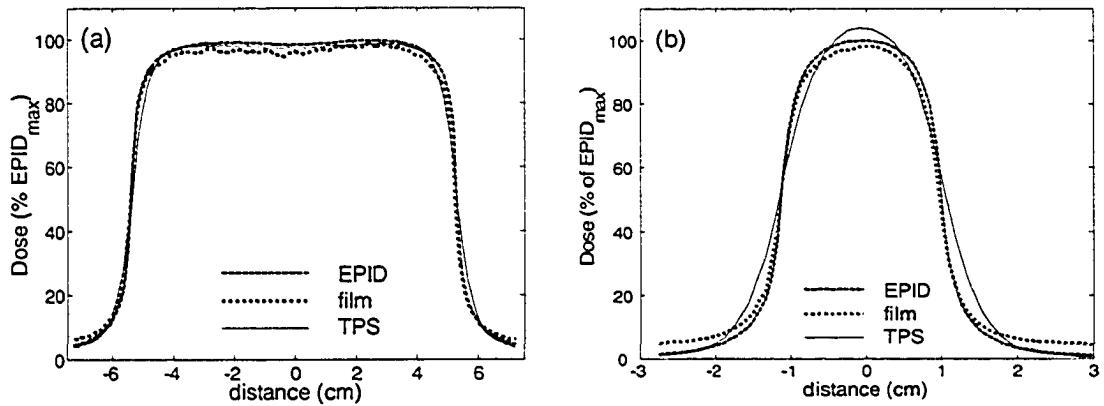


**Figure 3.17.** Dose profiles (centre of the field, cross-plane) derived from the EPID, film, and TPS for a (a) 10x 10 cm<sup>2</sup> and a (b) 2 x 2 cm<sup>2</sup> open field.

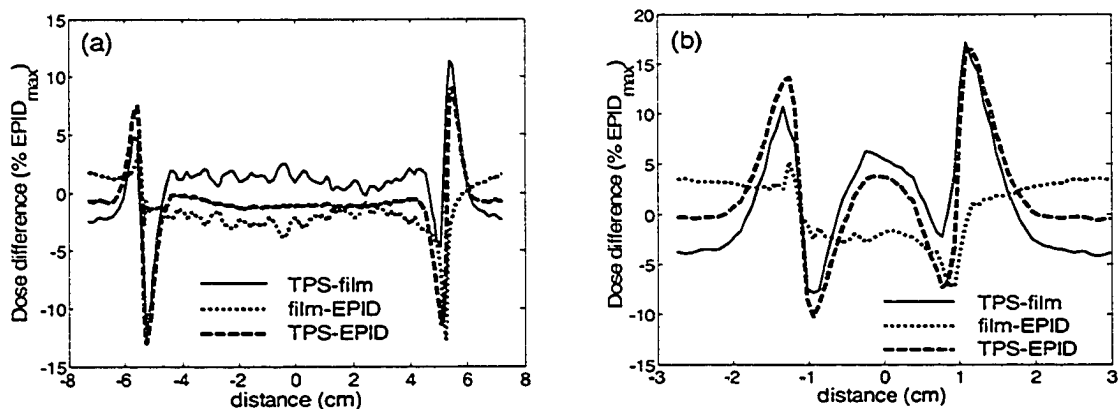


**Figure 3.18.** Dose differences (as a percent of the maximum EPID dose) between the EPID, film, and TPS for the profiles of a (a) 10 x 10 cm<sup>2</sup> and a (b) 2 x 2 cm<sup>2</sup> open field shown in Figure 3.17.

### *iii. 2-D IMRT Verifications for three patient treatment plans*

The film, EPID, and TPS doses are compared for a clinical IMRT patient field in Figs. 3.19 and 3.20. The three BEV dose distributions and the three BEV dose difference distributions are shown in Fig. 3.19(a) and (b), respectively. In Fig. 3.20, profiles along the vertical dashed line in Fig. 3.19(a) are also depicted for these dose and dose difference distributions. For each dose difference distribution shown in Fig. 3.19(b), a dose difference histogram and associated mean and standard deviation statistics are calculated (Fig. 3.19(c)) for the pixels within the ROI (region of interest) delineated by the dashed line in Fig. 3.19(b). The ROI is positioned slightly outside the edge of the IMRT field to include the penumbra. The doses and dose difference values are again expressed as percentages of the maximum dose in the EPID image.

The previous clinical method of IMRT verification consisted of the (TPS – Film) comparison shown in Fig. 3.19. As illustrated by the (TPS – EPID) comparison, similar verification results are obtained when using the EPID instead of film. More directly, the (Film – EPID) dose difference distribution and histogram show that the film and EPID doses are in good agreement. For the IMRT field of this example, the standard deviation in the (Film – EPID) difference is 2.0 %, compared with 3.1 and 3.2 % for the (TPS – Film) and (TPS – EPID) differences, respectively. Small deviations between dose distributions can be attributed to sub-pixel misalignments of the two dose images. Thus, perhaps more indicative of the superior film/EPID agreement is that there are fewer pixels with large deviations (*e.g.* > 5 %) between the film and EPID doses than found between the TPS dose and either of the measurement-based doses. The large discrepancies found between the TPS dose and the measured doses are most prevalent in the penumbral regions, near the edges of the MLC leaves.

The results of 2-D IMRT verifications for three clinical IMRT treatment plans comprising 24 fields (eight per plan) are summarized in Table 3.8. All verifications were performed with a 15 MV beam. As discussed above, there is good agreement between the film and EPID doses: averaged over the 24 fields, the mean and standard deviation in the (Film – EPID) dose differences are  $0.3 \pm 1.0$  % (one standard deviation) and  $1.9 \pm 0.3$  %, respectively. Consequently, there is little difference between the statistical results of the film-based verification and the EPID-based one.

patient	TPS – Film (%)		Film–EPID (%)		TPS–EPID (%)	
	mean	std. dev.	mean	std. dev.	mean	std. dev.
1 (8 fields)	$-1.6 \pm 0.6$	$2.8 \pm 0.3$	$-0.1 \pm 0.5$	$1.8 \pm 0.2$	$-1.7 \pm 0.7$	$3.1 \pm 0.3$
2 (8 fields)	$-2.2 \pm 0.4$	$2.9 \pm 0.5$	$1.1 \pm 0.7$	$1.7 \pm 0.1$	$-1.1 \pm 0.7$	$3.1 \pm 0.4$
3 (8 fields)	$-1.3 \pm 0.6$	$2.9 \pm 0.3$	$-0.2 \pm 1.0$	$2.2 \pm 0.2$	$-1.5 \pm 0.9$	$3.0 \pm 0.4$
<b>Average (24 fields)</b>	<b><math>-1.7 \pm 0.6</math></b>	<b><math>2.9 \pm 0.4</math></b>	<b><math>0.3 \pm 1.0</math></b>	<b><math>1.9 \pm 0.3</math></b>	<b><math>-1.5 \pm 0.8</math></b>	<b><math>3.0 \pm 0.4</math></b>

**Table 3.8.** Results from 2-D IMRT verifications of three clinical IMRT treatment plans based on comparison of TPS doses to measured film or EPID doses. The BEV doses are expressed as percentages of the maximum dose in the EPID distribution. The dose difference statistics (mean and standard deviation) are calculated for pixels lying within a ROI defined just outside the perimeter of each IMRT field. The given errors are the standard deviation in the mean and standard deviation for each set of values.

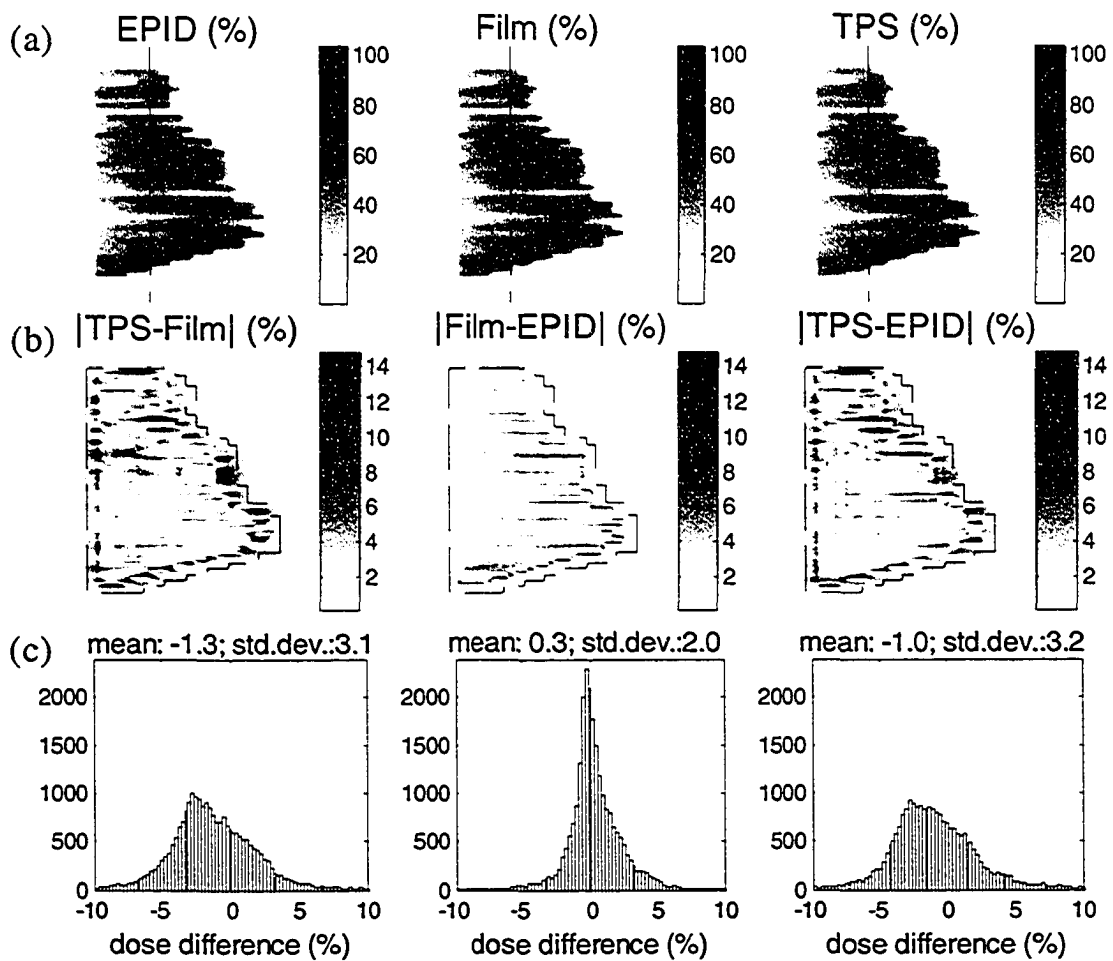


**Figure 3.19.** (a) Dose distributions for an IMRT field based on EPID and film measurements and TPS calculations. (b) Dose difference distributions for:  $|TPS-Film|$ ,  $|Film-EPID|$ , and  $|TPS-EPID|$ . (c) Dose difference histogram corresponding to each dose difference image directly above it in (b). The histograms are calculated for the ROI demarcated by the dashed line around the IMRT field in (b). Doses and dose differences are expressed as a percentage of the maximum dose in the EPID image.

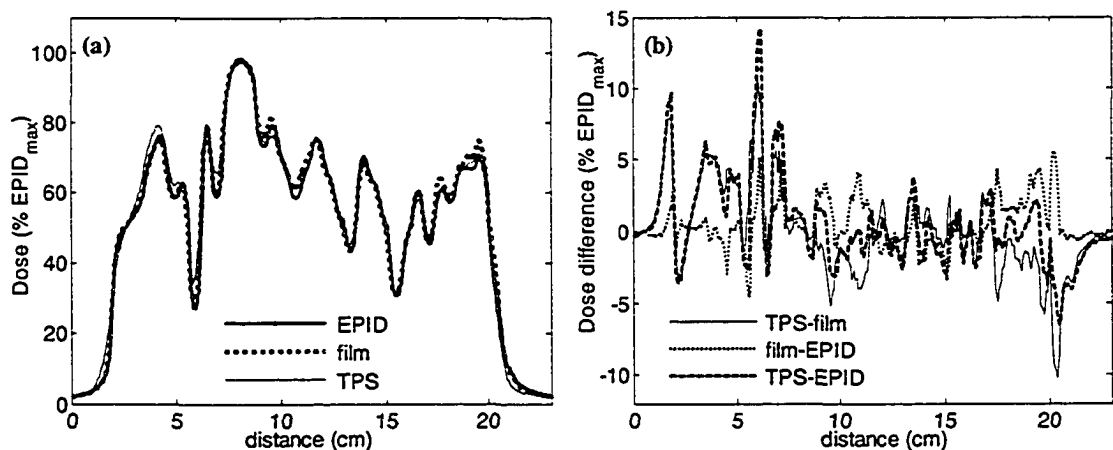


**Figure 3.20.** (a) Dose profiles along the dashed line through the IMRT field in Fig. 3.19(a) for EPID and film measurements and TPS calculations. (b) Dose difference profiles corresponding to the profiles in (a), expressed as a percentage of the maximum EPID dose.

The results reported in Table 3.8 were generated using the older version of the  $K_{EPID}$  kernel,  $K_{EPID}^{15MV}|_{old}$ . We re-generated these results with the newer version of the kernel,  $K_{EPID}^{15MV}|_{new}$ , to test the sensitivity of the 2-D verification to the exact form of  $K_{EPID}$ . As shown in Table 3.9, there is a negligible difference between the “new” and “old” verification results. The mean and standard deviation in the (TPS – EPID) dose differences change by only  $0.2 \pm 0.1 \%$  and  $0.02 \pm 0.05 \%$ , respectively, when using the “new” kernel in lieu of the “old” kernel.

	TPS – EPID (%)					
	$K_{EPID}^{15MV} _{new}$		$K_{EPID}^{15MV} _{old}$		Change	
	mean	std. dev.	mean	std. dev.	mean	std. dev.
<b>Average (24 fields)</b>	$-1.3 \pm 0.8$	$3.0 \pm 0.4$	$-1.5 \pm 0.8$	$3.0 \pm 0.4$	$0.2 \pm 0.1$	$0.02 \pm 0.05$

**Table 3.9.** Comparison of the 2-D EPID-based verification results when using the  $K_{EPID}^{15MV}|_{new}$  kernel instead of  $K_{EPID}^{15MV}|_{old}$  to describe scattering processes in the EPID.

We also evaluated how the 2-D IMRT verification results would change if no processing (*i.e.* no deconvolution/convolution) of the EPID images of the step-window and IMRT treatment fields were performed. For this purpose, a verification of one clinical IMRT treatment plan was repeated assuming that  $D_{EPID}$  was proportional to the raw EPID image – *i.e.*  $D_{EPID}(x, y) = n_{frame} \cdot EPID_{PV}(x, y) \cdot k_{cal}$ . A comparison (Table 3.10) of “unprocessed” to “processed” ( $D_{EPID}$  calculated using Eqs. (2.6), (2.14) and (2.17)) results illustrates the importance of the deconvolution/convolution procedure to the accuracy of the IMRT verification. Without image processing, the agreement between film and EPID doses is much worse, as evidenced by the near doubling of the standard deviation in the (Film – EPID) dose difference from 1.8 % to 3.5 %. Similarly, the standard deviation of the (TPS – EPID) difference increases from 3.0 % to 4.4 %, suggesting that the EPID-based 2-D IMRT verification would significantly over-predict the errors in the TPS dose calculations if the EPID doses were based solely on raw EPID images.

patient 1 (8 fields)	Processed EPID image		Raw EPID image	
	Film-EPID	TPS-EPID	Film-EPID	TPS-EPID
std. dev. (%)	1.8	3.0	3.5	4.4

**Table 3.10.** The impact of image processing on the results of 2-D EPID-based verifications. The “unprocessed” verification assumed that  $D_{EPID}$  is simply proportional to the raw EPID image, whereas the “processed” verification involved first executing image processing steps (cf. Eqs. (2.6), (2.14), (2.17)) that include deconvolution and convolution of the raw image.

An EPID-based IMRT verification can be completed within approximately one hour, for a typical treatment plan with eight fields. This is considerably shorter than the roughly two and one half hours required for film-based verification. For this reason, and since the EPID-based and film-based verification results are similar, the EPID-based technique is now used in clinical practice at our institution.

## F. 3-D Verification Results

### *i. Comparisons of 2-D dose distributions: $D_{EPID\text{flu}}$ , $D_{EPID\text{flu}/\text{pnt}}$ , $D_{EPID}$ , and $D_{TPS}$*

To verify the accuracy of the 3-D method of dose calculation,  $D_{EPID\text{flu}}$  (3-D method) BEV dose distributions at 10 cm depth in a water phantom are compared to the analogous  $D_{EPID}$  doses (2-D method), which the results in Section 3.E.ii suggest are accurate even for small field sizes. Recall that  $D_{EPID\text{flu}}$  doses are based on measurement of  $\Psi_{\text{mod}}$ , import of this modulation matrix into the TPS, and use of the TPS to perform the dose convolution. The  $D_{EPID\text{flu}}$  BEV dose distributions are converted to doses in cGy using the same normalization technique used to calculate absolute  $D_{TPS}$  doses (see Section 2.E.i): each IMRT field dose distribution is normalized to the isocenter of a 5 x 5 cm<sup>2</sup> open field, and a dose conversion factor is then determined from the measured dose for this 5 x 5 field. In contrast,  $D_{EPID}$  doses are based on calculation of  $\Psi_p$  using Eq. (2.14), TPS-independent convolution (Eq. (2.17)), and the step-window absolute dose-calibration technique (Section 2.E.ii). Both  $D_{EPID\text{flu}}$  and  $D_{EPID}$  doses are based on EPID-measured fluences. Thus, any discrepancies between  $D_{EPID\text{flu}}$  and  $D_{EPID}$  result from differences between our method of dose convolution and our convolution kernel (Eq. (2.17)) and those of the TPS; and from any errors introduced in the (3-D method)

process of importing the fluence modulation into the TPS. Hence, calculation of the difference,  $D_{EPIDflu} - D_{EPID}$  (or  $D_{EPIDflu/pnt} - D_{EPID}$ ), is one means of assessing the accuracy of the dose calculation step of the TPS, particularly for small fields.

The difference  $D_{TPS} - D_{EPID}$  is used to quantify the combined effects of both differences between the TPS-optimized and EPID-measured fluences, and between the TPS-dependent and TPS-independent dose calculations. This  $D_{TPS} - D_{EPID}$  comparison is the same one utilized for 2-D IMRT verification.

The 2-D BEV dose distributions  $D_{EPIDflu}$ ,  $D_{EPID}$ , and  $D_{TPS}$  were generated for both 6 MV and 15 MV photon beam energies for a number of fields: 2 x 2, 4 x 4, 10 x 10, 15 x 15, 10 x 1, and 1 x 10 cm<sup>2</sup> open fields defined by the MLC with the secondary collimators set to 20x20 cm<sup>2</sup>; a single segment of a step-and-shoot IMRT field; and the entire IMRT fields of the three treatment plans for which 2-D (Section 3.E.iii) and 3-D IMRT (Section 3.F.iii) verifications were performed. The EPID images, required to calculate  $D_{EPIDflu}$  and  $D_{EPID}$ , were acquired using 40 MUs/image for the open and IMRT-segment fields, and 100 MUs/image for the multi-segment IMRT fields (all at 100 MU/min).

#### *a. Open fields and IMRT- segment field*

Comparisons of the  $D_{EPIDflu}$ ,  $D_{EPID}$ , and  $D_{TPS}$  BEV dose distributions are summarized for open fields and a single IMRT-segment in Tables 3.11(a) and 3.11(b) for incident photon energies of 6 MV and 15 MV, respectively. The means and standard deviations of the 2-D dose difference maps are calculated for the three comparisons:  $D_{EPIDflu} - D_{EPID}$ ,  $D_{TPS} - D_{EPID}$ , and  $D_{EPIDflu/pnt} - D_{EPID}$ . These statistics are calculated for two regions of interest (ROIs): a ROI (ROI1) encompassing the central quarter of the open fields – e.g. the central 5x5 cm<sup>2</sup> for the 10x10 cm<sup>2</sup> field; and a second ROI (ROI2) that includes the entire field and its penumbra, and is described by a perimeter positioned 0.5 cm outside the nominal field edge as defined by the MLC. The means and standard deviations are reported as a percentage of the maximum in the  $D_{EPID}$  dose for the given field.

(a) 6 MV		$D_{EPIDflu} - D_{EPID}$		$D_{TPS} - D_{EPID}$		$D_{EPIDflu/pnt} - D_{EPID}$	
ROI	Field (cm <sup>2</sup> )	mean (%)	std. dev. (%)	mean (%)	std. dev. (%)	mean (%)	std. dev. (%)
ROI1: Central quarter of field area	15x15	0.2	0.3	0.2	0.5	0.2	0.3
	10x10	-0.1	0.5	0.1	0.6	-0.1	0.5
	4x4	-1.1	0.3	1.5	0.4	-1.1	0.3
	2x2	-1.6	0.3	4.8	0.3	-1.5	0.3
	10x1	-1.7	1.1	5.9	1.2	-0.5	0.8
	1x10	-0.5	0.6	-3.9	1.8	0.0	0.5
ROI2: entire field and penumbra	15x15	1.4	1.7	0.2	5.3	1.4	1.4
	10x10	0.9	1.9	0.2	4.5	0.9	1.4
	4x4	-0.4	2.9	0.4	5.0	-0.4	1.9
	2x2	-0.6	3.7	-4.5	9.7	-0.5	2.5
	10x1	-0.4	4.4	3.0	6.0	-0.3	3.0
	1x10	-0.1	3.4	-16.2	11.4	0.0	2.1
IMRT segment		0.5	3.3	1.1	6.3	0.6	2.1

(b) 15 MV		$D_{EPIDflu} - D_{EPID}$		$D_{TPS} - D_{EPID}$		$D_{EPIDflu/pnt} - D_{EPID}$	
ROI	Field (cm <sup>2</sup> )	mean (%)	std. dev. (%)	mean (%)	std. dev. (%)	mean (%)	std. dev. (%)
ROI1: Central quarter of field area	15x15	-1.1	0.6	-1.2	0.7	-1.1	0.6
	10x10	-1.2	0.2	-1.1	0.3	-1.2	0.2
	4x4	-0.6	0.4	0.1	0.7	-0.6	0.4
	2x2	2.4	1.0	3.7	1.8	2.7	0.7
	10x1	-0.8	1.6	3.7	1.2	0.4	1.6
	1x10	1.4	0.9	-10.6	2.0	2.1	0.8
ROI2: entire field and penumbra	15x15	-0.2	1.9	-1.9	5.4	-0.2	1.7
	10x10	0.2	2.2	-1.1	4.6	0.2	2.0
	4x4	-0.1	2.8	-0.7	4.9	0.0	2.4
	2x2	0.6	3.5	-4.8	8.4	0.7	3.0
	10x1	0.6	3.8	3.3	6.2	0.7	3.0
	1x10	0.9	4.1	-17.4	9.3	1.0	3.8
IMRT segment		-0.1	3.9	-0.3	6.0	0.0	2.9

Table 3.11. Statistical comparison of different methods of calculating dose at 10 cm depth in a water phantom:  $D_{EPIDflu}$  (EPID  $\Psi_{mod}$ , TPS convolution),  $D_{TPS}$  (TPS  $\Psi_{mod}$ , TPS convolution),  $D_{EPIDflu/pnt}$  (EPID  $\Psi_{mod}$ , TPS convolution with a "point" source), and  $D_{EPID}$  (EPID  $\Psi_{mod}$ , TPS-independent convolution). Mean dose differences and standard deviations as percentages of the maximum  $D_{EPID}$  dose are calculated for two ROIs (regions of interest) and a number of different fields for photon beam energies of (a) 6 MV and (b) 15 MV.

For the larger open field sizes – 4 x 4, 10 x 10 and 15 x 15 cm<sup>2</sup> – there is good agreement between all methods of calculating the 2-D dose in the central ROI (ROI1), for both photon energies. The mean dose differences are less than 2% in all cases, and the standard deviations are less than or equal to 0.7%. For the larger ROI (ROI2), which also includes penumbral regions, the standard deviations ranging from 1.7 – 2.9 % for the  $D_{EPIDflu} - D_{EPID}$  comparison do suggest a non-negligible difference between the two EPID-based methods of calculating dose. However, the standard deviations of 4.5 – 5.4% for  $D_{TPS} - D_{EPID}$  indicate a significantly larger disagreement between the reference  $D_{EPID}$  dose and the dose calculated by the TPS using the TPS-optimized  $\Psi_{mod}$ . This suggests that even for these relatively large field sizes, the penumbra modeling of the TPS is less than ideal.

Differences between  $D_{TPS}$  and the two EPID-based doses are much more pronounced for the smaller field sizes (2 x 2, 10 x 1, and 1 x 10 cm<sup>2</sup>). The mean  $D_{EPIDflu}$  dose differs from the mean  $D_{EPID}$  dose by at most 2.4 % and 0.9 % in ROI1 and ROI2, respectively. In contrast, mean dose differences between  $D_{TPS}$  and  $D_{EPID}$  are as large as 10.6 % in the central ROI and 17.4 % in the larger ROI2: in ROI1, the mean ( $D_{TPS} - D_{EPID}$ ) ranges from -3.9 % – 5.9 % for 6 MV and from -10.6 % – 3.7 % for 15 MV; in ROI2, these ranges are -16.2 % – 3.0 % (6 MV) and -17.4 % – 3.3 % (15 MV). Deficiencies in the TPS's fluence modeling of small fields are further emphasized by the standard deviations in ROI2. These values range from 6.0 % – 11.4 %, much larger than the analogous values of 3.4 % – 4.4 % for  $D_{EPIDflu} - D_{EPID}$ . Noteworthy is that the apparent errors in  $D_{TPS}$  are much worse when the narrow dimension of the field is in the direction of MLC leaf travel. For example, for the 6 MV case and ROI2, the mean dose difference and standard deviation in  $D_{TPS} - D_{EPID}$  are -16.2 % and 11.4 % for the 1 x 10 cm<sup>2</sup> field, while only 3.0 % and 6.0 % for the 10 x 1 cm<sup>2</sup> field. Results for the IMRT-segment field, a relatively large field with a highly irregular shape, fall in-between those obtained for the smaller and larger open field sizes. The standard deviations of 6.3 % (6 MV) and 6.0 % (15 MV) for  $D_{TPS} - D_{EPID}$  are not as large as for the 2 x 2 and 1 x 10

cm<sup>2</sup> fields, but still significantly larger than the corresponding values of 3.3 % and 3.9 % for the  $D_{EPIDflu} - D_{EPID}$  comparison.

For the three smaller open field sizes and the IMRT-segment field, the standard deviation in  $D_{EPIDflu/pnt} - D_{EPID}$  is on average 1.2 % and 0.6 % lower for 6 and 15 MV, respectively, in comparison to the  $D_{EPIDflu} - D_{EPID}$  case. Therefore, use of the point-source model in the 3-D technique improves the agreement between the 2-D and 3-D EPID-based methods of dose calculation.

Fig. 3.21 illustrates the differences between the methods of calculating dose for the worst-case 1 x 10 cm<sup>2</sup> field and a 6 MV beam. The 2-D dose difference maps are shown for  $D_{EPIDflu} - D_{EPID}$ ,  $D_{TPS} - D_{EPID}$ , and  $D_{EPIDflu/pnt} - D_{EPID}$ , as well as a cross-plane profile through the center of the field along the narrow dimension for each dose distribution. The broad line to the left of the 1 x 10 cm<sup>2</sup> field in the  $D_{TPS} - D_{EPID}$  difference map also clearly depicts the failure of the TPS to model leakage radiation at the junctions of MLC leaves.

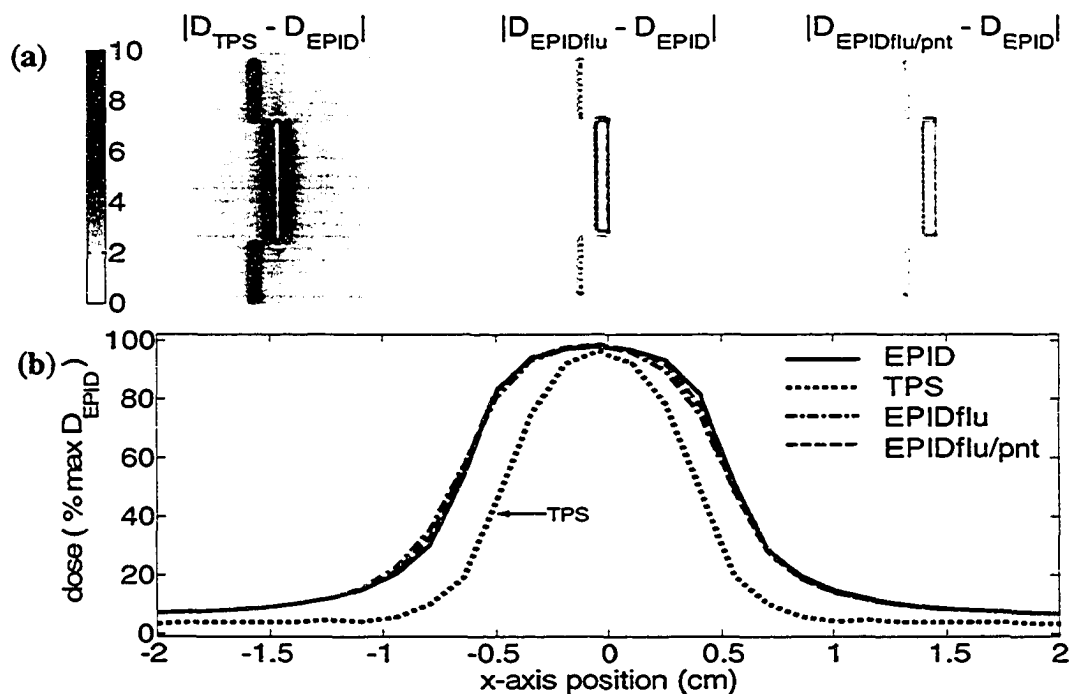


**Figure 3.21.** Results for a 1 x 10 cm<sup>2</sup> field and a 6 MV beam: (a) 2-D dose difference maps (absolute values of the differences are shown) and (b) cross-plane profile through the center of the field. The doses and dose differences are expressed as percentages of the maximum  $D_{EPID}$  dose. The  $D_{TPS}$  dose deviates significantly from the other three doses based on EPID measurements.

*b. Multi-segment IMRT fields*

Comparisons similar to those described for open fields in Section 3.F.iii.a above are summarized in Table 3.12 for the multi-segment, “step-and-shoot” IMRT fields comprising three clinical IMRT treatment plans. Statistics are calculated for ROI2, which includes the entire field and the penumbra. The mean ROI doses agree well among the different methods of dose calculation: when averaging over the three patients (irrespective of beam energy),  $D_{EPIDflu}$  and  $D_{TPS}$  are 0.7 % larger and 1.1 % smaller, respectively, than  $D_{EPID}$ . The average standard deviation of 3.4 % for the  $D_{TPS} - D_{EPID}$  comparison, which is typical of 2-D IMRT verification results at our clinic, is approximately twice the 1.8 % and 1.5 % calculated for the  $D_{EPIDflu} - D_{EPID}$  and  $D_{EPIDflu/pnt} - D_{EPID}$  dose differences.

Patient / no. IMRT fields	$D_{EPIDflu} - D_{EPID}$		$D_{TPS} - D_{EPID}$		$D_{EPIDflu/pnt} - D_{EPID}$	
	Avg. mean	Avg. std. dev.	Avg. mean	Avg. std. dev.	Avg. mean	Avg. std. dev.
	(%)	(%)	(%)	(%)	(%)	(%)
Patient 1: 8 - 15MV fields	0.93	1.68	-1.14	3.69	0.97	1.39
Patient 2: 8 - 6 MV fields	0.43	2.07	-1.20	3.13	0.51	1.82
Patient 3: 6 - 15 MV, 2 - 6 MV	0.86	1.67	-1.03	3.43	0.91	1.34

**Table 3.12.** Comparisons of different methods of calculating the 2-D dose (10 cm depth, water phantom) for the multi-segment IMRT fields comprising three clinical IMRT treatment plans. Statistics are calculated for ROI2, which includes the entire field and the penumbra.

*ii. Comparison of 3-D EPID doses with TLD Measurements*

For further validation, our 3-D EPID-based verification technique was compared to an IMRT verification procedure employing TLD (thermoluminescent dosimeter) dose measurements. The latter verification had been performed as a requirement for participation in an IMRT protocol (RTOG H-0022), and involved generating and delivering an IMRT treatment plan for a hypothetical treatment of an anthropomorphic head and neck phantom. A dosimetry insert for the phantom contains regions describing primary, and secondary PTVs (planning tumor volumes), and a critical structure. (Further details of this phantom and the verification procedures can be found in Refs.

[7,8].) After irradiation of the phantom, the doses recorded by the TLDs placed in each of these regions were measured by the RPC (Radiological Physics Center, M.D. Anderson Cancer Center, Houston, TX). The locations of the TLDs were also delineated on the CT scan of the phantom.

The TLD doses ( $D_{TLD}$ ) reported by the RPC are compared to the analogous mean doses calculated by the TPS using the EPID-measured  $\Psi_{\text{mod}}$  ( $D_{EPIDflu}$ ) and the TPS-optimized  $\Psi_{\text{mod}}$  ( $D_{TPS}$ ) in Table 3.13. As indicated, there is slightly better agreement with the TLD doses for  $D_{EPIDflu}$  than for  $D_{TPS}$  in the low-gradient regions located in the primary and secondary PTVs, though there is substantial agreement between all three doses. However, in the high-gradient region where the TLD was placed in the simulated critical structure, the  $D_{TPS}$  dose under-predicts the TLD-measured dose by 16%. In contrast, the  $D_{EPIDflu}$  and  $D_{TLD}$  doses agree within the RPC-estimated uncertainty of  $\pm 3\%$  in the TLD doses. The results using  $D_{EPIDflu/pnt}$  are nearly identical to those obtained using  $D_{EPIDflu}$ .

Region of Interest	$D_{TPS}$ (Gy)	$D_{EPIDflu}$ (Gy)	$D_{EPIDflu/pnt}$ (Gy)	$D_{TLD}$ (Gy)	$\frac{D_{TPS}}{D_{TLD}}$	$\frac{D_{EPIDflu}}{D_{TLD}}$	$\frac{D_{EPIDflu/pnt}}{D_{TLD}}$
Primary PTV	7.10	7.38	7.37	7.31	0.97	1.01	1.01
Secondary PTV	5.63	5.65	5.62	5.70	0.99	0.99	0.99
Critical Struct.	3.16	3.85	3.86	3.76	0.84	1.02	1.03

**Table 3.13.** Measured TLD doses ( $\pm 3\%$ ) compared to TPS-calculated doses using fluences modeled by the TPS ( $D_{TPS}$ ) and EPID-measured fluences ( $D_{EPIDflu}$  and  $D_{EPIDflu/pnt}$ ) for an IMRT treatment of an anthropomorphic head and neck phantom.

One potential limitation of our method of verifying the 3-D dose distributions calculated by our TPS is that the calculation of our EPID-based 3-D doses ( $D_{EPIDflu}$ ) relies on the TPS itself to perform the convolution step of the dose calculation. Thus, errors introduced in this step by the TPS will not be identified by our verification procedure. However, the good agreement between  $D_{TLD}$  and  $D_{EPIDflu}$ , and the large discrepancy between either of these measurement-based doses and  $D_{TPS}$  in a high gradient region, suggest that a large portion of the dose calculation errors of our TPS are

introduced prior to the convolution step, *e.g.* in the fluence modeling stage of the calculations.

### iii. 3-D IMRT Verification of clinical IMRT treatment plans

Analysis of the 3-D verification results was performed using an in-house software (Fig. 3.22) tool developed in the MATLAB programming environment to show the 3-D dose difference distribution overlaid on a patient's CT anatomy. The software tool also allows display of the tumor and normal tissue contours delineated previously in the TPS. Dose differences in these volumes are summarized in terms of DVHs (dose-volume histograms) and dose difference statistics. Results are reported for 3-D verifications that were performed retrospectively on three clinical head-and-neck cancer IMRT treatment plans: one comprised of eight 15 MV beams, another of eight 6 MV beams, and a third of six 15 MV and two 6 MV beams.

VOI	$D_{TPS}$ (Gy)		$D_{EPIDflu} - D_{TPS}$ (Gy)		$D_{EPIDflu / pnt} - D_{TPS}$ (Gy)		$\frac{D_{EPIDflu}}{D_{TPS}}$	$\frac{D_{EPIDflu / pnt}}{D_{TPS}}$
	mean	std.dev.	mean	std.dev.	mean	std.dev.	mean	mean
<b>Patient 1</b>								
PTV	73.3	5.9	1.9	1.4	1.9	1.5	1.03	1.03
spinal cord	30.1	9.3	3.8	1.1	3.7	1.1	1.13	1.12
left parotid	24.0	16.9	4.3	1.9	4.2	1.8	1.18	1.18
right parotid	29.6	18.1	3.8	1.5	3.7	1.5	1.13	1.12
<b>Patient 2</b>								
PTV	61.4	5.4	0.9	1.0	1.2	1.1	1.01	1.02
spinal cord	15.6	8.8	3.1	1.4	3.1	1.4	1.20	1.20
left parotid	23.6	12.7	4.1	1.2	4.2	1.1	1.17	1.18
right parotid	50.3	14.1	2.1	1.7	2.5	1.7	1.04	1.05
<b>Patient 3</b>								
PTV	70.7	3.6	1.6	1.2	1.6	1.2	1.02	1.02
spinal cord	28.2	10.9	4.3	1.4	4.1	1.4	1.15	1.15
left parotid	36.9	22.6	4.9	2.6	4.9	2.5	1.13	1.13
right parotid	24.5	13.6	4.8	1.6	4.8	1.6	1.20	1.20

Table 3.14. 3-D IMRT verification results: comparison of TPS ( $D_{TPS}$ ) and EPID-based ( $D_{EPIDflu}$  or  $D_{EPIDflu / pnt}$ ) 3-D dose distributions for three clinical IMRT treatment plans.

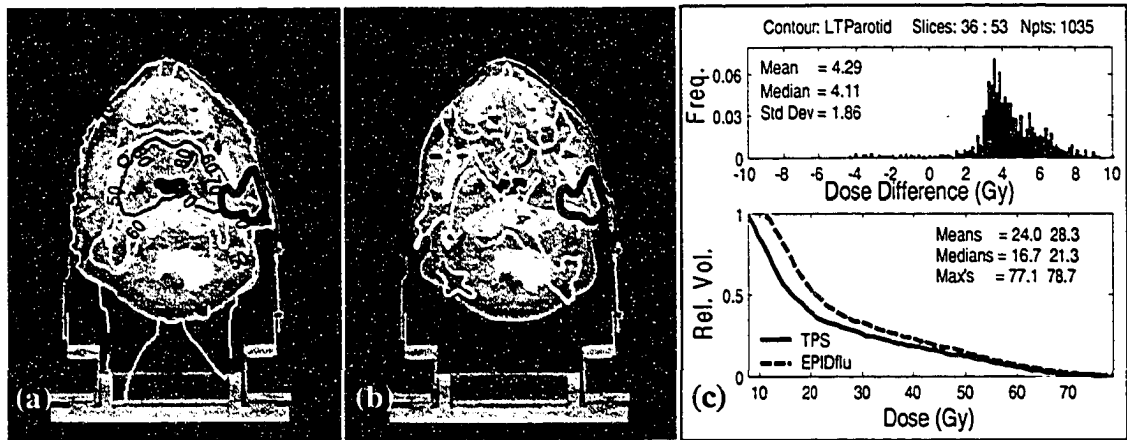


**Figure 3.22.** Example output from the software developed for the analysis of 3-D IMRT verifications. (a) Original TPS dose distribution,  $D_{TPS}$ . The thicker black line delineates the left parotid gland. The other lines are isodose lines, with the thinner black line representing the 70 Gy line (prescription dose = 74 Gy). (b) Dose differences between TPS and EPID-based 3-D doses,  $D_{EPIDflu} - D_{TPS}$ . The thinner white lines are the 4 Gy isodose contours for the dose difference. (c) Dose difference frequency distribution (top) and associated statistics, and the DVHs (bottom) for the selected volume of interest (left parotid) for the  $D_{TPS}$  and  $D_{EPIDflu}$  distributions.

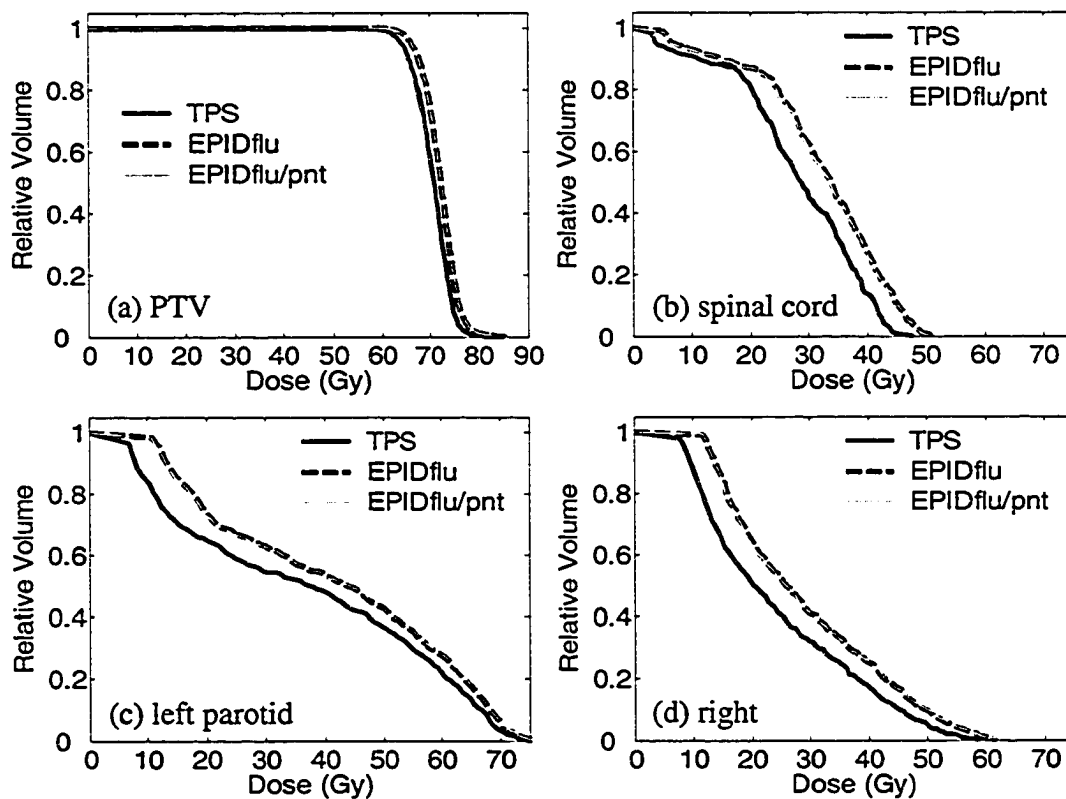


**Figure 3.23.** Comparison of DVHs derived from TPS ( $D_{TPS}$ ) and EPID-based ( $D_{EPIDflu}$  or  $D_{EPIDflu/pnt}$ ) dose distributions generated during 3-D IMRT verifications of patient 3's treatment plan.

Results from the retrospective 3-D verification of three clinical head-and-neck cancer IMRT treatment plans are summarized in Table 3.14. For each patient, the original dose distribution calculated by the TPS,  $D_{TPS}$ , and the dose difference distribution,  $D_{EPIDflu} - D_{TPS}$  (or  $D_{EPIDflu/prt} - D_{TPS}$ ), are characterized by mean and standard deviation statistics for four volumes of interest (VOIs) – PTV, spinal cord, right parotid and left parotid. The dose distributions were normalized such that the median doses in the PTV for  $D_{TPS}$  were 74, 62, and 71 Gy for patient 1, 2, and 3, respectively. As was found for the head-and-neck phantom, TPS and EPID-based doses agree well in the PTV, with the mean dose difference of 1.4 Gy (averaged over the three patients) corresponding to a 2 % difference. However, in the high-gradient regions of the critical structures, there is once again a large discrepancy: the EPID-based doses are on average 3.7 Gy (16 %), 4.4 Gy (16 %), and 3.6 Gy (12 %) higher than the TPS doses for the spinal cord, left parotid, and right parotid, respectively. DVHs for the PTV and critical structures derived from the TPS and EPID-based dose distributions for patient 3 are compared in Fig. 3.23.

As was done for the 2-D IMRT verification (Section 3.E.iii), we also generated a 3-D IMRT verification of patient 1’s treatment plan using unprocessed EPID images. In this case, no deconvolution was performed, and it was assumed that the incident fluences in Eq. (2.18) were proportional to the raw, integrated EPID image – *i.e.*  $\Psi_p(x, y) = n_{frame} \cdot EPID_{PV}(x, y)$ . In comparison to the processed doses, the unprocessed  $D_{EPIDflu}$  mean doses were 0.2, 2.2, and 2.0 Gy higher for the spinal cord, left parotid, and right parotid, respectively, and 2.7 Gy lower in the PTV. Also, the  $D_{EPIDflu} / D_{TPS}$  ratios of 1.13, 1.18, 1.13, 1.03 (spinal cord, left parotid, right parotid, PTV) in Table 3.14 changed to values of 1.13, 1.27, 1.19, 0.99 when the raw EPID images were used. Thus in this example, a 3-D verification using the unprocessed EPID fluence instead of the processed one would indicate a significantly larger (9 %) error in the TPS’s prediction of the mean dose in the right parotid gland. Akin to the similar 2-D verification comparison, this suggests that the EPID image processing steps are necessary to achieve accurate 3-D verification results.

#### *iv. Radiobiological significance of 3-D verification results*

Differential dose-volume histograms (DDVHs) for the critical structure VOIs listed in Table 3.14 were also generated and used to calculate radiobiological estimates of normal tissue complication probabilities (NTCPs) arising from the TPS and EPID-based dose distributions. NTCP calculations employing the Lyman sigmoidal dose-response model were performed using software and methods described in Chapter 4. Model parameter values for both the spinal cord and the parotid glands are available from the Burman *et al.*<sup>9</sup> fits to the Emami *et al.*<sup>10</sup> dose-response database; additional NTCP estimates for the parotids are possible using more recent Lyman model parameter estimates published in Eisbruch *et al.*<sup>11</sup> and Roesink *et al.*<sup>12</sup> Since large uncertainties are currently inherent in such radiobiological modeling exercises, these calculations are used only to provide insight into the *potential* consequences of TPS dose modeling errors.

The radiobiological predictions (Table 3.15) suggest that for these three treatment plans, the spinal cord is sufficiently spared such that the additional ~ 4 Gy predicted by the EPID-based dose for this structure has little impact on the predicted rate of complication – the NTCP is  $\leq 2\%$  for all dose distributions. The NTCP estimates for the parotid glands vary widely, depending on which set of model parameter values are used. The Burman *et al.* parameters yield the lowest NTCPs. The approximately 4 Gy larger  $D_{EPIDflu}$  dose results in an increase in the predicted NTCP of  $\leq 5\%$  with one exception, the increase from 22 % to 40 % for the right parotid of Patient 3. Much higher parotid NTCPs result from the more recent (and statistically-based) parameter estimates. A modest but potentially significant increase of between 3 and 13 % is predicted with the Roesink *et al.* parameters, whereas the much steeper dose-response described by the Eisbruch *et al.* parameters lead to NTCP estimates up to 39 % higher (Patient 3, right parotid) when using  $D_{EPIDflu}$ .

Despite the apparent improvement in the 2-D comparisons obtained with the “point-source” model (Section 3.F.iii), the results in Tables 3.13, 3.14 and 3.15 suggest the use of  $D_{EPIDflu/pnt}$  instead of  $D_{EPIDflu}$  has little practical impact on the 3-D verifications.

VOI	model param. Ref. #	NTCP (%)			$\Delta$ NTCP (%)	
		$D_{TPS}$	$D_{EPIDflu}$	$D_{EPIDflu/pnt}$	$D_{EPIDflu} - D_{TPS}$	$D_{EPIDflu/pnt} - D_{TPS}$
<b>Patient 1</b>						
spinal cord	[9,10]	1	2	2	1	1
left parotid	[9,10]	0	1	1	1	1
	[12]	9	28	28	20	19
	[11]	16	22	22	6	6
right parotid	[9,10]	4	8	9	4	5
	[12]	60	79	82	19	23
	[11]	30	36	37	6	7
<b>Patient 2</b>						
spinal cord	[9,10]	0	0	0	0	0
left parotid	[9,10]	0	2	2	2	1
	[12]	12	45	38	32	26
	[11]	17	26	25	9	7
right parotid	[9,10]	78	83	84	5	6
	[12]	100	100	100	0	0
	[11]	77	80	80	3	3
<b>Patient 3</b>						
spinal cord	[9,10]	1	2	2	1	1
left parotid	[9,10]	22	39	40	18	18
	[12]	94	100	100	5	5
	[11]	44	56	56	13	14
right parotid	[9,10]	1	4	4	3	3
	[12]	23	62	63	39	40
	[11]	21	30	31	10	10

**Table 3.15.** Comparison of radiobiological modeling predictions of the NTCP based on TPS ( $D_{TPS}$ ) and EPID-based ( $D_{EPIDflu}$  or  $D_{EPIDflu/pnt}$ ) 3-D dose distributions for three clinical IMRT treatment plans.

## G. Comparison and summary of 2-D and 3-D IMRT verification procedures

The advantage of 3-D IMRT verification is that dosimetric uncertainties can be quantified directly with respect to anatomical volumes of interest, making possible a more direct evaluation of the clinical consequence of errors in TPS calculation. By comparison, the information provided by the simpler 2-D IMRT verification method is generally insufficient for such assessments. The beam-by-beam 2-D verification identifies potential problems by the presence of large “hot” (or “cold”) regions in the 2-D  $D_{EPID} - D_{TPS}$  dose difference map, or by mean difference and standard deviation

statistics for this map that fail specified criteria (*e.g.*  $\geq 2\%$  and  $4\%$  for the mean difference and standard deviation, respectively). The 2-D verification is thus effective at detecting larger errors, including procedural mistakes in the delivery – *e.g.* incorrect transfer of a MLC leaf sequence file to the linac – and planning – *e.g.* alignment of MLC leaf junctions with a critical structure – stages of an IMRT treatment. The 2-D method is ineffective, however, in quantifying the effect of smaller errors that, though present, do not arouse concern. For example, each field of the three IMRT patient treatments “passed” the 2-D verification tests, as supported by the average mean dose difference of  $-1.1\%$  and standard deviation of  $3.4\%$  reported for these verifications in Table 3.12. Nevertheless, the results in Tables 3.14 and 3.15 imply that these small errors may lead to considerably larger than expected cumulative dose errors of up to  $20\%$  in the critical structures, and further, that they may have potential clinical implications as to the acceptability of these treatments.

The tests detailed in Sections 3.F.i and 3.F.ii substantiate that the results of the 3-D verification method are not simply spurious. For the IMRT irradiation of an anthropomorphic head and neck phantom, the large TPS underestimate of the dose in the simulated critical structure suggested by the EPID-based 3-D dose was confirmed by a TLD measurement. Comparisons between  $D_{EPIDflu}$ ,  $D_{EPID}$ , and  $D_{TPS}$  BEV dose distributions in a water phantom for various open and IMRT fields were also instructive. There was reasonable agreement between the 2-D EPID-based method of calculating  $D_{EPID}$  from an EPID-derived fluence and an independent dose convolution, and the 3-D method of using EPID fluences and the TPS dose algorithm to generate  $D_{EPIDflu}$ . Much larger discrepancies were found between either of these two EPID-based doses and the TPS dose,  $D_{TPS}$ , particularly for small fields. These results support the conclusion that the large errors in  $D_{TPS}$  doses apparent in the 3-D IMRT verifications originate mainly from errors in the TPS’s modeling of the incident fluence. One potential source of error is the TPS’s inadequate modeling of the geometry of the MLC. Cadman *et al.*<sup>7</sup> cite the failure of their commercial TPS (Philips ADAC Pinnacle, Philips Medical Systems, Markham, ON) to model transmission through rounded leaf ends as the probable reason for their similar finding of TPS dose underestimation in critical structure regions.

Evidence that this may also be a serious limitation of our TPS is that the largest errors in the  $D_{TPS}$  BEV water phantom doses were observed for the  $1 \times 10 \text{ cm}^2$  field, where opposing leaf pairs defined the narrow dimension of this field. Cadman *et al.* also found that better agreement between TPS-calculated and measured doses could be achieved by making the gaps between each pair of MLC leaves 1.4 mm narrower than the original gap widths in the TPS-optimized IMRT step-and-shoot fields. So far, this potential solution has not been investigated at our clinic.

Despite the limitations of the 2-D IMRT verification method, it is still a useful clinical quality assurance tool. In its current implementation, our 3-D method is hampered by the excessive time required to perform the verification. Although the time necessary for acquisition of the required EPID images is not long ( $\sim \frac{1}{2}$  hour), the process of converting the calculated fluence modulation matrices to the appropriate “compensator” file format, and particularly the actual import of these “compensator” files on a beam-by-beam basis into the TPS is time-consuming and tedious. It is anticipated that the 3-D method could be streamlined considerably using a TPS with a “script-based” user interface. Such streamlining could make the 3-D IMRT verification method clinically feasible, and hence, an effective complement to the existing 2-D technique.

## H. References

<sup>1</sup>P. Stavrev, A. Niemierko, N. Stavreva, and M. Goitein, “The application of biological models to clinical data,” *Physica Medica* **17** (2), 71-82 (2001).

<sup>2</sup>Jeffrey V. Siebers, Jong Oh Kim, Lung Ko, Paul J. Keall, and Radhe Mohan, “Monte Carlo computation of dosimetric amorphous silicon electronic portal images,” *Medical Physics* **31** (7), 2135-2146 (2004).

<sup>3</sup>J. H. Chang, G. S. Mageras, C. C. Ling, and W. Lutz, “An iterative EPID calibration procedure for dosimetric verification that considers the EPID scattering factor,” *Medical Physics* **28** (11), 2247-2257 (2001).

<sup>4</sup>Faiz M. Khan, *The Physics of Radiation Therapy*, 3rd ed. (Lippincott Williams & Wilkins, Philadelphia, 2003).

<sup>5</sup>L. N. McDermott, R. J. W. Louwe, J. J. Sonke, M. B. van Herk, and B. J. Mijnheer, “Dose-response and ghosting effects of an amorphous silicon electronic portal imaging device,” *Medical Physics* **31** (2), 285-295 (2004).

- <sup>6</sup>M. B. Sharpe and J. J. Battista, "Dose calculations using convolution and superposition principles: the orientation of dose spread kernels in divergent x-ray beams," *Medical Physics* **20** (6), 1685-94 (1993).
- <sup>7</sup>P. Cadman, R. Bassalow, N. P. S. Sidhu, G. Ibbott, and A. Nelson, "Dosimetric considerations for validation of a sequential IMRT process with a commercial treatment planning system," *Physics in Medicine and Biology* **47** (16), 3001-3010 (2002).
- <sup>8</sup>G. Ibbott, A. Nelson, D. Followill, P. Balter, and W. Hanson, "An anthropomorphic head and neck phantom for evaluation of intensity modulated radiation therapy," <http://rpc.mdanderson.org/rpc> (2002).
- <sup>9</sup>C. Burman, G. J. Kutcher, B. Emami, and M. Goitein, "Fitting of Normal Tissue Tolerance Data to an Analytic-Function," *International Journal of Radiation Oncology Biology Physics* **21** (1), 123-135 (1991).
- <sup>10</sup>B. Emami, J. Lyman, A. Brown, L. Coia, M. Goitein, J. E. Munzenrider, B. Shank, L. J. Solin, and M. Wesson, "Tolerance of Normal Tissue to Therapeutic Irradiation," *International Journal of Radiation Oncology Biology Physics* **21** (1), 109-122 (1991).
- <sup>11</sup>A. Eisbruch, R. K. Ten Haken, H. M. Kim, L. H. Marsh, and J. A. Ship, "Dose, volume, and function relationships in parotid salivary glands following conformal and intensity-modulated irradiation of head and neck cancer," *International Journal of Radiation Oncology Biology Physics* **45** (3), 577-587 (1999).
- <sup>12</sup>J. M. Roesink, M. A. Moerland, J. J. Battermann, G. J. Hordijk, and C. H. J. Terhaard, "Quantitative dose-volume response analysis of changes in parotid gland function after radiotherapy in the head-and-neck region," *International Journal of Radiation Oncology Biology Physics* **51** (4), 938-946 (2001).

## Chapter 4: TCP-NTCP Estimation Module

This chapter discusses a computer module used to estimate, using current radiobiological models, the TCP (tumor control probability) and NTCP (normal tissue complication probability) values resulting from radiotherapy treatment plans. Thus, the focus of this chapter is the *application* of radiobiological modeling. A more elaborate discussion of fundamental radiobiological modeling concepts, and some studies exploring current topics of interest to the further development of radiobiological models, are presented in the next chapter (Chapter 5).

### A. Introduction

Radiotherapy treatment plans are assessed by evaluating the 3-D dose distributions calculated by a treatment planning system (TPS). Typically, the evaluation process includes: 1) looking at the dose distribution superimposed on images of the patient anatomy; and 2) examining DVHs (dose-volume histograms), which are 1-D representations of 3-D dose information, for each organ or tumor volume of interest. With these methods of assessment, acceptance or rejection of a plan relies on an implicit estimation of the TCP and NTCP arising from the dose distribution. This estimation is based on clinical experience with respect to appropriate target doses and corresponding dose-volume constraints. The advent of more sophisticated radiotherapy techniques such as intensity-modulated radiotherapy (IMRT) has led to more complex and heterogeneous dose distributions, making such implicit evaluations more difficult. For example, different treatment plans may lead to dose distributions having similar gross dose measures (such as mean dose), but characterized by DVHs with very different shapes. To determine the best plan in this case, clinicians may need to rely on relatively vague notions of dose-volume characteristics of different tissues.

Clearly, a natural application of radiobiological modeling to radiotherapy is the ranking of treatment plans, via a more explicit calculation of TCP and NTCP values using models that automatically incorporate the available clinical data regarding the dose-volume characteristics of different tissues. Unfortunately, the predictive capabilities of

current radiobiological models in this regard are still limited.<sup>1,2</sup> Presently there is still insufficient clinical data on the dose-response characteristics of human tissues and tumors on which to base reliable estimates of model parameters. This precludes the use of model predictions as a primary evaluative tool. However, such predictions are still a valuable complement to clinical experience. Further, as a result of increased archiving of 3D dose distributions and corresponding treatment outcomes, the quality and quantity of clinical data has begun to improve significantly in the last few years. Since this will surely enhance the reliability of model predictions, it is plausible that radiobiological modeling will play an important role in treatment plan evaluation and optimization in the future.<sup>3</sup>

We developed a convenient software tool for estimating the TCP or NTCP arising from differential (frequency) dose volume histograms (DDVHs).<sup>4</sup> The program, TCP\_NTCP\_CALC, was designed to amalgamate relevant current radiobiological modeling knowledge, and make it accessible to clinicians, treatment planners, and researchers. It serves the following functions: 1) as an aid in the prospective evaluation of rival treatment plans, by allowing evaluation and comparison of different model predictions; and 2) as an analysis tool in the retrospective study of radiotherapy treatments that may help establish or repudiate the predictive capabilities of different model/parameter sets.

During the development of this software, we became aware of a software package (BIOPLAN) designed with a similar intent published by Sanchez-Nieto and Nahum.<sup>5</sup> Although the two packages share some similarities, a number of differences also exist. For example, our module includes the Critical Volume (CV) NTCP model<sup>6-8</sup> and the recent Zaider-Minerbo/LQ TCP model<sup>9</sup> which are not available in BIOPLAN. TCP\_NTCP\_CALC also includes several different parameter databases, and provides a convenient method of archiving (and using) newly published parameter databases. Thus this additional software is a useful complement or alternative.

## **B. Methods**

### ***i. Radiobiological Models***

In general, clinical dose-response data only have sufficient diversity to support the use of relatively simple radiobiological models; use of complex models with many

parameters typically results in significant parameter correlation, and ambiguity in biological interpretation. Our NTCP and TCP calculation module incorporates a total of four radiobiological models. Included are two NTCP models: the Lyman model, and individual-based and population-based variants of the Critical Volume (CV) model; and two TCP models: a two-parameter Poisson-based model, and a model employing linear-quadratic cell kill and the formalism developed by Zaider and Minerbo<sup>9</sup> to account for repopulation. The simple Lyman and Poisson models have been most frequently applied in the analysis of normal tissue complication and tumor response data, respectively. The CV NTCP and the Zaider-Minerbo TCP models are slightly more complex, but are founded on more specific biological descriptions. The four models are briefly discussed in the following paragraphs, and the parameters used in each of the models are summarized in Table 4.1.

NTCP Model	param.	descriptor of:	TCP Model	param.	descriptor of:
<b>Lyman</b>	$n$	dose-volume relationship	<b>Poisson</b>	$D_{50}$	position of dose-response
	$m$	slope of dose-response		$\gamma_{50}$	slope of dose-response
	$D_{50}$	position of dose-response			
<b>CV (individual)</b>	$\mu_{cr}$	critical relative volume	<b>Zaider-Minerbo LQ</b>	$N$	no. of tumor clonogens
	$N$	no. of FSUs in organ		$\alpha, \beta$	radiosensitivity – LQ parameters
	$\alpha$	cellular radiosensitivity		$\lambda$	repopulation rate
	$N_0$	no. of cells in FSU		$n$	no. of fractions in treatment
<b>CV (population)</b>	$\mu_{cr}$	critical volume			
	$\sigma$	population variation			
	$D_{50}^{FSU}$	position of FSU dose-response			
	$\gamma_{50}^{FSU}$	slope of FSU dose-response			

**Table 4.1.** A list of the parameters and their description for each of the models used in the module. Abbreviations: FSU = functional sub-unit, CV=Critical Volume, LQ = linear-quadratic.

a. Lyman (Sigmoidal Dose Response) NTCP model

The Lyman model<sup>10</sup> describes the sigmoidal dose-response curve of normal tissues using the following probit form,

$$NTCP = \Phi\left(\frac{EUD - D_{50}}{mD_{50}}\right), \quad (4.1)$$

where  $\Phi(x)$  is the probit function,

$$\Phi(x) = \frac{1}{\sqrt{2\pi}} \int_{-\infty}^x \exp(-t^2/2) dt = \frac{1}{2} \left[ 1 + \operatorname{erf}\left(\frac{x}{\sqrt{2}}\right) \right], \quad (4.2)$$

with  $x = (EUD - D_{50})/mD_{50}$ . In Eq. (4.1),  $EUD$  is the equivalent uniform dose, which represents the dose that if delivered uniformly to the entire organ would produce the same effect as the given heterogeneous dose distribution, as specified by the DVH. Here it is assumed that the  $EUD$  is equal to a generalized mean dose ( $GMD$ ), calculated from the dose-volume pairs  $\{D_i, v_i\}$  of the DDVH using:

$$GMD = \left( \sum_i v_i D_i^{1/n} \right)^n. \quad (4.3)$$

For the Lyman model, the above method of DVH reduction, which reduces a full DVH to a single dose ( $GMD$ ) delivered to the entire volume, is equivalent<sup>11,12</sup> to the ‘‘Kutcher-Burman’’ reduction method,<sup>13</sup> which reduces a DVH to a reference dose delivered to an effective fractional volume. Other methods of reducing dose-volume histograms to a single dose or volume parameter have been proposed. The work of Cozzi *et al.*<sup>14</sup> suggested that most current DVH reduction schemes are somewhat error-prone, as they can lead to DVH reductions inconsistent with the expected biological effect. The ‘‘Kutcher-Burman’’ (KB) method was found to be one of the more robust of the available DVH reduction schemes.

The Lyman model has three parameters,  $n$ ,  $m$  and  $D_{50}$ :  $n$  determines the dose-volume dependence of a tissue and thus accounts for differences in tissue architecture;  $m$  controls the slope of the dose-response curve (in the case of homogeneous irradiation); and  $D_{50}$  represents the dose at which there is a 50% chance of complication, and thus dictates the position of the dose-response curve. Though largely phenomenological, the

Lyman model can be interpreted as predicting the NTCP for a population where individuals each have a threshold-like dose-response behaviour, and the different values of the dose threshold within the population are normally distributed.

*b. Critical Volume (CV) NTCP model*

The Critical Volume (CV) model<sup>6,7</sup> is based on the premises that organs are composed of functional sub-units (FSUs), and that organ function is compromised when a certain critical fraction ( $\mu_{cr}$ ) of these FSUs are damaged. For a uniformly irradiated organ with  $N$  FSUs and a reserve capacity of  $L-1$  FSUs (*i.e.*  $\mu_{cr} = L/N$ ), the probability of complication can be expressed mathematically as,

$$NTCP = \sum_{M=L}^N \frac{N!}{M!(N-M)!} p_{FSU}^M(D) (1-p_{FSU}(D))^{N-M}, \quad (4.4)$$

where  $p_{FSU}(D)$  is the probability of damage to an FSU after receiving a dose  $D$ . Since the number of FSUs is always quite large, the cumulative binomial distribution in Eq. (4.4) can be approximated by a cumulative normal distribution,<sup>15</sup>

$$NTCP = \Phi \left( \frac{\sqrt{N}(p_{FSU}(D) - \mu_{cr})}{\sqrt{p_{FSU}(D)(1-p_{FSU}(D))}} \right), \quad (4.5)$$

where the  $\Phi$  (probit) function is as defined in Eq. (4.2). For the case of a heterogeneously irradiated organ, the probability of complication becomes,

$$NTCP = \Phi \left( \frac{\sqrt{N} \left( \sum_i v_i p_{FSU}(D_i) - \mu_{cr} \right)}{\sqrt{\sum_i v_i p_{FSU}(D_i) (1-p_{FSU}(D_i))}} \right). \quad (4.6)$$

Eq. (4.6) assumes that the total damage to the organ can be treated as the sum of damage to independent sub-volumes. In Eq. (4.6), the sum  $\sum_i v_i p_{FSU}(D_i)$  can be identified as the mean relative damaged volume,  $\bar{\mu}_d$ . For our implementation of this CV model, the probability of damage to an FSU is calculated using,

$$p_{FSU}(D) = (1 - e^{-\alpha D})^{N_0}. \quad (4.7)$$

The parameters  $\alpha$  and  $N_0$  describe the cellular radiosensitivity and the number of cells in the FSU, respectively, and it is assumed that the FSU is only irreparably damaged when all cells are killed.

The above CV model is appropriate for description of the dose-response of an individual patient; clinical data, however, describe dose-response averaged over a population of individuals. We have thus incorporated in our module a “population” variant of the CV model<sup>8</sup> which takes into account inter-patient variability in normal tissue dose-response. This CV model assumes that the NTCP for an individual is step-like,

$$NTCP_{ind} = \begin{cases} 1 & \bar{\mu}_d \geq \mu_{cr} \\ 0 & \bar{\mu}_d < \mu_{cr} \end{cases}, \quad (4.8)$$

*i.e.* a complication will occur (and only occur) if the mean relative damaged volume is greater than or equal to the critical relative volume. Using the DDVH to calculate  $\bar{\mu}_d$ , we now assume that the damage to an FSU can be described by a probit ( $\Phi$ ) function parametrized using position and slope parameters,  $D_{50}^{FSU}$  and  $\gamma_{50}^{FSU}$ :

$$\bar{\mu}_d = \sum_i v_i P_{FSU}(D_i) = \sum_i v_i \Phi \left( \sqrt{2\pi} \gamma_{50}^{FSU} \ln \frac{D_i}{D_{50}^{FSU}} \right). \quad (4.9)$$

The “population-averaged” CV model is then formulated by further assuming that inter-patient variability is limited to the critical relative volume (mean =  $\mu_{cr}$ ), and that values for this parameter are log-log normally distributed in the population with a standard deviation of  $\sigma$  ( $\sigma \approx -\sigma_{\mu_{cr}} / (\mu_{cr} \ln \mu_{cr})$ ). It can be shown that  $NTCP_{pop}$  can then be represented by a probit function,<sup>8</sup>

$$NTCP_{pop} \approx \Phi \left( \frac{-\ln(-\ln \bar{\mu}_d) + \ln(-\ln \mu_{cr})}{\sigma} \right), \quad (4.10)$$

which is the form that we used for calculation purposes.

### *c. TCP model based on Poisson statistics*

TCP models generally rely on the assumption that tumor control requires the killing of all tumor clonogens. Poisson statistics predict that the probability of this occurring is

$$TCP = \exp(-N p_s(D)), \quad (4.11)$$

where  $N$  is the initial number of clonogens and  $p_s(D)$  is the cell survival fraction after a dose  $D$ . If it is assumed that cell survival can be described by single-hit mechanics,

$$p_s(D) = \exp(-\alpha D), \quad (4.12)$$

the expression in Eq. (4.11) can be re-written in terms of the two parameters describing the dose and normalized slope at the point of 50 % probability of control,  $D_{50}$  and  $\gamma_{50}$ :

$$TCP = \left(\frac{1}{2}\right)^{\exp[2\gamma_{50}(1-D/D_{50})/\ln 2]}. \quad (4.13)$$

Using the assumption of independent sub-volumes, for the case of heterogeneous irradiation, the overall probability of tumor control is the product of the probabilities of killing all clonogens in each tumor sub-volume described by the DDVH,

$$TCP = \prod_i TCP(D_i, v_i). \quad (4.14)$$

Thus, for a given DDVH  $\{D_i, v_i\}$ , the TCP can be calculated using the following two parameter TCP formula:

$$TCP = \left(\frac{1}{2}\right)^{\sum_i v_i \exp[2\gamma_{50}(1-D_i/D_{50})/\ln 2]}. \quad (4.15)$$

The above formula originates from an attempt to predict the TCP for an individual patient from a mechanistic perspective. However, because of its relative simplicity, Eq. (4.13) (or Eq. (4.15) for the case of a heterogeneous tumor dose) is often conveniently used to fit clinical data describing the tumor response of a population of individuals. In this case, the parameters  $D_{50}$  and  $\gamma_{50}$  are phenomenological in nature.

#### *d. TCP model incorporating radiobiological data*

Since the application of Eq. (4.15) is mainly phenomenological, we believed it would be useful to include a second TCP model that is parametrized in terms of fundamental cellular radiation response characteristics. Recently, Zaider and Minerbo<sup>9</sup> derived a conceptually robust expression for tumor control probability that incorporates the effect of tumor repopulation. The original Zaider-Minerbo expression, valid for any temporal protocol of dose delivery, has been adapted for the case of a fractionated

delivery with varying time intervals between fractions by Stavreva *et al.*<sup>16</sup> This adapted expression predicts that the TCP after the delivery of  $n$  fractions is,

$$TCP = \left[ 1 - \frac{p_s(T_n)e^{\lambda T_n}}{\left( 1 + p_s(T_n)e^{\lambda T_n} \sum_{k=1}^{n-1} \frac{1}{p_s(T_k)} \left[ e^{-\lambda T_{k+1}} - e^{-\lambda T_k} \right] \right)} \right]^N, \quad (4.16)$$

where  $\lambda$  is the rate of cellular repopulation,  $T_k$  is the time between the  $k^{\text{th}}$  fraction and the first fraction, and  $p_s(T_k)$  is the cell survival after the  $k^{\text{th}}$  fraction. Here cell survival was predicted using the familiar linear-quadratic (LQ) model. Assuming that there is complete repair of sub-lethal cellular damage between fractions, the LQ prediction of cell survival after the  $k^{\text{th}}$  fraction is,

$$p_s(T_k) = \exp \left( -\alpha \left( \frac{k}{n} D \right) - \frac{\beta \left( \frac{k}{n} D \right)^2}{k} \right), \quad (4.17)$$

where  $\alpha$  and  $\beta$  are cellular radiosensitivity parameters,  $D$  is the total dose delivered in the  $n$ -fraction treatment, and it is assumed that the dose delivered in each fraction is the same. To treat the case of heterogeneous irradiation, Eq. (4.16) is used in conjunction with Eq. (4.14), with each  $TCP(D_i, v_i)$  in Eq. (4.14) being calculated by evaluating Eq. (4.16) after making the substitution  $N \rightarrow Nv_i$ , and using  $D \rightarrow D_i$  in Eq. (4.17).

## ii. Parameter Databases

One of the main purposes of the TCP\_NTCP\_CALC program is to provide a convenient means of accessing and archiving current and future radiobiological knowledge as it pertains to treatment plan evaluation. The program contains parameter databases for three of the models described above: the Lyman NTCP model, the CV NTCP model (“population” variant only), and the Poisson TCP model. For each of these three models there are two databases: a “default” one which can not be altered by the user, and a “user” database, for which the user is allowed to add and delete database entries via a menu-driven interface. Each database entry includes the following data: model name, organ/endpoint or tumor/grade descriptor, parameter values (and

corresponding confidence intervals if desired), and descriptors of the parameter database and the clinical data on which it is based.

Although there are published parameter estimates for the “individual” CV model for a few single organs, a comprehensive database of parameter estimates for a large number of normal tissues is not available. Thus no databases for this model are included in our module. However, if the user is more familiar with or prefers the “individual” CV model, the user has the option of using this model by specifying their own parameters.

There are no estimates of the various parameters used in the Zaider-Minerbo/LQ TCP model for clinical tumor response data. Again, however, users may utilize the Zaider-Minerbo/LQ model by specifying their own parameter values. This may be valuable when investigating the sensitivity of TCP predictions to parameter uncertainties (e.g. in the values of the LQ radiosensitivity parameters,  $\alpha$  and  $\beta$ ), and the effects of repopulation defined with parameter  $\lambda$ .

#### *a. Lyman databases*

For normal tissues, the first and still largest compilation of dose-response data is that published by Emami *et al.*<sup>17</sup> in 1991. This data provides estimates of up to six dose-volume points – doses leading to 5 and 50% complication rates for irradiation of one-third, two-thirds and all of an organ – for many different normal tissue types. Based on this data, estimates of the Lyman model parameters for 27 of these normal tissues were provided by Burman *et al.*<sup>18</sup> This parameter set comprises the “default” Lyman database in our module.

Until recently, works estimating normal tissue complications have almost exclusively relied on the Burman/Emami Lyman parameter set. Unfortunately, the Emami *et al.* data are not statistical in nature, being based on limited data and estimates made by clinicians as to appropriate dose values;<sup>17</sup> as a result, uncertainties in the parameter values are indeterminate, as are the corresponding uncertainties in the calculated NTCPs. The development of 3D treatment planning systems and the resulting potential for archival of 3D dose distributions with treatment outcome has much improved the quality of clinical data sets, making them more amenable to radiobiological analysis. In recent years, a number of works have provided parameter estimates, including statistical uncertainties, for several different normal tissues. Recent Lyman

model parameter estimates include those for the parotid gland,<sup>19-21</sup> the heart,<sup>22</sup> the lung,<sup>23-25</sup> and the liver.<sup>26,27</sup> For further details (e.g. treatment techniques, parameters) about the clinical data on which each of these parameter estimates are based, the reader is referred to the original papers. These parameter sets have been included in the “user” Lyman database, so that the user can delete them if desired, e.g. if the user prefers a given parameter set for a specific organ.

#### *b. Critical Volume (“population”) databases*

The default database for the population-averaged CV model incorporates the parameters published by Stavrev *et al.*<sup>8</sup> for sixteen types of normal tissue. Since these estimates are again based on the Emami *et al.* data, no parameter uncertainties are available. Stavrev *et al.* noted that the CV model was flexible enough to describe the data not only of “traditional” CV organs such as liver and lung, but also of organs such as spinal cord and stomach that are believed to have a more “critical element” architecture. However, they caution that though the CV model has a biological foundation, extracted parameter values should be considered phenomenological, owing perhaps to a large degree of parameter correlation inherent in the model. There are a few works that provide estimates for the CV model for single organs. Parameters (including uncertainties) for this particular variant of the CV model based on liver data published by Jackson *et al.*<sup>6</sup> were also extracted in Ref. [8], and have been included in the “user” CV database of our program.

#### *c. Poisson TCP databases*

A large collection of tumor dose-response parameters ( $D_{50}$  and  $\gamma_{50}$ ) extracted from single- and multi-institution tumor data sets from a variety of sources for many different tumor sites and grades has been compiled and published by Okunieff *et al.*<sup>28</sup> Sixty-two of the Okunieff *et al.* entries are included in our “default” Poisson database.  $D_{50}$  and  $\gamma_{50}$  values for non-small-cell lung cancer (NSCLC) from Willner *et al.*<sup>29</sup> and for prostate cancer from Cheung *et al.*<sup>30</sup> and Levegrün *et al.*<sup>31</sup> are included in the “user” database.

### *iii. Program Architecture*

The TCP\_NTCP\_CALC software has been developed in the MATLAB (The Mathworks Inc., Natick, USA) programming environment, and has been designed for use on a Windows-based computer (Pentium 3 or faster recommended) with MATLAB (version 6 or greater) software installed. TCP\_NTCP\_CALC has a menu-driven user interface, designed for convenient, straight-forward use. The framework of the program is simple: the user inputs a differential dose-volume histogram (DDVH); based on user selection from parameter databases or from user input, appropriate parameters for the available radiobiological models are retrieved; NTCP or TCP calculations are performed based on these parameter values; a convenient display of the relevant model predictions and the DVH are provided. Further details of the program functionality are provided below.

#### *a. Input*

The program accepts DDVHs in either of two formats:

- 1) the DVH file output from the HELAX-TMS (Nucletron B.V., Veenendaal, The Netherlands) commercial treatment planning system, or
- 2) a two-column text file of  $\{D_i, v_i\}$  values.

DDVHs can be evaluated either on an individual basis, in which case a single DDVH file is specified by the user, or as a group, in which case the user need only specify the directory in which the DDVH files are located. The former option (“single-mode”) is suited for using the program as an aid in treatment plan evaluation, while the latter option (“group-mode”) is convenient when retrospectively comparing actual treatment outcomes of a cohort of patients with radiobiological model predictions.

#### *b. Parameter Selection/Retrieval*

After selecting the input DDVH file(s), a menu prompts the user to 1) identify the file as either a normal tissue or a tumor DDVH file, and to 2) choose between using parameters stored in the parameter databases or specifying their own values for one or more of the models for calculation of the NTCPs or TCPs. For normal tissues, the user can access the parameter databases in one of two ways. The first method is to select an

organ type from a list of the normal tissues present in the databases. If the DDVH is in HELAX-TMS format, the program will attempt to automatically identify the organ and ask for user confirmation. After determining the organ type, the program retrieves all available parameter estimates in the databases for this organ, which may include parameters for different complication end-points and for one or both of the Lyman and CV (“population”) models. The user can also access the normal tissue databases in a second way, by selecting any number of entries from listings of the four normal tissue databases (Lyman-default, Lyman-user, CV-default, CV-user). For tumors, user selection from the databases is facilitated by listings of the 62 Okunieff *et al.* entries entered in the default Poisson TCP database, as well as the entries residing in the user database.

As mentioned above, the user can instead choose to specify their own parameters for any of the models: Lyman, CV (“population”), CV (“individual”), Poisson TCP, and Zaider-Minerbo/LQ. Confidence intervals for each of the parameters and the confidence level (*e.g.* 68% or 95%) can be also be entered. This option allows users to test the sensitivity of radiobiological model predictions of NTCP or TCP to different parameter sets and/or parameter uncertainties.

### *c. Calculation of the NTCP / TCPs*

Using the retrieved parameters and the DDVH  $\{D_i, v_i\}$ , NTCPs are calculated using Eqs. (4.1) and (4.3) for the Lyman model, Eqs. (4.6) and (4.7) for the individual CV model, and Eqs. (4.9) and (4.10) for the population CV model. TCP predictions are based on Eq. (4.15) for the Poisson model, and Eqs. (4.14), (4.16), and (4.17) for the Zaider-Minerbo/LQ model.

When parameter uncertainties are available, the corresponding uncertainties in the TCP or NTCP are estimated using the following Monte-Carlo method. A large number (500) of sets of parameter values are generated by randomly sampling a probability distribution of values for each parameter of the model. A distribution of NTCP (or TCP) values is then generated by evaluating the NTCP (or TCP) for each of the sampled parameter sets. The standard deviation of this NTCP (or TCP) distribution is calculated to furnish a measure of the uncertainty in the predicted NTCP (or TCP) value. As described by Schilstra *et al.*,<sup>32</sup> the probability distribution for each parameter should be

related to the value of the likelihood function in a maximum likelihood fitting analysis. The shape of the likelihood contour is, however, unavailable in this case, since only the confidence interval and confidence level is specified. We thus assumed that parameter values were normally distributed, equivalent to assuming that the likelihood function has a normal shape with respect to the model parameters. The confidence interval and level are used to determine the width of the distribution. Since the above assumption is not always valid, the provided NTCP (or TCP) uncertainties should be treated as approximate indicators of the degree of confidence one should have in the different model predictions.

*d. Calculation of the probability distribution of the expected number of complications*

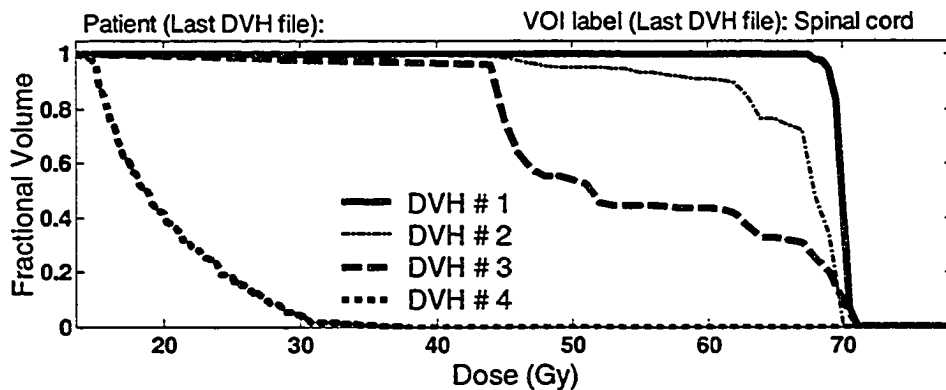
When the user chooses to input a group of DDVH files for analysis (“group-mode” of the program), in addition to calculating the mean NTCP (or TCP) for this cohort, the program will also calculate the probability of observing any number of complications (or controls). This provides an additional and more in-depth characterization of the radiobiological modeling predictions than use of the mean NTCP (or TCP) alone. The complication (or tumor control) probability distribution is generated using a Monte-Carlo method outlined in Ref. [8]. For a cohort with  $n_{pat}$  patients, for each DDVH file a corresponding model prediction of the NTCP is calculated,  $NTCP_i$  ( $i=1$  to  $n_{pat}$ ), and a random number between zero and one is generated,  $RN_i$ . The random numbers are used to represent pseudo-data of a clinical trial with  $n_{pat}$  patients. A complication for patient  $i$  is assigned if  $RN_i < NTCP_i$ , and thus the number of complications in this trial is equal to the number of times this inequality is true for the  $n_{pat}$  random numbers. This procedure is then repeated a large number of times (10,000 trials) to generate a probability distribution for the number of complications. This probability distribution provides another useful means of retrospectively comparing model predictions to actual treatment outcomes. The described Monte-Carlo method of calculating this distribution is a much faster surrogate for explicit calculation of the corresponding multi-variate binomial probability distribution.

*e. Display and output*

The main output of the TCP\_NTCP\_CALC is a figure containing the following items:

- 1) a plot of the cumulative DVH. In “group-mode” analysis, the mean cumulative DVH is displayed.
- 2) text describing the location of the DDVH file (or directory) being analyzed.
- 3) a table which includes: calculated NTCP/TCP predictions for each of the models for which parameters were available/specified; descriptors of the parameter database and the clinical data relevant to each model prediction; database descriptors of the tissue/tumor for each prediction.

More than one DVH and corresponding set of model predictions can be displayed in one figure, if desired. Fig. 4.1 is representative of the output figure for a case where the user has chosen to display DVHs for a prostate target, and the normal tissues of the bladder, rectum and spinal cord. The figure conveniently summarizes the analysis, and is suitable for printing. This may be useful for archiving or consultation purposes. Analysis results are also output to a text file.



DVH File 1: C:\USERS\TMP\DDVHs\PTV.DVH  
 2: C:\USERS\TMP\DDVHs\BLADDER.DVH  
 3: C:\USERS\TMP\DDVHs\RECTUM.DVH  
 4: C:\USERS\TMP\DDVHs\spinalcord.DVH

DVH #	Model	TCP/NTCP (%)	Param. DB	Data Src.	DB descriptor
1	Poisson	84.44	Okunieff95	various	Prostate: T3, multi
2	Lyman	6.71	Burman91	Emami91	Bladder
2	CV (pop)	6.58	Stavrev01	Emami91	bladder
3	Lyman	7.14	Burman91	Emami91	Rectum
4	Lyman	0.07	Burman91	Emami91	spinal cord
4	CV (pop)	0.25	Stavrev01	Emami91	spinal cord

Figure 4.1. Example output from the program for a case where the user has chosen to display and analyze DDVHs for the bladder, rectum, spinal cord, and a prostate tumor.

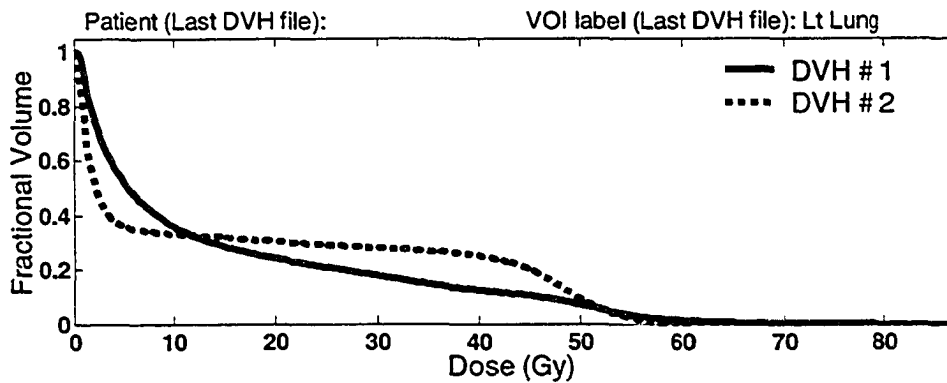
When using “group-mode” analysis, TCP\_NTCP\_CALC will also display an additional figure showing the predicted probability distribution for the number of complications in the cohort of patients described by the supplied set of DDVHs. This probability distribution is calculated and can be displayed for each of the models/parameter sets evaluated.

## C. Results and Discussion

A few brief examples of potential uses of the TCP\_NTCP\_CALC module are demonstrated in this section.

### *i. Retrospective analysis of treatments for a cohort of patients*

The analysis of a group of DVHs corresponding to a cohort of patients treated with a given treatment technique is one useful application of the module. The display output for such an application is illustrated in Figs. 4.2 and 4.3. Fig. 4.2 shows the results of a comparison of the lung toxicity arising from two different breast-cancer treatment techniques – “five-field” and “wide-tangent”.<sup>33</sup> The same set of 16 patients was retrospectively planned using both techniques. In Fig. 4.2, the mean cumulative DVH for each technique is shown, and indicates that for this example, a larger fraction of the lung is exposed to both very small doses and to large doses with the “wide-tangent technique” (DVH #2): *e.g.* approximately 25% less lung is exposed to doses exceeding 5 Gy, but about 8% more lung is exposed to doses exceeding 40 Gy with the “wide-tangent” technique. For each set of DVHs, Fig. 4.2 also displays the mean NTCP model predictions based on Lyman parameter sets from four different sources<sup>18,23-25</sup> and one Critical Volume parameter set.<sup>8</sup> For the parameter sets shown, the estimated mean probability of lung pneumonitis ranges from 0.4 to 4.3 % for the “5-field” technique; a similar probability of pneumonitis is predicted with the “wide-tangent” technique, with corresponding mean NTCPs ranging from 0.4 to 4.0 %. For both techniques, the NTCP predictions based on the Emami *et al.* (Lyman and Critical Volume models) are appreciably lower than the complication probabilities estimated using more recently published Lyman parameter sets.



Patient (Last DVH file):  
 VOI label (Last DVH file): Lt Lung

DVH Directory 1: C:\USERS\TMP\DDVHs\LTLUNG\5FLD\  
 2: C:\USERS\TMP\DDVHs\LTLUNG\WIDET\

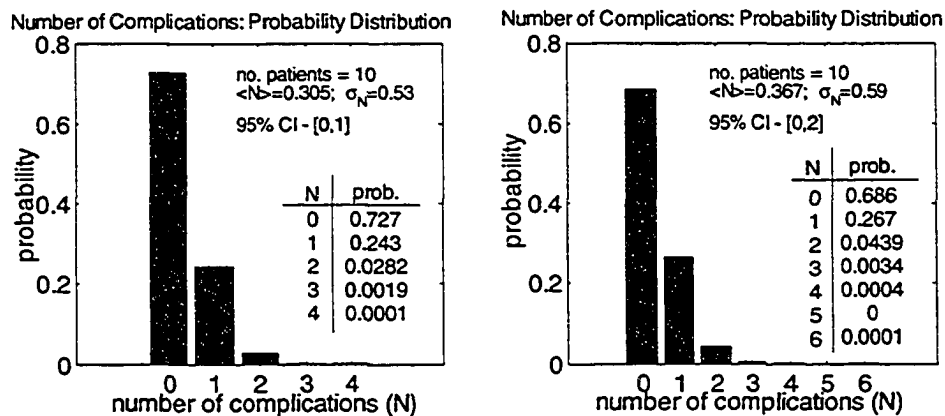
DVH #	Model	NTCP (%)	Param. DB	Data Src.	DB descriptor
1	Lyman	0.66	Burman91	Emami91	lung/pneumonitis
1	Lyman	1.82 ± 0.47	Kwa98	5 institute	lung/pneumonitis
1	Lyman	4.04 ± 31.53	Moiseenko03	Moiseenko03	lung/symp pneum
1	Lyman	0.21 ± 25.81	Moiseenko03	Moiseenko03	lung/symp fibrosis
1	Lyman	4.28 ± 3.55	Seppenw03	Seppenw03	lung/pneumonitis
1	CV (pop)	0.36	Stavrev01	Emami91	lung/pneumonitis
2	Lyman	0.50	Burman91	Emami91	lung/pneumonitis
2	Lyman	1.62 ± 0.45	Kwa98	5 institute	lung/pneumonitis
2	Lyman	3.19 ± 36.86	Moiseenko03	Moiseenko03	lung/symp pneum
2	Lyman	0.13 ± 36.16	Moiseenko03	Moiseenko03	lung/symp fibrosis
2	Lyman	4.04 ± 4.44	Seppenw03	Seppenw03	lung/pneumonitis
2	CV (pop)	0.37	Stavrev01	Emami91	lung/pneumonitis

Figure 4.2. Program output after analysis of lung DVHs generated from the retrospective treatment planning of a cohort of 16 breast-cancer patients using two different treatment techniques. DVH #1 (solid line) is the cumulative DVH (averaged over the 16 patients) for a “5-field” technique, while DVH #2 (dotted line) is the corresponding DVH for a “wide-tangent” technique. For each set of DVHs, radiobiological model predictions of the mean NTCP are displayed for a number of different parameter sets available in the literature.

As shown in Fig. 4.2, there are considerable uncertainties in the NTCP predictions based on the Moiseenko *et al.* and (to a lesser extent) the Seppenwoolde *et al.* Lyman model parameters. These parameters were derived from analyses of clinical data sets consisting of 55 and 382 patients, respectively. This once again underlines the challenge in generating precise radiobiological predictions: the statistics and diversity of clinical data are in general insufficient to define narrow confidence intervals for parameter estimates. The uncertainties in the NTCP predictions based on the Kwa *et al.* model parameters are significantly lower than the other error estimates. However, this is at least partly due to the fact that Kwa *et al.* fixed the parameter  $n = 1$ , which also led to tighter confidence intervals for the other two parameters,  $m$  and  $D_{50}$ . The validity of these NTCP predictions is thus implicitly dependent on the validity of the assumption that the

mean lung dose (*MLD*) is an accurate predictor of lung response to a heterogeneous dose delivery. Note also that the Kwa *et al.* NTCP predictions shown do not incorporate the offset of 0-11% in the NTCP reported in their work.

Fig. 4.3 shows the second program output, the predicted probability distribution of the number of complications, when a group of ten DDVHs describing dose distributions in the mandible is analyzed. For this normal tissue, the program database contains the Lyman and Critical Volume parameter sets based on the Emami *et al.* data. As shown, the complication distributions are similar for these two parameter sets: using the Lyman parameters, the program predicts probabilities of 73, 24 and 3 % for observing zero, one, and two or more complications; using the Critical Volume parameters, the corresponding probabilities are 69, 27, and 4 %. The mean, standard deviation, and 95% confidence interval of these distributions are also included in the output, and are as shown.

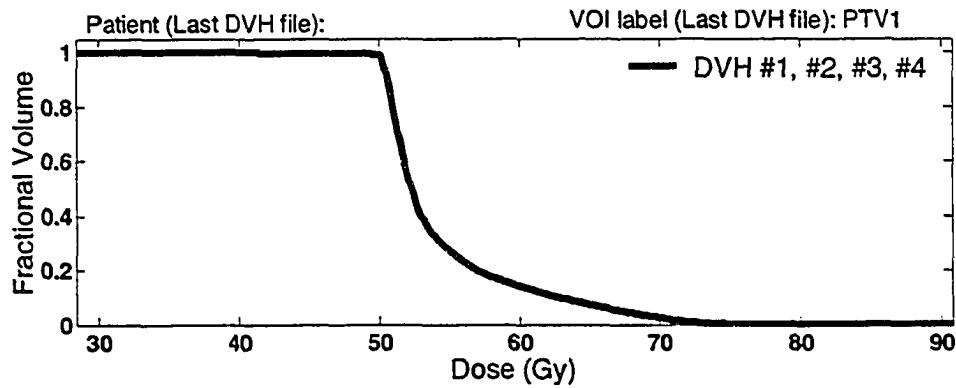


(a) Model/Database: Lyman / Burman91 (b) Model/Database: CV (pop) / Stavrev01

Figure 4.3. Program output displaying the distribution of the number of complications predicted from the DVHs for the mandible for a group of 10 patients based on two sets of radiobiological predictions based on the Emami *et al.*<sup>17</sup> data: (a) Lyman model, Burman *et al.*<sup>18</sup> parameters (b) "population" Critical Volume model, Stavrev *et al.*<sup>8</sup> parameters.

## *ii. Testing of the sensitivity of model predictions to parameter values*

The TCP\_NTCP\_CALC program is also useful to those seeking to test the sensitivity of model predictions to different model parameter values. Fig. 4.4 displays the program output for the case when a user has chosen to specify four sets of parameter values for the Zaider-Minerbo/LQ TCP model, in the analysis of a given tumor DDVH file. The first time the following parameters have been specified: LQ cellular radiosensitivity values of  $\alpha = 0.30 \text{ Gy}^{-1}$  and  $\beta = 0.03 \text{ Gy}^{-2}$  (i.e.  $\alpha/\beta = 10 \text{ Gy}$ );  $N = 10^6$  for the number of tumor clonogens;  $\lambda = 0.05 \text{ days}^{-1}$ , which corresponds to a potential doubling time  $\left(\ln 2/\lambda\right)$  of about 14 days; and  $n = 25$  fractions. These parameters lead to a predicted TCP of 91.5 %. For the second set of parameters, the radiosensitivity is reduced by 10 %, with values of  $\alpha = 0.27 \text{ Gy}^{-1}$  and  $\beta = 0.027 \text{ Gy}^{-2}$  being specified (all other parameters the same as the first set). This reduces the predicted TCP by 22 % to 69.5 %, demonstrating the considerable sensitivity of the TCP calculation to small changes or uncertainties in the cellular radiosensitivity. A similar reduction of 24 % in the TCP (to 67.5 %) is also predicted if instead of changing the radiosensitivity, the repopulation rate is doubled to  $\lambda = 0.10 \text{ days}^{-1}$  (parameter set #3). Use of the fourth set of parameter values –  $\alpha = 0.17 \text{ Gy}^{-1}$ ,  $\beta = 0.017 \text{ Gy}^{-2}$ ,  $N = 10^3$ ,  $\lambda = 0.05 \text{ days}^{-1}$ ,  $n = 25$  fractions – is used to describe a much smaller tumor with increased cellular radioresistance. The predicted TCPs of 91.2 % and 91.5 % for the fourth and first sets of parameters, respectively, are nearly the same. This indicates that the 1000-fold decrease in the size of the tumor can be offset by a reduction in the radiosensitivity parameters of only 43 %. Indirectly this also suggests, as has been observed in numerous radiobiological modeling works, that in a heterogeneous tumor, tumor response is determined mainly by the most radioresistant sub-population within the tumor.



DVH File      1: C:\USERS\TMP\DDVHs\PTV1.DVH  
 2: C:\USERS\TMP\DDVHs\ PTV1.DVH  
 3: C:\USERS\TMP\DDVHs\ PTV1.DVH  
 4: C:\USERS\TMP\DDVHs\ PTV1.DVH

DVH #	Model	TCP (%)	Param. DB	Data Src.	DB descriptor
1	Zaid-Min/LQ	91.49	user specified	N/A	$\alpha=0.30, N=10^6, \lambda=0.05$
2	Zaid-Min/LQ	69.54	user specified	N/A	$\alpha=0.27, N=10^6, \lambda=0.05$
3	Zaid-Min/LQ	67.53	user specified	N/A	$\alpha=0.30, N=10^6, \lambda=0.10$
4	Zaid-Min/LQ	91.20	user specified	N/A	$\alpha=0.17, N=10^3, \lambda=0.05$

Figure 4.4. Program output displaying TCP predictions for the same DDVH for four sets of user-specified parameters: (i)  $\alpha = 0.30 \text{ Gy}^{-1}$ ,  $\beta = 0.03 \text{ Gy}^{-2}$ ,  $N = 1e6$ ,  $\lambda = 0.05 \text{ days}^{-1}$ ,  $n = 25$  fractions; (ii) same as (i), but with slightly decreased cellular radiosensitivity,  $\alpha = 0.27 \text{ Gy}^{-1}$ ,  $\beta = 0.027 \text{ Gy}^{-2}$ ; (iii) same as (i), but with the rate of repopulation doubled,  $\lambda = 0.10 \text{ days}^{-1}$ ; (iv)  $\alpha = 0.17 \text{ Gy}^{-1}$ ,  $\beta = 0.017 \text{ Gy}^{-2}$ ,  $N = 1e3$ ,  $\lambda = 0.05 \text{ days}^{-1}$ ,  $n = 25$  fractions.

## D. Conclusion

An NTCP-TCP estimation module, TCP\_NTCP\_CALC, was developed which can be used as a research tool and as a clinical aid. Our module can assist in the evaluation of treatment plans by conveniently providing access to current radiobiological model predictions. It also provides a means of assessing the reliability and utility of common radiobiological models, both by facilitating comparison of model predictions (based on available clinical data) to actual clinical outcomes, and by testing of the sensitivity of model predictions to uncertainties in the model parameters.

## E. References

<sup>1</sup>M. Langer, S. S. Morrill, and R. Lane, "A test of the claim that plan rankings are determined by relative complication and tumor-control probabilities," *International Journal of Radiation Oncology Biology Physics* **41** (2), 451-7 (1998).

<sup>2</sup>V. Moiseenko, J. Battista, and J. Van Dyk, "Normal tissue complication probabilities: Dependence on choice of biological model and dose-volume histogram reduction

scheme," *International Journal of Radiation Oncology Biology Physics* **46** (4), 983-993 (2000).

<sup>3</sup>J. O. Deasy, A. Niemierko, D. Herbert, D. Yan, A. Jackson, R. K. Ten Haken, M. Langer, and S. Sapareto, "Methodological issues in radiation dose-volume outcome analyses: summary of a joint AAPM/NIH workshop," *Medical Physics* **29** (9), 2109-27 (2002).

<sup>4</sup>B. Warkentin, P. Stavrev, N. Stavreva, C. Field, and B. Fallone, "A TCP-NTCP estimation module using DVHs and known radiobiological models and parameter sets," *Journal of Applied Clinical Medical Physics* **5** (1), 50-63 (2004).

<sup>5</sup>B. Sanchez-Nieto and A. E. Nahum, "Bioplan: software for the biological evaluation of radiotherapy treatment plans," *Medical Dosimetry* **25** (2), 71-76 (2000).

<sup>6</sup>A. Jackson, G. J. Kutcher, and E. D. Yorke, "Probability of Radiation-Induced Complications for Normal-Tissues with Parallel Architecture Subject to Nonuniform Irradiation," *Medical Physics* **20** (3), 613-625 (1993).

<sup>7</sup>A. Niemierko and M. Goitein, "Modeling of Normal Tissue-Response to Radiation - the Critical Volume Model," *International Journal of Radiation Oncology Biology Physics* **25** (1), 135-145 (1993).

<sup>8</sup>P. Stavrev, A. Niemierko, N. Stavreva, and M. Goitein, "The application of biological models to clinical data," *Physica Medica* **17** (2), 71-82 (2001).

<sup>9</sup>M. Zaider and G. N. Minerbo, "Tumour control probability: a formulation applicable to any temporal protocol of dose delivery," *Physics in Medicine and Biology* **45** (2), 279-293 (2000).

<sup>10</sup>J. T. Lyman, "Complication Probability as Assessed from Dose Volume Histograms," *Radiation Research* **104** (2), S13-S19 (1985).

<sup>11</sup>A. Niemierko and M. Goitein, "Calculation of Normal Tissue Complication Probability and Dose-Volume Histogram Reduction Schemes for Tissues with a Critical Element Architecture," *Radiotherapy and Oncology* **20** (3), 166-176 (1991).

<sup>12</sup>J. O. Deasy, "Comments on the use of the Lyman-Kutcher-Burman model to describe tissue response to nonuniform irradiation," *International Journal of Radiation Oncology Biology Physics* **47** (5), 1458-1459 (2000).

<sup>13</sup>G. J. Kutcher and C. Burman, "Calculation of Complication Probability Factors for Non-Uniform Normal Tissue Irradiation - the Effective Volume Method," *International Journal of Radiation Oncology Biology Physics* **16** (6), 1623-1630 (1989).

- <sup>14</sup>L. Cozzi, F. M. Buffa, and A. Fogliata, "Comparative analysis of dose volume histogram reduction algorithms for normal tissue complication probability calculations," *Acta Oncologica* **39** (2), 165-171 (2000).
- <sup>15</sup>P. Stavrev, N. Stavreva, A. Niemierko, and M. Goitein, "Generalization of a model of tissue response to radiation based on the idea of functional subunits and binomial statistics," *Physics in Medicine and Biology* **46** (5), 1501-1518 (2001).
- <sup>16</sup>N. A. Stavreva, P. V. Stavrev, B. Warkentin, and B. G. Fallone, "Investigating the effect of cell repopulation on the tumor response to fractionated external radiotherapy," *Medical Physics* **30** (5), 735-742 (2003).
- <sup>17</sup>B. Emami, J. Lyman, A. Brown, L. Coia, M. Goitein, J. E. Munzenrider, B. Shank, L. J. Solin, and M. Wesson, "Tolerance of Normal Tissue to Therapeutic Irradiation," *International Journal of Radiation Oncology Biology Physics* **21** (1), 109-122 (1991).
- <sup>18</sup>C. Burman, G. J. Kutcher, B. Emami, and M. Goitein, "Fitting of Normal Tissue Tolerance Data to an Analytic-Function," *International Journal of Radiation Oncology Biology Physics* **21** (1), 123-135 (1991).
- <sup>19</sup>R. Scrimger, P. Stavrev, M. Parliament, C. Field, and H. Thompson, "Physical parameters to describe flow normal tissue complication probability (NTCP) for parotid gland irradiation with intensity-modulated radiotherapy (IMRT)." presented at the Canadian Association of Radiation Oncologists (CARO), Toronto, 2002.
- <sup>20</sup>A. Eisbruch, R. K. Ten Haken, H. M. Kim, L. H. Marsh, and J. A. Ship, "Dose, volume, and function relationships in parotid salivary glands following conformal and intensity-modulated irradiation of head and neck cancer," *International Journal of Radiation Oncology Biology Physics* **45** (3), 577-587 (1999).
- <sup>21</sup>J. M. Roesink, M. A. Moerland, J. J. Battermann, G. J. Hordijk, and C. H. J. Terhaard, "Quantitative dose-volume response analysis of changes in parotid gland function after radiotherapy in the head-and-neck region," *International Journal of Radiation Oncology Biology Physics* **51** (4), 938-946 (2001).
- <sup>22</sup>M. K. Martel, W. M. Sahijdak, R. K. Ten Haken, M. L. Kessler, and A. T. Turrisi, "Fraction size and dose parameters related to the incidence of pericardial effusions," *International Journal of Radiation Oncology Biology Physics* **40** (1), 155-161 (1998).
- <sup>23</sup>S. L. S. Kwa, J. V. Lebesque, J. C. M. Theuws, L. B. Marks, M. T. Munley, G. Bentel, D. Oetzel, U. Spahn, R. K. Ten Haken, R. E. Drzymala, J. A. Purdy, A. S. Lichter, and M. K. Martel, "Radiation pneumonitis as a function of mean lung dose: An analysis of pooled data of 540 patients," *International Journal of Radiation Oncology Biology Physics* **42** (1), 1-9 (1998).

- <sup>24</sup>V. Moiseenko, T. Craig, A. Bezjak, and J. Van Dyk, "Dose-volume analysis of lung complications in the radiation treatment of malignant thymoma: a retrospective review," *Radiotherapy and Oncology* **67** (3), 265-274 (2003).
- <sup>25</sup>Y. Seppenwoolde, J. V. Lebesque, K. de Jaeger, J. S. A. Belderbos, L. J. Boersma, C. Schilstra, G. T. Henning, J. A. Hayman, M. K. Martel, and R. K. Ten Haken, "Comparing different NTCP models that predict the incidence of radiation pneumonitis," *International Journal of Radiation Oncology Biology Physics* **55** (3), 724-735 (2003).
- <sup>26</sup>L. A. Dawson, D. Normolle, J. M. Balter, C. J. McGinn, T. S. Lawrence, and R. K. Ten Haken, "Analysis of radiation-induced liver disease using the Lyman NTCP model," *International Journal of Radiation Oncology Biology Physics* **53** (4), 810-821 (2002).
- <sup>27</sup>J. C. H. Cheng, J. K. Wu, C. M. Huang, H. S. Liu, D. Y. Huang, S. H. Cheng, S. Y. Tsai, J. J. M. Jian, Y. M. Lin, T. I. Cheng, C. F. Horng, and A. T. Huang, "Radiation-induced liver disease after three-dimensional conformal radiotherapy for patients with hepatocellular carcinoma: Dosimetric analysis and implication," *International Journal of Radiation Oncology Biology Physics* **54** (1), 156-162 (2002).
- <sup>28</sup>P. Okunieff, D. Morgan, A. Niemierko, and H. D. Suit, "Radiation dose-response of human tumors," *International Journal of Radiation Oncology Biology Physics* **32** (4), 1227-1237 (1995).
- <sup>29</sup>J. Willner, K. Baier, E. Caragiani, A. Tschammler, and M. Flentje, "Dose, volume, and tumor control predictions in primary radiotherapy of non-small-cell lung cancer," *International Journal of Radiation Oncology Biology Physics* **52** (2), 382-389 (2002).
- <sup>30</sup>R. Cheung, S. L. Tucker, L. Dong, and D. Kuban, "Dose-response for biochemical control among high-risk prostate cancer patients after external beam radiotherapy," *International Journal of Radiation Oncology Biology Physics* **56** (5), 1234-1240 (2003).
- <sup>31</sup>S. Levegrun, A. Jackson, M. J. Zelefsky, E. S. Venkatraman, M. W. Skwarchuk, W. Schlegel, Z. Fuks, S. A. Leibel, and C. C. Ling, "Risk-group dependence of dose-response for biopsy outcome after three-dimensional conformal radiation therapy of prostate cancer," *Radiotherapy and Oncology* **63** (1), 11-26 (2002).
- <sup>32</sup>C. Schilstra and H. Meertens, "Calculation of the uncertainty in complication probability for various dose-response models, applied to the parotid gland," *International Journal of Radiation Oncology Biology Physics* **50** (1), 147-158 (2001).
- <sup>33</sup>D. Severin, S. Connors, H. Thompson, S. Rathee, P. Stavrev, and J. Hanson, "Breast radiotherapy with inclusion of internal mammary nodes: A comparison of techniques with three-dimensional planning," *International Journal of Radiation Oncology Biology Physics* **55** (3), 633-644 (2003).

# Chapter 5: Investigations of Current Radiobiological Models

Studies involving current radiobiological models are presented in this chapter. The further development of such models will, it is hoped, lead to a greater integration of radiobiological considerations in radiotherapy treatment planning, aimed towards improved customization of patient treatments. This chapter is divided into three sections. The first (Section A) provides theoretical background about cell survival and dose response models that is necessary to understand the projects discussed in Sections B and C. Section A culminates with a description of our derivation of explicit expressions relating the shape (position and slope) of dose response curves to parameters describing fundamental radiobiological properties. The project presented in Section B examines the potential ambiguities in biological interpretation introduced by the population heterogeneity that is inherent in clinical data. In the final section (Section C), we endeavor to investigate the descriptive capabilities of the LQ model, and the importance of incorporation of dynamic tumor processes in TCP modeling, with respect to the description of fractionation effects.

## A. Theoretical Background: Cell Survival and Dose Response Relationships

### *i. Linear Quadratic Cell Survival Model*

The linear quadratic (LQ) model employs the following equation to predict the probability of cell survival,  $p_s$ , after delivery of a dose  $D$  in a single fraction:

$$p_s = \exp(-\alpha D - \beta D^2). \quad (5.1)$$

The parameters  $\alpha$  and  $\beta$  are used to characterize the intrinsic radiosensitivity of a particular cell type. On a conventional survival curve, where  $\log(p_s)$  is plotted versus dose, the  $\alpha$  term will describe the initial linear part of the curve, while  $\beta$  will produce a downward bend in the curve. In general, the shape of cell survival curves for mammalian cell lines can be well described by the LQ equation.<sup>1,2</sup>

A fairly conventional mechanistic interpretation of the LQ model is as follows. The  $\alpha$  term describes a “single-hit” mechanism where an un-repairable lethal cell lesion (*e.g.* a DNA double-strand break) results from dose deposited by a single particle track. The number of such lethal lesions is assumed to be proportional to the amount of dose deposited. The  $\beta$  term is associated with lethal damage resulting from the combined effect of two sub-lethal lesions. Assuming that the production of sub-lethal lesions is also proportional to dose, the probability of a lethal lesion arising from the interaction of sub-lethal lesions will be proportional to the square of the dose. The value of  $\beta$  is thus related to the efficiency with which sub-lesions are produced per unit dose, and the likelihood that sub-lethal lesions will interact to produce lethal damage.

There is still considerable debate about how correctly the LQ model can be identified with a simple biological interpretation,<sup>1,3-5</sup> such as that given above. As discussed in (for *e.g.*) Refs. [2,6,7], more complex cell survival models formulated on specific biological assumptions can often be approximated by an LQ expression under certain conditions. It is further noted that Brenner *et al.*<sup>8</sup> have found that the LQ prediction of fractionation dependencies is consistent with the predictions of more complex mechanistic models. An example of a more complex mechanistic model is the lethal-potentially lethal (LPL) model of Curtis.<sup>9</sup> This model again incorporates two types of damage, lethal and potentially lethal lesions (PLLs). The PLLs can either be repaired, or be converted into lethal lesions by improper repair involving interaction of two PLLs. Individual parameters are used to describe the proportionality constant between dose and the number of PLLs produced, the rate of enzymatic repair of PLLs, and the rate of interaction of the PLLs to form lethal lesions.<sup>6</sup> Using a low-dose approximation of the LPL model, these three parameters can be related to the LQ  $\beta$  term.<sup>6</sup> An alternative explanation of the LQ shape of cell survival curves that differs conceptually from the simplified interpretation given in the previous paragraph is provided by repair saturation models.<sup>2</sup> In these models, in contrast to the LPL model, the interaction of potentially lethal lesions is not a mechanism of cell death. Rather, cell death results from a single type of lesion produced by single-hit mechanics. A certain fraction of these lesions can be enzymatically repaired, and initially, at lower doses, the rate of this repair is proportional to the amount of damage. However, the repair capacity is limited – *e.g.* due

to the limited number of available repair enzymes. Therefore, as the dose increases, the rate of repair will no longer be able to keep pace with the accumulation of the damage. Eventually, the rate of repair will saturate – *i.e.* reach a constant value. Thus, in these models, it is the saturation of cellular repair that dictates the downward bend of the survival curve (and hence the LQ  $\beta$  value). For convenience, when referring to the mechanism of the LQ model in the following paragraphs, we will adopt a simplified LQ interpretation involving interaction of sub-lethal lesions.

Though its applicability to radiotherapy is still disputed by some,<sup>10</sup> the LQ model is likely the most commonly used cell survival model in radiotherapy. In addition to its mathematical simplicity, use of the LQ expression is also very convenient because it leads to a simple parameterization of fractionation effects<sup>11</sup> in terms of  $\alpha/\beta$  ratios. If it is assumed that the percentage cell survival for each dose fraction is independent of the dose delivered in prior fractions, the LQ model predicts that the net cell survival after delivery of a total dose  $D$  in  $n$  fractions of dose  $d$  is:

$$p_s = \prod_{i=1}^n \exp(-\alpha d - \beta d^2) = \exp\left(-\alpha D - \frac{\beta}{n} D^2\right) = \exp\left(-\alpha D \left(1 + \frac{\beta D}{\alpha n}\right)\right). \quad (5.2)$$

This assumption is equivalent to presuming that all sub-lethal lesions are repaired between fractions, *i.e.* that no sub-lethal lesions remain from previous fractions that can interact with the sub-lethal lesions produced by the current fraction. From Eq. (5.2) it is clear that as the number of fractions increases, the cell survival increases in comparison to the delivery of the same dose  $D$  in a single fraction, which would produce cell survival of  $\exp(-\alpha D - \beta D^2)$ . The size of this fractionation effect is larger for smaller  $\alpha/\beta$  (larger  $\beta/\alpha$ ) values. The response of most tumor types can be characterized by a large  $\alpha/\beta$  value (*e.g.* 10 Gy), while the late effects of normal tissues are typically described by smaller (*e.g.* 0.5 – 6 Gy [Ref. 12,13])  $\alpha/\beta$  values. Exploiting these differences between tumor response and normal tissue late effects is the basis of fractionation in radiotherapy. A convenient concept developed to compare the doses delivered using different fractionation regimens, is that of Biologically Effective Dose (*BED*), which can be defined as:<sup>11</sup>

$$BED = -\frac{\ln(p_s)}{\alpha}. \quad (5.3)$$

Thus, for the LQ expression of Eq. (5.2), the *BED* becomes,

$$BED = D \left( 1 + \frac{d}{\alpha / \beta} \right), \quad (5.4)$$

In principle, the suitability of different fractionation regimes can be assessed by calculating how the *BED* values for the tumor and surrounding normal tissues change when the dose per fraction,  $d = \frac{D}{n}$ , is varied.

The expression in Eq. (5.2) represents the simplest variant of the LQ model for fractionated treatments. It is time-independent, and therefore is unable to incorporate any dynamic cell processes. A common extension of this LQ model is one that introduces an explicit time-dependence into the repair mechanism, by assuming that the repair of sub-lethal lesions is governed by the rate equation,

$$\frac{dN_{SL}}{dt} = -\frac{1}{\tau} N_{SL}, \quad (5.5)$$

where  $N_{SL}$  is the number of sub-lethal lesions and  $\tau$  is the repair rate constant. It can be shown<sup>14,15</sup> that the cell survival for fractionated treatments then becomes,

$$p_s = \exp \left( -\alpha D - \beta \sum_{i=1}^n d_i^2 - 2\beta \sum_{i=1}^{n-1} \sum_{j=i+1}^n d_i d_j \exp(-\Delta T_{ij} / \tau) \right), \quad (5.6)$$

where  $d_i$  is the dose for fraction  $i$  and  $\Delta T_{ij}$  is the time interval between fractions  $i$  and  $j$ . The third term in the exponent in Eq. (5.6) describes additional cell death resulting from the interaction of newly produced sub-lethal lesions with sub-lethal lesions remaining from previous fractions. Eq. (5.6) is thus referred to as the “incomplete repair” LQ (LQ-IR) model. When the time intervals between fractions are very large compared to the repair rate constant, this incomplete repair term in Eq. (5.6) will be negligible, and Eq. (5.6) reduces to the time-independent form in Eq. (5.2). Since estimates of  $\tau$  for normal tissue late reactions are of the order of a few hours,<sup>12</sup> use of Eq. (5.2) is typically assumed to be sufficient when applied to most conventional fractionation schemes, where there is at least one day between fractions. However, the LQ-IR model may be necessary for hyper-fractionated regimens, where multiple fractions are delivered in the same day. Consideration of the time-dependence of repair mechanism is particularly important for treatments involving continuous dose delivery, such as brachytherapy, where repair is on-

going during the irradiation. However, in this case, the form of the LQ model is significantly different than that in Eq. (5.6), and is given by,

$$p_s(D) = \exp(-\alpha D - \beta G(t)D^2), \quad (5.7)$$

where, if  $T$  is the total time of irradiation, then <sup>15</sup>

$$G(t) = \frac{2}{(T/\tau)^2} [(T/\tau) - 1 + \exp(-T/\tau)]. \quad (5.8)$$

Additional modifications to the simplified LQ model of Eq. (5.2) have also been proposed to account for dynamic processes other than repair. For example, an attempt to incorporate cellular repopulation into the LQ model is represented by the following expression:<sup>11,16</sup>

$$p_s = \exp\left(-\alpha D - \frac{\beta}{n} D^2 + \lambda \max(T - T_{lag}, 0)\right), \quad (5.9)$$

where  $\max(T - T_{lag}, 0)$  is equal to  $T - T_{lag}$  if  $T > T_{lag}$ , and 0 otherwise. In Eq. (5.9),  $\lambda$  is the rate of repopulation, which can also be expressed in terms of the potential doubling time ( $T_p$ ):  $\lambda = \ln 2/T_p$ . The  $T_{lag}$  parameter is used to accommodate a potential delay between start of treatment and the onset of tumor repopulation.<sup>17,18</sup> Often this type of repopulation term is *not* included in the cell survival expression used in conjunction with a tissue dose response model. Instead, an LQ expression such as Eq. (5.2) or (5.6) is used, and repopulation is incorporated explicitly in the equation describing the tissue dose response model. Repopulation in tumor response models is discussed in more detail in Section 5.C.ii.

Efforts have also been made to incorporate into the LQ model the dynamic resensitization processes of reoxygenation and redistribution,<sup>19</sup> the remaining two of the four “R’s” of radiotherapy, in addition to repair and repopulation. Resensitization processes can alter the radiosensitivity characteristics of a tumor and/or normal tissue. The potential effects of redistribution of the percentages of cells in the different stages of the cell cycle stem from the dependence of a cell’s radiosensitivity on where it is in the cycle: *e.g.* cells undergoing mitosis are more sensitive to radiation than those in the S stage of the cell cycle, when DNA is actively being synthesized. The reoxygenation of initially hypoxic tumor cells is advantageous for tumor control because of the increased

radiosensitivity of cells within oxygenated environments. Reoxygenation occurs when the outer layers of the tumor are killed and removed during radiotherapy, allowing oxygen to diffuse to previously inaccessible inner layers of the tumor. In Section 5.C.ii.c, we discuss use of a time-dependent expression for the  $\alpha$  radiosensitivity parameter to accommodate potential reoxygenation effects.

One consequence of modifying the simple time-independent LQ expression of Eq. (5.2) to include dynamic cell processes is that fractionation effects can no longer be characterized solely by the single parameter, the  $\alpha/\beta$  ratio. For example, if the LQ expression incorporating repopulation, Eq. (5.9), is used, the corresponding expression for the *BED* becomes:

$$BED = D \left( 1 + \frac{d}{\alpha/\beta} \right) - \frac{\lambda}{\alpha} \max(T - T_{lag}, 0). \quad (5.10)$$

In this case, the *BED* is dependent on  $\alpha/\beta$ ,  $\alpha$ ,  $\lambda$ , and  $T_{lag}$ . Thus, if repopulation is not negligible, description of fractionation effects requires knowledge of not only  $\alpha/\beta$ , but also of the cellular radiosensitivity parameter  $\alpha$  and the constants  $\lambda$  and  $T_{lag}$  characterizing cell proliferation.<sup>11</sup>

## ii. Tumor and Normal Tissue Dose Response Models

### a. Phenomenological Expressions

Plots of the dose response probability  $P$  (either tumor control probability, TCP, or normal tissue complication probability, NTCP) as a function of dose ( $D$ ) are characterized by a sigmoidal shape. As discussed by Bentzen and Tucker,<sup>20</sup> this sigmoidal shape is often described by one of three types of mathematical expression: Poisson, logit, or probit. An example of each of these expressions is shown below.

$$\text{Poisson:} \quad P(D) = \left( \frac{1}{2} \right)^{\exp \left[ \frac{2}{\ln 2} \gamma_{50} \left( 1 - \frac{D}{D_{50}} \right) \right]} \quad (5.11a)$$

$$\text{Logit:} \quad P(D) = \Phi \left[ -\sqrt{2\pi} \gamma_{50} \left( 1 - \frac{D}{D_{50}} \right) \right] \quad (5.11b)$$

$$\text{where } \Phi(x) = \frac{1}{\sqrt{2\pi}} \int_{-\infty}^x \exp(-t^2/2) dt$$

$$\text{Probit: } P(D) = \frac{1}{1 + \exp\left[4\gamma_{50}\left(1 - \frac{D}{D_{50}}\right)\right]} \quad (5.11c)$$

Note that the Poisson expression in Eq. (5.11a) is the same as the TCP model described in Eq. (4.13), and that the logit expression is identical to the Lyman NTCP model for a uniform irradiation, with Eq. (5.11b) being equal to Eq. (4.1) with  $m = \frac{1}{\sqrt{2\pi} \gamma_{50}}$ . In

each of the three expressions, the shape of the probability curve is determined by two parameters, one each describing the position and slope of the curve. The position parameter  $D_{50}$  is the dose at which the probability is equal to 50 %. The slope  $\theta$  of a probability curve at dose  $D$  is,

$$\theta(D) = \frac{dP(D)}{dD}, \quad (5.12)$$

while the *normalized slope*,<sup>21</sup>  $\gamma$ , is defined as the slope  $\theta$  multiplied by the dose  $D$ ,

$$\gamma(D) = D \frac{dP(D)}{dD}, \quad (5.13)$$

and thus has units of (*e.g.*) Gy. The slope parameter  $\gamma_{50}$  utilized in the expressions of Eq. (5.11) is the normalized slope evaluated at the  $D_{50}$  dose:

$$\gamma_{50} = D_{50} \left. \frac{dP(D)}{dD} \right|_{D=D_{50}}. \quad (5.14)$$

The sigmoidal shapes described by the three expressions in Eq. (5.11) are not identical. This is shown in Fig. 5.1, where probability curves for each of the three models are shown for identical  $D_{50}$  and  $\gamma_{50}$  values. However, in general, the shape of actual dose response data can be reasonably well described by any one of the three models.<sup>22</sup>

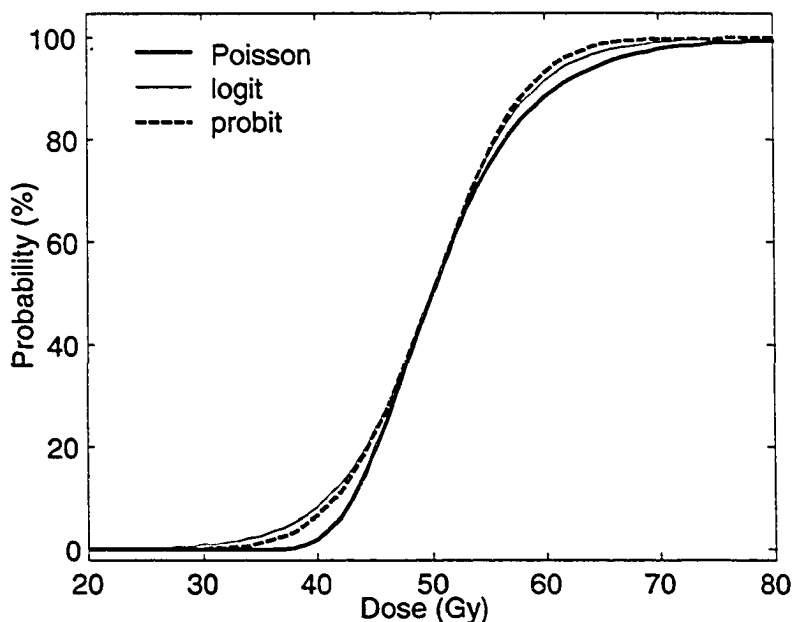


**Figure 5.1.** Probability curves as calculated with the Poisson, logit, and probit models defined in Eq. (5.11) and using identical parameter values of  $D_{50} = 50$  Gy and  $\gamma_{50} = 3$  Gy.

### *b. Mechanistic Models*

The expressions in Eq. (5.11) are essentially phenomenological. However, it is often desirable to use more mechanistic dose response models, since these may directly relate dose response probabilities to inherent radiobiological characteristics of tissues. This is particularly important for potential customization of radiotherapy treatments, since at least in theory, radiobiological characteristics such as cellular radiosensitivity and tumor doubling times can be estimated using radiobiological assays. The incorporation of patient-specific values for parameters such as  $\alpha$ ,  $\beta$  and  $\lambda$  in mechanistic models would then lead to predictions of the NTCP and/or TCP values resulting for a given treatment that are valid for an individual patient. A few mechanistic models are briefly described below for the simple case of uniform dose delivery to an organ or tumor.

The Critical Volume (CV) NTCP model<sup>23-25</sup> was introduced in Chapter 4. To review, it can be approximated by a probit-type equation,

$$NTCP = \Phi \left( \frac{\sqrt{N}(p_{FSU}(D) - \mu_{cr})}{\sqrt{p_{FSU}(D)(1 - p_{FSU}(D))}} \right), \quad (5.15)$$

where  $N$  is the number of functional sub-units (FSUs) comprising the organ and  $\mu_{cr}$  is the critical fraction of the volume that must be damaged before a complication occurs. Assuming that an FSU is irreparably damaged only if all of the  $N_0$  cells contained in the FSU are killed, the probability of FSU damage,  $p_{FSU}(D)$ , can be calculated using,

$$p_{FSU}(D) = (1 - p_s(D))^{N_0}. \quad (5.16)$$

The dependence of the NTCP on cellular radiosensitivity parameters is introduced by using one of the LQ cell survival expressions, *e.g.*  $p_s(D) = \exp\left(-\alpha D - \frac{\beta}{n} D^2\right)$ .

A special case of the CV model occurs when it is assumed that an organ has *no* reserve capacity, and thus a normal tissue complication occurs if any of the  $N$  FSUs are damaged. Such an organ is said to have a Critical Element (CE) architecture.<sup>24</sup> Formally, an NTCP expression for a CE organ can be derived by setting  $L = 1$  (where  $L - 1$  represents the number of reserve FSUs) in the basic CV model expression given by Eq. (4.4) in Chapter 4.<sup>26</sup> The resulting equation can be simplified to yield the following formula describing the CE “model” prediction of the NTCP,

$$NTCP = 1 - (1 - p_{FSU}(D))^N, \quad (5.17)$$

where  $(1 - p_{FSU}(D))^N$  can be identified with the probability of survival of all  $N$  FSUs. In Eq. (5.17), the probability of FSU incapacitation can again be described by Eq. (5.16) in conjunction with one of the LQ cell survival models (*e.g.* Eq. (5.2)).

Based on the assumption that all  $N$  tumor clonogens must be killed to achieve tumor control, a “binomial” formulation of a TCP model is given by,

$$TCP = (1 - p_s(D))^N. \quad (5.18)$$

The probability of cell survival can again be described by one of the LQ expressions. To incorporate repopulation in the TCP model, Eq. (5.9) could be implemented to describe  $p_s(D)$ . An alternative method of accommodating repopulation is to make the replacement  $N \rightarrow N \exp(\lambda T)$  in Eq. (5.18) to yield,

$$TCP = (1 - p_s(D))^{N \exp(\lambda T)}, \quad (5.19)$$

with  $p_s(D)$  being described by an LQ expression *without* repopulation, e.g. Eq. (5.2) or Eq. (5.6). In Eq. (5.19), it is assumed that there is no delay between the start of treatment and the onset of repopulation (*i.e.*  $T_{lag} = 0$ ), or equivalently that  $T$  represents the duration of treatment after the onset of repopulation (*i.e.*  $T - T_{lag} \rightarrow T$ ). A Poisson approximation to the binomial expression of Eq. (5.19) is,

$$TCP = \exp(-N \exp(\lambda T) p_s(D)). \quad (5.20)$$

This becomes,

$$TCP = \exp\left(-N \exp\left(-\alpha D - \frac{\beta}{n} D^2 + \lambda T\right)\right), \quad (5.21)$$

when Eq. (5.2) is explicitly substituted for  $p_s(D)$ . Though convenient, the simple method of including repopulation in a TCP model represented by Eqs. (5.19) and (5.21) does suffer from some limitations. These limitations and an improved TCP model incorporating repopulation are discussed in Section 5.C.ii.

### iii. Expressions relating $D_{50}$ and $\gamma_{50}$ to Radiobiological Parameter Values

We derived expressions explicitly relating the radiobiological model parameters present in the mechanistic models outlined above to the position and slope parameters  $D_{50}$  and  $\gamma_{50}$  often used to describe the shape of dose-response curves. The first step in deriving a relation for  $D_{50}$  is to set the NTCP or TCP expression equal to one-half, and then to solve for the corresponding value of the cell survival,  $p_s(D_{50})$ . Thus for the binomial and Poisson TCP model cases, the equations,

$$\text{Binomial TCP:} \quad 0.5 = (1 - p_s(D_{50}))^{N \exp(\lambda T)}$$

$$\text{Poisson TCP:} \quad 0.5 = \exp(-N \exp(\lambda T) p_s(D_{50})),$$

are solved to yield:

$$\text{Binomial TCP:} \quad p_s(D_{50}) = 1 - (0.5)^{1/(N \exp(\lambda T))} \quad (5.22a)$$

$$\text{Poisson TCP:} \quad p_s(D_{50}) = \frac{\ln 2}{N \exp(\lambda T)}. \quad (5.22b)$$

For the CE and CV NTCP models, the equations to be solved are:

$$\text{CE NTCP:} \quad 0.5 = 1 - (1 - p_{FSU}(D_{50}))^N$$

$$\text{CV NTCP: } 0.5 = \Phi \left( \frac{\sqrt{N}(p_{FSU}(D_{50}) - \mu_{cr})}{\sqrt{p_{FSU}(D_{50})(1 - p_{FSU}(D_{50}))}} \right).$$

This leads to expressions for  $p_{FSU}(D_{50})$ ,

$$\text{CE NTCP: } p_{FSU}(D_{50}) = 1 - (0.5)^{1/N} \quad (5.23a)$$

$$\text{CV NTCP: } p_{FSU}(D_{50}) = \mu_{cr}, \quad (5.23b)$$

where the latter CV expression makes use of the fact that  $\Phi(0) = 0.5$ . Using Eq. (5.16), expressions for  $p_s(D_{50})$  can then be derived:

$$\text{CE NTCP: } p_s(D_{50}) = 1 - \sqrt[n]{1 - (0.5)^{1/N}} \quad (5.24a)$$

$$\text{CV NTCP: } p_s(D_{50}) = 1 - \sqrt[n]{\mu_{cr}}. \quad (5.24b)$$

For all four model expressions (binomial and Poisson TCP, CE and CV NTCP), the time-independent LQ expression (Eq. (5.2)) was used to describe cell survival, which can be re-written as,

$$\frac{\beta}{n} D^2 + \alpha D + \ln(p_s(D)) = 0. \quad (5.25)$$

Evaluating Eq. (5.25) at the dose  $D_{50}$  and then solving for  $D_{50}$  yields,

$$D_{50} = \frac{n}{2\beta} \left( -\alpha + \sqrt{\alpha^2 - 4 \frac{\beta}{n} \ln(p_s(D_{50}))} \right). \quad (5.26)$$

The  $D_{50}$  relevant for each of the four models can be obtained by substitution of the appropriate  $p_s(D_{50})$  expression (Eq. (5.22a), (5.22b), (5.24a), or (5.24b)).

To calculate expressions relating  $\gamma_{50}$  to radiobiological parameters, we first calculate the (un-normalized) slope (Eq. (5.12)) for each of the models. First, taking the derivative of Eq. (5.19) with respect to dose yields the slope for the binomial TCP model,

$$\text{Binomial TCP: } \theta(D) = N \exp(\lambda T) \frac{TCP(D)}{(1 - p_s(D))} \left( -\frac{dp_s(D)}{dD} \right). \quad (5.27)$$

The derivative of the LQ cell survival expression (Eq. (5.2)) can be expressed as:

$$\frac{dp_s(D)}{dD} = -p_s(D) \left( \alpha + \frac{2\beta}{n} D \right). \quad (5.28)$$

Evaluating Eq. (5.27) at  $D = D_{50}$  and using Eq. (5.28) and Eq. (5.22a), the slope can be simplified to:

$$\text{Binomial TCP: } \theta_{50} = \frac{N \exp(\lambda T)}{2} \left( 2^{1/(N \exp(\lambda T))} - 1 \right) \left( \alpha + \frac{2\beta}{n} D_{50} \right). \quad (5.29)$$

By taking the derivative of Eq. (5.21), it is easy to show that the slope for the Poisson TCP model is,

$$\text{Poisson TCP: } \theta(D) = -TCP(D) \ln(TCP(D)) \left( \alpha + \frac{2\beta}{n} D \right), \quad (5.30)$$

which for  $D = D_{50}$  becomes

$$\text{Poisson TCP: } \theta_{50} = \frac{\ln 2}{2} \left( \alpha + \frac{2\beta}{n} D_{50} \right). \quad (5.31)$$

Continuing with the CE NTCP model, the derivative of Eq. (5.12) gives the slope:

$$\begin{aligned} \text{CE NTCP: } \theta(D) &= N \frac{(1 - p_{FSU}(D))^N}{(1 - p_{FSU}(D))} \left( \frac{d p_{FSU}(D)}{dD} \right) \\ &= N \frac{(1 - NTCP(D))}{(1 - NTCP(D))^{1/N}} \left( \frac{d p_{FSU}(D)}{dD} \right). \end{aligned} \quad (5.32)$$

Eq. (5.16) and Eq. (5.28) can be used to derive the relation,

$$\frac{d p_{FSU}(D)}{dD} = N_0 p_{FSU}(D) \frac{p_s(D)}{(1 - p_s(D))} \left( \alpha + \frac{2\beta}{n} D \right). \quad (5.33)$$

Then substituting expressions for  $p_{FSU}(D_{50})$  (Eq. (5.23a)) and  $p_s(D_{50})$  (Eq. (5.24a)) into Eq. (5.33), the following expression for  $\theta_{50}$  can be derived from Eq. (5.32):

$$\text{CE NTCP: } \theta_{50} = \frac{N N_0}{2} (2^{1/N} - 1) \left( \frac{1}{\sqrt[N_0]{1 - (0.5)^{1/N}}} - 1 \right) \left( \alpha + \frac{2\beta}{n} D_{50} \right). \quad (5.34)$$

Finally, the slope of a dose response curve described by the CV model is

$$\text{CV NTCP: } \theta(D) = \frac{d\Phi(x)}{dD} = \frac{1}{\sqrt{2\pi}} \exp(-x^2) \frac{dx}{dD}, \quad (5.35)$$

where,  $x = \frac{\sqrt{N}(p_{FSU} - \mu_{cr})}{\sqrt{p_{FSU}(1 - p_{FSU})}}$ , and

$$\frac{dx}{dD} = \frac{\sqrt{N}}{\sqrt{p_{FSU}(1 - p_{FSU})}} \left( \frac{d p_{FSU}}{dD} \right) \left[ 1 - \left( \frac{p_{FSU} - \mu_{cr}}{2 p_{FSU}(1 - p_{FSU})} \right) (1 - 2 p_{FSU}) \right]. \quad (5.36)$$

Eqs. (5.23b), (5.24b), and (5.33) facilitate the calculation of the slope at the dose corresponding to a 50 % probability of complication, yielding:

$$\text{CV NTCP: } \theta_{50} = N_0 \sqrt{\frac{N \mu_{cr}}{2\pi(1-\mu_{cr})}} \left( \frac{1}{\sqrt[N_0]{\mu_{cr}}} - 1 \right) \left( \alpha + \frac{2\beta}{n} D_{50} \right). \quad (5.37)$$

Expressions for the normalized slope,  $\gamma_{50}$ , for each model are obtained by multiplying the un-normalized slope,  $\theta_{50}$  – Eq. (5.29), (5.31), (5.34) or (5.37) – by the expressions for  $D_{50}$  – Eq. (5.26) in combination with Eq. (5.22a), (5.22b), (5.24a), or (5.24b).

The final expressions for  $D_{50}$  and  $\gamma_{50}$  are tabulated in Table 5.1. Their use is appropriate when characterizing the position and slope of a dose response curve comprised of points that all correspond to the same number of fractions,  $n$ , *i.e.* the dose per fraction varies for each point describing a different total dose  $D$ . Equivalent expressions can also be derived for the case when all dose points correspond to the same dose per fraction,  $d$ , *i.e.* the number of fractions varies for the different dose points. In this case, the appropriate time-independent LQ model expression is  $p_s(D) = \exp(-D(\alpha + \beta d))$ . Also, since  $d$  is a constant, the equations corresponding to

Eqs. (5.26) and (5.28) would become,  $D_{50} = -\frac{\ln(p_s(D_{50}))}{\alpha + \beta d}$  and  $\frac{dp_s}{dD} = -p_s(\alpha + \beta d)$ . If

tumor repopulation is to be included in the TCP expressions, the implicit dependence of dose on the treatment time  $T$  would also require consideration, since the different dose points would likely correspond to different values of both  $T$ , as well as  $n$ . The  $D_{50}$  and  $\gamma_{50}$  expressions for both cases – (1) when  $n$  is constant, and (2) when  $d$  is constant (assuming no repopulation) – along with further details of the derivations, are reported in our published work, Ref. [27]. When the number of FSUs ( $N$ ) and the number of cells in an FSU ( $N_0$ ) are large, the approximation  $\lim_{x \rightarrow \infty} x(a^{1/x} - 1) = \ln a$ , with  $x$  representing  $N$  or  $N_0$ , can be used to render expressions for the CE and CV NTCP models that are in slightly more convenient forms than those provided in Table 5.1. These expressions are also included in Ref. [27].

Model	$D_{50}$
Binomial TCP	$\frac{n}{2\beta} \left( \sqrt{\alpha^2 - \frac{4\beta}{n} \ln(1 - (0.5)^{1/(N \exp(\lambda T))})} - \alpha \right)$
Poisson TCP	$\frac{n}{2\beta} \left( \sqrt{\alpha^2 - \frac{4\beta}{n} \ln\left(\frac{\ln 2}{N \exp(\lambda T)}\right)} - \alpha \right)$
Critical Element NTCP	$\frac{n}{2\beta} \left( \sqrt{\alpha^2 - \frac{4\beta}{n} \ln\left(1 - \sqrt[N_0]{1 - (0.5)^{1/N}}\right)} - \alpha \right)$
Critical Volume NTCP	$\frac{n}{2\beta} \left( \sqrt{\alpha^2 - \frac{4\beta}{n} \ln\left(1 - \sqrt[N_0]{\mu_{cr}}\right)} - \alpha \right)$
Model	$\gamma_{50}$
Binomial TCP	$\frac{n N \exp(\lambda T)}{4\beta} \left( 2^{1/(N \exp(\lambda T))} - 1 \right) \left( \sqrt{\alpha^2 - \frac{4\beta}{n} \ln(1 - (0.5)^{1/(N \exp(\lambda T))})} \right) \times \left( \sqrt{\alpha^2 - \frac{4\beta}{n} \ln(1 - (0.5)^{1/(N \exp(\lambda T))})} - \alpha \right)$
Poisson TCP	$\frac{n \ln 2}{4\beta} \left( \sqrt{\alpha^2 - \frac{4\beta}{n} \ln\left(\frac{\ln 2}{N \exp(\lambda T)}\right)} \right) \left( \sqrt{\alpha^2 - \frac{4\beta}{n} \ln\left(\frac{\ln 2}{N \exp(\lambda T)}\right)} - \alpha \right)$
Critical Element NTCP	$\frac{n N N_0}{4\beta} \left( 2^{1/N} - 1 \right) \left( \frac{1}{\sqrt[N_0]{1 - (0.5)^{1/N}}} - 1 \right) \left( \sqrt{\alpha^2 - \frac{4\beta}{n} \ln\left(1 - \sqrt[N_0]{1 - (0.5)^{1/N}}\right)} \right) \times \left( \sqrt{\alpha^2 - \frac{4\beta}{n} \ln\left(1 - \sqrt[N_0]{1 - (0.5)^{1/N}}\right)} - \alpha \right)$
Critical Volume NTCP	$\frac{n N_0}{2\beta} \sqrt{\frac{N \mu_{cr}}{2\pi(1 - \mu_{cr})}} \left( \frac{1}{\sqrt[N_0]{\mu_{cr}}} - 1 \right) \left( \sqrt{\alpha^2 - \frac{4\beta}{n} \ln\left(1 - \sqrt[N_0]{\mu_{cr}}\right)} \right) \times \left( \sqrt{\alpha^2 - \frac{4\beta}{n} \ln\left(1 - \sqrt[N_0]{\mu_{cr}}\right)} - \alpha \right)$

**Table 5.1.** Expressions relating the position and slope parameters,  $D_{50}$  and  $\gamma_{50}$ , for dose response curves calculated using the binomial TCP, Poisson TCP, Critical Element NTCP, or Critical Volume NTCP models to the radiobiological parameters for each of these models. The expressions are valid assuming that cell survival is described by the time-independent LQ model (Eq. (5.2)), and that all dose points in the dose response curves correspond to the same number of fractions,  $n$ .

The expressions in Table 5.1 are useful if one wants to determine the change in the position or slope of a TCP or NTCP curve when a given model parameter is varied, without having to calculate an entire TCP or NTCP curve for each new parameter value. An example of this application is illustrated in Fig. 5.2, where the value of  $D_{50}$  is plotted as a function of  $n$ , the number of fractions. The four curves shown in Fig. 5.2 correspond to calculations for the following models and parameter values: (1) CV NTCP model, with parameter values of  $\alpha = 0.07 \text{ Gy}^{-1}$ ,  $\alpha/\beta = 2 \text{ Gy}$ ,  $N = 10^6$ ,  $N_0 = 10^3$ , and  $\mu_{cr} = 0.10$ ; (2) CV NTCP model, with  $\alpha = 0.12 \text{ Gy}^{-1}$ ,  $\alpha/\beta = 10 \text{ Gy}$ , and  $N$ ,  $N_0$ , and  $\mu_{cr}$  having the same values as in (1); (3) Poisson TCP model, with  $\alpha = 0.30 \text{ Gy}^{-1}$ ,  $\alpha/\beta = 10 \text{ Gy}$ ,  $N = 10^6$ ,  $\lambda = 0$  (*i.e.* no repopulation); and (4) Poisson TCP model, with  $\alpha$ ,  $\alpha/\beta$ , and  $N$  the same as in (3), but with  $\lambda = 0.10 \text{ days}^{-1}$  (*i.e.* potential tumor doubling time of  $\sim$  one week). Note that the  $\alpha$  and  $\alpha/\beta$  values for (1) and (2) yield the same survival fraction at 2 Gy, defined as  $SF_2 = \exp(-2\alpha - 4\beta)$ , with  $\alpha$  and  $\beta$  in units of  $\text{Gy}^{-1}$  and  $\text{Gy}^2$ , respectively. Fig. 5.2 depicts how the lower  $\alpha/\beta$  values for normal tissues lead to a fractionation benefit. The curves for the TCP and NTCP models when the value of  $\alpha/\beta$  is the same ( $= 10 \text{ Gy}$ ) exhibit a similar dependence of  $D_{50}$  on the number of fractions. However, when the normal tissue  $\alpha/\beta$  ratio is reduced from ten to a more realistic value of two, the dose at which a complication rate of 50 % occurs increases much more rapidly, manifesting the fractionation advantage. The negative effect of tumor repopulation is also illustrated in Fig. 5.2. As shown, increasing  $\lambda$  from 0 to  $0.10 \text{ days}^{-1}$  results in a substantial increase in the dose required to achieve 50 % tumor control when a large number of fractions is used. Notice also that for this example, the curves corresponding to cases (1) and (4) above have nearly the same general shape, implying that a repopulation rate of  $\lambda = 0.10 \text{ days}^{-1}$  essentially negates any fractionation benefit that could be realized from the low  $\alpha/\beta$  ratio of the normal tissue.

The expressions in Table 5.1 may also yield other useful insights on the shape of the dose response curves predicted by the different models. One example is that the  $D_{50}$  expression for the CV NTCP model has no explicit dependence on  $N$ , the number of FSUs in the organ. The normalized slope ( $\gamma_{50}$ ), however, varies according to  $\sqrt{N}$ . This

would imply that, for organs with a “critical volume” architecture, the position of the NTCP curve is independent of the size of organ irradiated, but the normalized slope of the curve will get steeper as the size of the organ increases.

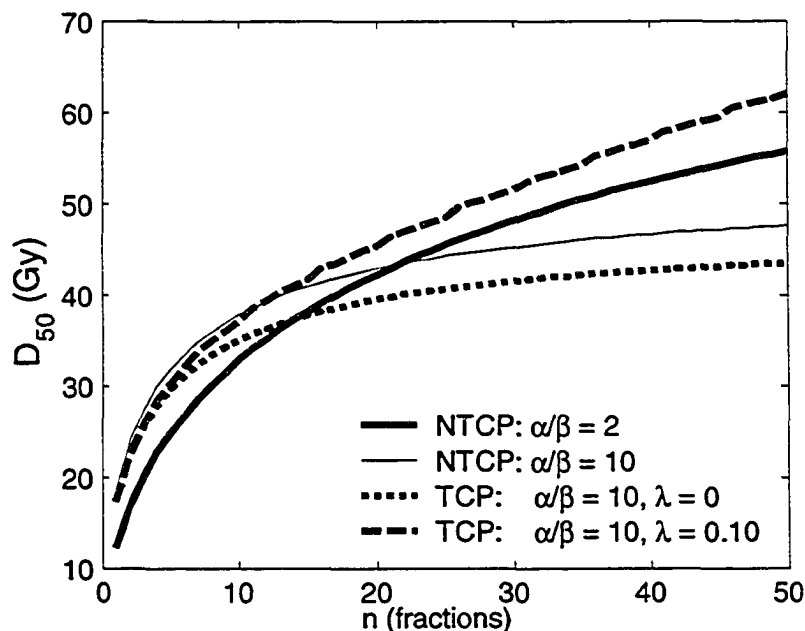


Figure 5.2. Dependence of  $D_{50}$  on the number of fractions ( $n$ ), as predicted by the expressions in Table 5.1 for the CV NTCP model and the Poisson TCP model. The two NTCP curves illustrate the effect of changing the  $\alpha/\beta$  ratio, while the two TCP curves show the impact of repopulation ( $\lambda = 0 \rightarrow$  no repopulation.) The other parameter values for each of the four curves are given in the text.

## B. Evaluation of a TCP model incorporating population heterogeneity

### i. Introduction

The motivation for using radiobiological modeling in radiotherapy lies in the potential to use such models to customize radiotherapy treatments for each individual patient, in order to maximize the probability of a positive clinical outcome. Ideally, accurate *in vitro* assays of the clonogen density, radiosensitivity, and repopulation capabilities would be used in conjunction with appropriate radiobiological models to accurately predict an individual’s radiation response to any given treatment regime, and to suggest appropriate adjustments to a treatment plan. Significant effort has thus been invested in studying how closely current *in vitro* assays (e.g.  $SF_2$ ) are correlated to *in vivo*

tissue radiation response [e.g. Refs. 28-39]. A number of works have used models to assess the potential gains in TCP (tumor control probability) achievable with assay-based treatment customization.<sup>40-42</sup> The potential advantage of using radiobiological models for treatment customization was highlighted in one such work by Buffa *et al.*,<sup>40</sup> which illustrated that a TCP model incorporating individual assay results has greater prognostic power than the *in vitro* assays alone.

Clearly, the understanding of the relationship between *in vitro* and *in vivo* radiosensitivities is an important objective. It is expected that *in vitro* and *in vivo* radiosensitivities will differ due to the impact of *in vivo* hypoxia, and differences in repair capabilities. The extent of influence these and other factors have is difficult to assess. Comparisons between *in vitro* and *in vivo* data are unfortunately complicated by factors that make the extraction of radiosensitivity parameters ( $\alpha$  and  $\beta$ ) from clinical data difficult. As is well-known, clinical data is composed of a population of individuals having a distribution of radiation responses. As discussed by a number of authors,<sup>43-46</sup> the shallow dose-response observed in clinical data sets may be attributable to variability in radiation-response parameters within the population. Until recently, however, clinical data was fit using tissue-response models characterizing the response of an individual. Failure to account for inter-tumor heterogeneities in the TCP model used to fit a clinical data set can lead to distortion of the extracted parameter values. It has been suggested that this is one reason why values of  $\alpha$  extracted from clinical data sets have been lower by a factor as large as ten than values of  $\alpha$  derived from *in vitro* data.<sup>47</sup>

The incorporation of inter-tumor heterogeneities into TCP models has been addressed in the works given in Refs. [47-49]. In this work we evaluate one of these attempts, a model developed by Roberts and Hendry,<sup>47</sup> in order to further explore this model's applicability. We fit this population model to various sets of pseudo-data that we generated, to determine how closely and reliably the fit values match the parameter values used to generate the pseudo-data. Our results serve as an illustrative example of the limitations common to the use of population models in general. Specifically, we will show the difficulty in extracting reliable estimates from fits to clinical data sets of either the degree of heterogeneity present in a clinical data set, or of the value of the  $\beta/\alpha$  ratio, which is often used to characterize the fractionation sensitivity of a cell line.

## ii. Theory

The Poisson TCP model given in Eq. (5.21) describes the dose response of an individual patient. This equation can be re-written in a slightly different form to give,

$$TCP_{ind} = \exp\left(-\exp\left(\kappa - \alpha D - \beta D^2 / n + \lambda \max(T - T_{lag}, 0)\right)\right), \quad (5.38)$$

with  $\kappa$  being defined as the natural logarithm of the initial number of clonogens:

$$\kappa \equiv \ln N.$$

In Eq. (5.38),  $\kappa$ ,  $\alpha$ ,  $\beta$ ,  $\lambda$ , and  $T_{lag}$  are the (previously-defined) parameters characterizing the individual's tumor, and the symbol  $TCP_{ind}$  is used to explicitly indicate that this represents an *individual* TCP model. As mentioned above, the fitting of an individual TCP model such as this to clinical data can lead to apparently unrealistic values for the radiation response parameters ( $\kappa$ ,  $\alpha$ ,  $\beta$ ,  $\lambda$ , and  $T_{lag}$ ). To extract meaningful estimates of these parameters from fits to clinical data requires that patient-to-patient variations in these parameters be incorporated in the formulation of the TCP model. Typically this is done by integrating the individual tumor response function with respect to each of the parameters, weighted by the probabilities of finding given parameter values in the population of individuals –  $f_{\kappa}(\kappa)$ ,  $f_{\alpha}(\alpha)$ ,  $f_{\beta}(\beta)$ ,  $f_{\lambda}(\lambda)$ ,  $f_{T_{lag}}(T_{lag})$ . Thus, accommodating variation in the  $\kappa$ ,  $\alpha$ , and  $\lambda$  parameters, the general expression for a *population* TCP model ( $TCP_{pop}$ ) is:

$$TCP_{pop} = \int_{-\infty}^{\infty} d\alpha f_{\alpha}(\alpha) \int_{-\infty}^{\infty} d\lambda f_{\lambda}(\lambda) \int_{-\infty}^{\infty} d\kappa f_{\kappa}(\kappa) TCP_{ind}(\kappa, \alpha, \beta, \lambda, T_{lag}). \quad (5.39)$$

Assuming (for mathematical convenience, and as is conventionally done) that the radiation response parameters are normally distributed within the population, the population-averaged TCP response can be written as:<sup>47</sup>

$$TCP_{3D} = \frac{1}{(2\pi)^{3/2} \sigma_{\kappa} \sigma_{\alpha} \sigma_{\lambda}} \int_{-\infty}^{\infty} \int_{-\infty}^{\infty} \int_{-\infty}^{\infty} \exp\left(-\exp\left(\kappa' - \alpha' D - \frac{\beta D^2}{n} + \lambda' \max(T - T_{lag}, 0)\right)\right) \\ \times \exp\left(\frac{-(\kappa' - \kappa)^2}{2\sigma_{\kappa}^2}\right) \exp\left(\frac{-(\alpha' - \alpha)^2}{2\sigma_{\alpha}^2}\right) \exp\left(\frac{-(\lambda' - \lambda)^2}{2\sigma_{\lambda}^2}\right) d\kappa' d\alpha' d\lambda'. \quad (5.40)$$

In Eq. (5.40),  $\sigma_\kappa$ ,  $\sigma_\alpha$ , and  $\sigma_\lambda$  are the variances, and  $\kappa$ ,  $\alpha$ , and  $\lambda$  are the population means of the normal distributions of each of the parameters. This population model will be referred to as  $TCP_{3D}$ , since it involves an explicit 3-dimensional integration.

The effect of population heterogeneity on the shape of TCP curves is illustrated in Fig. 5.3. A TCP curve generated using the individual TCP model (Eq. (5.38)) is compared to TCP curves calculated using the population model (Eq. (5.40) for different values of  $\sigma_\alpha$ . For this exercise, it is assumed that there is no variability in the other parameters, *i.e.*  $\sigma_\kappa = 0$ ,  $\sigma_\lambda = 0$ . The parameter values common to the individual and population TCP curves are the same:  $\kappa = 13.8$ ,  $\alpha = 0.30 \text{ Gy}^{-1}$ ,  $\beta = 0.03 \text{ Gy}^{-2}$ ,  $\lambda = 0.10 \text{ days}^{-1}$ , and  $T_{lag} = 0$ , with  $\alpha$  referring to the mean value in the case of the population model. As evident from Fig. 5.3, the main effect of an increase in population variability is to make the slope of the TCP curve shallower.

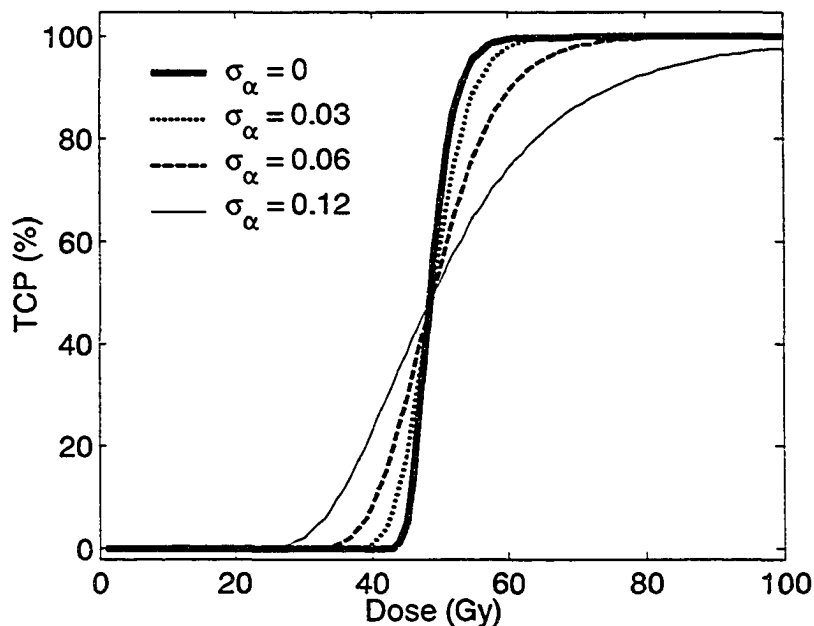


**Figure 5.3.** Effect of patient-to-patient variation in  $\alpha$  on the shape of TCP curves. The population model in Eq. (5.40) was used to generate curves corresponding to increasing values of  $\sigma_\alpha$  (*i.e.* increasing heterogeneity). The other parameter values were  $\kappa = 13.8$ ,  $\alpha = 0.30 \text{ Gy}^{-1}$ ,  $\beta = 0.03 \text{ Gy}^{-2}$ ,  $\lambda = 0.10 \text{ days}^{-1}$ , and  $T_{lag} = 0$  (and  $\sigma_\kappa = 0$ ,  $\sigma_\lambda = 0$ ). The curve labeled  $\sigma_\alpha = 0$  was generated using the individual TCP model (Eq. (5.38)) and the same parameter values for  $\kappa$ ,  $\alpha$ ,  $\beta$ ,  $\lambda$ , and  $T_{lag}$ .

The main drawback to the population model in Eq. (5.40) is the introduction of three new independent fitting parameters ( $\sigma_\kappa, \sigma_\alpha, \sigma_\lambda$ ), bringing the total number of

model parameters to eight. Clinical data sets do not have sufficient diversity to support the use of such a model without introducing considerable parameter correlations. When correlations occur, different sets of parameters will provide equally good fits to the clinical data. Attempts to extract biological information from the fits then often become ambiguous, essentially rendering the fits phenomenological.

An approximate “closed-form” solution to Eq. (5.40) was proposed by Roberts and Hendry.<sup>47</sup> This solution represents an attempt to provide a population TCP model that, in comparison to the  $TCP_{3D}$  model, is simpler mathematically, requires fewer parameters, and yet preserves the main dependencies of TCP on the effects of population variability. The first assumption of the Roberts and Hendry derivation is that the most important source of heterogeneity is variability in  $\alpha$ , and that heterogeneity in the other parameters (*e.g.*  $\kappa$  and  $\lambda$ ) can be neglected. On this basis, Eq. (5.40) can be reduced to a population model,  $TCP_{1D}$ , that requires only a one-dimensional integration:

$$TCP_{1D} = \frac{1}{\sqrt{2\pi}\sigma_\alpha} \int_{-\infty}^{\infty} \exp\left(-\exp\left(\kappa - \alpha'D - \frac{\beta D^2}{n} + \lambda \max(T - T_{lag}, 0)\right)\right) \times \exp\left(\frac{-(\alpha' - \alpha)^2}{2\sigma_\alpha^2}\right) d\alpha' \quad (5.41)$$

For the case of large  $\sigma_\alpha$ , Roberts and Hendry then approximated the first exponential (*i.e.* the individual TCP function) in the integrand by a Heaviside step function,

$$\exp(-\exp z) \approx \begin{cases} 1 & \text{if } z \leq 0 \\ 0 & \text{if } z > 0 \end{cases}, \text{ where } z = \left(\kappa - \alpha D - \frac{\beta D^2}{n} + \lambda \max(T - T_{lag}, 0)\right). \quad (5.42)$$

This is equivalent to assuming that the slope of the individual TCP dose-response curve is infinitely steep. Using Eq.(5.42), the integral in Eq. (5.41) can be expressed in terms of the complementary error function (*erfc*),

$$TCP_{pop} = \frac{1}{2} \operatorname{erfc}\left(\frac{\kappa - \alpha D - \beta D^2 / n + \lambda \max(T - T_{lag}, 0)}{\sqrt{2D}\sigma_\alpha}\right), \quad (5.43)$$

where  $erfc(x) = \int_x^{\infty} \exp(-t^2) dt$ . The number of parameters in the population TCP model is further reduced by introducing a heterogeneity parameter,

$$\mu = \frac{\alpha}{\sigma_{\alpha}}, \quad (5.44)$$

and by expressing the parameters  $N$ ,  $\beta$ , and  $\lambda$  as ratios relative to  $\alpha$ . The Roberts and Hendry population TCP expression, now designated  $TCP_{RH}$ , is thus a function of five parameters,  $\mu$ ,  $\kappa/\alpha$ ,  $\beta/\alpha$ ,  $\lambda/\alpha$ , and  $T_{lag}$ :

$$TCP_{RH} = \frac{1}{2} erfc \left( \frac{\mu}{\sqrt{2D}} \left( \frac{\kappa}{\alpha} - D - \frac{\beta}{\alpha} \frac{D^2}{n} + \frac{\lambda}{\alpha} \max(T - T_{lag}, 0) \right) \right). \quad (5.45)$$

The number of parameters used in this population model is the same as found in the individual TCP model given by Eq. (5.38). Roberts and Hendry proffered that fits employing the ratios  $\kappa/\alpha$ ,  $\beta/\alpha$ , and  $\lambda/\alpha$  are more stable and perhaps more biologically meaningful than fits done with the absolute values of the parameters. This assumption is consistent with the findings of previous authors<sup>43,50</sup> regarding the advantages of using ratios of parameter values.

The predicted  $D_{50}$  in terms of the radiobiological parameters for the  $TCP_{RH}$  expression can be calculated using the observation that  $TCP_{RH} = 0.5$  when the argument of the  $erfc$  function in Eq. (5.45) is zero. This gives:

$$D_{50(RH)} = \frac{n}{2\beta/\alpha} \left[ \sqrt{1 + \frac{4\beta/\alpha}{n} \left( \frac{\kappa}{\alpha} + \frac{\lambda}{\alpha} \max(T - T_{lag}, 0) \right)} - 1 \right]. \quad (5.46)$$

The position of the  $TCP_{RH}$  curve is independent of both the absolute value of  $\alpha$ , and the level of heterogeneity,  $\mu$ . Taking the derivative of the expression in Eq. (5.45) and evaluating at the  $D_{50}$  dose given in Eq. (5.46) provides the value of  $\theta_{50}$  characterizing the (un-normalized) slope of the curve:

$$\theta_{50(RH)} = \frac{\mu}{\sqrt{2\pi} D_{50}} \left( 1 + 2 \frac{\beta}{\alpha} \frac{D_{50}}{n} \right). \quad (5.47)$$

### iii. Methods

Like any TCP model, a population model can be evaluated with respect to two considerations: (i) the ability to fit the shape of clinical TCP data with the model, and (ii) the ability to extract parameter values that accurately reflect the radiobiological characteristics inherent in the data. Roberts and Hendry found that in fitting two clinical data sets, their closed-form heterogeneity model produced slightly better fits than those achieved with a standard individual TCP model. They also suggested that their model yielded biologically significant parameters: values for the radiosensitivity, clonogen number, and repopulation parameters that were consistent with relevant *in vitro* measurements, in addition to a stable estimate for the parameter characterizing the degree of population heterogeneity. One disadvantage of using real clinical data to test a model is, however, that the “true” parameter values of any clinical data set are never known with a great degree of certainty. It is thus not always easy to assess whether the best-fit parameter values obtained using a given TCP model are “biological”, or should rather be considered more “phenomenological” in nature. In an effort to establish more definitively the capabilities of the Roberts and Hendry (RH) closed-form population model, we fitted  $TCP_{RH}$  (Eq. (5.45)) to different sets of “pseudo-data”<sup>26</sup> that have been generated with known parameter values

#### a. Generation of Pseudo-data

The pseudo-data was generated by writing MATLAB computer code to implement the following technique.<sup>26,51</sup> First values for the parameters  $\kappa$ ,  $\alpha$ ,  $\beta$ ,  $\lambda$ ,  $T_{lag}$ ,  $\sigma_\kappa$ ,  $\sigma_\alpha$ , and  $\sigma_\lambda$ , which describe the means and variances of the radiobiological characteristics of a population, were selected, as were values for  $n$  and  $T$ , which specify the fractionation regime(s). Also chosen were an appropriate set of dose points,  $D_j$  with  $j = 1$  to  $ndpts$ , and the number of patients per dose point,  $npat$ , contained in the pseudo-data set. The data set thus consisted of a total of  $ndpts \times npat$  patients. A set of parameters describing the radiation response of each *individual* patient was generated: for the  $i^{th}$  patient these parameters are designated  $\kappa_i$ ,  $\alpha_i$ ,  $\beta_i$ ,  $\lambda_i$ ,  $T_{lag-i}$ . The same  $\beta$  and  $T_{lag}$  values were used for each patient, while the values of  $\kappa_i$ ,  $\alpha_i$ , and  $\lambda_i$ , were randomly sampled from normal distributions described by the population mean and variance

parameters. Based on each individual's parameters, the dose delivered and the fractionation regime, an individual TCP value,  $TCP_i$ , was calculated with Eq. (5.38). To simulate statistical fluctuations in the data set, each  $TCP_i$  value was compared to a random number  $RN_i$  sampled from a uniform distribution defined between zero and one: the instances where  $TCP_i > RN_i$  were assigned as treatment successes (*i.e.* tumor controls), the others as treatment failures. We will designate the number of "controls" and "failures" at a given dose point  $j$  as  $ncon_j$  and  $nfail_j$ , respectively. The TCP at each point is thus given by  $TCP_{data}(D_j) = ncon_j / npat_j$ .

Different pseudo-data sets were generated using the sets of parameter values given in Table 5.2. Though not derived from any particular clinical data set, they represent plausible radiobiological values; they are similar, but not identical, to those used by Roberts and Hendry during their preliminary testing of their model. Set #1 is our "base" set of parameters. The population heterogeneity for this set is characterized by the values of  $\sigma_\kappa = 2$ ,  $\sigma_\alpha = 0.075 \text{ Gy}^{-1}$  and  $\sigma_\lambda = 0.05 \text{ days}^{-1}$ . The  $\sigma_\kappa$  value is the same as that assumed by Roberts and Hendry, while the  $\sigma_\alpha$  and  $\sigma_\lambda$  values are somewhat smaller. However, our  $\sigma_\alpha$  and  $\sigma_\lambda$  values still represent considerable population heterogeneity, corresponding to a coefficient of variation,  $CV = x/\sigma_x$  (where  $x$  is a parameter), equal to 25 % for both  $\alpha$  and  $\lambda$ . The parameters of set #2 were chosen to reflect a data set without population heterogeneity ( $\sigma_\kappa, \sigma_\alpha$  and  $\sigma_\lambda = 0$ ). Sets #3 and #4 are used to explore the dependence of the fitting results on the LQ model's  $\beta$  term, and differ from set #1 only in the values of  $\kappa$  and  $\beta$ . Set #3 assumes no  $\beta$ -mechanism is present, whereas set #4 assumes a much larger  $\beta$  strength corresponding to an  $\alpha/\beta$  ratio of three, instead of the value of ten assumed for set #1. The values of  $\kappa$  for sets #3 and #4 were decreased and increased with respect to the  $\kappa = 16$  of set #1 to maintain a similar value of  $D_{50}$  for a treatment consisting of 30 fractions in 39 days.

Two types of pseudo-data sets were generated: those including only a single fractionation regime of  $n = 30$  fractions in  $T = 39$  days; and those consisting of data for three fractionation regimes – 15, 30, and 45 fractions delivered in 18, 39 and 60 days, respectively. Note that when there is no variation in the treatment time between the data

points of a set of TCP data, fits will not be able to discriminate between the  $\frac{\kappa}{\alpha}$  and  $\frac{\lambda}{\alpha} \max(T - T_{lag}, 0)$  terms in Eq. (5.45). The parameters describing the clonogen number and repopulation characteristics are thus inherently correlated in this case. For this reason, when fits were done to the single fractionation sets of pseudo-data, we fixed the values of  $\lambda/\alpha$  and  $T_{lag}$  to zero, which effectively combined these two parameters and  $\kappa/\alpha$  into a single fitting parameter,

$$\frac{\kappa'}{\alpha} = \frac{\kappa}{\alpha} + \frac{\lambda}{\alpha} \max(T - T_{lag}, 0). \quad (5.48)$$

The data sets with three fractionation regimes were used to investigate how diversification of the data with respect to the  $n$  and  $T$  variables affected the fitting results. These diversified data sets allowed the  $\kappa/\alpha$ ,  $\lambda/\alpha$ , and  $T_{lag}$  parameters to be treated independently for fitting purposes.

Except as noted below, the pseudo-data sets were generated assuming a sample size ( $n_{pat}$ ) of 50 patients at each of the dose points, which were defined at 2 Gy intervals between 30 and 90 Gy for the single fractionation sets, and 30 to 100 Gy for the multiple fractionation sets. These dose ranges were selected to generate full TCP curves that had points covering essentially the entire range of TCP values from 0 to 100 %. An additional pseudo-data set was also created that had fewer dose points – seven, rather than thirty-six, for each of the three fractionation regimes – to determine how the results would change if fits were performed to a more clinically realistic data set. The effect of sample size was also studied by generating a set with a sample size of 20 patients per dose point.

Set #	$\kappa$	$\sigma_{\kappa}$	$\alpha$ (Gy <sup>-1</sup> )	$\sigma_{\alpha}$ (Gy <sup>-1</sup> )	$\lambda$ (days <sup>-1</sup> )	$\sigma_{\lambda}$ (days <sup>-1</sup> )	$\beta$ (Gy <sup>-2</sup> )	$T_{lag}$ (days)
#1	16	2	0.30	0.075	0.20	0.05	0.03	25
#2	11	0	0.20	0	0.20	0	0	25
#3	13	2	0.30	0.075	0.20	0.05	0	25
#4	23	2	0.30	0.075	0.20	0.05	0.10	25

**Table 5.2.** Radiobiological parameters used to generate the pseudo-data sets employed in the fitting exercises designed to test the RH heterogeneity model.

*b. Fitting Techniques: Maximum-Likelihood and p-values*

The fits to the pseudo-data employed a maximum-likelihood fitting methodology.<sup>25,51</sup> The specific method, outlined below, is one detailed in the work of Stavrev *et al.*<sup>25</sup> For a given set of fitted model parameter values,  $\bar{p}$ , the corresponding TCP values,  $TCP_{fit}(\bar{p}, D_j)$ , are calculated for all dose points  $D_j$ . In the case of the RH model, the fit parameters are  $\bar{p} = (\mu, \kappa/\alpha, \beta/\alpha, \lambda/\alpha, T_{lag})$ . If it were assumed that these are the “true” parameters describing the data, the “likelihood”  $L$  (*i.e.* probability) predicted by binomial statistics of observing the generated pseudo-data set, described by the  $ncon_j$  and  $nfail_j$  values, is

$$L = \prod_{j=1}^{ndpts} B(ncon_j, nfail_j) TCP_{fit}(\bar{p}, D_j)^{ncon_j} (1 - TCP_{fit}(\bar{p}, D_j))^{nfail_j}, \quad (5.49)$$

where  $B(ncon_j, nfail_j) = (ncon_j + nfail_j)! / (ncon_j! nfail_j!)$  is the binomial coefficient.

According to this method, the set of “best-fit” parameters,  $\bar{p}_{best}$ , is the one that maximizes the likelihood function  $L$ . For optimization purposes it is more convenient and conventional to work with the natural logarithm of this function,  $\ln L$ . Also, since the product of the binomial coefficients,  $\prod_{j=1}^{ndpts} B(ncon_j, nfail_j)$ , represents a common factor in Eq. (5.49) that is independent of the parameter values, this factor can be removed and the function to be maximized can be written as:

$$\ln L_{fit} = \sum_{j=1}^{ndpts} ncon_j \ln TCP_{fit}(\bar{p}, D_j) + nfail_j \ln (1 - TCP_{fit}(\bar{p}, D_j)). \quad (5.50)$$

If an “ideal” fit were achieved, the fitted and data TCP values would coincide exactly, *i.e.*  $TCP_{fit}(\bar{p}, D_j) = TCP_{data}(D_j)$ . The log-likelihood function in this case,  $\ln L_{ideal}$ , is:

$$\ln L_{ideal} = \sum_{j=1}^{ndpts} ncon_j \ln TCP_{data}(D_j) + nfail_j \ln (1 - TCP_{data}(D_j)). \quad (5.51)$$

A fit deviance parameter,  $Dev_{fit}$ , can be then defined,

$$Dev_{fit} = -2(\ln L_{fit} - \ln L_{ideal}), \quad (5.52)$$

and used to quantify the quality of the fit. In our fitting technique, *minimization* of the  $Dev_{fit}$  metric was utilized to steer the fits. A Monte Carlo method was used to search the

parameter space, with the new parameters for each fitting iteration being sampled randomly from normal distributions centered at the parameter values giving the best fit up to that point in the optimization. This fitting algorithm was executed using code we wrote in MATLAB.

The fit deviance metric is expected to follow an approximate chi-square ( $\chi^2$ ) distribution.<sup>25</sup> Under this assumption, the probability of observing a given  $Dev_{fit}$  is equal to the value of the chi-square function,  $\chi^2_v(Dev_{fit})$ , where  $v$  is the number of degrees of freedom, and is equal to the number data points minus the number of free fitting parameters. This then allows  $Dev_{fit}$  to be related to the  $p$ -value metric, defined as

$$p - value = \int_{Dev_{fit}}^{\infty} \chi^2_v(x) dx , \quad (5.53)$$

the probability of finding a  $Dev_{fit}$  value larger than the one obtained for the given set of parameters. The  $p$ -value ranges from zero to one, with larger values suggesting a better fit. Consistent with convention, fits yielding a  $p$ -value less than 0.05 are considered statistically unacceptable.

To test the reliability of the RH model parameter  $\mu$  as a quantitative measure of the heterogeneity present in a clinical data set, we used the maximum-likelihood fitting technique described above to fit single sets of pseudo-data multiple times. In this fitting procedure,  $\mu$  was fixed at a specified value, while the other parameters were treated as free fitting parameters. This was repeated several times for different fixed values of  $\mu$  to determine a range of  $\mu$  values for which a fit with a  $p$ -value of at least 0.05 could be found, *i.e.*  $\mu$  values that satisfactorily describe the given pseudo-data set from a statistical perspective.

A second type of fitting exercise was also performed to illustrate the presence of parameter correlations in the RH population model. For this exercise, a large number (1000) of different sets of pseudo-data were generated for the same set of values for the population radiobiological parameters ( $\kappa$ ,  $\alpha$ ,  $\beta$ ,  $\lambda$ ,  $T_{lag}$ ,  $\sigma_{\kappa}$ ,  $\sigma_{\alpha}$ , and  $\sigma_{\lambda}$ ). Each of these sets was then fit to the RH heterogeneity model. For the sake of speed and automation in fitting this number of different sets, we used a built-in MATLAB function for multi-dimensional minimization (**fminsearch**) based on a Nelder-Mead simplex search

method<sup>52</sup> to minimize  $Dev_{fit}$ . In an attempt to assist the routine in finding reasonable fits, the parameters were constrained to the limits,  $\mu \in [0.4, 40]$ ,  $\kappa'/\alpha \in [20, 200]$ , and  $\beta/\alpha \in [0, 2]$ . For each fit, the *best-fit* parameters and the corresponding value of  $Dev_{fit}$  were stored. Since it is not guaranteed that the minimization routine will always return a suitable fit, those fits returning a  $Dev_{fit}$  corresponding to a  $p$ -value of less than 0.05 were discarded. The remaining fits were used to form histograms showing the number of fits returning a best-fit value within a specific range of values for a given parameter.

#### *iv. Results*

##### *a. Evaluation of the Validity of the RH Approximation: Comparison of $TCP_{RH}$ , $TCP_{1D}$ and $TCP_{3D}$*

We first examine how closely the Roberts and Hendry closed-form solution,  $TCP_{RH}$  (Eq. (5.45)), reproduces the TCP predictions of the population models involving explicit one- or three-dimensional integration,  $TCP_{1D}$  (Eq. (5.41)) or  $TCP_{3D}$  (Eq. (5.40)), respectively. Roberts and Hendry suggested that the expression in Eq. (5.45) is valid in cases of high heterogeneity (large  $\sigma_\alpha$ ). However, as noted by Buffa *et al.*,<sup>53</sup> explicit ranges of  $\sigma_\alpha$  for which this reasonably holds were not provided. To illustrate the limitations of the RH solution, Buffa *et al.* compared TCP curves calculated using  $TCP_{RH}$  and  $TCP_{1D}$  for two values of  $\sigma_\alpha$ , 0.03 and 0.10. A similar comparison is shown in Fig. 5.4. For this example, TCP curves were generated for  $TCP_{RH}$ ,  $TCP_{1D}$ , and  $TCP_{3D}$  based on the following radiobiological and treatment parameter values:  $\kappa = 16$ ,  $\alpha = 0.30 \text{ Gy}^{-1}$ ,  $\beta = 0.03 \text{ Gy}^{-2}$ ,  $\lambda = 0.20 \text{ days}^{-1}$ ,  $T_{lag} = 25 \text{ days}$ ,  $n = 30$  fractions, and  $T = 39 \text{ days}$ . A variation in  $\alpha$  characterized by  $\sigma_\alpha = 0.075 \text{ Gy}^{-1}$  was incorporated for all three TCP models, and additional population variability described by  $\sigma_\kappa = 2$  and  $\sigma_\lambda = 0.05 \text{ days}^{-1}$  was also included for the  $TCP_{3D}$  curve. Fig. 5.4 shows an appreciable difference in the shapes of the  $TCP_{RH}$  and  $TCP_{3D}$  curves, with a maximum difference of 6.6 % in the TCP predictions. Some of this discrepancy results from the fact that the RH expression neglects variability in  $\kappa$  and  $\lambda$ , as illustrated by differences between  $TCP_{1D}$  and  $TCP_{3D}$ . However, most of the discrepancy arises from differences between  $TCP_{RH}$  and  $TCP_{1D}$  – the maximum difference between these TCP values is 5.5 %. This

indicates that the RH approximation of the one-dimensional integral may not be sufficient for this value of  $\sigma_\alpha$ .

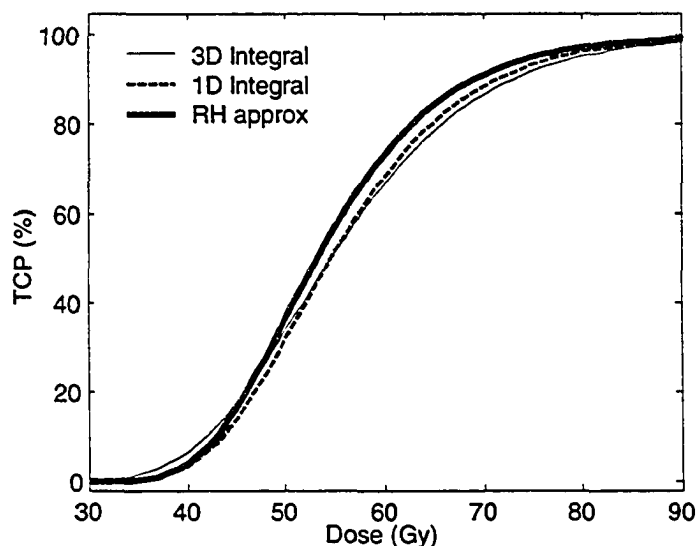


**Figure 5.4.** Comparison of population model predictions of  $TCP_{RH}$ ,  $TCP_{1D}$ , and  $TCP_{3D}$  for a population characterized by parameter values of  $\kappa = 16$ ,  $\alpha = 0.30$ ,  $\beta = 0.03$ ,  $\lambda = 0.10$ ,  $T_{lag} = 25$ ,  $\sigma_\alpha = 0.075$ ,  $\sigma_\kappa = 2$ , and  $\sigma_\lambda = 0.05$  for a treatment of  $n = 30$  fractions in  $T = 39$  days.

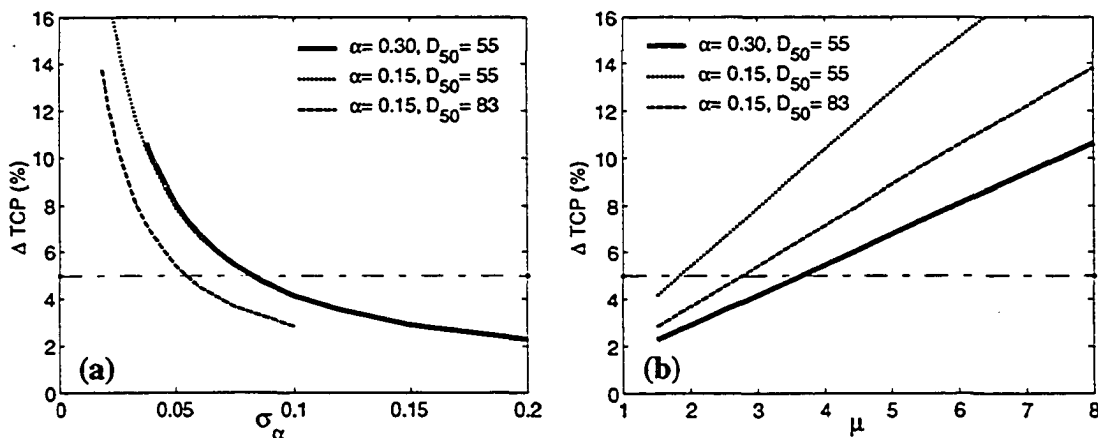


**Figure 5.5.** The maximum difference between  $TCP_{RH}$  and  $TCP_{1D}$ ,  $\Delta TCP$ , as a function of (a)  $\sigma_\alpha$  and (b)  $\mu$ . Curves are generated for three sets of radiobiological parameters corresponding to different values of  $\alpha$  and/or  $D_{50}$  values. The dash-dotted line demarcating the  $\Delta TCP = 5\%$  level is used for reference purposes.

As a means of quantifying the accuracy of the RH approximation, in Fig. 5.5 we plot the maximum difference between  $TCP_{RH}$  and  $TCP_{1D}$  as a function of (a)  $\sigma_\alpha$  and (b)  $\mu$  for values of  $\mu$  ranging from 1.5 (high heterogeneity) to 8 (low heterogeneity). The  $TCP_{RH}$  and  $TCP_{1D}$  curves were generated for three sets of parameter values. All

three sets used identical values of 0.03, 0.20, 25, 30, and 39 for the parameters  $\beta$ ,  $\lambda$ ,  $T_{lag}$ ,  $n$ , and  $T$ , respectively. For  $\alpha$  and  $\kappa$ , the first set used values of 0.30 and 16; the second set used 0.15 and 8, which gave dose response curves with approximately the same  $D_{50}$  values ( $\sim 55$  Gy) as the first set of parameters; the third set used  $\alpha = 0.15$  and  $\kappa = 16$ , which produced considerably larger  $D_{50}$  values of  $\sim 83$  Gy.

The curves corresponding to the three sets of parameters show that the error in  $TCP_{RH}$  decreases as  $\sigma_\alpha$  increases, as expected. The curves describing this decrease as a function of  $\sigma_\alpha$  are essentially identical for the first two parameter sets, despite the fact that the  $\alpha$  values differ by a factor of two; in contrast, the error in  $TCP_{RH}$  is much smaller for a given  $\sigma_\alpha$  for the third set of parameters, corresponding to a larger  $D_{50}$ . These results can be explained by examining the approximation in Eq. (5.42) used to generate the RH solution. As noted by Roberts and Hendry, this approximation assumes that the individual TCP model  $-\exp(-\exp z)$  with  $z = (\kappa - \alpha D - \beta D^2 / n + \lambda \max(T - T_{lag}, 0))$  goes from zero to one over a range of  $\alpha$  values that is small compared to  $\sigma_\alpha$ . Since the range of  $z$  values for which  $TCP_{ind}$  increases appreciably is a constant,  $\Delta z$ , and since changes in  $z$  are proportional to  $\alpha D$ , the corresponding range of relevant  $\alpha$  values,  $\Delta \alpha$ , is proportional  $\Delta z / D$ , or simply  $1/D$  ( $\Delta z$  being a constant). Thus, very roughly, the appropriate lower limit of  $\sigma_\alpha$  for which the RH approximation is reasonable is also proportional to  $1/D$ , but is not explicitly dependent on the absolute value of  $\alpha$ . A consequence of this is that the accuracy of the RH approximation as a function of  $\mu$  (where  $\mu = \alpha / \sigma_\alpha$ ) will depend on the absolute value of  $\alpha$ .<sup>53</sup> For example, Fig. 5.5(b) illustrates that to ensure that the maximum difference between  $TCP_{RH}$  and  $TCP_{1D}$  is no more than 5 %, the value of  $\mu$  can be as high as  $\sim 3.6$  (*i.e.* CV = 27 %) if  $\alpha = 0.30$ , but only as large as  $\sim 1.8$  (*i.e.* CV = 54 %) if  $\alpha = 0.15$  (for the sets with the same  $D_{50}$  of  $\sim 55$  Gy). In other words, this suggests that the reliability of the RH approximation will depend to some extent on how well  $\alpha$  is known, and that use of the RH model may only be appropriate for

populations manifesting large levels of heterogeneity when the true value of  $\alpha$  is relatively small.

Curves depicting the difference between the slope value,  $\theta_{50}$ , predicted by  $TCP_{RH}$ , as compared to the slope from  $TCP_{1D}$ , are shown in Fig. 5.6. These slope errors are shown for the same three sets of parameters used to generate the results in Fig. 5.5, and displayed as a function of  $\sigma_\alpha$  and  $\mu$ .

Buffa *et al.* have suggested a small modification to the Roberts and Hendry expression that somewhat improves the agreement between the closed-form solution and the explicit one-dimensional integration.<sup>53</sup> These authors also point to an alternative population TCP model that one of them developed,<sup>48</sup> and which they suggest yields more accurate results. This latter model, however, is more complex mathematically than the RH solution. Neither this model, nor the proposed modification of the RH model is analyzed in this work.

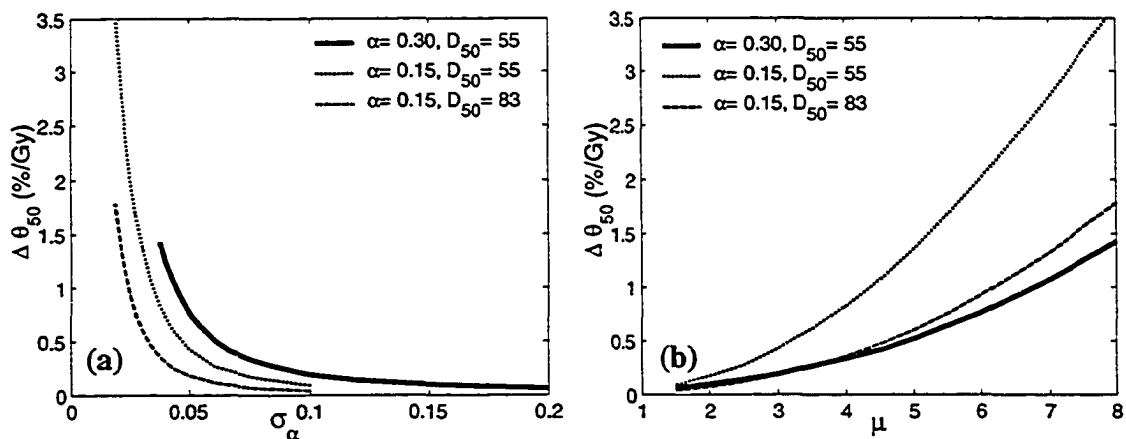


**Figure 5.6.** The difference between the slope ( $\theta_{50}$ ) of the  $TCP_{RH}$  and  $TCP_{1D}$  curves,  $\Delta\theta_{50}$ , as a function of (a)  $\sigma_\alpha$  and (b)  $\mu$ . Curves are generated for three sets of radiobiological parameters corresponding to different values of  $\alpha$  and/or  $D_{50}$  values. For reference, the  $\theta_{50}$  values for the  $TCP_{1D}$  curves range from 1.5 to 6.7 %/Gy for  $\mu$  values increasing from 1.5 to 8 for the first set; the corresponding ranges for the second and third sets are 1.9 – 6.6 and 1.5 – 6.4 %/Gy, respectively.

#### *b. Fits to Pseudo-Data Consisting of One Fractionation Regime*

Fits of the RH model to pseudo-data generated for a single fractionation regime ( $n = 30$ ,  $T = 39$ ) using the parameter values of set #1 in Table 5.2 are shown in Fig. 5.7(a). The value of the heterogeneity factor,  $\mu = \alpha/\sigma_\alpha$ , for this pseudo-data is four

(i.e. CV = 25 %). However, if no constraints are put on the free fitting parameters  $\kappa'/\alpha$  (Eq. (5.48)) and  $\beta/\alpha$ , statistically acceptable fits can be found to this data set with values for  $\mu$  ranging from almost 0 to 4.3. Depicted in Fig. 5.7(a) are three fitted curves with  $\mu$  values of four, two, and one that are equivalent to coefficients of variation of 25, 50 and 100 %, respectively. The three fits thus suggest widely different degrees of population heterogeneity, yet fit the pseudo-data almost equally well from a visual perspective. Statistically, it is in fact the fit using the “correct” (i.e. equal to that used to generate the pseudo-data) value of  $\mu = 4$  that fits the pseudo-data worst, as this fit yields a  $p$ -value of 0.07 that is appreciably smaller than the values of 0.21 and 0.28 for the  $\mu = 2$  and  $\mu = 1$  fits, respectively. If the level of heterogeneity present in the pseudo-data set is kept the same, but the assumed strength of the  $\beta$ -mechanism is increased, estimates of  $\mu$  from fits to the pseudo-data are even more uncertain. This was demonstrated in fits of the RH model to pseudo-data based on parameter set #4, which assumes the same  $\mu = 4$  as parameter set #1, but uses  $\beta/\alpha = 0.33$  instead of 0.10. The range of statistically acceptable  $\mu$  values for this data set was from nearly 0 to 9.7. Fits to this pseudo-data using the RH model with fixed  $\mu$  values of one and eight are shown in Fig. 5.7(b). These fits yielded particularly high  $p$ -values of 0.95 and 0.89.

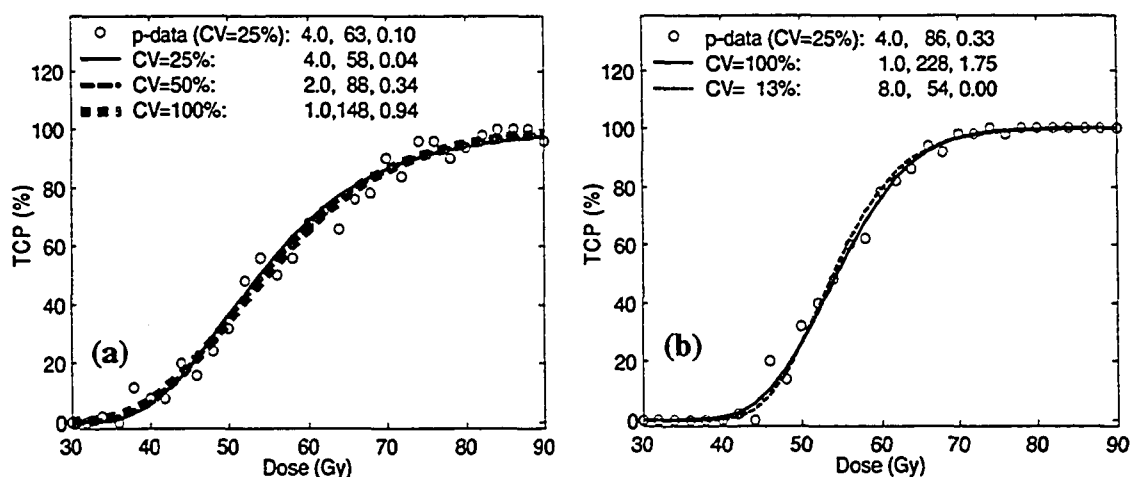


**Figure 5.7.** Fits (lines) of the RH model to pseudo-data (circles) generated for one fractionation regime and using parameter set (a) #1 and (b) #4, the latter set assuming greater  $\beta$  strength. The numbers in the legend correspond to the assumed (pseudo-data) or fitted values of the parameters  $\mu$ ,  $\kappa'/\alpha$ , and  $\beta/\alpha$ . As shown, fits with very different values for the heterogeneity parameter  $\mu$  can fit the pseudo-data well. (The fit lines are nearly indistinguishable visually).

The fits shown in Fig. 5.7 manifest a correlation between the fitting parameters,  $\mu$ ,  $\kappa'/\alpha$  and  $\beta/\alpha$ : the values of  $\kappa'/\alpha$  and  $\beta/\alpha$  both increase as  $\mu$  decreases. These correlations are perhaps more clearly seen in Figs. 5.8 and 5.9. These figures provide results from the second type of fitting exercise described in the Methods section (Section 5.B.iii), where a large number of different pseudo-data sets, all generated from set #1's parameter values, were fit individually. The histograms in Fig. 5.8 show the frequency of observing a given best-fit value for  $\mu$ . Although the exact shape of the histogram derived from this fitting exercise was found to depend somewhat on the start parameter values used for the MATLAB fitting routine, useful trends in the fits could still be deduced. First, Fig. 5.8(a) shows that, as implied by the previously discussed results, the best-fit values of  $\mu$  include a large range of values. Fig. 5.8(b) illustrates the correlation between the heterogeneity factor and the  $\beta$ -strength. Fits returning a small best-fit  $\beta/\alpha$  value less than 0.10, also yielded  $\mu$  values between about 3.5 and 4.5, near the  $\mu = 4$  of the pseudo-data itself;  $\beta/\alpha$  values between 0.1 and 0.5 corresponded to  $\mu$ 's of between 1.5 and 3.0; and large  $\beta/\alpha$  values of greater than 0.5 suggested large degrees of heterogeneity, with  $\mu$  being consistently less than 1.5 for these fits. The correlations between  $\kappa'/\alpha$  and each of the other two fitting parameters are shown in Fig. 5.9. Fits returning  $\kappa'/\alpha$  values less than 60 also gave high  $\mu$  values and  $\beta/\alpha$  values near zero; when  $\kappa'/\alpha$  was greater than 60 but less than 120,  $\mu$  and  $\beta/\alpha$  values were intermediate; and for large  $\kappa'/\alpha$  values greater than 120,  $\mu$  was low and  $\beta/\alpha$  was large. The correlation between  $\kappa'/\alpha$  and  $\beta/\alpha$  can be easily explained. Increasing  $\beta/\alpha$  values will move a TCP curve towards lower doses, while larger clonogen numbers and/or more repopulation (*i.e.* larger  $\kappa'/\alpha$ ) will move the TCP curve in the opposite direction towards higher doses. As noted in the Theory section (Section 5.B.ii), the position of a TCP curve is also essentially independent of the heterogeneity parameter  $\mu$ . Thus, to correctly fit the position (*i.e.*  $D_{50}$ ) of a given set of TCP data, the use of large (small) values for  $\beta/\alpha$  can be offset by large (small)  $\kappa'/\alpha$  values.

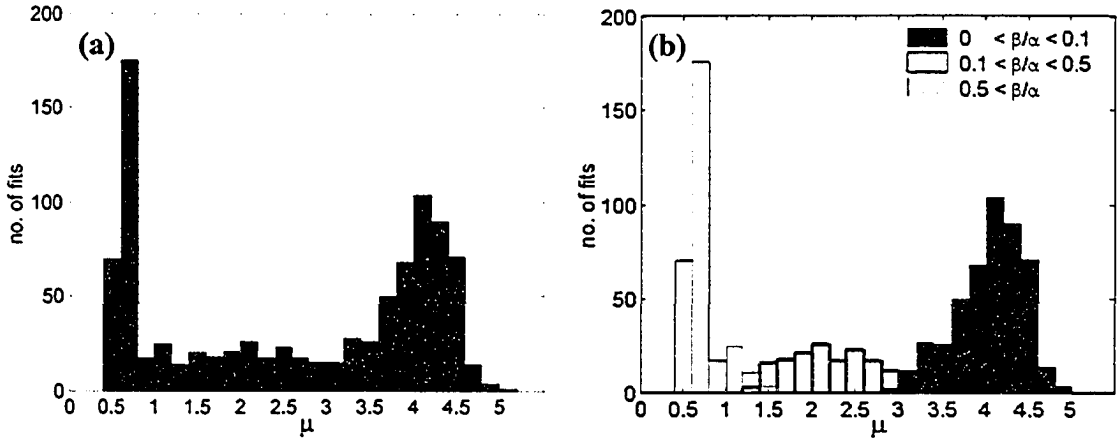


**Figure 5.8.** Best-fit values of  $\mu$  obtained from fits to a large number of pseudo-data sets. (a) Histogram showing the frequency of observing given values of  $\mu$ . (b) Histogram of  $\mu$  divided into three sub-groups corresponding to three different ranges of best-fit  $\beta/\alpha$  values. This illustrates the correlation between the  $\mu$  and  $\beta/\alpha$  fit parameters.

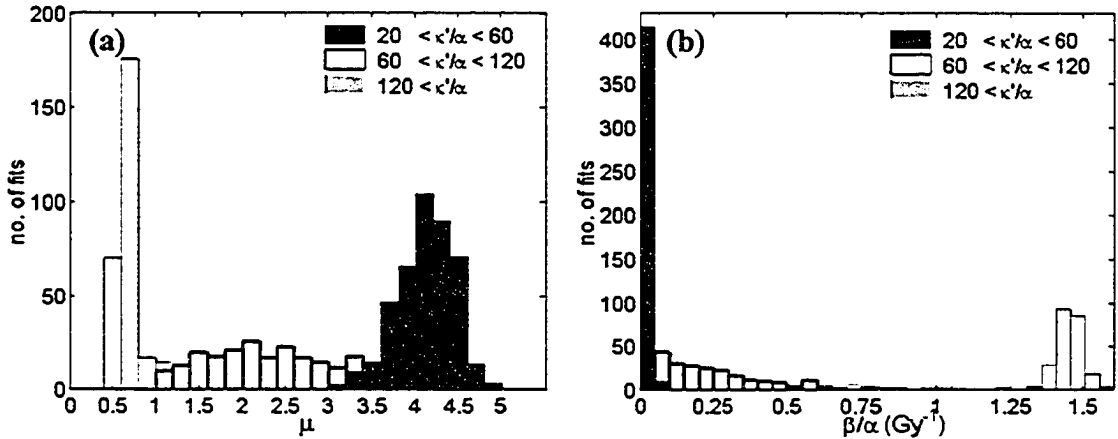


**Figure 5.9.** Histograms of the best-fit parameter values of (a)  $\mu$  and (b)  $\beta/\alpha$ , from fits to a large number of pseudo-data sets. Each histogram is divided into three sub-groups corresponding to three different ranges of best-fit  $\kappa'/\alpha$  values. This illustrates the correlation between  $\kappa'/\alpha$  and the other two fit parameters.

The observed correlation between  $\mu$  and  $\beta/\alpha$  can be elucidated from the equation for the slope of a TCP curve calculated using the RH model (Eq. (5.47)) –

$$\theta_{50(RH)} = \frac{\mu}{\sqrt{2\pi} D_{50}} \left( 1 + 2 \frac{\beta}{\alpha} \frac{D_{50}}{n} \right).$$

The value of  $\theta_{50(RH)}$  depends explicitly only on the  $D_{50}$  position of the curve, and on the  $\mu$  and  $\beta/\alpha$  parameters. Increases in either of these parameters lead to an increased slope value. Thus, a smaller fit value of  $\mu$  can always be compensated by a larger fit value of  $\beta/\alpha$  to achieve the actual  $\theta_{50}$  slope of the clinical

data being fit: this is why, without placing a constraint on  $\beta/\alpha$  (or  $\kappa'/\alpha$ ), essentially no lower limit was observed for  $\mu$  in the fits to individual sets of single-fractionation pseudo-data. From Eq. (5.47) it is also obvious that the upper limit for  $\mu$  is observed when  $\beta/\alpha = 0$ . Note that if the actual  $\beta/\alpha$  value inherent in a set of clinical data is larger, the slope of the TCP curve will also be larger. When fitting the RH model to such clinical data, the upper limit of acceptable fit  $\mu$  values will thus also increase, as observed in our fitting exercises.

Not only can fits with a population model suggest an incorrect amount of population heterogeneity when the data *does* contain heterogeneity, but it is also possible that fits may suggest population heterogeneity when the data actually has none. This is evidenced in Fig. 5.10 that shows fits of the RH model to pseudo-data that is based on set #2's parameter values, and thus contains no heterogeneity. The three fits illustrated correspond to significant coefficients of variation of 20, 30, and 40 % (or  $\mu = 5.0, 3.3,$  and  $2.5$ ). All three fits yield remarkably good  $p$ -values of greater than or equal to 0.50. This result can be explained from the slope equation for the individual Poisson

TCP model (Eq. (5.31)) –  $\theta_{50(ind)} = \frac{\ln 2}{2} \alpha \left( 1 + 2 \frac{\beta}{\alpha} \frac{D_{50}}{n} \right)$ . An *individual* TCP curve (or

a curve for a population without heterogeneity) will have a shallow slope if  $\alpha$  is small, and  $\beta/\alpha$  is close to zero. The shallower the slope of individual TCP dose-response data, the greater the degree of population heterogeneity that could be suggested by fits to this data using a population model. The value of  $\alpha = 0.20$  used to generate the pseudo-data represented in Fig. 5.10 is not, it is noted, especially small, yet this data could be confused with data containing a significant amount of heterogeneity.

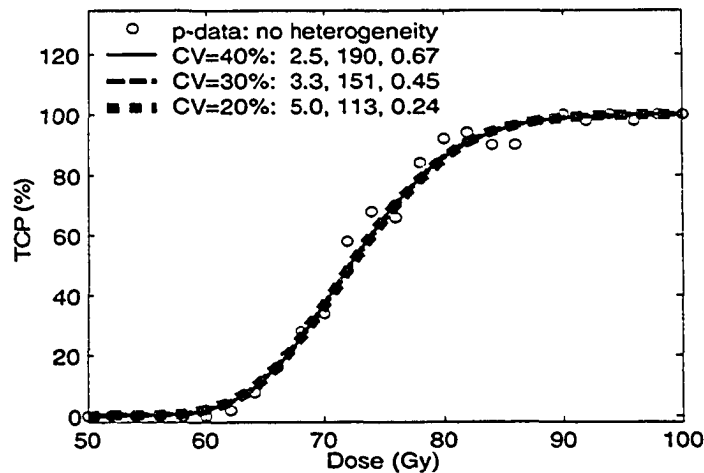


**Figure 5.10.** Fits (lines) of the RH model to pseudo-data (circles) based on parameter values (set #2) that describe a population without heterogeneity. The numbers in the legend correspond to fit values of  $\mu$ ,  $\kappa'/\alpha$ , and  $\beta/\alpha$ . Fits suggesting considerable population heterogeneity – e.g. CV's of 20, 30, or 40 % – all describe this data set well (fit lines are nearly indistinguishable).

There are potential clinical consequences to the apparent inability to distinguish between population heterogeneity and the strength of the  $\beta$ -mechanism when fitting clinical data. An example is illustrated in Fig. 5.11, which shows four theoretical TCP curves calculated using two sets of radiobiological parameters for each of two different fractionation regimes. The two sets of parameter values are: (i)  $\kappa = 11.6$ ,  $\sigma_\kappa = 0$ ,  $\alpha = 0.20$ ,  $\sigma_\alpha = 0.05$ ,  $\beta = 0.008$ ,  $\lambda = 0$ , and  $\sigma_\lambda = 0$ , which correspond to RH model parameters of  $\mu = 4$ ,  $\beta/\alpha = 0.04$ , and  $\kappa'/\alpha = 58$ ; and (ii)  $\kappa = 17.6$ ,  $\sigma_\kappa = 0$ ,  $\alpha = 0.20$ ,  $\sigma_\alpha = 0.10$ ,  $\beta = 0.064$ ,  $\lambda = 0$ , and  $\sigma_\lambda = 0$ , equivalent to  $\mu = 2$ ,  $\beta/\alpha = 0.32$ , and  $\kappa'/\alpha = 88$ . The two sets of parameters give nearly identical TCP curves for the first fractionation regime of  $n = 30$  fractions in  $T = 39$  days, but quite different TCP curves for the second regime of  $n = 45$  fractions in  $T = 60$  days. Now, consider the case of a clinical data set where the true radiobiological characteristics of the patient population are given by the second set of parameters –  $\mu = 2$ ,  $\beta/\alpha = 0.32$ , and all patients in this data set were treated with approximately 30 fractions. If this clinical data were fit, and it was mistakenly assumed that the  $\beta/\alpha$  ratio was low, a “best-fit” might return values similar to the first set of parameters above –  $\mu = 4$ ,  $\beta/\alpha = 0.04$ . Using this fitting result to predict the TCP for a prolonged treatment having 45 fractions would errantly suggest that, to maintain a TCP of 80 %, the total dose would have to be increased by only  $\sim 2$  Gy, when in fact it would

need to be increased by  $\sim 10$  Gy. Of course, failure to adequately increase the dose level would reduce the expected TCP substantially.

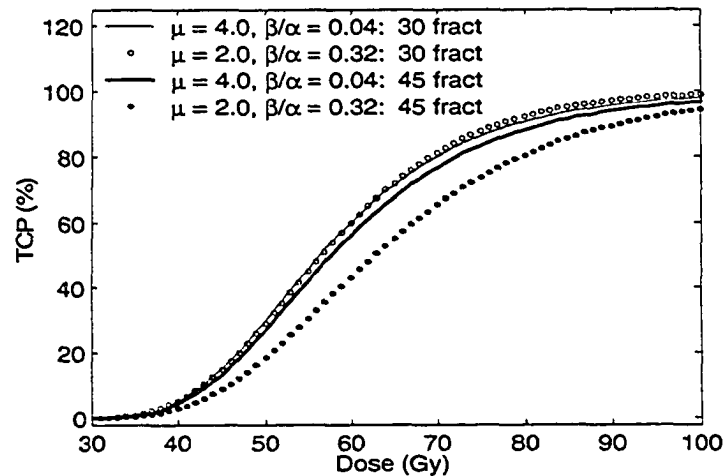


**Figure 5.11.** TCP curves generated for two parameter sets corresponding to different levels of heterogeneity and  $\beta$  strength, for each of two different fractionation regimes. The curves illustrate that if fitting to a clinical data set without sufficient diversity with respect to the number of fractions, the inability to distinguish between the  $\mu$  and  $\beta/\alpha$  fit parameters would lead to large uncertainties when predicting the TCP for a different fractionation regime.

### c. Fits to Pseudo-Data Consisting of Three Fractionation Regimes

Fits to pseudo-data sets containing data for three fractionation regimes ( $n = 15, 30,$  and  $45$ ) indicate that, though reduced, the correlation between the  $\mu$  and  $\beta/\alpha$  parameters is still a problem when fitting more diversified data sets. The results are shown in Figs. 5.12 and 5.13, and Table 5.3. Fits with  $\mu$  values ranging from 1.4 to 4.9 can be statistically supported when fitting the RH model to the diversified pseudo-data set generated from parameter set #1. The inclusion of three fractionation regimes in the data set does allow a lower limit of  $\mu$  to be established, in contrast to the fits to pseudo-data with only a single fractionation regime. Still, the range of  $\mu$  is quite large, suggesting that the coefficients of variation may be as low as 20 %, or as high as 70 %. A fit corresponding to a CV of 50 % to this pseudo-data with an inherent CV in  $\alpha$  of 25% is shown in Fig. 5.12. We also fit this data set using  $TCP_{1D}$ , which utilizes an explicit one-dimensional numerical integration over  $\alpha$ . It is interesting to note that for the latter model the range of statistically acceptable  $\mu$  values is considerably larger, from 1.1 to  $> 25$  (*i.e.* CV's of  $< 4\%$  up to  $\sim 90\%$ ). This is likely a result of additional

parameter correlations inherent in this model, which contains one more parameter than the RH model.

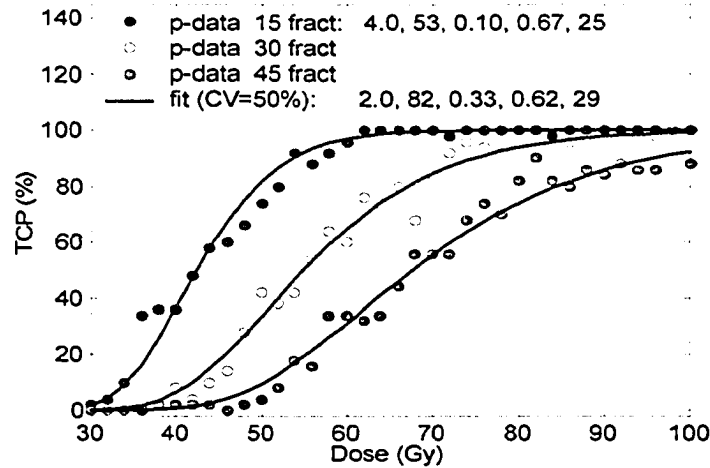
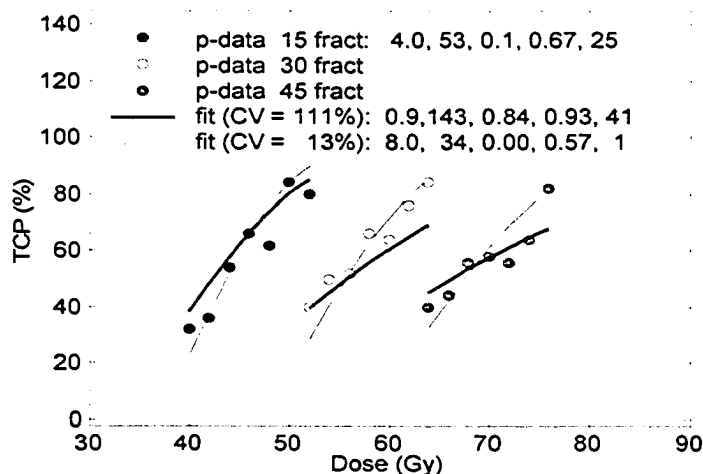


Figure 5.12. Example of a fit using the RH model assuming a CV of  $\mu = 2.0$  to pseudo-data generated for three fractionation regimes ( $n = 15, 30, 45$ ) that inherently contains heterogeneity characterized by  $\mu = 4.0$ . The  $p$ -value of the fit is 0.19. The numbers in the legend correspond to the parameter values  $\mu$ ,  $\kappa/\alpha$ ,  $\beta/\alpha$ ,  $\lambda/\alpha$ , and  $T_{lag}$ .

The impact of the sample size (*i.e.* number of patients), the number of dose points in the data set, and the relative strength of the  $\beta$ -mechanism are summarized in Table 5.3. Reducing the sample size from 50 to 20 patients increased the acceptable range of  $\mu$  values slightly from [1.4,4.9] to [1.0,5.4]. Decreasing the number of data points had a larger effect on the reliability of the  $\mu$  value extracted from fits: Fig. 5.13 shows fits corresponding to the lower and upper limits of the statistically acceptable range of 0.9 and 8.0 for this case. This pseudo-data set with fewer points is more representative of a real clinical data set, since it covers a TCP range of approximately 30 to 80 % for each fractionation regime, rather than the 0 to 100 % for the larger data set. The  $\beta$  strength inherent in the pseudo-data also has a large influence on the range of acceptable  $\mu$  values. The range increases from [1.4,4.9] to  $[-0.8,7]$  when the  $\beta/\alpha$  of the data increases from 0.10 to 0.33. Noteworthy is that when there is a strong  $\beta$  component in the data, the lower limit of  $\mu$  is no longer well constrained, indicating that fits to such data can plausibly suggest large degrees of population heterogeneity. When the actual  $\beta$  component of the data is zero, the heterogeneity factor is constrained to a significantly smaller range of  $\mu \in [1.8,3.9]$  (*i.e.* CV of between  $\sim 26$  to 55 %); the range is however, not *negligibly* small. The initial fitting exercises undertaken by Roberts and Hendry

using clinical data assumed a value of  $\beta = 0$ . This is a potential reason why they extracted values of  $\mu$  with reasonably small uncertainties:  $\mu \in [1.5, 2.3]$  and  $\mu \in [1.9, 4.1]$  for the two clinical data sets they fit.



**Figure 5.13.** Fits to pseudo-data (three fractionation regimes,  $\mu = 4.0$ ) with a smaller number of dose points. Statistically acceptable ( $p$ -value  $> 0.05$ ) fits to this data can be found with  $\mu$  values as low as 0.9 and as high as 8.0. The numbers in the legend correspond to the parameters  $\mu$ ,  $\kappa/\alpha$ ,  $\beta/\alpha$ ,  $\lambda/\alpha$ , and  $T_{lag}$ .

description	pseudo-data					fit	
	parameter set #	$\mu$	$\beta/\alpha$ ( $\text{Gy}^{-1}$ )	$npat$	$ndpts$	fit model	fit range: $\mu$
default data and fit	1	4.0	0.10	50	108	$TCP_{RH}$	[1.4, 4.9]
fit: uses $TCP_{ID}$	1	4.0	0.10	50	108	$TCP_{ID}$	[1.1, 25+]
data: smaller $npat$	1	4.0	0.10	20	108	$TCP_{RH}$	[1.0, 5.4]
data: fewer dose pts	1	4.0	0.10	50	21	$TCP_{RH}$	[0.9, 8.0]
data: no $\beta$	3	4.0	0	50	108	$TCP_{RH}$	[1.8, 3.9]
data: larger $\beta$	4	4.0	0.33	50	108	$TCP_{RH}$	[0, 8.7]

**Table 5.3.** The effect of different variables on the statistically acceptable range of fit values for the heterogeneity factor  $\mu$  extracted from fits to pseudo-data generated for three fractionation regimes. The variables investigated are the model ( $TCP_{ID}$  or  $TCP_{RH}$ ) used to fit the pseudo-data, and the characteristics of the pseudo-data: the number of patients per dose point ( $npat$ ), the number of data points ( $ndpts$ ), and the inherent strength of the  $\beta$ -mechanism.

## v. Discussion and Conclusion

A number of conclusions can be drawn from our fitting exercises. First, the results suggest that use of the Roberts and Hendry model to extract accurate estimates of

the population heterogeneity inherent in a clinical data set may be error-prone. This problem is, however, not a unique feature of the RH model, but would also likely plague any other population model. The reason is that, *populations representing very different radiobiological characteristics can produce data sets that are, within statistical errors, very similar*. This was illustrated, for example, by the fact that TCP curves generated with the  $TCP_{1D}$  model corresponding to very dissimilar amounts of heterogeneity could adequately describe a TCP data set containing data from three different fractionation regimes. The underlying explanation for this is the correlation between heterogeneity ( $\mu$ ) and cellular radiosensitivity ( $\alpha$  and particularly  $\beta$ ) with respect to tumor dose response. The changes in slope of TCP curves that result from differing amounts of population heterogeneity can generally also be effected by differing levels of  $\beta/\alpha$ .

An obvious corollary to the first conclusion is that, accurate estimates of  $\beta/\alpha$  can not be made from fits to clinical data without knowledge of the inherent heterogeneity of the data set. A similar point was made recently in the work of Carlone *et al.*<sup>54</sup> The relation between heterogeneity and estimates of the  $\alpha/\beta$  ratio is of some current interest. Typically, it has been assumed that most tumors have an  $\alpha/\beta$  ratio of  $\sim 10$  Gy. There have been several recent reports that prostate tumors have a low  $\alpha/\beta$  ratio (large  $\beta/\alpha$ ) of approximately 3 Gy,<sup>55,56</sup> with one report giving a value as low as 1.2 Gy.<sup>57,58</sup> Such low  $\alpha/\beta$  ratios would make estimation of tumor heterogeneity more difficult. Conversely, Carlone *et al.* indicated that population heterogeneity introduces large uncertainties in the determination of  $\alpha/\beta$ : in their study, the upper 95 % confidence limit for  $\alpha/\beta$  was  $\sim 7$  Gy for the case when the best estimate for this ratio was only 2.5 Gy.

A distinction between heterogeneity and  $\beta$  strength could be made if the other fitting parameters were constrained to rather tight limits. Knowledge of the clonogen number and repopulation characteristics would largely fix the fit value of  $\beta/\alpha$ , which would in turn constrain  $\mu$ . However, constraints on the other parameters would require accurate in-vitro assays assessing these radiobiological characteristics, and knowledge of the true relationship between *in vitro* and *in vivo* parameter values. Sufficient parameter constraints can not be imposed simply on the basis of plausibility. This is particularly true when using a model that is parameterized in terms of ratios of parameters. For

instance, it is difficult to determine appropriate limits for the parameter  $\kappa/\alpha$ . Without *a priori* knowledge of  $\alpha$ , a range of  $\kappa/\alpha$  of *e.g.* 40 to 180 can not be dismissed as biologically unreasonable. A value of  $\alpha = 0.10$ , would mean that  $\kappa/\alpha = 180$  gives a clonogen number ( $N$ ) of  $6.6 \times 10^8$ , whereas if  $\alpha = 0.30$ ,  $\kappa/\alpha = 40$  suggests  $N = 1.6 \times 10^5$ , which is also credible. As shown in *e.g.* Fig. 5.7, this range of  $\kappa/\alpha$  values admits at least a four-fold difference in  $\mu$  values, and  $\beta/\alpha$  values that range from nearly zero to about one.

A familiar conundrum in radiobiological modeling has thus been illustrated: we would like to be able to extract radiobiological parameter values from clinical data so that they can be compared to estimates from *in vitro* assays; however, the unambiguous extraction of these parameters themselves relies on the use of accurate and representative *in vitro* assays.

## **C. Application of Robust TCP Models Incorporating Tumor Dynamics to Describe Fractionation Effects**

### ***i. Introduction***

Radiotherapy treatments are fractionated to take advantage of the greater recovery capabilities of many normal tissues as compared to some types of tumors. Tumor control probability (TCP) models can be useful in aiding in the design of optimal fractionation regimes.

The most common TCP models used to predict fractionation effects are based on use of the linear-quadratic (LQ) model of cell survival in conjunction with a Binomial or Poisson TCP expression. Frequently, the simplest time-independent variant of the LQ model assuming complete repair of sub-lethal damage between fractions is applied. If tumor repopulation is also assumed to be negligible, fractionation effects are then solely characterized by the familiar  $\alpha/\beta$  ratio. Reliance on such a simple characterization of fractionation is of course inadequate, however, if the dynamics of cellular repair, and the processes of repopulation and resensitization (reoxygenation and redistribution) are an important contributor to fractionation effects.<sup>59</sup>

In this work, we seek to elucidate the role of these time-dependent mechanisms in TCP models, and the predictive capabilities of the LQ model. To this end, we will fit a diverse set of fractionated dose response animal data published by Fischer and Moulder<sup>45</sup> using various TCP models. Specifically, a time-dependent repair expression, a TCP formulation derived by Zaider and Minerbo<sup>60</sup> that represents a theoretically robust treatment of repopulation, and a time-dependent expression describing cellular radiosensitivity that potentially accounts for reoxygenation effects, will be investigated.

## ii. Theory

### a. Repopulation: Limitations of the Poisson or Binomial TCP models

As noted in Section 5.A.ii.b, the conventional approach of accommodating repopulation in TCP models is through use of a simple exponential re-growth term via the substitution  $N \rightarrow N \exp(\lambda T)$  in either of the basic TCP formulations based on Binomial or Poisson statistics (cf. Eqs. (5.19) and (5.20)):

$$TCP_{Binomial} = (1 - p_s(D))^{N \exp(\lambda T)}$$

$$TCP_{Poisson} = \exp(-N \exp(\lambda T) p_s(D)).$$

(For simplicity, we will ignore the  $T_{lag}$  parameter in the above and subsequent formulas). The theoretical weaknesses of this approach have been discussed by Tucker *et al.*<sup>61</sup> Tucker *et al.* used numerical simulations to show that when repopulation is present, the distribution of surviving clonogens is not always well described by Binomial (or Poisson) statistics. The Binomial (or Poisson) formulation will in fact under-predict the true TCP. The reason stems from the fact that both the Binomial and the Poisson expressions are founded simply on *mean* cell survival probabilities ( $p_s(D)$ ), with the result that the stochasticity of cell kill and birth in combination is not properly modeled. Implicitly the Binomial (or Poisson) expression implies that repopulation continues even if all tumor clonogens are killed (*i.e.* after tumor control has been achieved).

Results from simulations similar to those done by Tucker *et al.*<sup>61</sup> are depicted in Fig. 5.14. A population of  $10^4$  identical tumors with radiobiological parameter values of  $N = 10^4$  initial clonogens,  $\alpha = 0.30 \text{ Gy}^{-1}$ ,  $\beta = 0.03 \text{ Gy}^{-2}$ , and  $\lambda = 0.17 \text{ days}^{-1}$  (potential doubling time of  $\sim 4$  days) was simulated for a treatment requiring  $T = 32$  days to deliver

$n = 25$  fractions of 1.7 Gy dose each. To simulate the stochasticity of cell kill, random numbers were generated and compared to the mean survival probability to determine if each remaining clonogen (in each tumor) would survive or be killed after each fraction of dose delivery. Similar Monte Carlo methods were also used to decide if each surviving clonogen would repopulate or not on any given day during the treatment. The distribution of the surviving number of clonogens at the end of treatment for the simulated population of tumors is compared to the corresponding predictions based on Binomial statistics in Fig. 5.14(a). The simulation suggests that the TCP, the probability of observing zero clonogens, is 53 %, which is 10 % higher than the Binomial prediction.

A second problem with the simple Binomial and Poisson TCP expressions is that they do not allow an evaluation of the TCP at times after treatment. Both these expressions predict that the TCP will approach zero as  $T$  increases towards infinity. In reality, in the absence of *spontaneous* tumor recurrence, the TCP should remain constant after treatment, since once killed, a tumor will remain killed. This is illustrated in Fig. 5.14(b). A simulation identical to the one above, except that the value of  $T$  is increased from 32 to 46 days, suggests the same value of 53 % for the TCP; in contrast, the model based on binomial statistics predicts a TCP of 0.01 %.

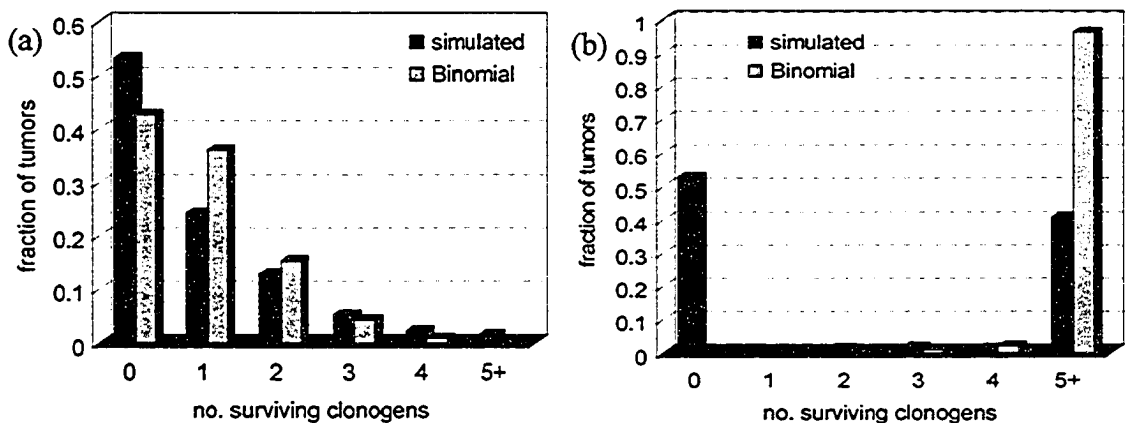


**Figure 5.14.** Comparison of simulated surviving clonogen distribution and corresponding predictions of binomial statistics for radiobiological parameter values of  $N = 10^4$ ,  $\alpha = 0.30$ ,  $\beta = 0.03$ , and  $\lambda = 0.17$ , and a treatment of 25 fractions of 1.7 Gy delivered in 32 days. (a) TCP immediately after treatment: simulated = 0.53, Binomial = 0.43. (b) TCP 2 weeks after treatment: simulated = 0.53, Binomial TCP = 0.

*b. Zaider-Minerbo TCP model: A Robust Method of Including Repopulation*

Zaider and Minerbo<sup>60</sup> derived a TCP expression incorporating repopulation that accounts for the stochasticity of both cell death and birth. Their TCP model is a solution to the following differential equation<sup>62</sup> describing the rate of change in  $P_i$ , the probability of  $i$  remaining clonogens, when the cell birth and death rates are  $\lambda$  and  $\delta$ :

$$\frac{dP_i(t)}{dt} = (i-1)[\lambda]P_{i-1}(t) - i[\lambda + \delta]P_i(t) + (i+1)[\delta]P_{i+1}(t). \quad (5.54)$$

The rate of cell death is composed of two terms,  $\delta = \delta_{nat} + \delta_{rad}(t)$ , one each describing death from natural cell processes ( $\delta_{nat}$ ) and from radiation-induced damage ( $\delta_{rad}(t)$ ). The Zaider-Minerbo solution to the differential equation is,

$$TCP(t) = \left[ 1 - \frac{p_s(t) e^{(\lambda - \delta_{nat})t}}{1 + \lambda \int_0^t \frac{p_s(t') e^{(\lambda - \delta_{nat})t'}}{p_s(t') e^{(\lambda - \delta_{nat})t'}} dt'} \right]^N, \quad (5.55)$$

where,  $t$  is the time from the start of treatment,  $p_s(t)$  is the probability of cell survival at time  $t$ , and as before,  $N$  and  $\lambda$  are the initial number of clonogens and the repopulation rate. Eq. (5.55) is a general expression that can be adapted for any temporal protocol of dose delivery. In our work, Ref. [14], we use Eq. (5.55) to derive the following expression applicable to the case of fractionated radiotherapy:

$$TCP_{ZM}(T_n) = \left[ 1 - \frac{p_s(T_n) e^{\lambda T_n}}{1 - p_s(T_n) e^{\lambda T_n} \sum_{k=1}^{n-1} \frac{1}{p_s(T_k)} [e^{-\lambda T_{k+1}} - e^{-\lambda T_k}]} \right]^N. \quad (5.56)$$

In Eq. (5.56),  $n$  is the number of fractions,  $T_k$  is the time from the start of treatment of the  $k^{th}$  fraction, and it is assumed that the rate of natural cell loss ( $\delta_{nat}$ ) is negligible in comparison to the rate of repopulation. It is important to note that our expression does not assume that the time interval between all fractions is the same, as is commonly done in TCP expressions for fractionated radiotherapy. By using the appropriate values for  $T_k$ , Eq. (5.56) will more accurately account for the repopulation that occurs during a realistic

fractionation schedule, e.g. one fraction per day during weekdays, with a three-day interval between Friday and subsequent Monday fractions.

Though more complicated, the Zaider-Minerbo TCP model is theoretically more robust than the Binomial TCP expression. As illustrated in Fig. 5.15, the Zaider-Minerbo model reduces to the Binomial expression when there is no repopulation, but also predicts the appropriate deviation from Binomial statistics when repopulation is present. In addition, it can be shown<sup>14</sup> that the Zaider-Minerbo model predicts that the TCP remains constant at times after completion of treatment ( $t > T_n$ ), as desired.

The magnitude of the error in the Binomial prediction of the TCP is depicted in Fig. 5.16, which plots the difference,  $TCP_{ZM} - TCP_{Binomial}$ , as a function of  $\lambda$  for several different values of  $N$ . This difference was evaluated at the  $D_{50}$  dose for the  $TCP_{Binomial}$  curve, which was calculated for each pair of  $\lambda$  and  $N$  values (and fixed values of  $\alpha = 0.30$ ,  $\beta = 0.03$ ,  $n = 25$ , and  $T = 32$ ). The under-prediction of the Binomial TCP model is most severe for rapidly proliferating tumors with fewer clonogens. Since it has been shown that the TCP of a larger tumor may be predominantly determined by the characteristics of a small radioresistant subpopulation within the tumor, the under-prediction of the Binomial expression may also be relevant for somewhat larger tumors than strictly implied by Fig. 5.16.

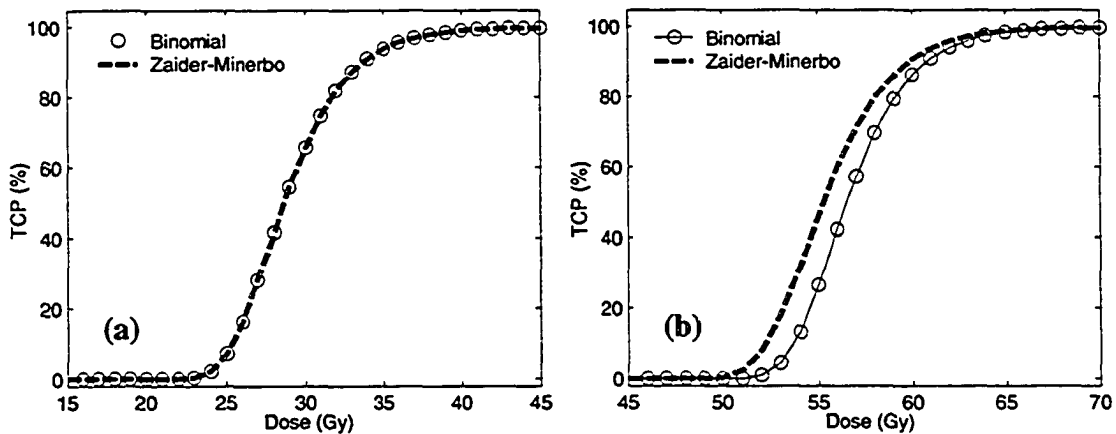


**Figure 5.15.** Comparison of Zaider-Minerbo and Binomial TCP model predictions for parameter values of  $N = 10^4$ ,  $\alpha = 0.30$ ,  $\beta = 0.03$ ,  $n = 25$ ,  $T = 32$  and (a)  $\lambda = 0$  or (b)  $\lambda = 0.35$ .

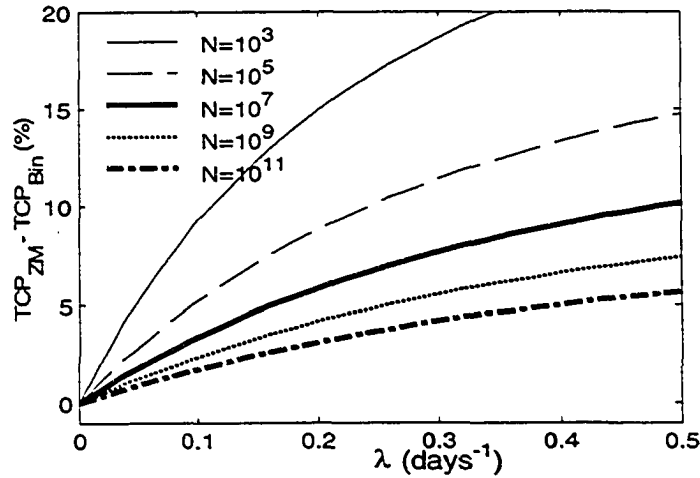


**Figure 5.16.** Magnitude of the error in the TCP based on Binomial statistics. The difference between the reference Zaider-Minerbo TCP,  $TCP_{ZM}$  and the Binomial TCP,  $TCP_{Bin}$ , is plotted as a function of  $\lambda$  for various values of  $N$ .  $TCP_{ZM}$  and  $TCP_{Bin}$  are evaluated at the predicted  $D_{50}$  dose for the  $TCP_{Bin}$  curve.

### c. Repair

Cellular repair is incorporated in TCP models via the expression for cell survival,  $p_s(D)$ . As discussed in Section 5.A.i, the simple time-*independent* LQ model in Eq. (5.2) is most commonly used when fitting data for fractionated treatments. To consider the dynamic nature of repair, the time-*dependent* incomplete repair LQ expression given in Eq. (5.6) is an alternative. This expression introduces the additional parameter  $\tau$ , which characterizes the rate of repair of sub-lethal damage.

### d. Reoxygenation: Incorporation of time-dependent radiosensitivity

Tumor reoxygenation may cause cellular radiosensitivity to vary during the course of a treatment. In this study, we employ a time-dependent expression for the  $\alpha$  radiosensitivity parameter,

$$\alpha(t) = \alpha_0 \exp(-c_1 t - c_2 t^2 / 2) + \alpha_m \left(1 - \exp(-c_1 t - c_2 t^2 / 2)\right), \quad (5.57)$$

to account for reoxygenation. The basic assumptions used to derive this expression are as follows. (A detailed derivation is given in Ref. [63]). The tumor is modeled as consisting of an inner hypoxic core of cells surrounded by an outer region of oxygenated tumor cells. It is assumed that the radiosensitivity of the entire tumor is determined by the value of  $\alpha(t)$  of the inner core of cells, with  $\alpha_0$  representing the initial value (value at

time,  $t = 0$ ) of this radiosensitivity. A uniform flux of oxygen diffusing from the outer to inner tumor regions, and a uniform oxygen concentration in the inner tumor core is assumed. The rate of change in the oxygen concentration of the inner core is then proportional to the difference in the oxygen concentrations of the inner and outer layers of the tumor, and is dependent on the permeability between the inner and outer layers. It is assumed that this permeability constant,  $k_{perm}$ , which is determined by the thickness of the outer tumor layer and the diffusion coefficient of oxygen, increases linearly with time:  $k_{perm}(t) = c_1 + c_2 t$ . Eq. (5.57) is also based on the further assumptions that the rate of change in the value of  $\alpha(t)$  is proportional to the rate of change in the oxygen concentration of the inner region, and that the  $\alpha$  values themselves of the inner and outer tumor regions are proportional to the oxygen concentrations in each region. Since the oxygen concentration in the outer, fully oxygenated region is assumed to remain constant (being equal to the concentration outside the tumor), the radiosensitivity of the outer region is also assumed to have a constant value, designated  $\alpha_m$ . The radiosensitivity of the inner region,  $\alpha(t)$ , approaches a maximum value equal to  $\alpha_m$  asymptotically in time (*i.e.* as  $t \rightarrow \infty$ ). The biological interpretation of  $\alpha(t) \rightarrow \alpha_m$  is that eventually enough of the tumor is destroyed to allow the entire tumor to become fully oxygenated. Although other processes besides reoxygenation (*e.g.* cell cycle redistribution) may alter cellular radiosensitivity during a treatment, these additional factors are not investigated in this work.

### *iii. Methods*

#### *a. Experimental Data*

The importance of including different dynamic cell processes – repair, repopulation, and resensitization – in TCP models used to describe fractionation effects was studied by fitting experimental *in vivo* dose-response data for rat rhabdomyosarcoma tumors (strain BA1112) published by Fischer and Moulder.<sup>45</sup> This data offers a number of advantages for modeling investigations. First, the population heterogeneity that is present in human clinical data should be largely absent from this animal data set. Since the rats came from the same genetic strain, it is expected that there will be minimal variability between the rats with respect to their radiosensitivity characteristics. Further,

as discussed by Fischer and Moulder, the initial tumor sizes for all the rats were very nearly the same, since the size of the tumors could be measured. For these reasons, it should be appropriate to use *individual* TCP models to fit the data. Thus, much of the ambiguity of biological interpretation potentially introduced by population heterogeneity (see Section 5.B) should be avoided.

Also useful is the diversity of the Fischer and Moulder data set. Included is data for seven different fractionation regimes – 1, 3, 5, 7, 10, 15, and 22 fractions delivered (Monday-Wednesday-Friday) in 1, 5, 10, 15, 22, 32, and 50 days, respectively. The  $D_{50}$  doses range from 57 to 118 Gy for these x-ray treatment regimes. An interesting feature of this data set is an “inverse” dose behavior manifest in the dose-response of the three and five fraction treatments. Increased fractionation generally leads to an increase in the dose required to achieve a given level of tumor control. However, the opposite is true for the three and five fraction schedules, with the three-fraction TCP data lying to the right (instead of the left) of the data corresponding to five fractions. It is noteworthy that a similar “inverse” fractionation behavior has also been observed for mouse mammary tumors by Fowler *et al.* <sup>64,65</sup>

We fit two different sets of the Fischer and Moulder data: one that excluded the three fraction data, and thus did not exhibit the inverse fractionation effect; and a second that included all seven fractionation regimes, and thus did show the effect. As demonstrated in the Results (Section 5.C.iv), the inverse behavior of the three and five fraction data could only be satisfactorily described if resensitization was explicitly incorporated in the TCP model.

#### *b. Fitting Technique*

For our fitting exercises, TCP models incorporating different combinations of the repair, repopulation, and resensitization mechanisms were constructed using combinations of the Binomial or Zaider-Minerbo TCP expressions in conjunction with various cell survival expressions. For example, to consider only repair processes, the Binomial TCP expression (Eq. (5.18)) was used with either the complete (Eq. (5.2)) or incomplete repair (Eq. (5.6)) LQ expressions. Using the Zaider-Minerbo (Eq. (5.56)) model, repopulation was incorporated. Repopulation effects were studied in combination

with repair, by using one of the aforementioned LQ models, or in isolation, by using a “single-hit” cell survival model where it is assumed that  $\beta$  is zero. Replacing the constant  $\alpha$  in the single-hit or LQ cell survival expressions with the time-dependent  $\alpha(t)$ , given in Eq. (5.57) and parameterized by  $\alpha_0$ ,  $\alpha_m$ ,  $c_1$  and  $c_2$ , accommodated potential resensitization effects.

The same fitting methodology – maximum-likelihood evaluation / Monte Carlo search – described in Section 5.B.iii.b was implemented here to derive best-fit parameter values. The quality of each fit was again assessed by calculating a  $p$ -value (*cf.* Eq. (5.53)), which requires knowledge of the statistics for each data point. However, the exact number of animals irradiated to each dose was only specified in Ref. [45] for one (5 fraction/10 days) fractionation schedule. An average of 12 rats per point was used for this five fraction data, and a total of 616 rats at 53 dose points (11.6 per point) were used for all seven fractionation regimes. Thus, we assumed statistics of twelve rats for each dose point of the six regimes for which statistics were not explicitly provided.

#### *iv. Results*

##### *a. Repair and Repopulation*

The effect of repair and repopulation processes on tumor control is clarified by the fits to the set of data which consists of six fractionation regimes, but excludes the data from the three fraction schedule. These fits are depicted in Fig. 5.17, with the corresponding best-fit parameter values presented in Table 5.4. We first fit the simplest TCP model, the Binomial TCP model without repopulation combined with the LQ expression assuming complete sub-lethal repair between fractions. This model contains no time-dependence, with fractionation effects being determined solely by the relative strength of the  $\beta$ -mechanism (*i.e.* the  $\alpha/\beta$  ratio) and the number of fractions. It is obvious both visually (Fig. 5.17(a)) and from the extremely low best-fit  $p$ -value of  $6 \times 10^{-15}$  that this model is unable to describe this fractionated TCP data. The second model also neglects repopulation, but adds an explicit time-dependence through use of the LQ-IR expression, which allows for partial repair of sub-lethal damage between fractions. The fit using this model (Fig. 5.17(b)) was statistically acceptable ( $p$ -value = 0.36). However, the corresponding parameter values do not seem biologically realistic.

The fit suggested a tumor with  $2.4 \times 10^2$  clonogens, extreme radioresistance as indicated by the very low values of  $5.6 \times 10^{-4} \text{ Gy}^{-1}$  and  $0.0018 \text{ Gy}^{-2}$  for  $\alpha$  and  $\beta$ , as well as a very slow rate of recovery from sub-lethal damage ( $\tau = 8.5$  days).

The Zaider-Minerbo (ZM) model, which incorporates repopulation, describes the Fischer-Moulder data very well. In contrast to the fit using the Binomial model without repopulation, the best-fit parameters from the fit with the ZM model and the LQ-IR cell survival expression are much more realistic. With the ZM model, the value of  $N$  is approximately fifty times larger, the  $\alpha$  value of 0.165 is biologically reasonable, as is the value of  $\lambda = 0.187$ , which corresponds to a potential doubling time of 3.7 days. The  $p$ -value of 0.73 for this fit is also somewhat higher. As evidenced by the low value of  $\beta = 7.7 \times 10^{-5}$ , this fit also suggests a weak  $\beta$ -mechanism for this tumor type. This result prompted us to repeat the fit with the ZM model, this time assuming single-hit cell survival. This “single-hit” fit is nearly identical to the previous fit including the  $\beta$ -mechanism, yielding very similar best-fit values for  $N$ ,  $\alpha$ , and  $\lambda$ , and a  $p$ -value of 0.80 that is in fact slightly higher, resulting from the reduction in the number of free fitting parameters by two. These results suggest that repopulation, and not repair, is the dominant determinant of fractionation effects for this tumor type.

TCP model	Description	$N$	$\alpha$ ( $\text{Gy}^{-1}$ )	$\beta$ ( $\text{Gy}^{-2}$ )	$\lambda$ ( $\text{days}^{-1}$ )	$\tau$ (days)	$p$ -value
Bin. / LQ	Repair (complete)	75	0.052	$7.0 \times 10^{-4}$	$\equiv 0$	$\equiv 0$	$6.2 \times 10^{-15}$
Bin./ LQ-IR	Repair (partial)	239	$5.6 \times 10^{-4}$	0.0018	$\equiv 0$	8.5	0.36
ZM / LQ-IR	Repair + Repop.	10662	0.165	$7.7 \times 10^{-5}$	0.187	3.4	0.73
ZM / SH	Repop. only	10428	0.169	$\equiv 0$	0.194	$\equiv 0$	0.80

Table 5.4. Best-fit parameter values corresponding to the fits shown in Fig. 5.17.

A fit (not shown) to this set of data was also performed using a model comprised of the Binomial TCP expression incorporating repopulation (Eq. (5.19)) and the LQ-IR survival model. This was done to facilitate a comparison between the conventional repopulation approach involving the simple substitution  $N \rightarrow N \exp(\lambda t)$ , and the more

theoretically robust approach inherent in the Zaider-Minerbo model. For this particular case, there was little difference in the two repopulation approaches: the fit with the Binomial repopulation model gave similar best-fit parameter values, and a  $p$ -value of 0.71 that was nearly as good as the ZM fit. Despite the fact that the Binomial approach may be sufficient in many circumstances, the general applicability of the Zaider-Minerbo model still makes its use preferable.

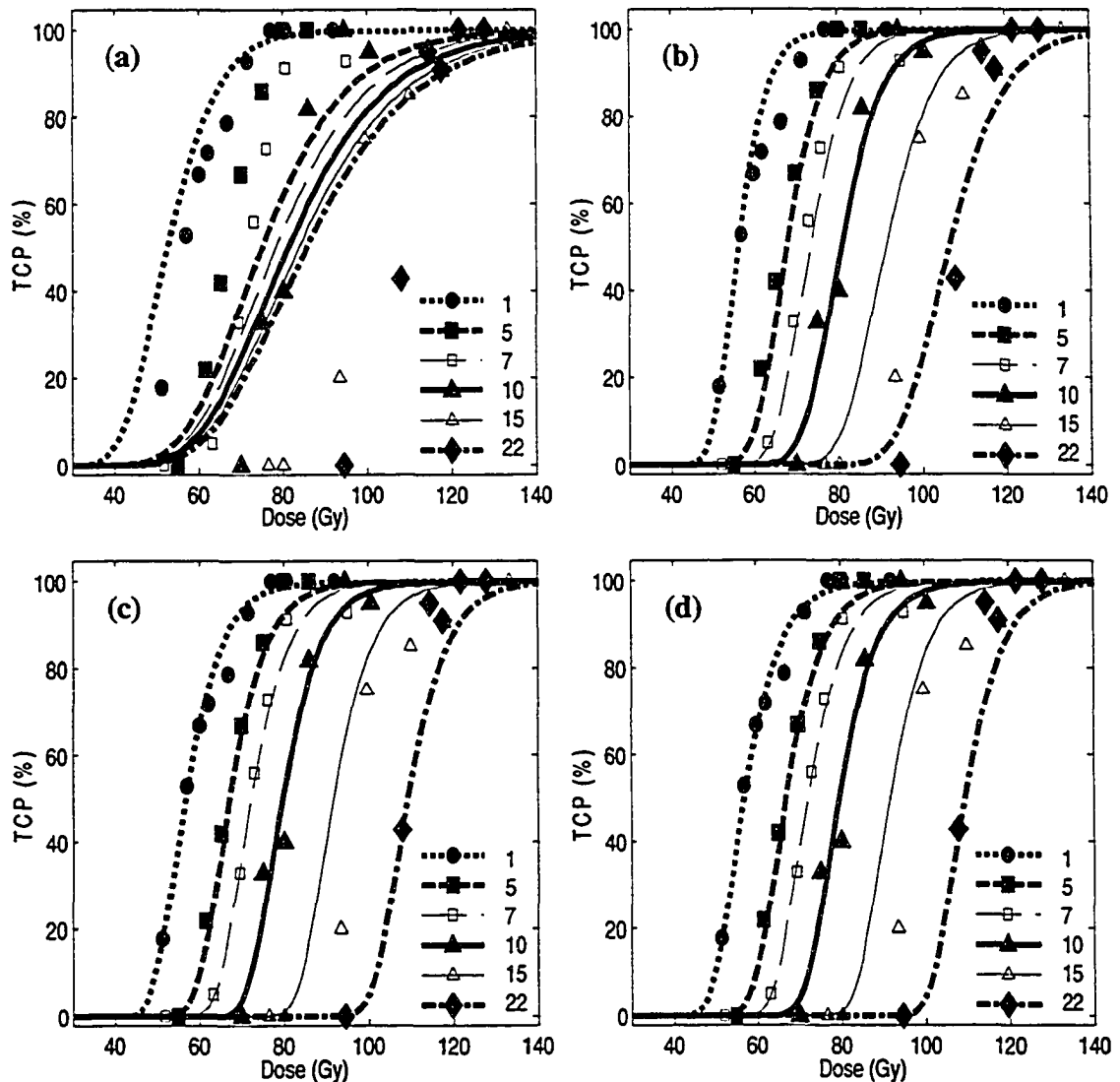


**Figure 5.17.** Fits (lines) of TCP models to six fractionation regimes ( $n$  as indicated in the legend) of the Fischer-Moulder data (symbols). (a) Binomial TCP / LQ survival: complete sub-lethal repair, no repopulation. (b) Binomial TCP / LQ-IR survival: partial sub-lethal repair, no repopulation. (c) Zaider-Minerbo (ZM) TCP / LQ-IR survival: partial sub-lethal repair, with repopulation. (d) Zaider-Minerbo TCP / single-hit (SH) survival: no repair, with repopulation.

In addition to best-fit values, we also determined ranges for the parameters  $N$ ,  $\alpha$ ,  $\beta$ , and  $\lambda$  that gave statistically *acceptable* fits, as conventionally defined by a  $p$ -value greater or equal to 0.05. For the purpose of this exercise, the Zaider-Minerbo model with the complete repair LQ survival expression was used. The ranges are as follows:  $N \in [3 \times 10^2, 8.4 \times 10^5]$ ,  $\alpha \in [0.10, 0.25]$ ,  $\beta \in [0, 0.0006]$ , and  $\lambda \in [0.10, 0.29]$ . The value of  $\beta$  is constrained primarily by the data corresponding to the regimes with few fractions. For example, for the acute treatment, the  $\beta$  term in the LQ expression becomes very large at the doses involved ( $D_{50} = 57$  Gy for the acute treatment) unless  $\beta$  is small. The range of  $N$  from our fits is not consistent with the value of  $\log_{10} N = 7.55 \pm 0.21$  calculated by Fischer and Moulder for their rat tumors. Although only conjecture, one plausible explanation for the low  $N$  values extracted from our fits is that they represent the number of clonogens from the most radioresistant subpopulation within each tumor. It would also be of interest to compare our radiosensitivity parameter values to other *in vitro* or *in vivo* estimates. Fischer and Moulder provide *in vitro* cell survival parameters for this cell line; however, these parameters are for a multi-target cell survival expression, and are thus not directly comparable to our LQ parameters. A cell survival curve generated with the Fischer-Moulder multi-target parameters does seem to suggest a significantly more curved cell-survival shape, indicative of a relatively stronger  $\beta$ -mechanism than indicated by our fit values. LQ parameters for a tumor cell line (rhabdomyosarcoma R1H) derived from the BA1112 line used in the Fischer-Moulder experiments are given in the work of Vogler and Beck-Bornholdt.<sup>66</sup> These values are  $\alpha = 0.20$ ,  $\beta = 0.041$  for *in vitro* cells, and  $\alpha = 0.010$ ,  $\beta = 0.0081$  for *in vivo* hypoxic cells. Though likely not directly comparable to the values from the BA1112 tumor line, it is noteworthy that the *in vitro* and *in vivo* estimates differ substantially. A general comment made by Vogler and Beck-Bornholdt was that *in vivo* fractionation effects can not likely be accurately extrapolated from results of *in vitro* single-dose or split-dose experiments used to characterize cellular dose response.

### *b. Resensitization*

The results of fits using the Zaider-Minerbo model to the entire Fischer-Moulder data set (all seven fractionation regimes), are shown in Fig. 5.18 and Table 5.5. For the first fit shown (Fig. 5.18(a)), the complete repair LQ model was used, and  $\alpha$  was kept constant with respect to time. The  $p$ -value of 0.13 for this fit indicates that it is statistically acceptable. However, the value is much lower than that obtained for the fit with the same model to the set excluding the three fraction regime. The reason is that this model is unable to account for the inverse fractionation behavior expressed by the three and five fraction regimes – note that the fitted line for the three fraction regime lies to the left of the five fraction regime, opposite to the trend exhibited by the data. We then used a model employing the same LQ expression, but with the constant  $\alpha$  replaced by the time-dependent expression for  $\alpha(t)$  given in Eq. (5.57). As illustrated (Fig. 5.18(b)), the use of this resensitization expression provides an excellent fit ( $p$ -value = 0.79) that now can describe the inverse fractionation present in the data. The best-fit parameter values for  $N$  and  $\lambda$  are smaller, but comparable to those obtained from the Zaider-Minerbo fits to the reduced (six-regime) data set. The parameters describing  $\alpha(t)$  are  $\alpha_0 = 0.085 \text{ Gy}^{-1}$ ,  $\alpha_m = 0.136 \text{ Gy}^{-1}$ ,  $c_1 \equiv 0 \text{ days}^{-1}$ , and  $c_2 = 0.076 \text{ days}^{-2}$ , which produce the curve shown in Fig. 5.18(d). The value of  $c_1$  was fixed to zero for this fit, since fits with  $c_1 \equiv 0$  and those with  $c_1$  allowed to vary freely produced nearly identical  $\alpha(t)$  curves. The biological interpretation of the resensitization curve is that initially the tumor radiosensitivity is dictated by a radioresistant hypoxic core characterized by an  $\alpha$  value of  $0.085 \text{ Gy}^{-1}$ . As the outer layers of the tumor are killed and the previously hypoxic inner regions become reoxygenated, the value of  $\alpha$  increases, reaching a substantially higher value of  $0.136 \text{ Gy}^{-1}$  at about day ten, which corresponds to the completion of the five fraction schedule. After day ten, the fitted value of  $\alpha$  plateaus, as would be expected, since no inverse fractionation effect is evident in the data for the regimes with more than five fractions.

The best-fit value of  $\beta = 0.0011 \text{ Gy}^{-2}$  for the resensitization fit (Fig. 5.18(b)) is still very low, implying an  $\alpha/\beta$  ratio of  $\sim 100$ , but is larger than the statistically permissible values obtained by fits to the reduced (six-regime) Fischer-Moulder data set. In fact, this small  $\beta$  component plays an integral role in the fits to the full (seven-regime)

data set. This is demonstrated by the fit depicted in Fig. 5.18(c), based on use of a single-hit survival model incorporating the time-dependent resensitization expression for  $\alpha$ . In this case, the fit ( $p$ -value = 0.10) is *unable* to account for the inverse fractionation effect. It may seem surprising that this apparently insignificant  $\beta$  component can significantly affect the results; however, it is again simply a function of the constraint placed on the fit by the data from the acute (1 fraction) treatment. As implied by the resensitization parameter values (see also Fig. 5.18(d)) for the fit with  $\beta \equiv 0$ , the acute treatment essentially forces a rather large initial value of 0.15 for  $\alpha$ . This is also consistent with the fit in Fig. 5.18(b), where  $\beta$  is allowed to vary freely: the best-fit values of  $\alpha_0 = 0.085 \text{ Gy}^{-1}$  and  $\beta = 0.0011 \text{ Gy}^{-2}$  combine to produce an “effective”  $\alpha$  value ( $\alpha_0 + \beta D_{50}$ ) of approximately  $0.15 \text{ Gy}^{-1}$ . The fact that the acute treatment is constraining the appropriate value of  $\beta$  is also confirmed by another fit (not shown) that was performed to a set of data which excluded the acute treatment. In this case, the inverse fractionation effect *could* be described while assuming single-hit mechanics (*i.e.*  $\beta \equiv 0$ ), and suggested a radiosensitivity that increased from  $\alpha = 0.078$  to  $\alpha = 0.170$ .

TCP model	$N$	$\alpha$ ( $\text{Gy}^{-1}$ )	$\beta$ ( $\text{Gy}^{-2}$ )	$\lambda$ ( $\text{days}^{-1}$ )	$\tau$ (days)	$p$ -value
ZM / LQ	5204	0.146	$1.5 \times 10^{-4}$	0.152	$\equiv 0$	0.13
ZM / LQ / Resens.	4091	0.085 – 0.136	0.0011	0.149	$\equiv 0$	0.79
ZM / SH / Resens.	5839	0.151 – 0.158	$\equiv 0$	0.182	$\equiv 0$	0.10

Table 5.5. Best-fit parameter values corresponding to the fits shown in Fig. 5.18

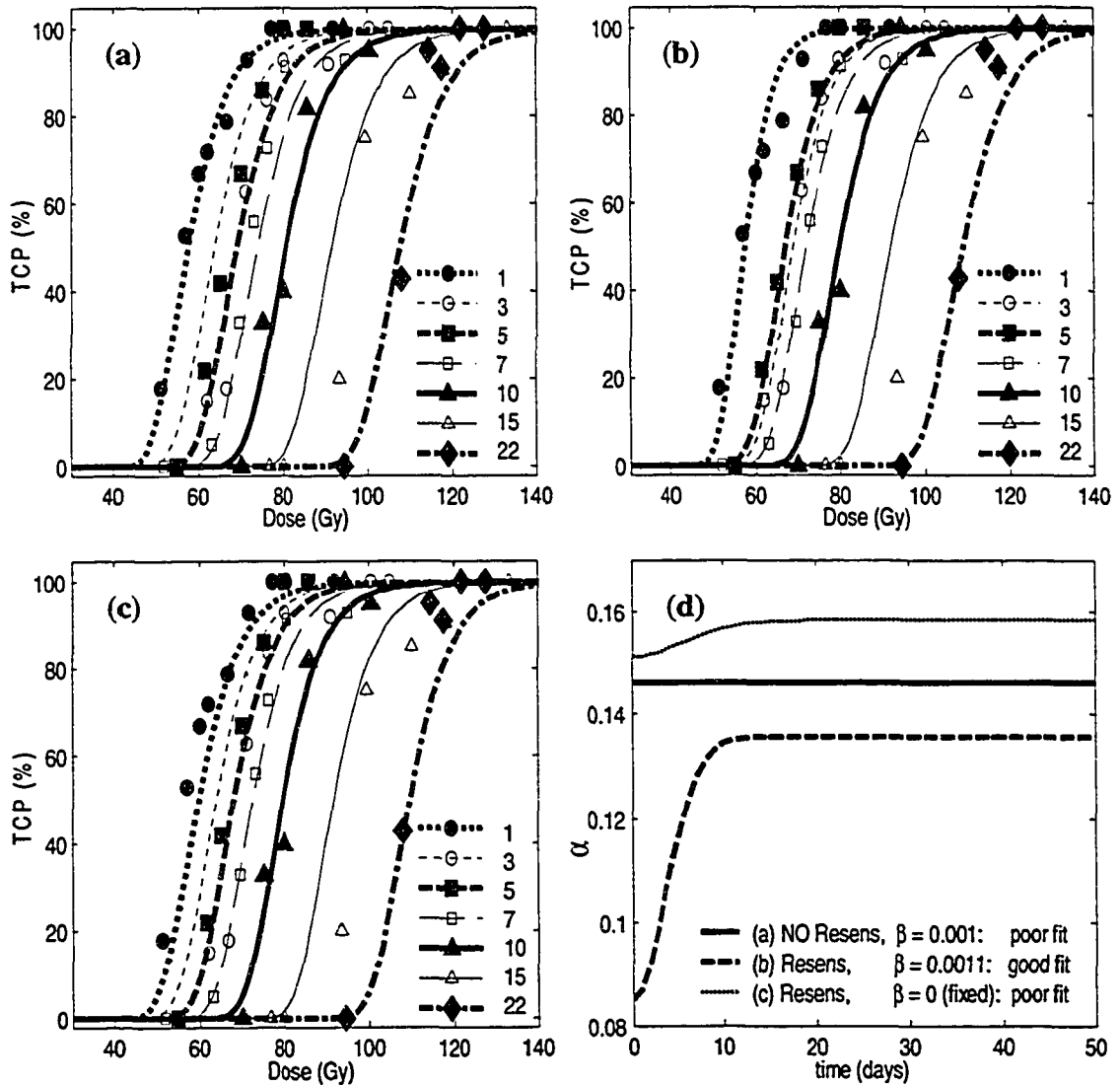


**Figure 5.18.** Fits (lines) with the Zaider-Minerbo (ZM) TCP model to all seven fractionation regimes of the Fischer-Moulder data (symbols). (a) Without resensitization ( $\alpha$  constant) and LQ cell survival. (b) With resensitization using time-dependent expression for  $\alpha$  (Eq. (5.57)) and LQ cell survival. (c) With resensitization and single-hit cell survival ( $\beta \equiv 0$ ). (d) Radiosensitivity  $\alpha$  as a function of time corresponding to plots in (a), (b), and (c). The radiosensitivity parameters for fit (b), the only one which can describe the inverse fractionation effect manifest between the three and five fraction data, are  $\alpha_0 = 0.085 \text{ Gy}^{-1}$ ,  $\alpha_m = 0.136 \text{ Gy}^{-1}$ ,  $c_1 \equiv 0 \text{ days}^{-1}$ , and  $c_2 = 0.076 \text{ days}^{-2}$ .

## v. Conclusion

The present work examined the role played by various dynamic tumor processes (repair, repopulation, and resensitization) in accounting for fractionation effects by fitting various TCP models to a diverse set of animal data.<sup>45</sup> A theoretically robust TCP expression derived by Zaider and Minerbo was used to study repopulation effects, while reoxygenation effects were incorporated with an explicit time-dependent expression for

the radiosensitivity parameter  $\alpha$ . The results in this study suggested for this tumor type the presence of only a weak  $\beta$ -mechanism, which only had a significant impact on the description of acute treatments. The observed fractionation pattern of this *in vivo* data could not be characterized simply by an  $\alpha/\beta$  ratio. Rather, for the multi-fraction treatments, repopulation seemed to be the dominant factor determining the effect of fractionation on dose-response. It is also interesting to note that the relative  $\beta$  strength suggested by our fits to the *in vivo* data is much smaller than would be predicted from *in vitro* experiments. This emphasizes that caution must be exercised when attempting to predict *in vivo* fractionation effects from *in vitro* estimates of the LQ cell survival parameters. This set of data also manifest an inverse fractionation effect which could be described by our resensitization model. Our fits suggested a radiosensitivity that increased during the first few fractions, consistent with an interpretation based on reoxygenation. Though this resensitization effect may not have a large influence on the observed dose response of treatments delivered with a large number of fractions, it could impact treatments that have few fractions, or those (such as brachytherapy) where the dose is delivered over a relatively short time period.

## D. References

<sup>1</sup>D. J. Brenner and D. E. Herbert, "The use of the linear-quadratic model in clinical radiation oncology can be defended on the basis of empirical evidence and theoretical argument," *Medical Physics* **24** (8), 1245-1248 (1997).

<sup>2</sup>M.C. Joiner, "Models of radiation cell killing," in *Basic Clinical Radiobiology*, edited by G. Steel (Oxford University Press, New York, 2002).

<sup>3</sup>R. K. Sachs and D. J. Brenner, "The mechanistic basis of the linear-quadratic formalism," *Medical Physics* **25** (10), 2071-2073 (1998).

<sup>4</sup>M. Zaider, "Sequel to the discussion concerning the mechanistic basis of the linear quadratic formalism," *Medical Physics* **25** (10), 2074-2075 (1998).

<sup>5</sup>M. Zaider, "There is no mechanistic basis for the use of the linear-quadratic expression in cellular survival analysis," *Medical Physics* **25** (5), 791-792 (1998).

<sup>6</sup>E. Alpen, *Radiation Biophysics* (Academic Press, San Diego, 1998).

- <sup>7</sup>R. K. Sachs, P. Hahnfeld, and D. J. Brenner, "The link between low-LET dose-response relations and the underlying kinetics of damage production/repair/misrepair," *International Journal of Radiation Biology* **72** (4), 351-374 (1997).
- <sup>8</sup>D. J. Brenner, L. R. Hlatky, P. J. Hahnfeldt, Y. Huang, and R. K. Sachs, "The linear-quadratic model and most other common radiobiological models result in similar predictions of time-dose relationships," *Radiation Research* **150** (1), 83-91 (1998).
- <sup>9</sup>S. B. Curtis, "Lethal and Potentially Lethal Lesions Induced by Radiation - a Unified Repair Model," *Radiation Research* **106** (2), 252-270 (1986).
- <sup>10</sup>D. Herbert, "Point/counterpoint: The use of the linear-quadratic model in clinical radiation oncology can be defended on the basis of empirical evidence and theoretical argument - Comment," *Medical Physics* **24** (8), 1329-1329 (1997).
- <sup>11</sup>J. F. Fowler, "The Linear-Quadratic Formula and Progress in Fractionated Radiotherapy," *British Journal of Radiology* **62** (740), 679-694 (1989).
- <sup>12</sup>M.C. Joiner and S.M. Bentzen, "Time-dose relationships: the linear-quadratic approach," in *Basic Clinical Radiobiology*, edited by G. Steel (Oxford University Press, New York, 2002).
- <sup>13</sup>S.M. Bentzen and M. Baumann, "The linear-quadratic model in clinical practice," in *Basic Clinical Radiobiology*, edited by G. Steel (Oxford University Press, New York, 2002).
- <sup>14</sup>N. A. Stavreva, P. V. Stavrev, B. Warkentin, and B. G. Fallone, "Investigating the effect of cell repopulation on the tumor response to fractionated external radiotherapy," *Medical Physics* **30** (5), 735-742 (2003).
- <sup>15</sup>H.D. Thames and J.H. Hendry, *Fractionation in Radiotherapy* (Taylor & Francis, Philadelphia, 1987).
- <sup>16</sup>E. L. Travis and S. L. Tucker, "Isoeffect Models and Fractionated Radiation-Therapy," *International Journal of Radiation Oncology Biology Physics* **13** (2), 283-287 (1987).
- <sup>17</sup>S. A. Roberts, J. H. Hendry, A. E. Brewster, and N. J. Slevin, "The Influence of Radiotherapy Treatment Time on the Control of Laryngeal-Cancer - a Direct Analysis of Data from 2 British-Institute-of-Radiology Trials to Calculate the Lag Period and the Time Factor," *British Journal of Radiology* **67** (800), 790-794 (1994).
- <sup>18</sup>S. A. Roberts and J. H. Hendry, "The Delay before Onset of Accelerated Tumor-Cell Repopulation During Radiotherapy - a Direct Maximum-Likelihood Analysis of a Collection of Worldwide Tumor-Control Data," *Radiotherapy and Oncology* **29** (1), 69-74 (1993).

- <sup>19</sup>D. J. Brenner, L. R. Hlatky, P. J. Hahnfeldt, E. J. Hall, and R. K. Sachs, "A Convenient Extension of the Linear-Quadratic Model to Include Redistribution and Reoxygenation," *International Journal of Radiation Oncology Biology Physics* **32** (2), 379-390 (1995).
- <sup>20</sup>S. M. Bentzen and S. L. Tucker, "Quantifying the position and steepness of radiation dose-response curves," *International Journal of Radiation Biology* **71** (5), 531-542 (1997).
- <sup>21</sup>A. Brahme, "Dosimetric precision requirements in radiation therapy," *Acta Radiologica Oncology* **23** (5), 379-391 (1984).
- <sup>22</sup>S.M.. Bentzen, "Dose-response relationships in radiotherapy," in *Basic Clinical Radiobiology*, edited by G. Steel (Oxford University Press, New York, 2002).
- <sup>23</sup>A. Jackson, G. J. Kutcher, and E. D. Yorke, "Probability of Radiation-Induced Complications for Normal-Tissues with Parallel Architecture Subject to Nonuniform Irradiation," *Medical Physics* **20** (3), 613-625 (1993).
- <sup>24</sup>A. Niemierko and M. Goitein, "Modeling of Normal Tissue-Response to Radiation - the Critical Volume Model," *International Journal of Radiation Oncology Biology Physics* **25** (1), 135-145 (1993).
- <sup>25</sup>P. Stavrev, A. Niemierko, N. Stavreva, and M. Goitein, "The application of biological models to clinical data," *Physica Medica* **17** (2), 71-82 (2001).
- <sup>26</sup>P. Stavrev, N. Stavreva, A. Niemierko, and M. Goitein, "Generalization of a model of tissue response to radiation based on the idea of functional subunits and binomial statistics," *Physics in Medicine and Biology* **46** (5), 1501-1518 (2001).
- <sup>27</sup>N. Stavreva, P. Stavrev, B. Warkentin, and B. G. Fallone, "Derivation of the expressions for gamma(50) and D50 for different individual TCP and NTCP models," *Physics in Medicine and Biology* **47** (20), 3591-3604 (2002).
- <sup>28</sup>G. Alsbeih, S. Malone, C. Lochrin, A. Girard, B. Fertil, and G. P. Raaphorst, "Correlation between normal tissue complications and in vitro radiosensitivity of skin fibroblasts derived from radiotherapy patients treated for variety of tumors," *International Journal of Radiation Oncology Biology Physics* **46** (1), 143-152 (2000).
- <sup>29</sup>S. M. Bentzen and S. L. Tucker, "Individualization of radiotherapy dose prescriptions by means of an in vitro radiosensitivity assay," *Radiotherapy and Oncology* **46** (2), 216-218 (1998).
- <sup>30</sup>W. Budach, J. Classen, C. Belka, and M. Bamberg, "Clinical impact of predictive assays for acute and late radiation morbidity," *Strahlentherapie Und Onkologie* **174**, 20-24 (1998).

- <sup>31</sup>E. Dikomey, K. Borgmann, J. Peacock, and H. Jung, "Why recent studies relating normal tissue response to individual radiosensitivity might have failed and how new studies should be performed," *International Journal of Radiation Oncology Biology Physics* **56** (4), 1194-200 (2003).
- <sup>32</sup>T. Girinsky, A. Bernheim, R. Lubin, T. Tavakolirazavi, F. Baker, F. Janot, P. Wibault, J. M. Cosset, P. Duvillard, A. Duverger, and B. Fertil, "In-Vitro Parameters and Treatment Outcome in Head and Neck Cancers Treated with Surgery and/or Radiation - Cell Characterization and Correlations with Local-Control and Overall Survival," *International Journal of Radiation Oncology Biology Physics* **30** (4), 789-794 (1994).
- <sup>33</sup>J. Haikonen, V. Rantanen, K. Pekkola, J. Kulmala, and R. Grenman, "Does skin fibroblast radiosensitivity predict squamous cancer cell radiosensitivity of the same individual?," *International Journal of Cancer* **103** (6), 784-788 (2003).
- <sup>34</sup>U. Oppitz, K. Baier, J. Wulf, R. Schakowski, and M. Flentje, "The in vitro colony assay: a predictor of clinical outcome," *International Journal of Radiation Biology* **77** (1), 105-110 (2001).
- <sup>35</sup>V. Rudat, A. Dietz, J. Nollert, C. Conradt, K. J. Weber, M. Flentje, and M. Wannemacher, "Acute and late toxicity, tumour control and intrinsic radiosensitivity of primary fibroblasts in vitro of patients with advanced head and neck cancer after concomitant boost radiochemotherapy," *Radiotherapy and Oncology* **53** (3), 233-245 (1999).
- <sup>36</sup>D. Slonina, M. Klimek, K. Szpytma, and A. Gasinska, "Comparison of the radiosensitivity of normal-tissue cells with normal-tissue reactions after radiotherapy," *International Journal of Radiation Biology* **76** (9), 1255-1264 (2000).
- <sup>37</sup>B. Stausbol-Gron, S. M. Bentzen, K. E. Jorgensen, O. S. Nielsen, T. Bundgaard, and J. Overgaard, "In vitro radiosensitivity of tumour cells and fibroblasts derived from head and neck carcinomas: mutual relationship and correlation with clinical data," *British Journal of Cancer* **79** (7-8), 1074-1084 (1999).
- <sup>38</sup>C. M. L. West, S. E. Davidson, S. A. G. Elyan, R. Swindell, S. A. Roberts, C. J. Orton, C. A. Coyle, H. Valentine, D. P. Wilks, R. D. Hunter, and J. H. Hendry, "The intrinsic radiosensitivity of normal and tumour cells," *International Journal of Radiation Biology* **73** (4), 409-413 (1998).
- <sup>39</sup>W. A. Brock, S. L. Tucker, F. B. Geara, I. Turesson, J. Wike, J. Nyman, and L. J. Peters, "Fibroblast Radiosensitivity Versus Acute and Late Normal Skin-Responses in Patients Treated for Breast-Cancer," *International Journal of Radiation Oncology Biology Physics* **32** (5), 1371-1379 (1995).
- <sup>40</sup>F. M. Buffa, S. E. Davidson, R. D. Hunter, A. E. Nahum, and C. M. L. West, "Incorporating biologic measurements (SF2, CFE) into a tumor control probability model

increases their prognostic significance: A study in cervical carcinoma treated with radiation therapy," *International Journal of Radiation Oncology Biology Physics* **50** (5), 1113-1122 (2001).

<sup>41</sup>B. Sanchez-Nieto, A. E. Nahum, and D. P. Dearnaley, "Individualization of dose prescription based on normal-tissue dose-volume and radiosensitivity data," *International Journal of Radiation Oncology Biology Physics* **49** (2), 487-499 (2001).

<sup>42</sup>R. I. Mackay and J. H. Hendry, "The modelled benefits of individualizing radiotherapy patients' dose using cellular radiosensitivity assays with inherent variability," *Radiotherapy and Oncology* **50** (1), 67-75 (1999).

<sup>43</sup>S. M. Bentzen, "Steepness of the Clinical Dose-Control Curve and Variation in the Invitro Radiosensitivity of Head and Neck Squamous-Cell Carcinoma," *International Journal of Radiation Biology* **61** (3), 417-423 (1992).

<sup>44</sup>G. K. Zagars, T. E. Schultheiss, and L. J. Peters, "Inter-Tumor Heterogeneity and Radiation Dose-Control Curves," *Radiotherapy and Oncology* **8** (4), 353-362 (1987).

<sup>45</sup>J. J. Fischer and J. E. Moulder, "Steepness of Dose-Response Curve in Radiation-Therapy - Theoretical Considerations and Experimental Results," *Radiology* **117** (1), 179-184 (1975).

<sup>46</sup>H. Suit, S. Skates, A. Taghian, P. Okunieff, and J. T. Efid, "Clinical Implications of Heterogeneity of Tumor Response to Radiation-Therapy," *Radiotherapy and Oncology* **25** (4), 251-260 (1992).

<sup>47</sup>S. A. Roberts and J. H. Hendry, "A realistic closed-form radiobiological model of clinical tumor-control data incorporating intertumor heterogeneity," *International Journal of Radiation Oncology Biology Physics* **41** (3), 689-699 (1998).

<sup>48</sup>J. D. Fenwick, "Predicting the radiation control probability of heterogeneous tumour ensembles: data analysis and parameter estimation using a closed-form expression," *Physics in Medicine and Biology* **43** (8), 2159-2178 (1998).

<sup>49</sup>S. Webb, "Optimum Parameters in a Model for Tumor-Control Probability Including Interpatient Heterogeneity," *Physics in Medicine and Biology* **39** (11), 1895-1914 (1994).

<sup>50</sup>B. M. Dubray and H. D. Thames, "The clinical significance of ratios of radiobiological parameters," *International Journal of Radiation Oncology Biology Physics* **35** (5), 1099-1111 (1996).

<sup>51</sup>W.H. Press, B.P. Flannery, S.A. Teukolsky, and Vetterling W.T., *Numerical Recipes* (Cambridge University Press, Cambridge, 1986).

- <sup>52</sup>J.C. Lagarias, J.A. Reeds, M.H. Wright, and P.E. Wright, "Convergence properties of the Nelder-Mead simplex method in low dimensions," *SIAM Journal of Optimization* **9** (1), 112-147 (1998).
- <sup>53</sup>F. M. Buffa, J. D. Fenwick, and A. E. Nahum, "Concerning Roberts and Hendry IJROBP 1998;41 : 689-699," *International Journal of Radiation Oncology Biology Physics* **44** (3), 737-739 (1999).
- <sup>54</sup>M. Carlone, D. Wilkins, B. Nyiri, and P. Raaphorst, "TCP isoeffect analysis using a heterogeneous distribution of radiosensitivity," *Medical Physics* **31** (5), 1176-1182 (2004).
- <sup>55</sup>J. Z. Wang, M. Guerrero, and X. A. Li, "How low is the alpha/beta ratio for prostate cancer?," *International Journal of Radiation Oncology Biology Physics* **55** (1), 194-203 (2003).
- <sup>56</sup>H. B. Kal and M. P. R. Van Gellekom, "How low is the alpha/beta ratio for prostate cancer?," *International Journal of Radiation Oncology Biology Physics* **57** (4), 1116-1121 (2003).
- <sup>57</sup>D. J. Brenner, A. A. Martinez, G. K. Edmundson, C. Mitchell, H. D. Thames, and E. P. Armour, "Direct evidence that prostate tumors show high sensitivity to fractionation (low alpha/beta ratio), similar to late-responding normal tissue," *International Journal of Radiation Oncology Biology Physics* **52** (1), 6-13 (2002).
- <sup>58</sup>J. Fowler, R. Chappell, and M. Ritter, "Is alpha/beta for prostate tumors really low?," *International Journal of Radiation Oncology Biology Physics* **50** (4), 1021-1031 (2001).
- <sup>59</sup>R. F. Kallman, "Facts and Models Applied to Tumor-Radiotherapy," *International Journal of Radiation Oncology Biology Physics* **5** (7), 1103-1109 (1979).
- <sup>60</sup>M. Zaider and G. N. Minerbo, "Tumour control probability: a formulation applicable to any temporal protocol of dose delivery," *Physics in Medicine and Biology* **45** (2), 279-293 (2000).
- <sup>61</sup>S. L. Tucker, H. D. Thames, and J. M. G. Taylor, "How Well Is the Probability of Tumor Cure after Fractionated-Irradiation Described by Poisson Statistics," *Radiation Research* **124** (3), 273-282 (1990).
- <sup>62</sup>D.G. Kendall, "On the generalized 'birth and death' process," *Annals of Mathematical Statistics* **19**, 1-15 (1948).
- <sup>63</sup>N. Stavreva, B. Warkentin, P. Stavrev, and B. Fallone, "Investigating the effect of clonogen resensitization on the tumor response to fractionated external radiotherapy," accepted for publication in *Medical Physics* (2005).

<sup>64</sup>J. F. Fowler, J. Denekamp, A. L. Page, A. C. Begg, S. B. Field, and K. Butler, "Fractionation with x rays and neutrons in mice: response of skin and C 3 H mammary tumours," *British Journal of Radiology* **45** (532), 237-49 (1972).

<sup>65</sup>J. F. Fowler, J. Denekamp, P. W. Sheldon, A. M. Smith, A. C. Begg, S. R. Harris, and A. L. Page, "Optimum fractionation in X-ray treatment of C3H mouse mammary tumours," *British Journal of Radiology* **47** (563), 781-9 (1974).

<sup>66</sup>H. Vogler and H. P. Beckbornholdt, "Radiotherapy of the Rhabdomyosarcoma R1h of the Rat - Kinetics of Cellular Inactivation by Fractionated-Irradiation," *International Journal of Radiation Oncology Biology Physics* **14** (2), 317-325 (1988).

## Chapter 6: Conclusion

In the first part of this work we have described the development of 2-D and 3-D pre-treatment procedures for dosimetric verification of IMRT (intensity-modulated radiotherapy) treatments using an amorphous silicon flat-panel electronic portal imaging device (EPID). Such procedures are used to identify differences between the predicted dose distribution calculated by a treatment planning system (TPS) and the actual dose delivered, resulting from systematic procedural errors, dose delivery inaccuracies, or TPS dose calculation errors.

Both the 2-D and the 3-D verification techniques we developed rely on our deconvolution technique allowing the measurement of 2-D primary fluence profiles of IMRT fields with the EPID. To characterize signal spread in the EPID due to radiation and optical scattering, we used deconvolution kernels derived using Monte Carlo simulations of dose deposition in the EPID and empirical fitting methods. Relative fluence profiles measured with the EPID were found to be in very good agreement with the corresponding measurements of fluence made with a diamond detector. In the 2-D verification, 2-D beam's eye view (BEV) dose distributions were generated for each IMRT field in a treatment by convolving the EPID-measured fluence with a kernel describing dose deposition in a water phantom. For absolute dose calibration, EPID-based doses were cross-calibrated with ion chamber measurements made in water. The beam-by-beam 2-D verifications of three step-and-shoot IMRT treatments using the EPID were in good agreement with those performed with a similar film-based technique, with a mean percent difference of  $0.3 \pm 1.0\%$  (24 fields).

We also developed a complementary 3-D verification technique that provides a full 3-D dose distribution in the patient anatomy based on EPID measurements. In the 3-D technique, EPID-measured 2-D fluence modulation profiles for each IMRT field are used as input for the TPS, which then generates the 3-D dose distributions. Verification is accomplished by comparing the EPID-based 3-D dose distribution to the original planned dose distribution calculated by the TPS. TLD point dose measurements for an IMRT irradiation of an anthropomorphic phantom were in good agreement with the

EPID-based 3-D doses; in contrast, the planned TPS dose under-predicted the TLD measurement in a high-gradient region by approximately 16 %. Similarly, large discrepancies between EPID-based and TPS doses were also evident in dose profiles of small fields incident on a water phantom. These results suggest that our 3-D EPID-based method is effective in quantifying uncertainties in the dose calculations of our TPS for IMRT treatments. For three clinical head and neck cancer IMRT treatment plans, our TPS underestimated the mean EPID-based doses in the critical structures of the spinal cord and the parotids by approximately 4 Gy (11 – 14 %). Radiobiological modeling calculations performed with the computational module we developed indicate that such underestimates may lead to clinically significant under-predictions of normal tissue complication rates. It is interesting to note that the corresponding 2-D verifications of the same IMRT treatments were deemed acceptable based on clinical criteria. The 3-D verification results thus imply that small errors in the 2-D BEV fluence distributions may in some cases lead to larger than expected errors in the patient 3-D dose distribution.

We have thus developed two EPID-based verification procedures useful in ensuring the efficacy and safety of IMRT treatments. Our 2-D EPID-based technique is much more convenient and requires approximately half the time to perform as a similar film-based one, and for this reason, has replaced it in clinical practice at our clinic (Cross Cancer Institute (CCI)). Though our 3-D EPID-based technique is not currently utilized clinically, it also is a potentially valuable quality assurance tool that allows a much more direct evaluation of the clinical consequence of dosimetric uncertainties in IMRT, providing information not easily accessible with more conventional 2-D methods. Additional automation of our 3-D verification, perhaps through use of a different TPS, would make the 3-D method more attractive as a clinical technique. If either the 2-D or 3-D verification method were to be used in conjunction with IMRT treatments employing dynamic multi-leaf collimation (DMLC), detector ghosting effects and corrections would have to be considered in more detail. There are no current plans, however, to employ DMLC in clinical practice at the CCI. In an extension to this project that is currently being pursued (by another graduate student), a potential method of facily incorporating daily patient positioning errors and internal tumor or organ motion effects in the estimates of dosimetric uncertainties of IMRT treatments is being investigated.

Further refinements and extensions of our EPID-based verification methods are also possible. The results generated in this work were generated using the pencil-beam convolution dose calculation algorithm of one TPS. Thus, if other TPS's were available, further testing could establish how representative the magnitude of the 2-D and 3-D dose uncertainties we observed are of modern treatment planning systems in general. In addition, we could investigate the dependence of the verification results on the type of dose calculation algorithm, by performing verifications with the other dose calculation algorithm available with this TPS – a collapsed cone algorithm. (This collapsed cone algorithm is not in clinical use at our institute, which is why we generated our results with the pencil-beam algorithm.) Perhaps of most current interest would be studies involving Monte Carlo-based treatment planning systems, which are now becoming commercially available. Monte Carlo systems directly simulate radiation transport from the linac target, through the linac head (including the MLC), and into the patient volume (as characterized by CT data). Thus, their dose calculations should be much more accurate than convolution/superposition algorithms in regions where charged particle equilibrium does not exist – *e.g.* in high-gradient regions or in small IMRT sub-fields. Also, the uncertainties in the modeling of the incident fluence which appear to hamper the accuracy of our TPS should be greatly reduced with Monte Carlo systems, provided the materials and geometry of the linac head and MLC are correctly specified. Thus, it is hoped that there will be greater consistency between IMRT verification measurements and TPS calculations when using Monte Carlo systems. This will lead to greater confidence in treatment planning decisions based on TPS dose distributions.

The second part of this thesis consisted of a number of studies investigating the application and development of radiobiological models. Radiobiological modeling has a potentially significant role to play in the optimization, adaptation, and patient-specific customization of radiotherapy treatments, particularly those involving IMRT. However, the limited reliability of current radiobiological model predictions severely restricts the use of such models.

In one of our radiobiological modeling projects, a convenient computational tool was developed that furnishes current modeling predictions of tumor control probability

(TCP) and normal tissue complication probability (NTCP) for 3-D dose distributions. In essence, this tool is designed to amalgamate and make accessible current radiobiological knowledge as it pertains to treatment planning, and to serve as a useful complement to clinical experience in treatment plan evaluation. In addition to its use in assessing the potential clinical significance of the dose calculation uncertainties assayed by our 3-D IMRT verification technique, the program has also already been used in a research capacity at our clinic in studies requiring the retrospective evaluation of treatment plans. As warranted, additional radiobiological models and clinical databases can be added to this NTCP-TCP calculation module.

We also conducted more fundamental investigations of issues of recent interest in radiobiological modeling. In one study, we evaluated a recently proposed TCP model incorporating population heterogeneity, and used it to illustrate some of the inherent difficulties in extracting reliable estimates for biological parameters from fits to clinical data. For example, the results of this analysis suggest that model parameter correlations make it difficult to discriminate between the level of heterogeneity intrinsic to a clinical data set and the strength of the  $\beta$ -mechanism of cell kill. Such ambiguities complicate attempts to extract estimates of the  $\alpha/\beta$  ratio from fits to clinical data, which may be important if one wishes to use these estimates to predict fractionation effects. In a separate work, we examined the role of the dynamic processes of repair, repopulation, and resensitization in TCP models by fitting different variants of TCP models to a diverse set of fractionated animal dose-response data. To incorporate repopulation effects, we used a theoretically robust TCP formulation recently derived by Zaider and Minerbo. For the particular tumor line represented in this data set, the fitting results suggested the dominance of repopulation in determining the fractionation pattern, and a weak  $\beta$ -mechanism (relative to the  $\alpha$  (or single-hit) mechanism). Since the implied strength of the  $\beta$ -mechanism is much weaker than would be predicted from *in vitro* experiments, one conclusion of this fitting exercise was to re-affirm that *in vitro* estimates of the linear-quadratic (LQ) model parameters are not in general sufficient descriptors of fractionation. We also found that an inverse fractionation behavior manifest in the data for treatments with a small number of fractions could be accounted for by incorporating resensitization

(specifically reoxygenation) effects in the TCP model via a time-dependent expression for the radiosensitivity parameter  $\alpha$ .

In general, a main contributor to the unreliability of radiobiological modeling predictions is the paucity of data, and the lack of diversity and large statistical uncertainties in the data that does exist. For example, there is still insufficient data available to draw definitive conclusions about the dose-volume relationships of different tissues. This is particularly limiting for applications of models to IMRT treatments, since IMRT dose distributions are characterized by large heterogeneities. Increased archiving of 3-D dose distributions of treatment plans and corresponding treatment outcomes should produce more numerous, high-quality treatment databases. Such data-sets will allow more precise determination of dose-response parameters for various normal tissues – e.g.  $n$ ,  $m$ , and  $D_{50}$  for the Lyman model. This will provide clinicians additional guidance as to appropriate dose tolerance levels.

Acquisition of such “macroscopic” dose-response data, however, essentially helps enhance the *descriptive* capabilities of radiobiological models, and usually only with respect to characterizing population-averaged responses. This is hopefully only a small first step in the full realization of the potential benefit of radiobiological modeling to radiotherapy. Greater progress will rely on the development of the *predictive* capabilities of models, so that they can be used to customize radiotherapy treatments for individual patients, and to adapt for changing treatment conditions. This will require a fuller understanding of radiation response mechanisms, and methods of accurately measuring the parameters associated with them. However, as illustrated by our investigations, simple dose-response data is inadequate in this regard, since population heterogeneity confounds attempts to extract mechanistic model parameters. Further development of *in vitro* radiobiological assays is promising, although their use requires establishment of the relationship between *in vitro* measurement and *in vivo* response.

Exploiting the increasing role of various imaging technologies in radiotherapy provides an alternative (or complementary) approach that may allow direct measurements of *in vivo* dose response characteristics,<sup>1</sup> which will also enable a more precise knowledge of the heterogeneity of such characteristics within a population. For example, the imaging of a patient every day of treatment with an image-guided adaptive

radiotherapy protocol allows tumor size to be tracked during the course of treatment. From this it may be possible to glean information about cellular radiosensitivity or tumor proliferative capabilities. Even more exciting is the emergence of molecular and functional imaging modalities,<sup>2</sup> such as positron emission tomography (PET), and functional and spectroscopic magnetic resonance imaging (MRI). These modalities can provide data about tissue functioning and cellular activities, which complement the anatomical information provided by a conventional imaging modality such as CT (computed tomography). For instance, it may be possible to predict changes in radiosensitivity during treatment based on functional MRI images measuring the oxygenation status of a tumor. Using PET techniques to measure the metabolic activities of a tumor may provide another means of characterizing *in vivo* dose response. Further, it may be possible to identify the types and locations of radiation damage via the imaging of molecular markers correlated with specific biological processes (*e.g.* apoptosis, angiogenesis, metastasis, *etc.*). Measurements using these and other (*e.g.* genetic profiling) emerging technologies should facilitate extraction of biologically-meaningful parameter estimates that can subsequently be used in predictive models, allowing radiobiological modeling to play a fruitful role in truly adaptive and individualized radiotherapy.

## References

<sup>1</sup>Carlone, M., personal communication.

<sup>2</sup>Raaphorst, G.P., personal communication (via comments of external thesis review).

# Bibliography

(page numbers in the brackets at the end of each entry identify the locations of each reference in the thesis)

- Ahnesjo, A. (1991). Dose Calculation Methods in Photon Beam Therapy using Energy Deposition Kernels. Department of Radiation Physics. Stockholm, Ph.D. Thesis, Stockholm University. [p. 63]
- Alber, M. and F. Nusslin (1999). "An objective function for radiation treatment optimization based on local biological measures." *Physics in Medicine and Biology* 44(2): 479-493. [p. 16]
- Almond, P. R., P. J. Biggs, et al. (1999). "AAPM's TG-51 protocol for clinical reference dosimetry of high-energy photon and electron beams." *Medical Physics* 26(9): 1847-1870. [p. 66]
- Alpen, E. (1998). Radiation Biophysics. San Diego, Academic Press. [p. 144]
- Alsbeih, G., S. Malone, et al. (2000). "Correlation between normal tissue complications and in vitro radiosensitivity of skin fibroblasts derived from radiotherapy patients treated for variety of tumors." *International Journal of Radiation Oncology Biology Physics* 46(1): 143-152. [p. 159]
- American Association of Physicists in Medicine (2001). AAPM TG-50: Basic applications of multileaf collimators, Madison, Medical Physics Publishing. [p. 7]
- Amols, H. I., C. C. Ling, et al. (2003). Overview of the IMRT Process. A Practical Guide to Intensity-Modulated Radiation Therapy. Madison, Medical Physics Publishing. [p. 2]
- Antonuk, L. E. (2002). "Electronic portal imaging devices: a review and historical perspective of contemporary technologies and research." *Physics in Medicine and Biology* 47(6): R31-R65. [p. 9]
- Araki, F., R. Ikeda, et al. (2000). "Dose calculation for asymmetric photon fields with independent jaws and multileaf collimators." *Medical Physics* 27(2): 340-5. [p. 11]
- Azcona, J. D., R. A. C. Siochi, et al. (2002). "Quality assurance in IMRT: Importance of the transmission through the jaws for an accurate calculation of absolute doses and relative distributions." *Medical Physics* 29(3): 269-274. [p. 7]
- Bentzen, S. M. (1992). "Steepness of the Clinical Dose-Control Curve and Variation in the Invitro Radiosensitivity of Head and Neck Squamous-Cell Carcinoma." *International Journal of Radiation Biology* 61(3): 417-423. [pp. 159, 163]
- Bentzen, S. M. (2002). Dose-response relationships in radiotherapy. Basic Clinical Radiobiology. G. Steel. New York, Oxford University Press. [p. 149]
- Bentzen, S. M. and M. Baumann (2002). The linear-quadratic model in clinical practice. Basic Clinical Radiobiology. G. Steel. New York, Oxford University Press. [p. 145]
- Bentzen, S. M. and S. L. Tucker (1997). "Quantifying the position and steepness of radiation dose-response curves." *International Journal of Radiation Biology* 71(5): 531-542. [p. 148]

- Bentzen, S. M. and S. L. Tucker (1998). "Individualization of radiotherapy dose prescriptions by means of an *in vitro* radiosensitivity assay." *Radiotherapy and Oncology* **46**(2): 216-218. [p. 159]
- Bortfeld, T. (1999). "Optimized planning using physical objectives and constraints." *Seminars in Radiation Oncology* **9**(1): 20-34. [p. 15]
- Boyer, A. L., E. B. Butler, et al. (2001). "Intensity-modulated radiotherapy: Current status and issues of interest." *International Journal of Radiation Oncology Biology Physics* **51**(4): 880-914. [pp. 2, 3, 5, 15]
- Brahme, A. (1984). "Dosimetric precision requirements in radiation therapy." *Acta Radiologica Oncology* **23**(5): 379-391. [pp. 1, 149]
- Brahme, A. (1987). "Design Principles and Clinical Possibilities with a New Generation of Radiation-Therapy Equipment - a Review." *Acta Oncologica* **26**(6): 403-412. [p. 2]
- Brahme, A. (1988). "Optimization of Stationary and Moving Beam Radiation-Therapy Techniques." *Radiotherapy and Oncology* **12**(2): 129-140. [p. 5]
- Brahme, A. (1999). "Biologically based treatment planning." *Acta Oncologica* **38**: 61-68. [p. 16]
- Brahme, A. (1999). "Optimized radiation therapy based on radiobiological objectives." *Seminars in Radiation Oncology* **9**(1): 35-47. [p. 16]
- Brahme, A. and A. K. Agren (1987). "Optimal Dose Distribution for Eradication of Heterogeneous Tumors." *Acta Oncologica* **26**(5): 377-385. [p. 5]
- Brenner, D. J. and D. E. Herbert (1997). "The use of the linear-quadratic model in clinical radiation oncology can be defended on the basis of empirical evidence and theoretical argument." *Medical Physics* **24**(8): 1245-1248. [pp. 143, 144]
- Brenner, D. J., L. R. Hlatky, et al. (1995). "A Convenient Extension of the Linear-Quadratic Model to Include Redistribution and Reoxygenation." *International Journal of Radiation Oncology Biology Physics* **32**(2): 379-390. [p. 147]
- Brenner, D. J., L. R. Hlatky, et al. (1998). "The linear-quadratic model and most other common radiobiological models result in similar predictions of time-dose relationships." *Radiation Research* **150**(1): 83-91. [p. 144]
- Brenner, D. J., A. A. Martinez, et al. (2002). "Direct evidence that prostate tumors show high sensitivity to fractionation (low alpha/beta ratio), similar to late-responding normal tissue." *International Journal of Radiation Oncology Biology Physics* **52**(1): 6-13. [p. 181]
- Brock, W. A., S. L. Tucker, et al. (1995). "Fibroblast Radiosensitivity Versus Acute and Late Normal Skin-Responses in Patients Treated for Breast-Cancer." *International Journal of Radiation Oncology Biology Physics* **32**(5): 1371-1379. [p. 159]
- Bucciolini, M., F. B. Buonamici, et al. (2004). "Verification of IMRT fields by film dosimetry." *Medical Physics* **31**(1): 161-168. [p. 9]
- Budach, W., J. Classen, et al. (1998). "Clinical impact of predictive assays for acute and late radiation morbidity." *Strahlentherapie Und Onkologie* **174**: 20-24. [p. 159]
- Buffa, F. M., S. E. Davidson, et al. (2001). "Incorporating biologic measurements (SF2, CFE) into a tumor control probability model increases their prognostic significance: A study in cervical carcinoma treated with radiation therapy." *International Journal of Radiation Oncology Biology Physics* **50**(5): 1113-1122. [pp. 18, 159]

- Buffa, F. M., J. D. Fenwick, et al. (1999). "Concerning Roberts and Hendry IJROBP 1998;41 : 689-699." *International Journal of Radiation Oncology Biology Physics* 44(3): 737-739. [pp. 169, 171, 172]
- Burman, C., C. S. Chui, et al. (1997). "Planning, delivery, and quality assurance of intensity-modulated radiotherapy using dynamic multileaf collimator: a strategy for large-scale implementation for the treatment of carcinoma of the prostate." *International Journal of Radiation Oncology Biology Physics* 39(4): 863-73. [pp. 5, 7-9]
- Burman, C., G. J. Kutcher, et al. (1991). "Fitting of Normal Tissue Tolerance Data to an Analytic-Function." *International Journal of Radiation Oncology Biology Physics* 21(1): 123-135. [pp. 116, 117, 129, 135, 137]
- Cadman, P., R. Bassalow, et al. (2002). "Dosimetric considerations for validation of a sequential IMRT process with a commercial treatment planning system." *Physics in Medicine and Biology* 47(16): 3001-3010. [pp. 8, 112, 118]
- Carlone, M., personal communication. [p. 208]
- Carlone, M., D. Wilkins, et al. (2003). "Comparison of alpha/beta estimates from homogeneous (individual) and heterogeneous (population) tumor control models for early stage prostate cancer." *Medical Physics* 30(10): 2832-2848. [p. 18]
- Carlone, M., D. Wilkins, et al. (2004). "TCP isoeffect analysis using a heterogeneous distribution of radiosensitivity." *Medical Physics* 31(5): 1176-1182. [p. 181]
- Chang, J. and C. C. Ling (2003). "Using the frame averaging of aS500 EPID for IMRT verification." *Journal of Applied Clinical Medical Physics* 4(4): 287-299. [pp. 37-9]
- Chang, J., C. H. Obcemea, et al. (2004). "Use of EPID for leaf position accuracy QA of dynamic multi-leaf collimator (DMLC) treatment." *Medical Physics* 31(7): 2091-2096. [pp. 7, 10]
- Chang, J. H., G. S. Mageras, et al. (2001). "An iterative EPID calibration procedure for dosimetric verification that considers the EPID scattering factor." *Medical Physics* 28(11): 2247-2257. [pp. 10, 92, 93]
- Chang, J. W., G. S. Mageras, et al. (2000). "Relative profile and dose verification of intensity-modulated radiation therapy." *International Journal of Radiation Oncology Biology Physics* 47(1): 231-240. [p. 9]
- Chao, K. S. C., D. A. Low, et al. (1997). "Clinical and technical considerations for head and neck cancers treated by IMRT: Initial experience." *International Journal of Radiation Oncology Biology Physics* 39(2): 238-238. [p. 5]
- Cheng, J. C. H., J. K. Wu, et al. (2002). "Radiation-induced liver disease after three-dimensional conformal radiotherapy for patients with hepatocellular carcinoma: Dosimetric analysis and implication." *International Journal of Radiation Oncology Biology Physics* 54(1): 156-162. [p. 130]
- Cheung, R., S. L. Tucker, et al. (2003). "Dose-response for biochemical control among high-risk prostate cancer patients after external beam radiotherapy." *International Journal of Radiation Oncology Biology Physics* 56(5): 1234-1240. [p. 130]
- Convery, D. J. and M. E. Rosenbloom (1992). "The Generation of Intensity-Modulated Fields for Conformal Radiotherapy by Dynamic Collimation." *Physics in Medicine and Biology* 37(6): 1359-1374. [p. 5]

- Corletto, D., M. Iori, et al. (2003). "Inverse and forward optimization of one- and two-dimensional intensity-modulated radiation therapy-based treatment of concave-shaped planning target volumes: the case of prostate cancer." *Radiotherapy and Oncology* 66(2): 185-195. [p. 3]
- Cormack, A. M. (1987). "A Problem in Rotation Therapy with X-Rays." *International Journal of Radiation Oncology Biology Physics* 13(4): 623-630. [p. 5]
- Cormack, A. M. and R. A. Cormack (1987). "A Problem in Rotation Therapy with X-Rays - Dose Distributions with an Axis of Symmetry." *International Journal of Radiation Oncology Biology Physics* 13(12): 1921-1925. [p. 5]
- Cozzi, L., F. M. Buffa, et al. (2000). "Comparative analysis of dose volume histogram reduction algorithms for normal tissue complication probability calculations." *Acta Oncologica* 39(2): 165-171. [p. 124]
- Curtis, S. B. (1986). "Lethal and Potentially Lethal Lesions Induced by Radiation - a Unified Repair Model." *Radiation Research* 106(2): 252-270. [p. 144]
- Dale, R. G., J. H. Hendry, et al. (2002). "Practical methods for compensating for missed treatment days in radiotherapy, with particular reference to head and neck schedules." *Clinical Oncology* 14(5): 382-393. [p. 17]
- Dawson, L. A., D. Normolle, et al. (2002). "Analysis of radiation-induced liver disease using the Lyman NTCP model." *International Journal of Radiation Oncology Biology Physics* 53(4): 810-821. [p. 130]
- Day, M. J. (1950). "A note on the calculation of dose in x-ray fields." *British Journal of Radiology* 23(270): 368-9. [p. 11]
- De Angelis, C., S. Onori, et al. (2002). "An investigation of the operating characteristics of two PTW diamond detectors in photon and electron beams." *Medical Physics* 29(2): 248-254. [p. 33]
- De Deene, Y., C. De Wagter, et al. (2000). "Validation of MR-based polymer gel dosimetry as a preclinical three-dimensional verification tool in conformal radiotherapy." *Magnetic Resonance in Medicine* 43(1): 116-125. [p. 8]
- De Gersem, W. R. T., S. Derycke, et al. (1999). "Inhomogeneous target-dose distributions: A dimension more for optimization?" *International Journal of Radiation Oncology Biology Physics* 44(2): 461-468. [p. 16]
- De Gersem, W. R. T., S. Derycke, et al. (2000). "Optimization of beam weights in conformal radiotherapy planning of stage III non-small cell lung cancer: Effects on therapeutic ratio." *International Journal of Radiation Oncology Biology Physics* 47(1): 255-260. [p. 16]
- De Meerleer, G. O., L. Vakaet, et al. (2000). "Radiotherapy of prostate cancer with or without intensity modulated beams: A planning comparison." *International Journal of Radiation Oncology Biology Physics* 47(3): 639-648. [p. 16]
- Deasy, J. O. (2000). "Comments on the use of the Lyman-Kutcher-Burman model to describe tissue response to nonuniform irradiation." *International Journal of Radiation Oncology Biology Physics* 47(5): 1458-1459. [p. 124]
- Deasy, J. O., A. Niemierko, et al. (2002). "Methodological issues in radiation dose-volume outcome analyses: summary of a joint AAPM/NIH workshop." *Medical Physics* 29(9): 2109-27. [p. 122]

- Dikomey, E., K. Borgmann, et al. (2003). "Why recent studies relating normal tissue response to individual radiosensitivity might have failed and how new studies should be performed." *International Journal of Radiation Oncology Biology Physics* 56(4): 1194-200. [p. 159]
- Dogan, N., L. B. Leybovich, et al. (2002). "Comparative evaluation of Kodak EDR2 and XV2 films for verification of intensity modulated radiation therapy." *Physics in Medicine and Biology* 47(22): 4121-30. [p. 9]
- Dubray, B. M. and H. D. Thames (1996). "The clinical significance of ratios of radiobiological parameters." *International Journal of Radiation Oncology Biology Physics* 35(5): 1099-1111. [p. 163]
- Eilertsen, K. (1997). "Automatic detection of single MLC leaf positions with corrections for penumbral effects and portal imager dose rate characteristics." *Physics in Medicine and Biology* 42(2): 313-334. [p. 7]
- Eisbruch, A., R. K. Ten Haken, et al. (1999). "Dose, volume, and function relationships in parotid salivary glands following conformal and intensity-modulated irradiation of head and neck cancer." *International Journal of Radiation Oncology Biology Physics* 45(3): 577-587. [pp. 116, 117]
- El-Mohri, Y., L. E. Antonuk, et al. (1999). "Relative dosimetry using active matrix flat-panel imager (AMFPI) technology." *Medical Physics* 26(8): 1530-1541. [p. 35]
- Emami, B., J. Lyman, et al. (1991). "Tolerance of Normal Tissue to Therapeutic Irradiation." *International Journal of Radiation Oncology Biology Physics* 21(1): 109-122. [pp. 116, 117, 129, 137]
- Essers, M., R. Boellaard, et al. (1996). "Transmission dosimetry with a liquid-filled electronic portal imaging device." *International Journal of Radiation Oncology Biology Physics* 34(4): 931-941. [p. 11]
- Fenwick, J. D. (1998). "Predicting the radiation control probability of heterogeneous tumour ensembles: data analysis and parameter estimation using a closed-form expression." *Physics in Medicine and Biology* 43(8): 2159-2178. [pp. 159, 172]
- Fidanzio, A., L. Azario, et al. (2000). "PTW-diamond detector: Dose rate and particle type dependence." *Medical Physics* 27(11): 2589-2593. [p. 33]
- Fischer, J. J. and J. E. Moulder (1975). "Steepness of Dose-Response Curve in Radiation-Therapy - Theoretical Considerations and Experimental Results." *Radiology* 117(1): 179-184. [pp. 159, 183, 188, 190, 196]
- Fowler, J., R. Chappell, et al. (2001). "Is alpha/beta for prostate tumors really low?" *International Journal of Radiation Oncology Biology Physics* 50(4): 1021-1031. [p. 181]
- Fowler, J. F. (1989). "The Linear-Quadratic Formula and Progress in Fractionated Radiotherapy." *British Journal of Radiology* 62(740): 679-694. [pp. 145, 147, 148]
- Fowler, J. F., J. Denekamp, et al. (1972). "Fractionation with x rays and neutrons in mice: response of skin and C 3 H mammary tumours." *British Journal of Radiology* 45(532): 237-49. [p. 189]
- Fowler, J. F., J. Denekamp, et al. (1974). "Optimum fractionation in X-ray treatment of C3H mouse mammary tumours." *British Journal of Radiology* 47(563): 781-9. [p. 189]

- Girinsky, T., A. Bernheim, et al. (1994). "In-Vitro Parameters and Treatment Outcome in Head and Neck Cancers Treated with Surgery and/or Radiation - Cell Characterization and Correlations with Local-Control and Overall Survival." *International Journal of Radiation Oncology Biology Physics* 30(4): 789-794. [p. 159]
- Glendinning, A. G., S. G. Hunt, et al. (2001). "Recording accelerator monitor units during electronic portal imaging: application to collimator position verification during IMRT." *Physics in Medicine and Biology* 46(6): N159-N167. [p. 9]
- Greer, P. B. and C. C. Popescu (2003). "Dosimetric properties of an amorphous silicon electronic portal imaging device for verification of dynamic intensity modulated radiation therapy." *Medical Physics* 30(7): 1618-1627. [p. 47]
- Gum, F., J. Scherer, et al. (2002). "Preliminary study on the use of an inhomogeneous anthropomorphic Fricke gel phantom and 3D magnetic resonance dosimetry for verification of IMRT treatment plans." *Physics in Medicine and Biology* 47(7): N67-N77. [p. 8]
- Gustafsson, A., B. K. Lind, et al. (1994). "A Generalized Pencil Beam Algorithm for Optimization of Radiation-Therapy." *Medical Physics* 21(3): 343-357. [p. 5]
- Gustafsson, H., A. Karlsson, et al. (2003). "MAGIC-type polymer gel for three-dimensional dosimetry: Intensity-modulated radiation therapy verification." *Medical Physics* 30(6): 1264-1271. [p. 8]
- Haikonen, J., V. Rantanen, et al. (2003). "Does skin fibroblast radiosensitivity predict squamous cancer cell radiosensitivity of the same individual?" *International Journal of Cancer* 103(6): 784-788. [p. 159]
- Heijmen, B. J. M., K. L. Pasma, et al. (1995). "Portal Dose Measurement in Radiotherapy Using an Electronic Portal Imaging Device (Epid)." *Physics in Medicine and Biology* 40(11): 1943-1955. [p. 11]
- Herbert, D. (1997). "Point/counterpoint: The use of the linear-quadratic model in clinical radiation oncology can be defended on the basis of empirical evidence and theoretical argument - Comment." *Medical Physics* 24(8): 1329-1329. [p. 145]
- Herman, M. G., J. M. Balter, et al. (2001). "Clinical use of electronic portal imaging: Report of AAPM radiation therapy committee Task Group 58." *Medical Physics* 28(5): 712-737. [p. 9]
- Ibbott, G., A. Nelson, et al. (2002). An anthropomorphic head and neck phantom for evaluation of intensity modulated radiation therapy. (<http://rpc.mdanderson.org/rpc>). [pp. 8, 112]
- Jackson, A., G. J. Kutcher, et al. (1993). "Probability of Radiation-Induced Complications for Normal-Tissues with Parallel Architecture Subject to Nonuniform Irradiation." *Medical Physics* 20(3): 613-625. [pp. 122, 125, 130, 150]
- James, H. V., S. Atherton, et al. (2000). "Verification of dynamic multileaf collimation using an electronic portal imaging device." *Physics in Medicine and Biology* 45(2): 495-509. [pp. 7, 9]
- Joiner, M. C. (2002). Models of radiation cell killing. *Basic Clinical Radiobiology*. G. Steel. New York, Oxford University Press. [pp. 143, 144]

- Joiner, M. C. and S. M. Bentzen (2002). Time-dose relationships: the linear-quadratic approach. Basic Clinical Radiobiology. G. Steel. New York, Oxford University Press. [pp. 145, 146]
- Jones, L. and P. Hoban (2002). "A comparison of physically and radiobiologically based optimization for IMRT." *Medical Physics* 29(7): 1447-1455. [p. 16]
- Kal, H. B. and M. P. R. Van Gellekom (2003). "How low is the alpha/beta ratio for prostate cancer?" *International Journal of Radiation Oncology Biology Physics* 57(4): 1116-1121. [p. 181]
- Kallman, P., B. Lind, et al. (1988). "Shaping of Arbitrary Dose Distributions by Dynamic Multileaf Collimation." *Physics in Medicine and Biology* 33(11): 1291-1300. [p. 5]
- Kallman, P., B. K. Lind, et al. (1992). "An Algorithm for Maximizing the Probability of Complication-Free Tumor-Control in Radiation-Therapy." *Physics in Medicine and Biology* 37(4): 871-890. [p. 16]
- Kallman, R. F. (1979). "Facts and Models Applied to Tumor-Radiotherapy." *International Journal of Radiation Oncology Biology Physics* 5(7): 1103-1109. [p. 182]
- Kapatoes, J. M., G. H. Olivera, et al. (2001). "On the accuracy and effectiveness of dose reconstruction for tomotherapy." *Physics in Medicine and Biology* 46(4): 943-966. [p. 13]
- Kapatoes, J. M., G. H. Olivera, et al. (2001). "A feasible method for clinical delivery verification and dose reconstruction in tomotherapy." *Medical Physics* 28(4): 528-542. [p. 13]
- Kausch, C., B. Schreiber, et al. (1999). "Monte Carlo simulations of the imaging performance of metal plate/phosphor screens used in radiotherapy." *Medical Physics* 26(10): 2113-24. [p. 58]
- Kawrakow, I. and D. W. Rogers (2002). "The EGSnrc Code System: Monte Carlo Simulation of Electron and Photon Transport." NRCC Report PIRS-701, NRC Canada. [pp. 12, 49]
- Keller, H., M. Fix, et al. (1998). "Calibration of a portal imaging device for high-precision dosimetry: A Monte Carlo study." *Medical Physics* 25(10): 1891-1902. [p. 11]
- Keller, H., M. K. Fix, et al. (2000). "Theoretical considerations to the verification of dynamic multileaf collimated fields with a SLIC-type portal image detector." *Physics in Medicine and Biology* 45(9): 2531-2545. [p. 9]
- Kendall, D. G. (1948). "On the generalized 'birth and death' process." *Annals of Mathematical Statistics* 19: 1-15. [p. 185]
- Khan, F. M. (2003). The Physics of Radiation Therapy. Philadelphia, Lippincott Williams & Wilkins. [pp. 10, 69, 93]
- Kim, J. O., J. V. Seibers, et al. (2002). "A Monte Carlo Model of an Amorphous Silicon Flat Panel Imager for Portal Dose Prediction." *Proceedings of the 7th International Workshop on Electronic Portal Imaging, Vancouver, Canada*. [pp. 54, 59]
- Ko, L., J. O. Kim, et al. (2004). "Investigation of the optimal backscatter for an aSi electronic portal imaging device." *Physics in Medicine and Biology* 49(9): 1723-1738. [p. 59]

- Kutcher, G. J. and C. Burman (1989). "Calculation of Complication Probability Factors for Non-Uniform Normal Tissue Irradiation - the Effective Volume Method." *International Journal of Radiation Oncology Biology Physics* 16(6): 1623-1630. [p. 124]
- Kwa, S. L. S., J. V. Lebesque, et al. (1998). "Radiation pneumonitis as a function of mean lung dose: An analysis of pooled data of 540 patients." *International Journal of Radiation Oncology Biology Physics* 42(1): 1-9. [p. 130, 135]
- Lagarias, J. C., J. A. Reeds, et al. (1998). "Convergence properties of the Nelder-Mead simplex method in low dimensions." *SIAM Journal of Optimization* 9(1): 112-147. [p. 169]
- Langer, M., S. S. Morrill, et al. (1998). "A test of the claim that plan rankings are determined by relative complication and tumor-control probabilities." *International Journal of Radiation Oncology Biology Physics* 41(2): 451-457. [pp. 16, 122]
- Lee, N., C. Akazawa, et al. (2004). "A forward-planned treatment technique using multisegments in the treatment of head-and-neck cancer." *International Journal of Radiation Oncology Biology Physics* 59(2): 584-594. [p. 3]
- Levegrun, S., A. Jackson, et al. (2002). "Risk-group dependence of dose-response for biopsy outcome after three-dimensional conformal radiation therapy of prostate cancer." *Radiotherapy and Oncology* 63(1): 11-26. [p. 130]
- Litzenberg, D. W., J. M. Moran, et al. (2002). "Verification of dynamic and segmental IMRT delivery by dynamic log file analysis." *Journal of Applied Clinical Medical Physics* 3(2): 63-72. [p. 42]
- LoSasso, T. (2003). Quality assurance of IMRT. A Practical Guide to Intensity-Modulated Radiation Therapy. Madison, Medical Physics Publishing. [p. 7]
- Louwe, R. J. W., E. M. F. Damen, et al. (2003). "Three-dimensional dose reconstruction of breast cancer treatment using portal imaging." *Medical Physics* 30(9): 2376-2389. [p. 13]
- Low, D. A., J. F. Dempsey, et al. (1999). "Evaluation of polymer gels and MRI as a 3-D dosimeter for intensity-modulated radiation therapy." *Medical Physics* 26(8): 1542-1551. [p. 8]
- Lyman, J. T. (1985). "Complication Probability as Assessed from Dose Volume Histograms." *Radiation Research* 104(2): S13-S19. [p. 124]
- Mackay, R. I. and J. H. Hendry (1999). "The modelled benefits of individualizing radiotherapy patients' dose using cellular radiosensitivity assays with inherent variability." *Radiotherapy and Oncology* 50(1): 67-75. [pp. 18, 19, 159]
- MacKenzie, M. A., M. Lachaine, et al. (2002). "Dosimetric verification of inverse planned step and shoot multileaf collimator fields from a commercial treatment planning system." *Journal of Applied Clinical Medical Physics* 3(2): 97-109. [pp. 9, 62, 63]
- Mackie, T. R., T. Holmes, et al. (1993). "Tomotherapy - a New Concept for the Delivery of Dynamic Conformal Radiotherapy." *Medical Physics* 20(6): 1709-1719. [p. 2]
- Mackie, T. R., T. W. Holmes, et al. (1995). "Tomotherapy - Optimized Planning and Delivery of Radiation-Therapy." *International Journal of Imaging Systems and Technology* 6(1): 43-55. [p. 2]

- Manser, P., R. Treier, et al. (2002). "Dose response of an A-Si : H EPID on static and dynamic photon beams." *Medical Physics* 29(6): 1269-1269. [p. 38]
- Martel, M. K., W. M. Sahijdak, et al. (1998). "Fraction size and dose parameters related to the incidence of pericardial effusions." *International Journal of Radiation Oncology Biology Physics* 40(1): 155-161. [p. 130]
- Maryanski, M. J., R. J. Schulz, et al. (1994). "Magnetic-Resonance-Imaging of Radiation-Dose Distributions Using a Polymer-Gel Dosimeter." *Physics in Medicine and Biology* 39(9): 1437-1455. [p. 8]
- McCurdy, B. M. C., K. Luchka, et al. (2001). "Dosimetric investigation and portal dose image prediction using an amorphous silicon electronic portal imaging device." *Medical Physics* 28(6): 911-924. [pp. 11, 35, 54, 59]
- McCurdy, B. M. C. and S. Pistorius (2000). "A two-step algorithm for predicting portal dose images in arbitrary detectors." *Medical Physics* 27(9): 2109-2116. [p. 11]
- McDermott, L. N., R. J. W. Louwe, et al. (2004). "Dose-response and ghosting effects of an amorphous silicon electronic portal imaging device." *Medical Physics* 31(2): 285-295. [pp. 40, 42, 95]
- McNutt, T. R., T. R. Mackie, et al. (1996). "Modeling dose distributions from portal dose images using the convolution/superposition method." *Medical Physics* 23(8): 1381-1392. [p.p. 9, 13]
- MDS-Nordion, Helax-TMS Optimization Algorithms (Reference Manual). Veenendaal, The Netherlands. [pp. 3, 4]
- Memorial Sloan-Kettering Cancer Center (2003). A Practical Guide to Intensity-Modulated Radiation Therapy. Madison, Medical Physics Publishing. [p. 7]
- Menon, G. V. and R. S. Sloboda (2004). "Compensator thickness verification using an a-Si EPID." *Medical Physics* 31(8): 2300-12. [p. 11]
- Mohan, R., G. S. Mageras, et al. (1992). "Clinically Relevant Optimization of 3-D Conformal Treatments." *Medical Physics* 19(4): 933-944. [p. 16]
- Mohan, R., X. H. Wang, et al. (1994). "The Potential and Limitations of the Inverse Radiotherapy Technique." *Radiotherapy and Oncology* 32(3): 232-248. [p. 15]
- Moiseenko, V., J. Battista, et al. (2000). "Normal tissue complication probabilities: Dependence on choice of biological model and dose-volume histogram reduction scheme." *International Journal of Radiation Oncology Biology Physics* 46(4): 983-993. [pp. 16, 122]
- Moiseenko, V., T. Craig, et al. (2003). "Dose-volume analysis of lung complications in the radiation treatment of malignant thymoma: a retrospective review." *Radiotherapy and Oncology* 67(3): 265-274. [p. 130, 135]
- Munro, P. (1995). "Portal Imaging Technology: Past, Present, and Future." *Seminars in Radiation Oncology* 5(2): 115-133. [p. 9]
- Munro, P. and D. C. Bouius (1998). "X-ray quantum limited portal imaging using amorphous silicon flat-panel arrays." *Medical Physics* 25(5): 689-702. [pp. 35, 54]
- Niemierko, A. and M. Goitein (1991). "Calculation of Normal Tissue Complication Probability and Dose-Volume Histogram Reduction Schemes for Tissues with a Critical Element Architecture." *Radiotherapy and Oncology* 20(3): 166-176. [p. 124]

- Niemierko, A. and M. Goitein (1993). "Modeling of Normal Tissue-Response to Radiation - the Critical Volume Model." *International Journal of Radiation Oncology Biology Physics* 25(1): 135-145. [pp. 122, 125, 150, 151]
- Niemierko, A., M. Urie, et al. (1992). "Optimization of 3d Radiation-Therapy with Both Physical and Biological End-Points and Constraints." *International Journal of Radiation Oncology Biology Physics* 23(1): 99-108. [p. 16]
- Nucletron (1998). *Helax-TMS Dose Calculation Reference Manual*. Veenendaal, The Netherlands. [p.63]
- Okunieff, P., D. Morgan, et al. (1995). "Radiation dose-response of human tumors." *International Journal of Radiation Oncology Biology Physics* 32(4): 1227-1237. [p. 130]
- Oldham, M., I. Baustert, et al. (1998). "An investigation into the dosimetry of a nine-field tomotherapy irradiation using BANG-gel dosimetry." *Physics in Medicine and Biology* 43(5): 1113-1132. [p. 8]
- Oppitz, U., K. Baier, et al. (2001). "The in vitro colony assay: a predictor of clinical outcome." *International Journal of Radiation Biology* 77(1): 105-110. [p. 159]
- Paliwal, B., W. Tome, et al. (2000). "A spiral phantom for IMRT and tomotherapy treatment delivery verification." *Medical Physics* 27(11): 2503-2507. [p. 8]
- Parsaei, H., E. El-Khatib, et al. (1998). "The use of an electronic portal imaging system to measure portal dose and portal dose profiles." *Medical Physics* 25(10): 1903-1909. [p. 47]
- Partridge, M., M. Ebert, et al. (2002). "IMRT verification by three-dimensional dose reconstruction from portal beam measurements." *Medical Physics* 29(8): 1847-1858. [pp. 10, 13]
- Partridge, M., P. M. Evans, et al. (2000). "Leaf position verification during dynamic beam delivery: A comparison of three applications using electronic portal imaging." *Medical Physics* 27(7): 1601-1609. [p. 7, 9]
- Pasma, K. L., M. L. P. Dirkx, et al. (1999). "Dosimetric verification of intensity modulated beams produced with dynamic multileaf collimation using an electronic portal imaging device." *Medical Physics* 26(11): 2373-2378. [p. 9]
- Pasma, K. L., M. Kroonwijk, et al. (1998). "Accurate portal dose measurement with a fluoroscopic electronic portal imaging device (EPID) for open and wedged beams and dynamic multileaf collimation." *Physics in Medicine and Biology* 43(8): 2047-2060. [p. 11]
- Ploeger, L. S., M. H. P. Smitsmans, et al. (2002). "A method for geometrical verification of dynamic intensity modulated radiotherapy using a scanning electronic portal imaging device." *Medical Physics* 29(6): 1071-1079. [p. 9]
- Press, W. H., B. P. Flannery, et al. (1986). *Numerical Recipes*. Cambridge, Cambridge University Press. [pp. 164, 167]
- Raaphorst, G.P., personal communication (via comments of external thesis review). [p.209]
- Renner, W. D., M. Sarfaraz, et al. (2003). "A dose delivery verification method for conventional and intensity-modulated radiation therapy using measured field fluence distributions." *Medical Physics* 30(11): 2996-3005. [p. 13]
- Richardson, S. L., W. A. Tome, et al. (2003). "IMRT delivery verification using a spiral phantom." *Medical Physics* 30(9): 2553-2558. [p. 8]

- Roberts, S. A. and J. H. Hendry (1993). "The Delay before Onset of Accelerated Tumor-Cell Repopulation During Radiotherapy - a Direct Maximum-Likelihood Analysis of a Collection of Worldwide Tumor-Control Data." *Radiotherapy and Oncology* 29(1): 69-74. [p. 147]
- Roberts, S. A. and J. H. Hendry (1998). "A realistic closed-form radiobiological model of clinical tumor-control data incorporating intertumor heterogeneity." *International Journal of Radiation Oncology Biology Physics* 41(3): 689-699. [pp. 19, 159, 160, 162]
- Roberts, S. A., J. H. Hendry, et al. (1994). "The Influence of Radiotherapy Treatment Time on the Control of Laryngeal-Cancer - a Direct Analysis of Data from 2 British-Institute-of-Radiology Trials to Calculate the Lag Period and the Time Factor." *British Journal of Radiology* 67(800): 790-794. [p. 147]
- Roesink, J. M., M. A. Moerland, et al. (2001). "Quantitative dose-volume response analysis of changes in parotid gland function after radiotherapy in the head-and-neck region." *International Journal of Radiation Oncology Biology Physics* 51(4): 938-946. [pp. 116, 117, 130]
- Rudat, V., A. Dietz, et al. (1999). "Acute and late toxicity, tumour control and intrinsic radiosensitivity of primary fibroblasts in vitro of patients with advanced head and neck cancer after concomitant boost radiochemotherapy." *Radiotherapy and Oncology* 53(3): 233-245. [p. 159]
- Sachs, R. K. and D. J. Brenner (1998). "The mechanistic basis of the linear-quadratic formalism." *Medical Physics* 25(10): 2071-2073. [p. 144]
- Sachs, R. K., P. Hahnfeld, et al. (1997). "The link between low-LET dose-response relations and the underlying kinetics of damage production/repair/misrepair." *International Journal of Radiation Biology* 72(4): 351-374. [p. 144]
- Sachs, R. K., W. F. Heidenreich, et al. (1996). "Dose timing in tumor radiotherapy: Considerations of cell number stochasticity." *Mathematical Biosciences* 138(2): 131-146. [p. 17]
- Samant, S. S., W. Zheng, et al. (2002). "Verification of multileaf collimator leaf positions using an electronic portal imaging device." *Medical Physics* 29(12): 2900-2912. [p. 7]
- Sanchez-Nieto, B. and A. E. Nahum (2000). "Bioplan: software for the biological evaluation of radiotherapy treatment plans." *Medical Dosimetry* 25(2): 71-76. [p. 122]
- Sanchez-Nieto, B., A. E. Nahum, et al. (2001). "Individualization of dose prescription based on normal-tissue dose-volume and radiosensitivity data." *International Journal of Radiation Oncology Biology Physics* 49(2): 487-499. [pp. 122, 159]
- Sandilos, P., A. Angelopoulos, et al. (2004). "Dose verification in clinical IMRT prostate incidents." *International Journal of Radiation Oncology Biology Physics* 59(5): 1540-1547. [p. 8]
- Sastre-Padro, M., U. A. van der Heide, et al. (2004). "An accurate calibration method of the multileaf collimator valid for conformal and intensity modulated radiation treatments." *Physics in Medicine and Biology* 49(12): 2631-2643. [p. 7]
- Sawant, A., H. Zeman, et al. (2002). "Theoretical analysis and experimental evaluation of a CsI(Tl) based electronic portal imaging system." *Medical Physics* 29(6): 1042-53. [p. 9]

- Schilstra, C. and H. Meertens (2001). "Calculation of the uncertainty in complication probability for various dose-response models, applied to the parotid gland." *International Journal of Radiation Oncology Biology Physics* 50(1): 147-158. [p. 132]
- Scrimger, R., P. Stavrev, et al. (2002). "Physical parameters to describe flow normal tissue complication probability (NTCP) for parotid gland irradiation with intensity-modulated radiotherapy (IMRT)." Presented at the Canadian Association of Radiation Oncologists (CARO) conference, Toronto. [p. 130]
- Seppenwoolde, Y., J. V. Lebesque, et al. (2003). "Comparing different NTCP models that predict the incidence of radiation pneumonitis." *International Journal of Radiation Oncology Biology Physics* 55(3): 724-735. [p. 130, 135]
- Severin, D., S. Connors, et al. (2003). "Breast radiotherapy with inclusion of internal mammary nodes: A comparison of techniques with three-dimensional planning." *International Journal of Radiation Oncology Biology Physics* 55(3): 633-644. [p. 135]
- Sharpe, M. B. and J. J. Battista (1993). "Dose calculations using convolution and superposition principles: the orientation of dose spread kernels in divergent x-ray beams." *Medical Physics* 20(6): 1685-94. [pp. 97, 98]
- Sheikh-Bagheri, D. and D. W. Rogers (2002). "Monte Carlo calculation of nine megavoltage photon beam spectra using the BEAM code." *Medical Physics* 29(3): 391-402. [pp. 34, 52, 53]
- Siebers, J. V., J. O. Kim, et al. (2004). "Monte Carlo computation of dosimetric amorphous silicon electronic portal images." *Medical Physics* 31(7): 2135-2146. [pp. 10, 54, 87]
- Siewerdsen, J. H. and D. A. Jaffray (1999). "A ghost story: Spatio-temporal response characteristics of an indirect-detection flat-panel imager." *Medical Physics* 26(8): 1624-1641. [p. 40]
- Slonina, D., M. Klimek, et al. (2000). "Comparison of the radiosensitivity of normal-tissue cells with normal-tissue reactions after radiotherapy." *International Journal of Radiation Biology* 76(9): 1255-1264. [pp. 19, 159]
- Soderstrom, S., A. Gustafsson, et al. (1993). "The Clinical-Value of Different Treatment Objectives and Degrees of Freedom in Radiation-Therapy Optimization." *Radiotherapy and Oncology* 29(2): 148-163. [p. 5]
- Stausbol-Gron, B., S. M. Bentzen, et al. (1999). "In vitro radiosensitivity of tumour cells and fibroblasts derived from head and neck carcinomas: mutual relationship and correlation with clinical data." *British Journal of Cancer* 79(7-8): 1074-1084. [pp. 19, 159]
- Stavrev, P., D. Hristov, et al. (2003). "Inverse treatment planning by physically constrained minimization of a biological objective function." *Medical Physics* 30(11): 2948-2958. [p. 16]
- Stavrev, P., A. Niemierko, et al. (2001). "The application of biological models to clinical data." *Physica Medica* 17(2): 71-82. [pp. 78, 122, 126, 130, 133, 135, 137, 150, 167, 168]
- Stavrev, P., N. Stavreva, et al. (2001). "Generalization of a model of tissue response to radiation based on the idea of functional subunits and binomial statistics." *Physics in Medicine and Biology* 46(5): 1501-1518. [pp. 125, 151, 164]

- Stavrev, P., B. Warkentin, et al. (2002). "Evaluation of a closed-form tumor control probability solution." *Medical Physics* 29(6): 1294-1294. [p. 21]
- Stavreva, N., P. Stavrev, et al. (2002). "Derivation of the expressions for gamma(50) and D50 for different individual TCP and NTCP models." *Physics in Medicine and Biology* 47(20): 3591-3604. [pp. 20, 155]
- Stavreva, N., B. Warkentin, et al. (2005). "Investigating the effect of clonogen resensitization on the tumor response to fractionated external radiotherapy." Accepted for publication in *Medical Physics*. [pp. 21, 187]
- Stavreva, N. A., P. V. Stavrev, et al. (2003). "Investigating the effect of cell repopulation on the tumor response to fractionated external radiotherapy." *Medical Physics* 30(5): 735-742. [pp. 21, 128, 146, 185, 186]
- Steciw, S., B. Warkentin, et al. (2005). "Three-dimensional IMRT verification with a flat-panel EPID." Accepted for publication in *Medical Physics*. [p. 20]
- Suit, H., S. Skates, et al. (1992). "Clinical Implications of Heterogeneity of Tumor Response to Radiation-Therapy." *Radiotherapy and Oncology* 25(4): 251-260. [p. 159]
- Sultanem, K., H. K. Shu, et al. (2000). "Three-dimensional intensity-modulated radiotherapy in the treatment of nasopharyngeal carcinoma: The University of California-San Francisco experience." *International Journal of Radiation Oncology Biology Physics* 48(3): 711-722. [p. 3]
- Takahashi, S. (1965). "Conformation radiotherapy: Rotation techniques as applied to radiography and radiotherapy of cancer." *Acta Radiologica Supplement*(242): 1-42. [p. 5]
- Thames, H. D. and J. H. Hendry (1987). Fractionation in Radiotherapy. Philadelphia, Taylor & Francis. [pp. 146, 147]
- Tome, W. A. and J. F. Fowler (2000). "Selective boosting of tumor subvolumes." *International Journal of Radiation Oncology Biology Physics* 48(2): 593-599. [p. 15]
- Travis, E. L. and S. L. Tucker (1987). "Isoeffect Models and Fractionated Radiation-Therapy." *International Journal of Radiation Oncology Biology Physics* 13(2): 283-287. [p. 147]
- Tsai, J. S., D. E. Wazer, et al. (1998). "Dosimetric verification of the dynamic intensity-modulated radiation therapy of 92 patients." *International Journal of Radiation Oncology Biology Physics* 40(5): 1213-30. [pp. 5, 7-9]
- Tucker, S. L., H. D. Thames, et al. (1990). "How Well Is the Probability of Tumor Cure after Fractionated-Irradiation Described by Poisson Statistics." *Radiation Research* 124(3): 273-282. [p. 183]
- van Dyk, J. (1999). The Modern Technology of Radiation Oncology. Madison, WI, Medical Physics Publishing. [p. 9]
- Van Esch, A., T. Depuydt, et al. (2004). "The use of an aSi-based EPID for routine absolute dosimetric pre-treatment verification of dynamic IMRT fields." *Radiotherapy and Oncology* 71(2): 223-234. [p. 10]
- Van Esch, A., B. Vanstraelen, et al. (2001). "Pre-treatment dosimetric verification by means of a liquid-filled electronic portal imaging device during dynamic delivery of intensity modulated treatment fields." *Radiotherapy and Oncology* 60(2): 181-190. [p. 9]

- van Luijk, P., T. C. Delvigne, et al. (2003). "Estimation of parameters of dose-volume models and their confidence limits." *Physics in Medicine and Biology* **48**(13): 1863-1884. [p. 18]
- Varian Medical Systems (2000). *PortalVision aS500 Rel.6, Reference Manual*. Palo Alto, CA. [pp. 36, 46]
- Verellen, D., N. Linthout, et al. (1997). "Initial experience with intensity-modulated conformal radiation therapy for treatment of the head and neck region." *International Journal of Radiation Oncology Biology Physics* **39**(1): 99-114. [p. 5]
- Vieira, S. C., M. L. P. Dirkx, et al. (2002). "Fast and accurate leaf verification for dynamic multileaf collimation using an electronic portal imaging device." *Medical Physics* **29**(9): 2034-2040. [p. 9]
- Vieira, S. C., M. L. P. Dirkx, et al. (2003). "Dosimetric verification of x-ray fields with steep dose gradients using an electronic portal imaging device." *Physics in Medicine and Biology* **48**(2): 157-166. [pp. 9, 11]
- Vogler, H. and H. P. Beckbornholdt (1988). "Radiotherapy of the Rhabdomyosarcoma R1h of the Rat - Kinetics of Cellular Inactivation by Fractionated-Irradiation." *International Journal of Radiation Oncology Biology Physics* **14**(2): 317-325. [p. 193]
- von Wittenau, A. E. S., C. M. Logan, et al. (2002). "Blurring artifacts in megavoltage radiography with a flat-panel imaging system: Comparison of Monte Carlo simulations with measurements." *Medical Physics* **29**(11): 2559-2570. [pp. 56-8]
- Wang, J. Z., M. Guerrero, et al. (2003). "How low is the alpha/beta ratio for prostate cancer?" *International Journal of Radiation Oncology Biology Physics* **55**(1): 194-203. [p. 181]
- Wang, X., S. Spirou, et al. (1996). "Dosimetric verification of intensity-modulated fields." *Medical Physics* **23**(3): 317-27. [p. 9]
- Wang, X. H., R. Mohan, et al. (1995). "Optimization of Intensity-Modulated 3d Conformal Treatment Plans Based on Biological Indexes." *Radiotherapy and Oncology* **37**(2): 140-152. [p. 16]
- Warkentin, B., P. Stavrev, et al. (2004). "A TCP-NTCP estimation module using DVHs and known radiobiological models and parameter sets." *Journal of Applied Clinical Medical Physics* **5**(1): 50-63. [pp. 20, 122]
- Warkentin, B., S. Steciw, et al. (2003). "Dosimetric IMRT verification with a flat-panel EPID." *Medical Physics* **30**(12): 3143-3155. [p. 20]
- Webb, S. (1994). "Optimum Parameters in a Model for Tumor-Control Probability Including Interpatient Heterogeneity." *Physics in Medicine and Biology* **39**(11): 1895-1914. [p. 159]
- Webb, S. (1998). "Intensity-modulated radiation therapy: Dynamic MLC (DMLC) therapy, multisegment therapy and tomotherapy - An example of QA in DMLC therapy." *Strahlentherapie Und Onkologie* **174**: 8-12. [p. 2]
- Webb, S., P. M. Evans, et al. (1994). "A Proof That Uniform Dose Gives the Greatest TCP for Fixed Integral Dose in the Planning Target Volume." *Physics in Medicine and Biology* **39**(11): 2091-2098. [p. 15]

- West, C. M. L., S. E. Davidson, et al. (1998). "The intrinsic radiosensitivity of normal and tumour cells." *International Journal of Radiation Biology* 73(4): 409-413. [p. 159]
- Willner, J., K. Baier, et al. (2002). "Dose, volume, and tumor control predictions in primary radiotherapy of non-small-cell lung cancer." *International Journal of Radiation Oncology Biology Physics* 52(2): 382-389. [p. 130]
- Wu, Q. W., R. Mohan, et al. (2002). "Optimization of intensity-modulated radiotherapy plans based on the equivalent uniform dose." *International Journal of Radiation Oncology Biology Physics* 52(1): 224-235. [p. 16]
- Yang, Y. and L. Xing (2003). "Using the volumetric effect of a finite-sized detector for routine quality assurance of multileaf collimator leaf positioning." *Medical Physics* 30(3): 433-441. [p. 7]
- Yang, Y. and L. Xing (2004). "Quantitative measurement of MLC leaf displacements using an electronic portal image device." *Physics in Medicine and Biology* 49(8): 1521-1533. [p. 7]
- Zagars, G. K., T. E. Schultheiss, et al. (1987). "Inter-Tumor Heterogeneity and Radiation Dose-Control Curves." *Radiotherapy and Oncology* 8(4): 353-362. [p. 159]
- Zaider, M. (1998). "Sequel to the discussion concerning the mechanistic basis of the linear quadratic formalism." *Medical Physics* 25(10): 2074-2075. [p. 144]
- Zaider, M. (1998). "There is no mechanistic basis for the use of the linear-quadratic expression in cellular survival analysis." *Medical Physics* 25(5): 791-792. [p. 144]
- Zaider, M. and G. N. Minerbo (2000). "Tumour control probability: a formulation applicable to any temporal protocol of dose delivery." *Physics in Medicine and Biology* 45(2): 279-293. [pp. 122, 123, 127, 183, 185]
- Zeidan, O. A., J. G. Li, et al. (2004). "Verification of step-and-shoot IMRT delivery using a fast video-based electronic portal imaging device." *Medical Physics* 31(3): 463-476. [p. 9]
- Zhou, S. M. and L. J. Verhey (1994). "A Robust Method of Multileaf Collimator (MLC) Leaf-Configuration Verification." *Physics in Medicine and Biology* 39(11): 1929-1947. [p. 7]